A Doctoral Dissertation

RESIDUAL STRESS ANALYSIS AND FATIGUE STRENGTH ASSESSMENT OF WELDED JOINTS WITH ULTRASONIC IMPACT TREATMENT (UIT)

超音波衝撃処理(UIT)を施した溶接継手の残留応力解析
及び疲労強度評価に関する研究

Graduate School of Engineering
Yokohama National University

Kuilin Yuan
袁奎霖

September 2015

RESIDUAL STRESS ANALYSIS AND FATIGUE STRENGTH ASSESSMENT OF WELDED JOINTS WITH ULTRASONIC IMPACT TREATMENT (UIT)

By

Kuilin Yuan

B.Sc., Dalian University of Technology, 2010

M.Sc., Yokohama National University, 2012

Submitted to the Graduate School of Engineering,

Yokohama National University,

In partial fulfillment of the requirements for the degree of

Doctor of Engineering

September 2015

ACKNOWLEDGEMENTS

I would like to express my deepest gratitude to my academic supervisor, *Professor Yoichi Sumi* for his generous support, patient guidance, invaluable suggestions and enthusiastic encouragement throughout all stages during this five-year study. Without his positive and supportive way of guiding my thesis, this journey would never have found its ways to completion. I am also honored by the distinction of being his last doctoral student.

I would like also to express gratefulness to my co-research supervisor, *Professor Yasumi Kawamura* for his valuable discussions, comments and help throughout this work. Sincere thanks go to other members of the doctoral committee, *Professor Tetsuo Okada*, *Professor Koji Takahashi, Professor Makoto Arai* and *Professor Kazuo Suzuki,* for their helpful comments and suggestions.

I acknowledge the technical discussions and information on UIT equipment provided by *Dr. Hiroshi Shimanuki* and *Dr. Teppei Okawa* of Nippon Steel & Sumitomo Metal Corporation.

I wish to thank *Mr. Shunichi Michiyama* for his considerate preparation and assistance of computers and software during this study period. I also wish to thank for their consistent help in a pleasant environment atmosphere from the all students of the Smart Structure and Systems laboratory.

Finally, I would like to thank my parents, *Chengliang Yuan* and *Yue Jin,* and my girlfriend, *Aimei Li*, for their love, support and encouragement during this hard period of my life. I would not have completed this study without their belief and trust in me.

ABSTRACT

Many steel structures such as ships, offshore structures and bridges are fabricated by welding steel materials together. The welds in structures are normally considered as the weakest points in terms of fatigue failure due to cyclic loading. The reason for this is that the weld zone is susceptible to high local stress concentration and tensile welding residual stress, and there is the possibility of various defects such as undercuts or cold laps. In shipbuilding industry, there is a growing tendency to pursue an increase in the performance to weight ratio by applying high strength steels. However, the fatigue strength of the most common welded joints normally does not increase with steel strength and can thus be a limiting factor in the design of high strength steel structures. With the aim of improving fatigue strength of the welded joints, the different post-weld improvement methods have been recently paid considerable attention.

Ultrasonic impact treatment (UIT) is a relatively novel post-weld improvement method by applying high frequency mechanical impacts in combination with ultrasonic oscillations in the treated welded joints. The fatigue strength improved by UIT is attributed to the improved weld toe geometry, micronized metal structures of the weld toe surface and induced beneficial compressive residual stress. In order to better understand the effects of UIT on fatigue performance of welded joints, its mechanism has been experimentally investigated in many studies. It has been demonstrated that the compressive residual stress and reduction of local stress concentration by enlarging weld toe radius are the dominant factors among the improvement mechanism. In addition, the ultrasonic vibration superimposed by UIT on metals has an acoustic softening effect on material properties undergoing deformation, leading to a better treatment efficiency of UIT compared to other post-weld treatments. Normally the experimentally methods for residual stress measurements in UIT-treated welded joints need considerable cost, time and skillful technique. The available numerical simulation method for predicting UIT-

induced residual stress distribution has been expected as an alternative of experimental measurements.

The objective of this study is to numerically predict the residual stress distributions in the welded joints before and after UIT treatment, in order to quantitatively evaluate the fatigue strengths improved by UIT. The first step of this research is to establish a numerical prediction method of welding residual stress by means of uncoupled thermo-mechanical finite element code SYSWELD. In order to verify the accuracy of welding residual stress analysis, a single weld bead laid down on the top surface of an austenitic stainless steel specimen, which is the benchmark problem in the frame of European round-robin project NeT, is selected as analysis object. The three dimensional finite element model is employed, in order to accurately capture the temperature field and welding residual stress distributions. By employing the combination of kinematic hardening model and hypothetical annealing temperature of 800 ^{o}C, the predicted welding residual stress shows best agreement with measured results.

The second step is to establish one three dimensional simulation approach for UIT process of welded joints, including the thermo-mechanical welding simulation by SYSWELD, transfer of the predicted distributions of welding residual stress and plastic strain to the initial-stress state of a dynamic elastic-plastic FE model of UIT by explicit method in LS-DYNA. The high frequency impacts induced by uninterrupted oscillations during ultrasonic impact and ultrasound induced material softening are considered as the most important aspects of the UIT technology. To construct the UIT FE model, one simplified model to describe the ultrasonic impact phenomenon is proposed based on the existing experimental observations. The effects of mesh sensitivity, material damping and yield stress reduction due to acoustic softening on predicted peening-induced residual stress distributions have been investigated in advance by one preliminary numerical study. In order to verify the effectiveness of the proposed simulation approach, one UIT-treated non-load-carrying cruciform joint, which has been used by Suzuki et al. (2014) for residual stress measurement by means of X-ray and neutron diffraction techniques, is selected as analysis object. The yield stress reduction due to acoustic softening effect is indirectly calibrated as 40% with the measured UIT-treated weld toe shape by trial and

error. The predicted internal residual stress distributions in the cruciform joint before and after UIT are compared with experimental results, showing a fairly good agreement with each other. In addition, the simulations of UIT-induced compressive residual stress relaxation after tensile or compressive preloads are carried out by implicit quasi-static analysis in LS-DYNA. Relatively high compressive residual stresses are predicted to be remained even after the occurrence of preloads.

The final step of this study is to evaluate the improved fatigue strength of non-load-carrying cruciform joints by UIT, using a fracture mechanics based analytical method. Considering the effect of weld toe geometry on the local stress concentration at the weld toes of as-weld and UIT-treated joints, the applied stress distributions along assumed crack path are estimated by the combination of elastic finite element analysis and empirical formulas. The stress intensity factors of surface crack under predicted thickness-varying applied and residual stresses are calculated based on weight function method standardized by code API 579-1. The modified Paris-Elber law is employed to predict the fatigue crack growth life of the welded joint. The calculation series as-weld (R=0.1), UIT (R=0.1 and 0.5) and UIT with preload (R=0.1) are performed respectively, of which the accuracy has been confirmed with corresponding fatigue test results. The results not only clearly distinguish the difference of the fatigue strengths of as-weld and UIT welds, but also show the influence of preload and stress ratio on the UIT improvement stability, so that the proposed numerical analysis method may provide an effective tool to optimize the UIT-process in engineering structures.

LIST OF FIGURES

Figure 1.1	Main benefits of ultrasonic impact treatment (UIT).	4
Figure 1.2	UIT treatment in 320,000 ton ore carrier “Brazil Maru” [4].	4
Figure 2.1	Classification of different post-weld improvement methods [11].	8
Figure 2.2	Depth and width of the groove after burr grinding [12].	9
Figure 2.3	(a) Typical position of torch (b) resulted weld profile after TIG dressing [20].	10
Figure 2.4	Hammer peening operation [12].	11
Figure 2.5	Variation of strain and stress in weld metal during cooling process; (a) strain, (b) stress [23].	13
Figure 2.6	Esonix® ultrasonic impact treatment equipment [26].	15
Figure 2.7	Ultrasonic impact treatment of a weld toe in progress [28].	15
Figure 2.8	Mechanism of UIT [3].	17
Figure 2.9	Oscilloscope picture of the impacts induced by Esonix UIT [3].	18
Figure 2.10	Indentation areas with ultrasonic and ultrasonic-free impact [3].	19
Figure 2.11	Distribution of plastic deformation during ultrasonic impact [31].	20
Figure 2.12	Ultrasonic-assisted compression test; (a) schematic diagram of test devices, (b) measured stress-strain data from static-ultrasonic compression test with two intervals of ultrasonic excitation [36].	21
Figure 2.13	Measured stress-strain curves of tensile specimen of stainless steel 315 with and without ultrasonic vibration [37].	22
Figure 2.14	Ultrasonic-assisted tension test; (a) schematic diagram of tests with different modes, (b) measured force-deformation curves [3].	23
Figure 2.15	S-N curves under different conditions of stress ratio [44].	25
Figure 2.16	(a) Surface residual stress change near the weld toe by preload, (b) S-N curves for fatigue tests with and without preload [48].	27
Figure 2.17	Results of fatigue tests with different time for application of ultrasonic peening [47].	28
Figure 2.18	(a) Cut-off from the load-time history, (b) S-N curves of fatigue	29

tests under constant and variable amplitude loading [50].

Figure 2.19 S-N curves of fatigue tests with S355 and S700 grade steels [30]. 30

Figure 2.20 Proposed maximum increases in the number of FAT classes as a function of σ_Y [51]. 31

Figure 2.21 S-N curves of fatigue tests with different corrosion time [53]. 32

Figure 2.22 Failures observed in specimens under CA loading; (a) plate edge failure, (b) start/stop position failure, (c) fretting failure in the gripping end, (d) root side failure [50]. 33

Figure 2.23 Fractured surfaces of stained specimens; left: as-weld under CA loading, middle: as-weld under VA loading, right: peened under CA loading [55]. 34

Figure 2.24 S-N curves for Weldox 420 fillet welds in the as-weld and improved conditions [3]. 35

Figure 2.25 Examples of the weld profiles of as-weld, burr grinding, TIG dressing and UIT [56]. 36

Figure 2.26 S-N curves for S700 T-joints in the as-weld and improved conditions [56]. 36

Figure 2.27 In-depth residual stress profiles in base metal specimens; (a) 25.4mm thick specimen by x-ray method, (b) in 12.7mm thick specimen by neutron diffraction method [6]. 37

Figure 2.28 In-depth residual stress profiles in UIT-treated butt-weld joint [57]. 38

Figure 2.29 In-depth residual stress distributions during fatigue test [58]. 39

Figure 2.30 Effect of maximum nominal stress on residual stress change at the weld toe due to cyclic loading [59]. 39

Figure 2.31 Predicted and measured in-depth residual stress profiles [60]. 41

Figure 2.32 Quasi-static FE model for UIT process [62]. 41

Figure 2.33 Dynamic FE model for UIT process [63]. 42

Figure 3.1 Goldak's double ellipsoidal heat source flux distribution [65] 45

Figure 3.2 Comparison of isotropic and kinematic hardening models. 47

Figure 3.3 Schematic diagram of NeT single weld bead-on-plate specimen. 49

Figure 3.4 Finite element model; (a) 3D mesh, (b) mesh on middle section. 51

Figure 3.5 (a) Temperature-dependent thermal properties of stainless steel 316L, (b) Temperature-dependent mechanical properties of stainless steel 316L [64]. 52

Figure 3.6 Comparison of macrostructure between prediction and 53

measurement.

Figure 3.7 Typical contour plots of predicted residual stress distributions; (a) transverse residual stress, (b) longitudinal residual stress. 55

Figure 3.8 Comparison of the predicted stresses with measured data along D2; (a) transverse residual stress, (b) longitudinal residual stress. 56

Figure 3.9 Comparison of the predicted stresses with measured data along B2; (a) transverse residual stress, (b) longitudinal residual stress. 57

Figure 3.10 Comparison of the predicted stresses with measured data along BD; (a) transverse residual stress, (b) longitudinal residual stress. 58

Figure 4.1 Modelling of ultrasonic impact. 62

Figure 4.2 Finite element model used for preliminary investigation (a) 3D mesh, (b) mesh on section A-A. 64

Figure 4.3 Measured geometry of the 3mm diameter pins [62]. 65

Figure 4.4 Illustration of in-depth (path 1) and on-surface (path 2) paths through which the numerical data have been extracted. 66

Figure 4.5 Effect of minimum element size on simulated residual stress profile; (a) in-depth path (path 1), (b) on-surface path (path 2). 67

Figure 4.6 Effect of mass proportional damping on the stabilization of surface residual stress; (a) stress history of node at impact center during first 5 times of impacts, (b) stress history of node at impact center during 5^{th} impact . 69

Figure 4.7 Mechanical properties considering acoustic softening. 71

Figure 4.8 Evolution of indentation depth considering acoustic softening. 72

Figure 4.9 Evolution of in-depth residual stress profiles considering acoustic softening; (a) η=0%, (b) η=20%, (c) η=40%, (d) η=60%. 73

Figure 4.10 Flowchart of welding-UIT process simulation. 75

Figure 4.11 Geometry and dimensions of UIT specimen. 76

Figure 4.12 Finite element model for welding simulation. 78

Figure 4.13 (a) Temperature-dependent thermal properties of structural steel SM490, (b) Temperature-dependent mechanical properties of structural steel SM490 [64]. 79

Figure 4.14 Constraint conditions of UIT process [82], [83]. 80

Figure 4.15 Finite element model for UIT simulation. 81

Figure 4.16 Mechanical properties considering acoustic softening. 82

Figure 4.17 (a) Schematic illustration of UIT-treated cruciform joint subjected to preload, (b) Load history of preload. 83

Figure 4.18	Predicted highest temperature distribution.	84
Figure 4.19	Contour plots of transverse residual stress; (a) predicted by SYSWELD, (b) remapped in LS-DYNA.	85
Figure 4.20	Predicted profiles of as-weld transverse residual stress; (a) in-depth (path1), (b) on top surface (path 2).	86
Figure 4.21	Determination of acoustic softening by comparing the treated weld toe shape; (a) simulated with η=0%, (b) simulated with η=40%, (c) measured by Suzuki et al [78].	88
Figure 4.22	Evolution of in-depth transverse residual stress distributions during one ultrasonic impact; (a) simulated without acoustic softening, (b) simulated with acoustic softening η=40%.	89
Figure 4.23	Transverse residual stress distributions and plastic deformation at the weld toe; (a) as-weld, (b) UIT with η=40%.	91
Figure 4.24	Distribution of transverse residual stress of as-weld and UIT specimens in the depth direction, and comparison with experimental results [78].	92
Figure 4.25	Comparison of predicted surface residual stress change nearby the weld toe by preload with experiment [48].	93
Figure 4.26	Predicted residual stress change near the weld toe by tensile preloads; (a) on surface after preloads, (b) in depth after preloads, (c) in depth at the maximum values of preloads.	94
Figure 4.27	Predicted residual stress change near the weld toe by compressive preloads; (a) on surface after preloads, (b) in depth after preloads, (c) in depth at the maximum values of preloads.	96
Figure 5.1	Semi-elliptical surface crack in a finite thickness plate.	99
Figure 5.2	Schematic illustration of principle of superposition.	100
Figure 5.3	Piece-wise representation of specified stress data at discrete locations.	106
Figure 5.4	Applied stress distributions on the crack surface .	108
Figure 5.5	Comparison of boundary correction factors obtained from weight function method and FEM data for constant stress distribution; (a) deepest point, (b) surface point .	110
Figure 5.6	Comparison of boundary correction factors obtained from weight function method and FEM data for linear stress distribution; (a) deepest point, (b) surface point .	111
Figure 5.7	Comparison of boundary correction factors obtained from weight function method and FEM data for quadratic stress distribution;(a) deepest point, (b) surface point .	112

Figure 5.8	Comparison of boundary correction factors obtained from weight function method and FEM data for cubic stress distribution ;(a) deepest point, (b) surface point.	113
Figure 5.9	Predicted surface crack growth lives in flat plate under $\Delta\sigma_{app}$= 200MPa and R=0.0.	116
Figure 5.10	Predicted surface crack shape evolution under tension.	117
Figure 5.11	Surface crack at the weld toe of cruciform joint.	118
Figure 5.12	Weld geometry parameters for non-load-carrying cruciform joint under tension load.	120
Figure 5.13	Symbol and coordinate used in Glinka's equation.	121
Figure 5.14	Assumed stress distribution near the weld toe.	121
Figure 5.15	Validation of predicted S-N curves of as-weld and UIT joint (R=0.1).	123
Figure 5.16	Predicted evolution of surface crack shapes.	123
Figure 5.17	Effect of high stress ratio on fatigue strength improvement by UIT.	124
Figure 5.18	Effect of preload on fatigue strength improvement by UIT.	125

LIST OF TABLES

Table 2.1	Overview of fatigue life improvement factors by selected guidelines.	8
Table 2.2	Specification of the 27 kHz UIT equipment [25, 30].	16
Table 2.3	Results of fatigue tests considering the stress ratio effect on UIT improvement.	26
Table 2.4	Summary of studies on numerical simulation of UIT.	40
Table 3.1	Welding process parameters of Task 1.	50
Table 3.2	Heat source parameters.	53
Table 4.1	Comparison of computational efficiency with different minimum element size.	66
Table 4.2	Hardening parameters in terms of stress-strain considering acoustic softening.	71
Table 4.3	Welding conditions.	76
Table 5.1	Fatigue strength at 2×10^6cyles (MPa).	125

CONTENTS

ACKNOWLEDGEMENTS **i**

ABSTRACT **ii**

LIST OF FIGURES **v**

LIST OF TABLES **x**

TABLES OF CONTENTS **xi**

CHAPTER 1: INTRODUCTION **1**

1.1 Background 1

1.2 Objectives 5

1.3 Overview of the thesis 5

CHAPTER 2: LITERATURE REVIEW **7**

2.1 Post-weld improvement methods 7

2.1.1 Burr grinding 9

2.1.2 Tungsten inert gas (TIG) dressing 10

2.1.3 Hammer peening 11

2.1.4 Shot peening 12

2.1.5 Low transformation temperature (LTT) welding wire 12

2.2 Ultrasonic impact treatment (UIT) 14

2.2.1 Equipment and mechanism 14

2.2.2 Acoustic softening effect 21

2.2.3 Experimental studies on fatigue strength improvement by UIT 25

2.2.3.1 Effect of stress ratio and preload 25

2.2.3.2 Effect of variable amplitude loading 28

2.2.3.3 Effect of material strength 29

2.2.3.4 Effect of corrosion 31
2.2.3.5 Failure modes and crack growth behavior 33
2.2.3.6 Comparison of UIT with other post-weld methods 35
2.2.4 Investigation of UIT-induced residual stress 37
2.2.4.1 Experimental measurement approach 37
2.2.4.2 Numerical simulation approach 40

CHAPTER 3: WELDING RESIDUAL STRESS ANALYSIS 43
3.1 Introduction 43
3.2 Heat source and thermal analysis 44
3.3 Mechanical analysis 46
3.4 Validation of bead-on-plate welding simulation 49
3.4.1 Experimental work in NeT Task 1 49
3.4.2 Finite element model 50
3.4.3 Welding residual stress results and observation 54

CHAPTER 4: NUMERICAL SIMULATION OF ULTRASONIC IMPACT TREATMENT 60
4.1 Introduction 60
4.2 Modelling of ultrasonic impact 61
4.3 Preliminary numerical investigations 63
4.3.1 Finite element model 63
4.3.2 Effect of mesh sensitivity 65
4.3.3 Effect of material damping 68
4.3.4 Effect of acoustic softening 70
4.4 Numerical simulation of UIT-treated welded joint 75
4.4.1 Analysis model and process parameters 76
4.4.2 Simulation of welding process 77
4.4.3 Simulation of UIT process 80
4.4.4 Simulation of preload after UIT 82
4.4.5 Validation of welding-UIT simulation 84

4.4.5.1 Results of welding simulation 84
4.4.5.2 Determination of acoustic softening parameter 87
4.4.5.3 Internal residual stress distributions before and after UIT 90
4.4.5.4 Residual stress distributions after preloads 93

CHAPTER 5: FATIGUE STRENGTH ASSESSMENT OF UIT WELDED JOINTS 98
5.1 Introduction 98
5.2 Stress intensity factor (SIF) of semi-elliptical surface crack in finite-thickness plate 99
5.2.1 The weight function method 99
5.2.2 Integration approach 105
5.2.3 Validation of SIF calculation 108
5.3 Fracture mechanics based method for fatigue strength assessment 114
5.3.1 Fatigue crack growth prediction method 114
5.3.2 Prediction of surface crack growth in flat plate 116
5.3.3 Prediction of fatigue strengths of cruciform joints 118
5.3.3.1 Estimation of stress concentration 119
5.3.3.2 Applied stress distribution along the crack path 120
5.3.3.3 Results of estimations and experiments (R=0.1) 122
5.3.3.4 Effect of high stress ratio and preload on UIT improvement 124

CHAPTER 6: CONCLUSIONS AND RECOMMENDATIONS 126
6.1 Conclusions 126
6.2 Recommendations for future work 128

REFERENCES 129
APPENDIX A: LIST OF PUBLICATIONS FROM THIS RESEARCH 138
APPENDIX B: KEYWORD FILE OF LS-DYNA 139

CHAPTER 1

INTRODUCTION

1.1 Background

Many steel structures such as ships, offshore structures and bridges are fabricated by welding steel materials together. The welds in structures are normally considered as the weakest points in terms of fatigue failure due to cyclic loading, which has been always been an important concern in the operations of ships, both in the maintenance of existing vessels and in the design of new vessels.The reasons for this are mainly due to the following three causes [1].

- Abrupt changes in geometry due to welding at discontinuities often cause geometric stress concentrations. The fatigue cracks are more likely to initiate and propagate in the vicinity of the weld zone, since the stresses are much higher there.
- Weld imperfections such as undercut and slag inclusions are always present in the welded joints, and most of these crack-like discontinuities are sharp enough to start growing right after the structure is subjected to cyclic loads. Thus the crack initiation stage of the fatigue life is reduced or eliminated.
- Tensile welding residual stresses are present in and near the weld toe because of the contraction of the weld metal during cooling and solidification, and can be as high as the yield stress in magnitude. These residual stresses accelerate fatigue crack growth by keeping the crack faces always open. Moreover, since the residual stress affect the fatigue behaviour in a similar manner to externally imposed mean loads, tensile applied

stress cycles become more damaging and compressive applied stress cycles can also contribute to fatigue cracking.

From the standpoint of cutting the life-cycle cost, reducing the environment impact and ensuring the safety, there is growing social expectation for ship structures to have a longer life and be lighter in weight. Accordingly, the application of high strength steel in ship structures is increasingly being sought [2]. However, the fatigue strength of the most common welded joints normally does not increase with steel strength and can thus be a limiting factor in the design of high strength steel structures. With the aim of improving fatigue strength of the welded joints, various efforts have been made, such as implementing structural design as well as post-weld improvement treatment methods, to prevent stress concentration and reduce welding tensile residual stress.

Ultrasonic impact treatment (UIT) is a novel post-weld treatment method, by using the combined effects of high frequency impacts and ultrasonic oscillations in the treated materials [3]. As shown in Fig.1.1, UIT is able to provide a more gradual transition from weld metal to base metal reducing the local stress concentration. The area being treated is highly plastically deformed which has the effects of both work hardening the material and introducing beneficial compressive residual stress. In addition, a thin layer of very fine microstructure with good wear and corrosion resistance, called as “white layer”, is created on the surface. Nowadays, in the field of shipbuilding UIT has been approved by some classification societies like ABS, LR and BV, and has begun to be applied at large shipbuilding companies, see Fig.1.2 [4].

Among the beneficial effects of UIT, the induced compressive residual stress and reduction of local stress concentration by enlarging weld toe radius are considered as the dominant ones [5]. In order to better understand the effects of UIT on fatigue performance of welded joints, some experimental studies have been performed with non-destructive measurements such as X-ray diffraction and neutron diffraction methods [6], [7], [8]. It has been found that the compressive residual stress is generated down to a depth of 1.5 to 2 mm, and the weld toe radius is averaged by 1.5 to 2mm with its groove depth of 0.1 to 0.2mm. A close relationship has been found between the measured groove depth and local

residual stress, indicating the groove depth as an important quality control parameter. In addition, very limited studies [1],[9] have demonstrated the ultrasonic vibration superimposed by UIT on metals has an acoustic softening effect on material properties undergoing deformation, leading to a better treatment efficiency of UIT compared to other post-weld treatments. Normally the experimental methods for residual stress measurements, which are still not fully developed and can be only accessed to limited research institutes, need considerable time, cost and skillful technique. It is practically impossible to obtain full field measurement of residual stress. As an alternative, the numerical simulation method is expected to predict the complete residual stress field before and after UIT process.

Various analytical approaches are used to assess the fatigue performance of weld structures and also the beneficial effects of post-weld improvement methods. In most codes and recommendations, variations of the "detail category" or "S-N curve" approach are employed. Recently, new IIW S-N curves for fatigue strengths of improved welded joints using high frequency mechanical impact (HFMI) methods including UIT has been prepared [10]. In these new S-N curves, the effect of stress ratio and base metal strength can be considered. However, this method may lead to non-conservative evaluation, because it ignores the possibility of compressive residual stress relaxation due to the preloads. Linear elastic fracture mechanics (LEFM) is considered as one of the most widely used approaches for making more precise predictions of the treatment benefit, which is suitable for considering the residual stress state after preloads that may be induced by static loading on a ship structures induced before service, such as tank test or launching.

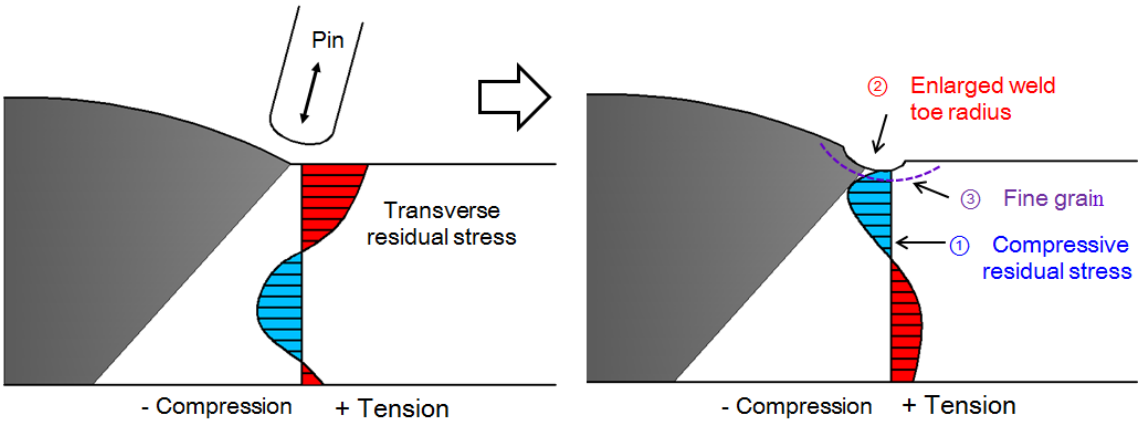

Figure 1.1 Main benefits of ultrasonic impact treatment (UIT).

Figure 1.2 UIT treatment in 320,000 ton ore carrier “Brazil Maru” (Nose & Okawa [4]).

1.2 Objectives

Based on the background presented in the previous section, the objectives of the current research are as follows:

1. To construct a new 3D simulation approach including welding residual stress analysis and numerical simulation of UIT-process for welded joint, taking actual treatment conditions and acoustic softening effect into account.
2. To validate the effectiveness of the proposed FE model with measured residual stress distributions and weld toe shape before and after UIT treatment.
3. To numerically investigate the effect of preloads on UIT-induced residual stress relaxation.
4. To quantitatively evaluate the fatigue strengths of as-weld and UIT-improved welded joints.
5. To identify the effects of preloads and high stress ratio, in order to keep UIT improvement in the case of ship structures.

1.3 Overview of the thesis

Following this introductory chapter, Chapter 2 of this thesis firstly gives a brief literature review on typical post-weld improvement methods, which have been divided according to main categories of weld geometry improvement and residual stress based methods and their subcategories. Short descriptions of some of the most common methods are presented. A detailed discussion of equipment and mechanism of ultrasonic impact treatment (UIT), and acoustic softening effect is followed. Some data of previous experimental studies on fatigue strength improvement by UIT are surveyed. At the end of Chapter 2, several experimental and numerical investigations of UIT-induced residual stresses are reviewed.

Chapter 3 describes the procedure of numerical simulation of welding process by means of uncoupled thermo-mechanical finite element (FE) method using commercial code SYSWELD [64]. In order to verify the accuracy of welding residual stress analysis, the predicted residual stress distributions in a single bead-on-plate specimen are compared to

the measured results of the benchmark problem in the project NeT [71],[72]. The effects of hardening models and hypothetical annealing temperature on predicted residual stress are investigated.

In Chapter 4, the details of numerical simulation of ultrasonic impact treatment by dynamic elastic-plastic FE code of LS-DYNA [77] are presented. To construct the UIT FE model, one simplified model to describe the ultrasonic impact phenomenon is first proposed based on existing experimental observations. The preliminary numerical studies are then performed to investigate the effect of mesh sensitivity, material damping and yield stress reduction due to acoustic softening on predicted peening-induced residual stress. One 3D numerical simulation of UIT process for a non-load-carrying cruciform joint is performed. The predicted residual stress distributions and weld toe shape before and after UIT are compared to the measured results in literature [48], [78]. In addition, the residual stress relaxation due to preloads is also numerically predicted by the proposed FE model.

In Chapter 5, the analytical work based on fracture mechanic to evaluate the improved fatigue strength of non-load-carrying cruciform joints by UIT is introduced. It begins with a stress intensity factor calculation for semi-elliptical surface crack based on weight-function method, which is verified with finite element solutions in literatures [86], [87], [88]. An analysis is then presented investigating the effects of weld toe geometry on the local stresses in the as-weld and UIT-treated welds by combination of elastic finite element analysis and empirical formulas. Considering the effects of local stress concentration and residual stress near the weld toe, the fatigue crack growth lives of welded joints are predicted by modified Paris-Elber law. In addition, the influences of preload and stress ratio on the fatigue strength improvement by UIT are also evaluated.

In Chapter 6, the conclusions and recommendations for future work are presented.

CHAPTER 2

LITERATURE REVIEW

2.1 Post-weld improvement methods

The improvement methods can generally be classified as weld geometry improvement methods and residual stress based methods. The former removes weld toe defects and/ or reduces the stress concentration. The latter introduces a compressive stress field in the area of crack initiation and propagation. Kirkhope et al. [11] have categorized the various available improvement techniques as shown in Fig.2.1.

There has been strong interest in the research community to quantify the benefits of different improvement techniques and prepare guidelines that represent good improvement procedure practice. One of the major documents is the International Institute of Welding (IIW) document "IIW Recommendations on Post Weld Improvement of Steel and Aluminium Structures", which covers improvement procedures and the S-N curves for four commonly applied post-weld treatment methods, i.e. burr-grinding, tungsten inert gas (TIG) dressing, hammer peening and needle peening [12]. Recently, new IIW guidance on fatigue strength improvement using high frequency mechanical impact (HFMI) methods including UIT has been prepared by Marquis et al. [10], [13]. Several ship rules and regulation today also have recommendations for different available methods (IACS [14], ABS [15], DNV-GL [16], and LR [17]), see Table 2.1.

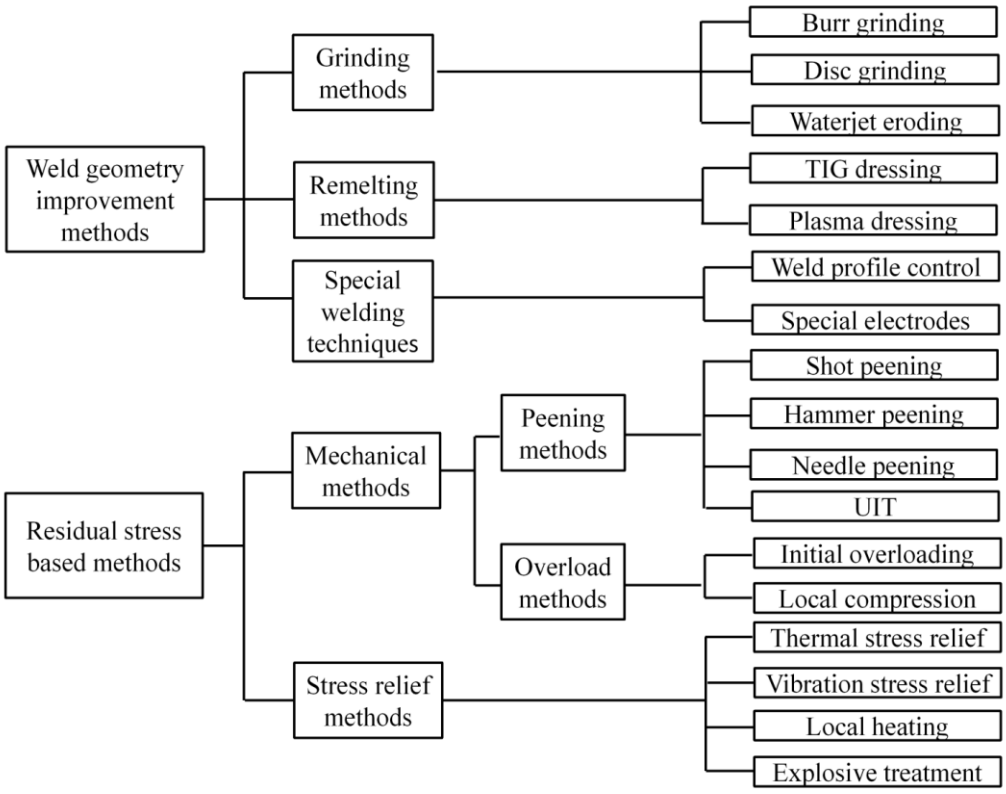

Figure 2.1 Classification of different post-weld improvement methods (Kirkhope et al. [11]).

Table 2.1 Overview of fatigue life improvement factors by selected guidelines*

Rules	Burr grinding	TIG dressing	Hammer peening	UIT
IIW XIII-1815-00 [12]	2.2	2.2	4.1	Not provided
IACS CSR [14]	2.2	Not provided	Not provided	Not provided
ABS Guide for the fatigue assessment of offshore structures [15]	2.0	Not provided	2.0	2.0
DNV-GL RP-C203 [16]	$0.01\sigma_Y$ (σ_Y**≤350MPa) 3.5 (σ_Y>350MPa)	$0.01\sigma_Y$ (σ_Y≤350MPa) 3.5 (σ_Y>350MPa)	$0.011\sigma_Y$ (σ_Y≤350MPa) 4.0 (σ_Y>350MPa)	Not provided
LR Shipright FDA [17]	2.0	2.0	1.3	2.5 (σ_Y≤315MPa) 3.5 (σ_Y>315MPa)

* No improvement can be expected if the potential fatigue failure arise from weld root.

** σ_Y: characteristic yield strength of the actual material.

2.1.1 Burr grinding

Burr grinding is carried out using a high speed pneumatic, hydraulic or electric grinder with rotational speed from 15000 to 40000 rpm. The primary aim of burr grinding is to remove weld toe defects from which fatigue cracks propagate. By removing these defects a new crack initiation period is introduced to fatigue endurance of the structures [18], [19]. The second benefit in terms of fatigue performance is achieved by reducing the local stress concentration at the weld toe by giving a favourable weld shape. Therefore, material is removed to a depth of at least of 0.5mm below any visible undercut, but should not exceed 2.0mm or 7% of the plate thickness, see Fig.2.2.

Burr grinding are very effective, reliable and use readily available tools, however, its disadvantages are slow, expensive and hard to maintain quality [11].

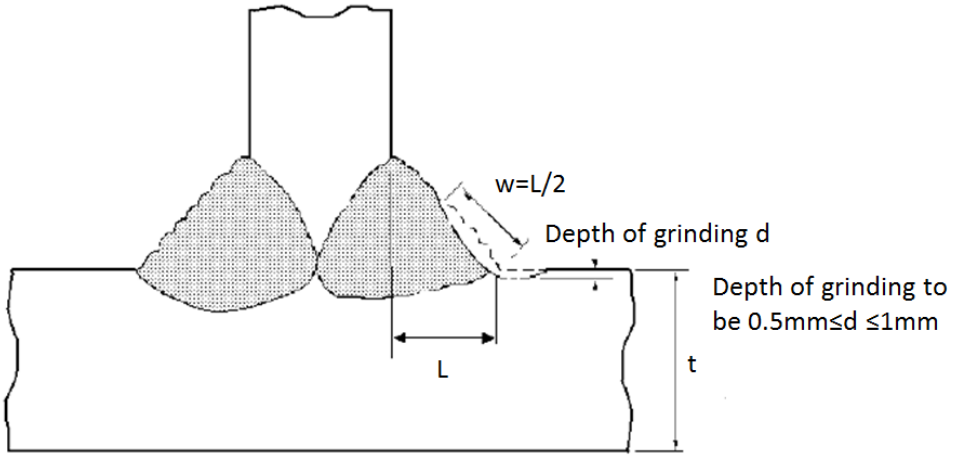

Figure 2.2 Depth and width of the groove after burr grinding (Haagensen & Maddox [12]).

2.1.2 Tungsten inert gas (TIG) dressing

Similar to burr grinding, the aim of TIG dressing is to remove the weld toe flaws by re-melting the weld toe area and reduce the local stress concentration effect by forming a smooth transition between the plate and the weld face. In this technique, standard TIG welding equipment can be used without the additional of any filler material; at typical heat inputs of 1.0-2.0 kJ/mm. Argon is the most commonly used shielding gas and the addition of helium could be a better choice to obtain a larger pool of melted metal due to a higher heat input [20]. Normally the best result is obtained when the arc center is located a small distance away from the weld toe, as indicated in Fig.2.3 (a), and a macrosection of an optimum weld toe shape is shown in Fig.2.3(b). TIG dressing in general can be highly effective for improving fatigue performance but they do require a high level of skill and proper cleaning of the weld [11].

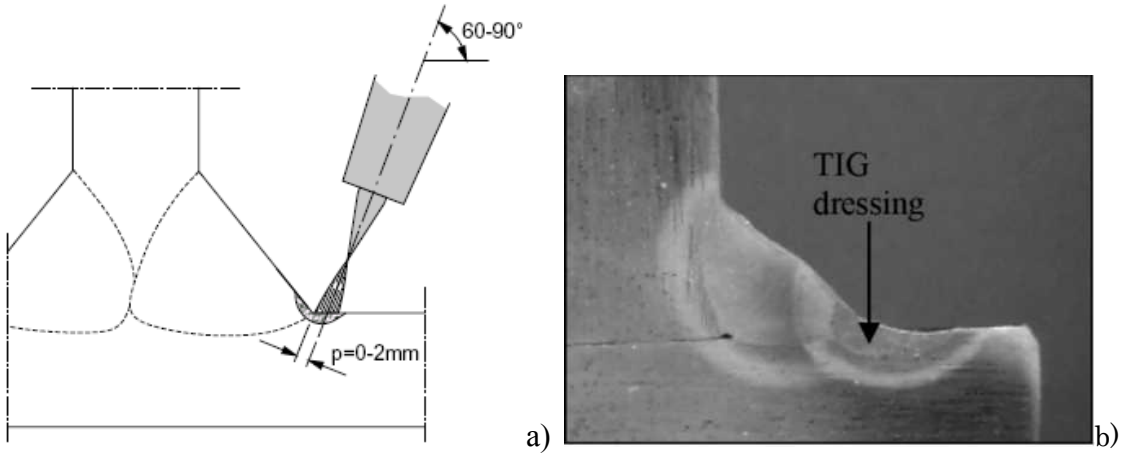

Figure 2.3 (a) Typical position of torch (b) resulted weld profile after TIG dressing (Perovic [20]).

2.1.3 Hammer peening

Hammer peening is performed manually using a pneumatic or electrical hammering operating at about 20-100 impacts/s. A hardened steel tool is used which has rounded hemispherical tips, diameters between 6 and 18mm, and typical length of 100 to 200mm. The surface of the component is impacted by the solid tool with sufficient force to create severe plastic deformation, which results in the beneficial compressive residual stresses in the plate, even up to a few millimetres depth [21]. If done correctly, after the peening, an almost uniform indentation could be created at the weld toe, which reduces the local stress concentration by improving the weld toe radius and angle. In general, an indentation depth of 0.5mm is a good compromise between the treatment time and effectiveness, and a typical hammer peening arrangement is shown in Fig.2.4. Hammer peening is considered as an effective and reliable method for improving the fatigue strength of the structure, even for poor-quality welds. On the other hand, it is a very noisy operation and is hard for operator to perform for long periods of time due to the heavy vibration transferred directly from the peening equipment. The required force of impacting tool against the work piece is > 200N. The peening tool may move in an unsteady manner and demands considerable effort from the operator to keep the tool along the weld toe line during treatment [11].

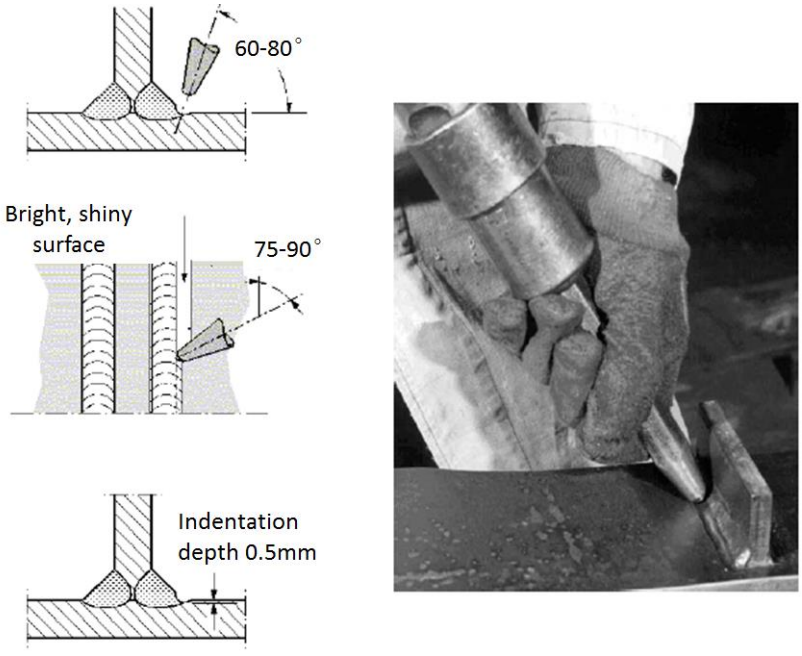

Figure 2.4 Hammer peening operation (Haagensen & Maddox [12]).

2.1.4 Shot peening

The shot peening process is a mechanical surface treatment process in which a large number of shots (round metallic, glass, or ceramic beads), with characteristic dimension in the range of 0.2-1.0mm, are propelled against the surface of a workpiece at high velocities, typically in the range of 25-100m/s, using compressed air [22]. Each piece of shot striking the material acts as a tiny peening hammer, introducing a small indentation to the surface. Overlapping of the surface indentations generates a sub-surface layer with compressive residual stresses of about 70-80% of the yield stress. The major advantage of shot peening is that it covers large areas at low cost. However, it is rare to apply to large scale structures because the special equipment is required for clean-up of shots. In addition, corrosion may quickly weaken the beneficial effects since only very thin surface layer of plate is deformed [11].

2.1.5 Low transformation temperature (LTT) weld filler

The technique of low transformation temperature (LTT) weld filler was firstly developed by National Research Institute for Metals in Japan and Kawasaki Steel Co., which can be categorized as residual stress method [23]. The LTT weld filler exploits the transformation expansion due to austenite to martensite begins at a relative low temperature. The goal is that the combination of thermal contraction due to cooling combined with transformation volume expansion should lead to a net volume increase, which introduces compressive residual stress at the weld toe. Alloying elements of about 10% Cr and 10% Ni content are added to lower the martensitic start temperature [24]. Fig.2.5 illustrates the difference between conventional and LTT weld filler material regarding the strain and residual stress during cooling. The martensitic start temperature M_s of LTT weld filler is lowered to about 200^{o}C as compared to 500^{o}C for conventional one.

It can be hopefully expected that the use of LTT weld filler could give sufficiently high fatigue performance without adding the improvement process like other post-weld treatments, including UIT, which would significantly increase the work and cost. But the very thin surface layer of compressive residual stress induced at the weld toe and no obvious improvement of weld geometry are the main disadvantages of this method [24].

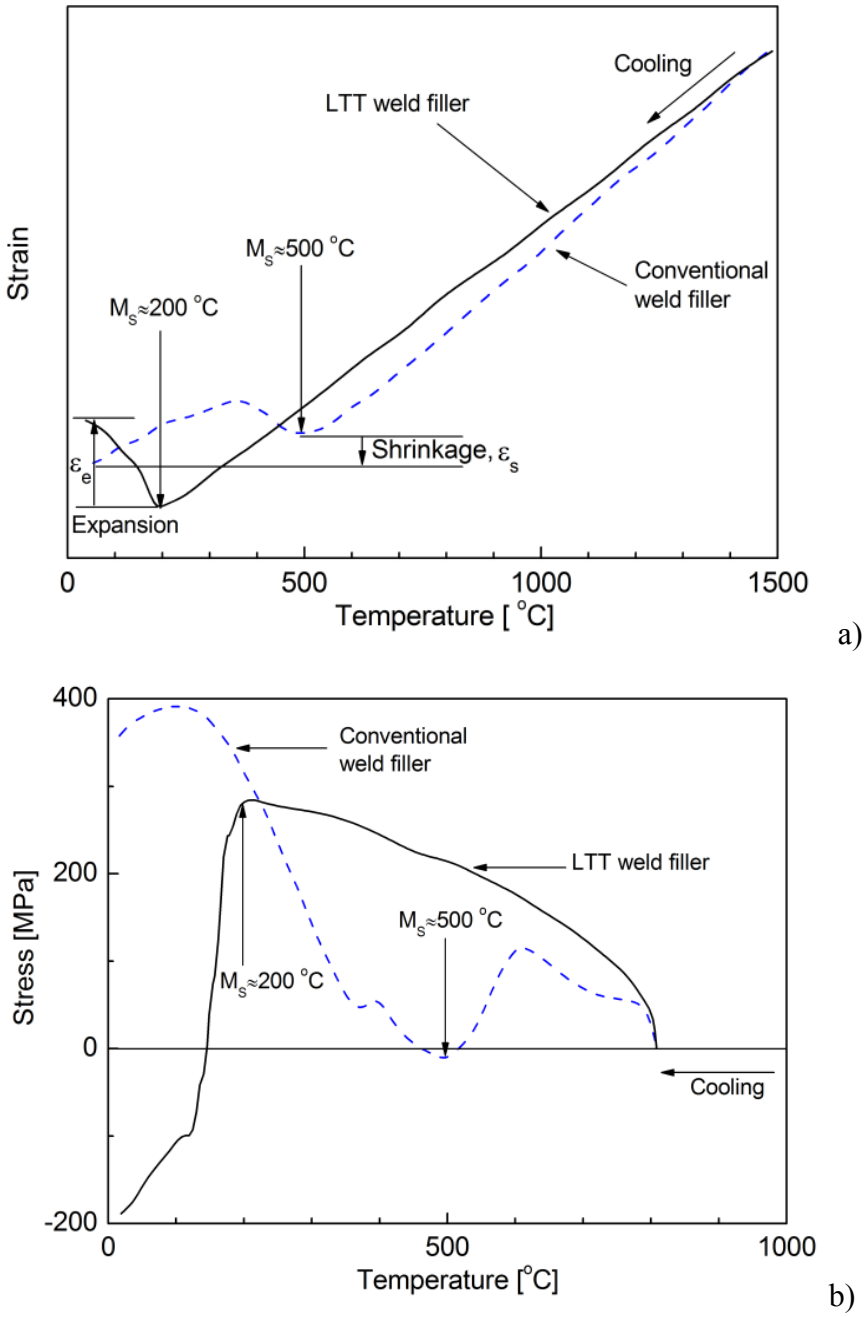

Figure 2.5 Variation of strain and stress in weld metal during cooling process; (a) strain, (b) stress (Ohta et al. [23]).

2.2 Ultrasonic impact treatment (UIT)

Ultrasonic impact treatment is a remarkable technique for enhancement of fatigue strength of welded joints by applying mechanical impact in combination with ultrasonic vibration. This UIT technique was originally developed by Statnikov [25] and his colleagues for the use in the shipbuilding and submarine construction, in the former Soviet Union since the 1970s. Further development was made by North Scientific and Technology Company (NSTC) in Russia and Paton Welding Institute in Ukraine. Nowadays, UIT has been developed and expanded by Applied Ultrasonics in USA for commercial and operational applications in various industries like bridge constructions, offshore structures, power stations and railways.

2.2.1 Equipment and mechanism

The UIT equipment consisting of ultrasonic generator, hand-tool containing ultrasonic transducer and a cooling unit is shown in Fig.2.6 [26]. The ultrasonic impact tool can be handheld, or mounted on the welding machine travellers for automatic treatment. The ultrasonic tools with frequency of 27, 36 and 44 kHz can be generated by means of the standardised ultrasonic transducers [25]. The specification of the 27 kHz UIT equipment is given by Table 2.2.

This equipment is more friendly and easier to use than the conventional peening methods like hammer peening and needle peening because it provides a comfortable work environment with negligible noise and vibration [27]. In addition, the required force of UIT tool against the work piece is approximately 30N, which can be created by the weight of the tool itself. The ease of the UIT equipment operation can result in considerable benefits in terms of treatment quality compared with conventional peening methods since the operator uses less effort in keeping the tool aligned with the weld toe being treated. When applying at the weld toe, the tool is suggested to keep an angle between 30^{o} and 60^{o} while the tool is moving parallel to the direction of weld toe line, like Fig.2.7 [28]. On average 3-5 passes are made at a particular location to ensure a smooth uniform profile of the weld toe [29].

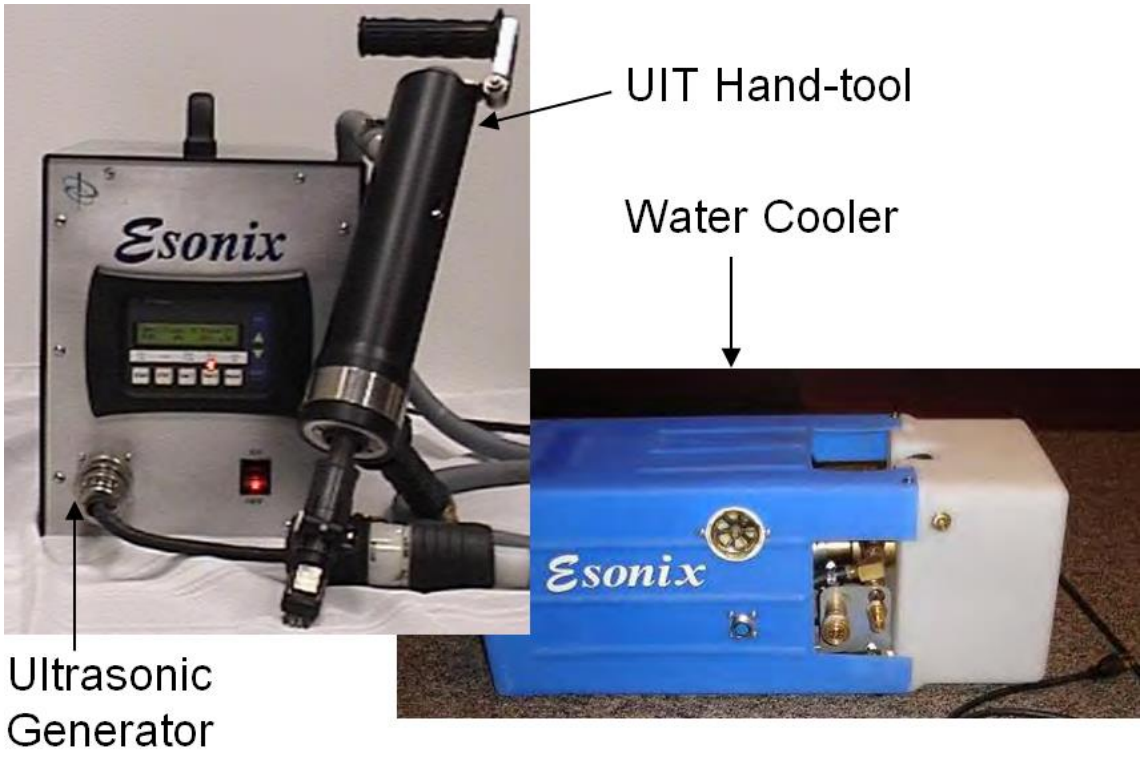

Figure 2.6 Esonix® ultrasonic impact treatment equipment (Applied Ultrasonics [26]).

Figure 2.7 Ultrasonic impact treatment of a weld toe in progress (Lihavainen et al. [28]).

Table 2.2 Specification of the 27 kHz UIT equipment [25], [30]

Operating ultrasonic frequency [kHz]	27
Impact frequency under loading [Hz]	100-120
Design	Manual or automatic treatment
Output power [W]	600-1200
Excitation voltage [V]	60-110
Bias current [A]	10-15
Oscillating amplitude of the output end of the waveguide [μm]	25-40
Treatment rate in manual mode [mm/s]	5-25
Pressed force against the workpiece [N]	20-40
Dimensions of manual tool [mm]	455×85×80
Manual tool weight [kg]	3.5
Cooling	Liquid
Indenter diameter [mm]	2-5
Hardness of the indenter [HRC]	62-64

The detailed description of each part in UIT hand-tool and its operation mechanism is illustrated in Fig.2.8. Firstly, electrical energy can be converted into forced harmonic oscillations by means of the magnetostrictive transducers. A waveguide is installed to enlarge the vibration amplitude from several micrometers to several tens of micrometers. The waveguide then impacts upon some installed cylindrical pins which can freely move in a gap between the waveguide end and treated surface, in order to efficiently transfer the energy into the work piece. During the treatment, the pins can cyclically impact the surface of the work piece at a relatively low frequency, and transfer the ultrasonic oscillations of high frequency into the work piece [3].

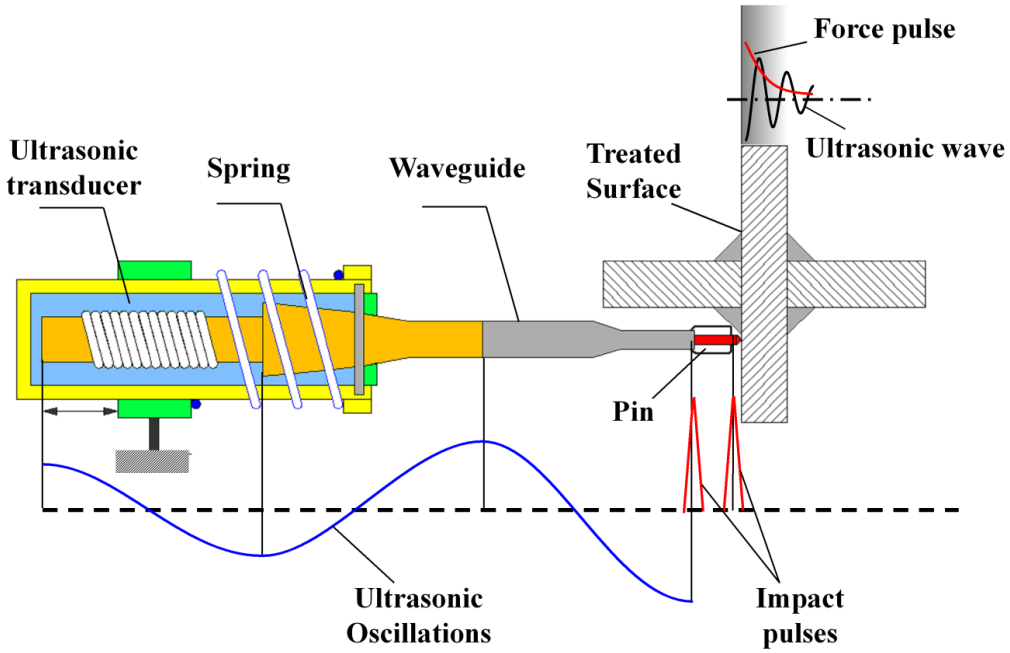

Figure 2.8 Mechanism of UIT (Statnikov [3]).

Impacts of the indenters upon the workpiece surface are accompanied by one of the following interactions between the indenters and workpiece [25].

- Ultrasonic periodic impact. In this case, the indenter induces plastic deformation of the metal with exciting ultrasonic periodic stress waves in the treated workpiece. Hereafter, both the indenter and the treated workpiece oscillate at the same frequency with continuous contact.
- Ultrasonic non-periodic impact. The result of ultrasonic non-periodic impact is that the indenter rebound off the workpiece and set off propagation of ultrasonic non-periodic stress waves in the treated material.
- Single contact of the indenter with a rebound off the workpiece. This causes the propagation of single impact pulse in the treated material.

For example, the oscilloscope picture of the impacts induced by UIT is shown in Fig.2.9. The top diagrams (magenta colour) represent the transducer excitation signal, while the bottom diagrams (yellow colour) represent the impacts/impulses initiated by transducer vibrations. The distinct ultrasonic vibrations and single impulse in the material of the impact surface can be both observed.

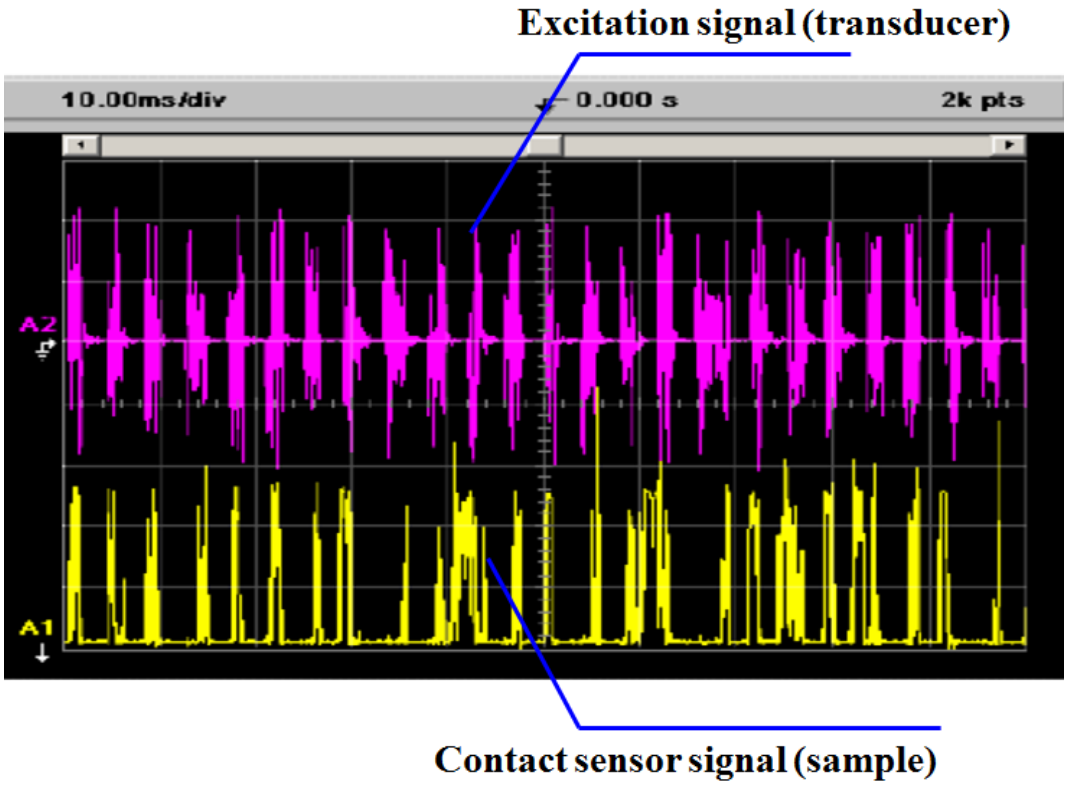

Figure 2.9 Oscilloscope picture of the impacts induced by Esonix UIT (Statnikov [3]).

Plastic deformation of the treated material induces compressive stresses at the near-surface layer of the workpiece, and the creation of ultrasonic stress waves and force pulses relax the welding residual stress in the depth of the treated materials.

This kind of high frequency impacts of the pins in combination with the ultrasonic stress waves transmitted into the work piece through the pin contacting the treated surface is nominated as ultrasonic impact by Statnikov [3]. The phase of uninterrupted oscillation during each ultrasonic impact defines the nature of UIT and is the most important aspect of this technology. The duration of ultrasonic impact is measured in the range from hundreds of microseconds to a few milliseconds depending on the resonant frequency of the ultrasonic transducer [31].

Investigation showed that the influence of ultrasound (more precisely, the ultrasonic stress wave in the treated material, which are initiated by reboundless oscillations of the indenter during impact) is the major factor responsible for intense plastic deformation during UIT [3]. Fig.2.10 shows indentation area of ultrasonic and ultrasonic-free impacting upon an aluminum specimen using indenter (diameter of 6.35mm and length of 25mm). When ultrasound is imposed during the impact (vibration amplitude 50 μm), the specimen becomes much softer and indentation area becomes larger than that without ultrasound. It has to be noticed that Statnikov did not mention how to switch on/ off ultrasound during treatment. It could be just be a comparison of a single impact appropriate to hammer peening and ultrasonic impact with the same initial conditions.

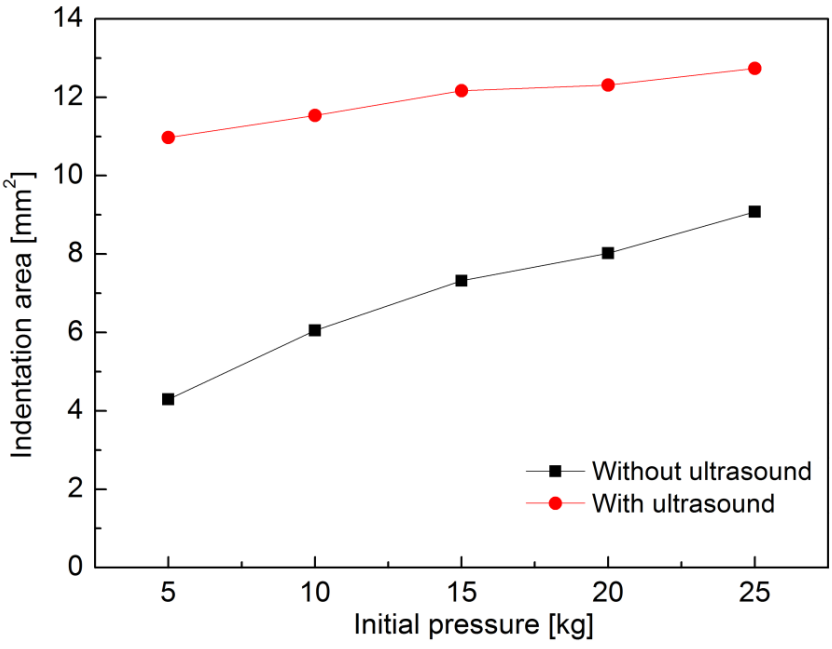

Figure 2.10 Indentation areas with ultrasonic and ultrasonic-free impact (Statnikov [3]).

The diagram shown in Fig.2.11 distinguishes the influence of single impulse and re-boundless ultrasonic vibrations on the plastic deformation efficiency. As can be seen, with comparable duration of single impulses at the onset of the ultrasonic impact, the total percentage of plastic deformation is only 3.6% during forming the saturation region, while during uninterrupted ultrasonic oscillations of the indenter for almost the same period of time, this is more than 78%.

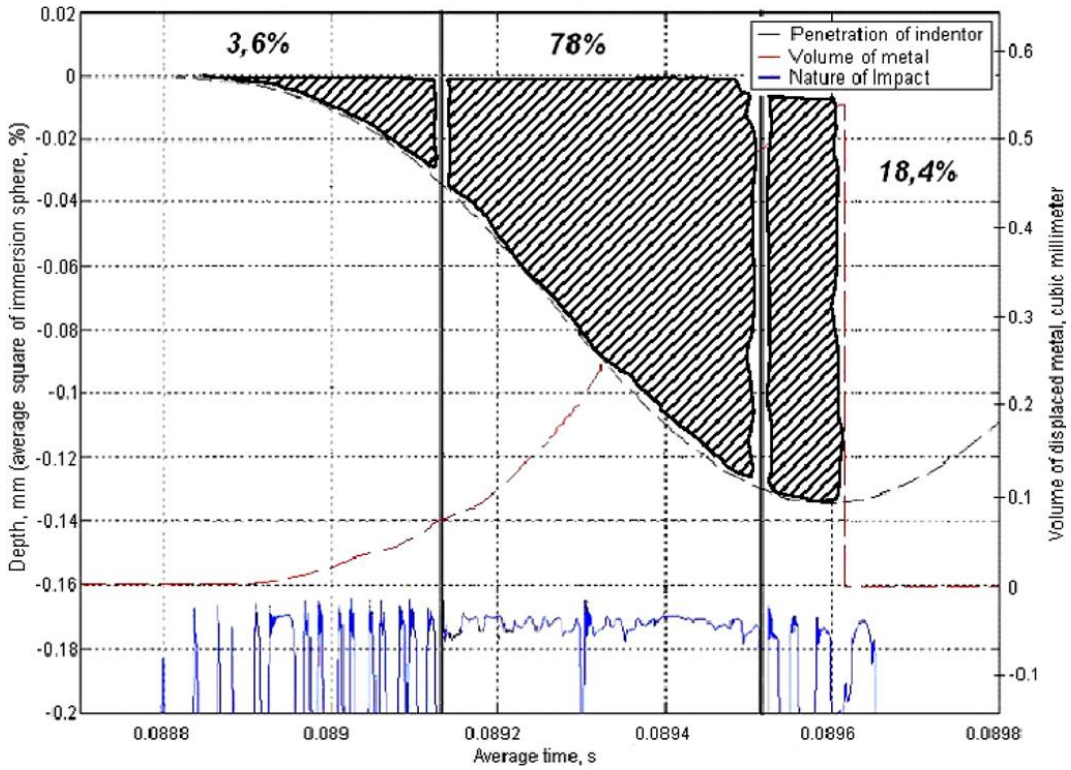

Figure 2.11 Distribution of plastic deformation during ultrasonic impact (Statnikov [31]).

2.2.2 Acoustic softening effect

The effect of ultrasonic energy on metal deformation behaviour for a wide range of metals, such as aluminium, steel, copper and magnesium has been well known since early 1950's. It was observed that the quasi-static stress required for plastic deformation in a material is reduced when ultrasonic vibration is applied. This phenomenon is called Blaha effect or acoustic softening effect [32], [33], [34], [35].

Various types of deformation test have been carried out to show the softening effect of superimposed ultrasonic vibrations on metals and alloys undergoing deformation. Daud et al. [36] performed the compression test of aluminium 1050 under the ultrasonic vibration amplitude of 10μm at a frequency of 20 kHz, as shown in Fig.2.12. It is observed that the yield stress is immediately reduced upon the application of ultrasonic energy and is immediately restored once the vibration is switched off.

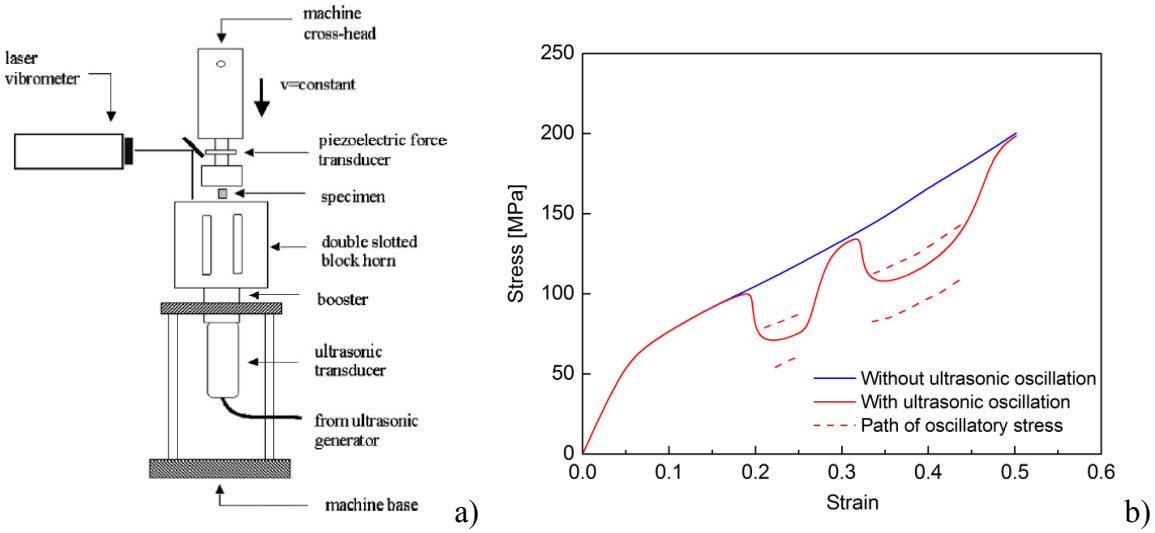

Figure 2.12 Ultrasonic-assisted compression test; (a) schematic diagram of test devices, (b) measured stress-strain data from static-ultrasonic compression test with two intervals of ultrasonic excitation (Daud et al.[36]).

Shalvandi et al. [37] carried out the ultrasonic-assisted tension test with stainless steel 316. The frequency and amplitude of the applied ultrasonic vibration are 24.5 kHz and 23/46 μm, respectively, and the stress-strain curves are plotted in Fig.2.13. The yield stress of the material reduced 32% and 45%, when the ultrasonic intensities of 300Watt and 600 Watt were applied, respectively. It can be concluded that the softening becomes more prominent as the ultrasonic intensity increases.

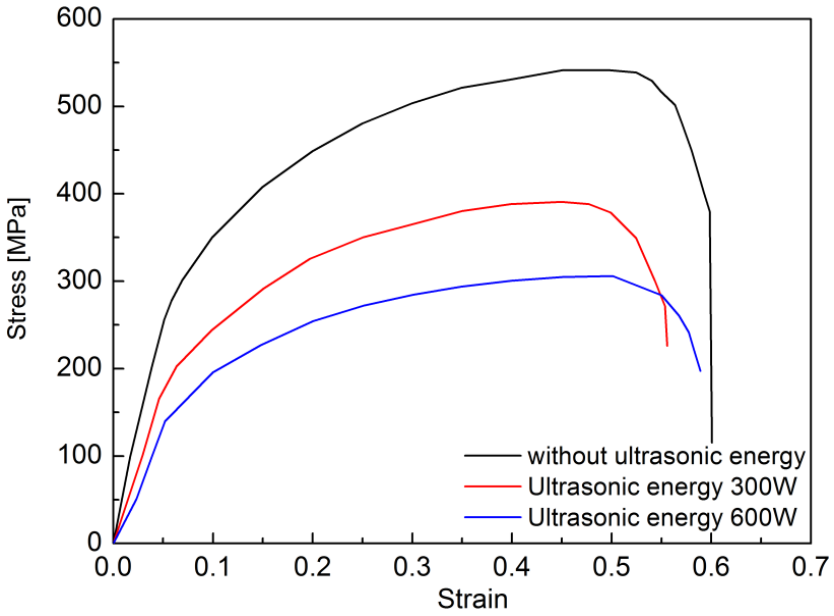

Figure 2.13 Measured stress-strain curves of tensile specimen of stainless steel 316 with and without ultrasonic vibration (Shalvandi et al. [37]).

As for UIT, the relative motion between the specimen and indenter complicates the acoustic softening process. Statnikov [3] performed an ultrasonic-assisted tension test, in order to confirm the effect of ultrasonic impact via an intermediate indenter on the deformation resistance reduction in comparison with a direct contact of the ultrasonic transducer and specimen, as shown in Fig.2.14. An obvious reduction about 24-26% in ultimate tensile strength under ultrasonic impact is observed, which is just a little less than the 27-30% reduction in the case of direct ultrasonic excitation. Nevertheless, the results suggest that the UIT could effectively introduce high-power ultrasonic oscillation and stress waves into the treated objects through the relatively small indenter contact area.

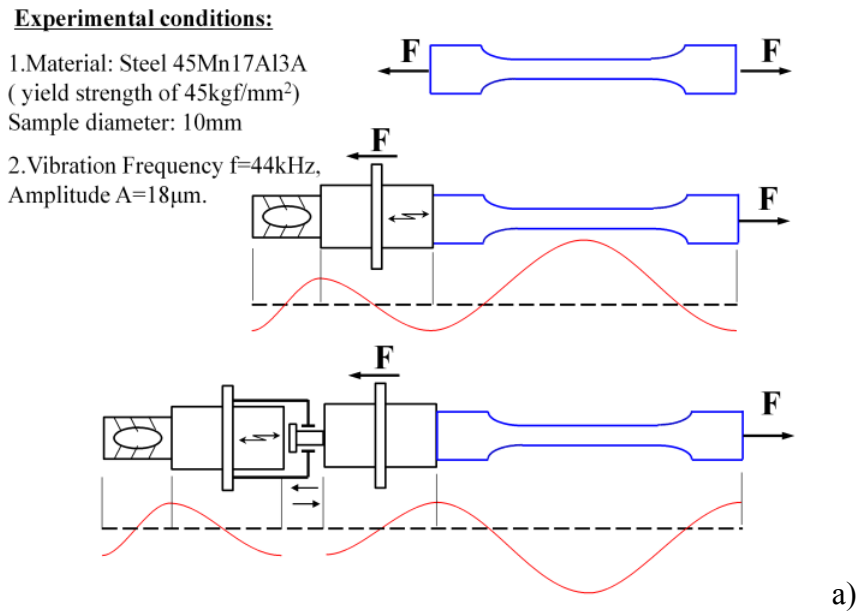

a)

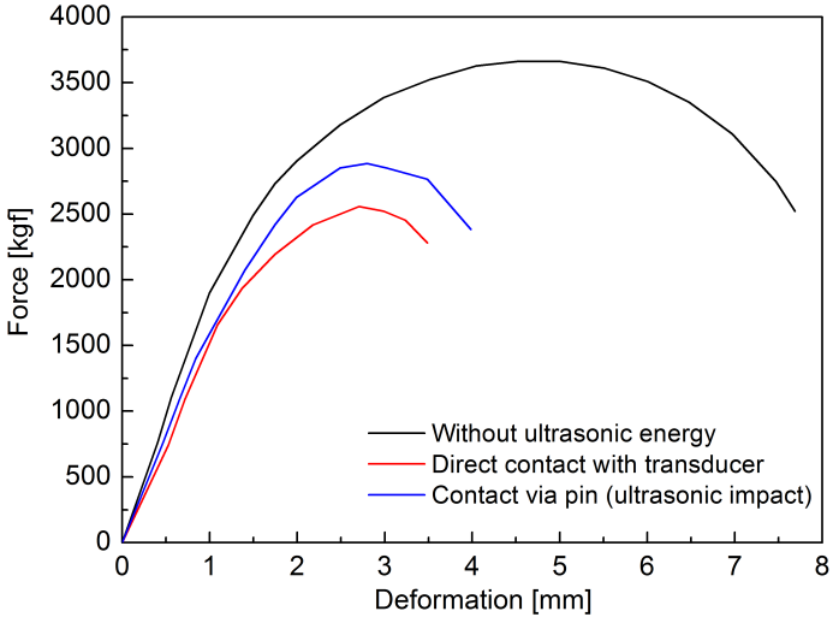

b)

Figure 2.14 Ultrasonic-assisted tension test; (a) schematic diagram of tests with different modes, (b) measured force-deformation curves (Statnikov [3]).

Besides UIT, there have been many industrial processes developed based on the reduction of deformation resistance induced by ultrasonic vibration, like vibration-assisted upsetting [36], ultrasonic welding [38], and impact peening to modify surface properties [39]. However, there is still no clear and comprehensive understanding of the mechanism responsible for the acoustic softening effect. Langenecker [33] proposed that under ultrasonic action, a change in the character of dislocation distribution and activation of new dislocation sources occurs, as a result of preferential absorption of the energy of ultrasonic oscillations at defects in the crystalline lattice. An increase in dislocation mobility allows the metal deforming at a lower load. Other hypothesises also include (i) the superposition of oscillatory stresses [40], [41], (ii) thermal softening of metals [34], and (iii) the surface friction reduction between the ultrasonic tool and the deformed materials [42]. These different possible mechanisms are inadequate to explain the stress reduction individually and usually coupled with each other [36], [43]. The investigation of exact mechanism of acoustic softening effect is not included in the scope of the current research.

2.2.3 Experimental studies on fatigue strength improvement by UIT

Numerous investigations have been carried out to experimentally verify the effectiveness of UIT on improvement of fatigue strengths of welded joints. The degree of improvement is found to depend on the fatigue load conditions (various stress ratios, preload, variable amplitude loading), the yield strength of material, and environment conditions (air and seawater).

2.2.3.1 Effect of stress ratio and preload

It is always observed that the fatigue strength of as-weld specimens does not depend on the stress ratio due to the existence of high tensile welding residual stress at the weld toe where fatigue cracks initiate. However, some recent fatigue tests focused on the effect of stress ratio indicate that after improving treatment, the fatigue performance of UIT welded joints is quite different from the as-weld ones. For example, Fig.2.15 shows the S-N curves of as-weld and UIT longitudinal fillet joints of Q235b steel under different stress ratios [44]. In addition, some other results of fatigue test considering the effect of stress ratio on fatigue strength of UIT specimen are summarized in Table 2.3. Based on these results, it can be confirmed that the fatigue strength of UIT-treated specimens is not independent of stress ratio any more, but decreases as R increases, even in few case of high stress ratio the beneficial effect is almost eliminated, compared to the as-weld ones.

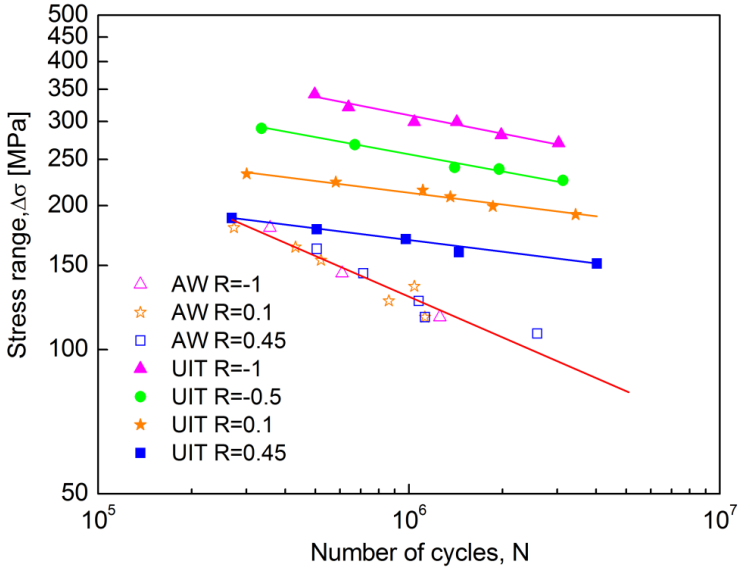

Figure 2.15 S-N curves under different conditions of stress ratio (Wang et al. [44]).

Table 2.3 Results of fatigue tests considering the stress ratio effect on UIT improvement

Ref	Steel (σ_Y [MPa])	Joint type	Thickness [mm]	Stress ratio R	Fatigue strength at 2×10^6 cycles [MPa]
Wang et al. [44]	Q235 (267)	Longitudinal fillet joint	8	AW*	104
				-1.0	280
				-0.5	240
				0.1	192
				0.45	164
Mori et al. [45]	SBHS500 (572)	Longitudinal fillet joint	12	AW	90
				0.0	169
				0.5	93
REFRESH Report [46]	S355J2 (434)	Butt joint	16	AW	90
				0.1	168
				0.5	138
	S690QL (719)	Butt joint	16	AW	90
				0.1	215
				0.5	157
Deguchi et al. [47]	KA36 (355)	Non-load carrying cruciform joint	16	AW	96
				0.0	229
				0.25	163
				0.5	134
Okawa et al. [48]	AH36 (392)	Non-load carrying cruciform joint	20	AW	87
				-1.0	386
				0.1	243
				0.5	142

* Regardless of the stress ratio in the as-weld cases

In UIT treated welded joints, important component of stress field affecting fatigue performance is the compressive residual stress. The question always arises whether the fatigue improvement would be still be applicable if UIT treated zone is subjected to overload which may cause relaxation of beneficial compressive residual stress. Several recent researches in Japan verified the influence of preload on the fatigue strength of welds improved by UIT [45], [47], [48].

Okawa et al. [48] investigated both tensile and compressive pre-fatigue loads effect using UIT-treated transverse non-load carrying cruciform joints. The X-ray measured surface residual stress distributions before and after preloads and corresponding fatigue test results are shown in Fig.2.16. It was found that either tensile or compressive preload indeed resulted in the relaxation of compressive residual stress near the UIT-treated zone; however, the improved fatigue strength by UIT was still greater than that of as-weld joints.

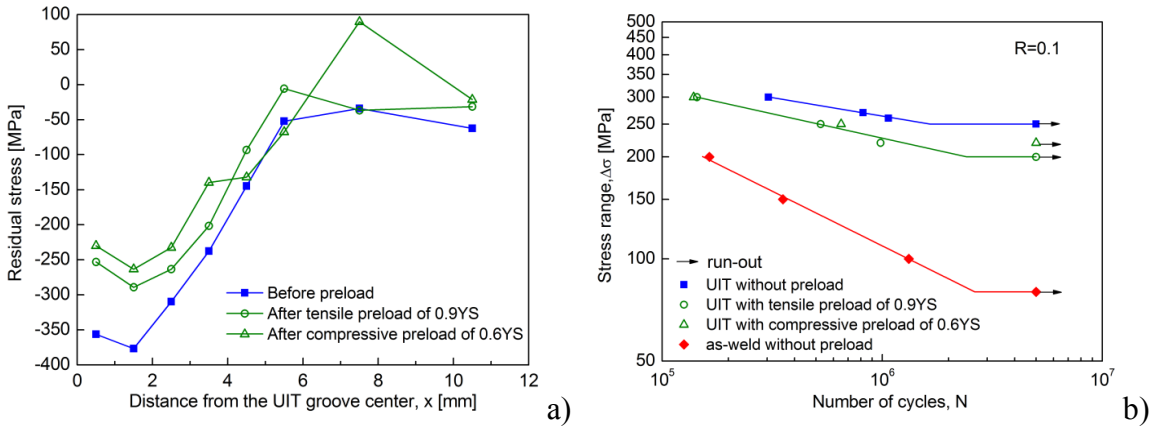

Figure 2.16 (a) Surface residual stress change near the weld toe by preloads, (b) S-N curves for fatigue tests with and without preloads (Okawa et al. [48]).

Deguchi et al. [47] used longitudinal non-load carrying fillet joints to confirm the benefits of the ultrasonic peening (UP), similar to UIT, for ship structures. They considered two load histories in conjunction with the treatment method; UIT improvement process is done before and after a scenario of ship launching. For the former case A, the specimens have been treated and then subjected to constant amplitude loading with a mean stress of 100MPa. For the latter one B, the specimens have been preloaded at 100MPa and then treated, followed by constant amplitude loading with a mean stress of 100MPa. According to the results in Fig.2.17, the application of UP after launching is recommended, because it avoids losing the beneficial effect due to the change of stress distribution at launch. Another explanation is that when UIT is given under the load, the compressive residual stress will be increased after unloading due to spring-back [45].

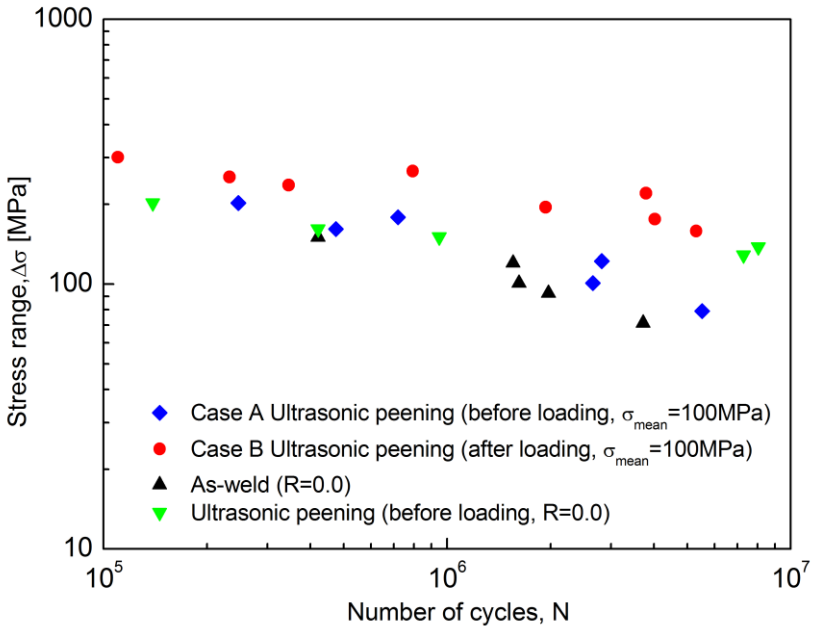

Figure 2.17 Results of fatigue tests with different time for application of ultrasonic peening (Deguchi et al. [47]).

2.2.3.2 Effect of variable amplitude loading

The studies on the beneficial effect of UIT for fatigue improvement of welded joints have been verified by many constant amplitude (CA) fatigue tests. However, there is the need to check the benefits under variable amplitude (VA) loading, which the real structures are inevitable to be subjected to.

Huo et al. [49] investigated UP-treated longitudinal fillet joints fabricated from 16Mn steel with yield strength 390MPa, subjected to both constant and variable amplitude block loading. The specimens were either in the as-weld condition, TIG-dressed or treated by UP. For constant amplitude loading, the fatigue strength improvement was 84% for UP and 37% for TIG dressing, compared to as-weld cases. For variable amplitude loading, the fatigue strength improvement was slightly less as 80% and 34%, respectively. However, it should be noted that the variable amplitude loading used in this study was not significantly different from the constant amplitude loading, i.e. the ratio between stress ranges of the smallest cycles to largest cycles in the spectrum was 0.73-0.83.

Marquis [50] reported the results of constant and variable amplitude fully reversed (R=-1.0) fatigue testing performed on UIT-improved longitudinal fillet joints of high strength steels S700 and S960. Fatigue failure sites in the improved specimens tested with variable amplitude loading always occurred at the weld toe while none of the specimens tested under constant amplitude loading failed in this location. In addition, the fatigue strength was significantly reduced due to VA loading as compared to CA loading, as shown in Fig. 2.18. For constant amplitude loading of R=-1.0, the fatigue strength was improved 330% with respect to the as-weld tests using similar loading. However, the improvement for VA loading was only 120%.

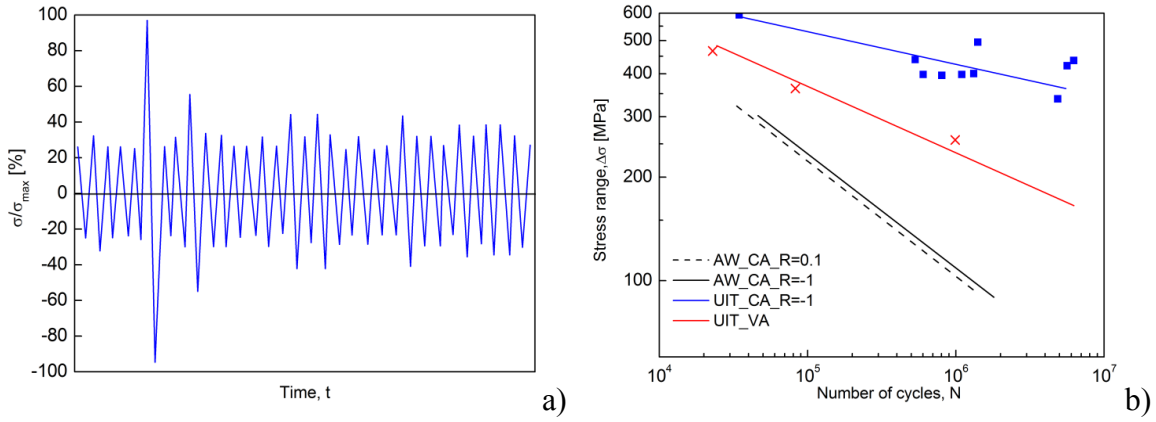

Figure 2.18 (a) Cut-off from the load-time history, (b) S-N curves of fatigue tests under constant and variable amplitude loading (Marquis [50]).

2.2.3.3 Effect of material strength

It is well known that the fatigue strength of welded structures is in general independent from the material yield strength. Nevertheless, in case of high-strength steels, it is possible to increase the fatigue behaviour by additional UIT improvement process significantly.

The constant amplitude fatigue tests were performed on UIT-treated T-joints of medium strength steel (nominal yield strength 355MPa) and high strength steel S700 (nominal yield strength 700MPa) by Galtier and Statnikov [30]. Based on the results shown in

Fig.2.19, it can be confirmed that more benefits of UIT can be obtained with steel of higher strength.

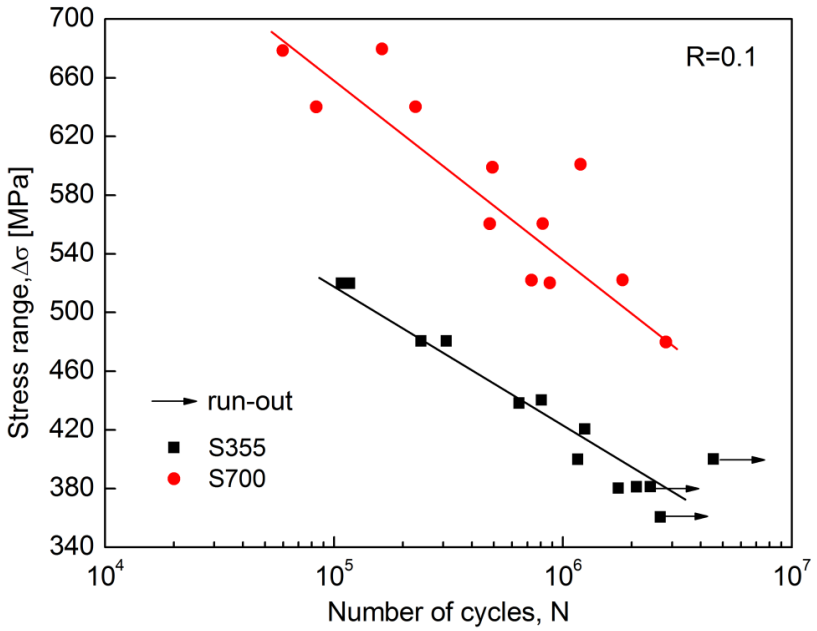

Figure 2.19 S-N curves of fatigue tests with S355 grade and S700 grade steels (Galtier & Statnikov [30])

Similarly, Wang et al. [44] investigated the material strength effect on the fatigue performance of UIT-treated butt joints and longitudinal fillet joints. Three different strength level materials, low carbon steel Q235B with yield strength 267MPa, medium strength steel 16Mn with yield strength 390MPa and high strength steel SS800 with yield strength 700MPa were selected. Based on the fatigue test results, considering a yield-strength dependent bonus factor in fatigue strength assessment was recommended. One reason for this enhancement can be explained that due to the higher yield strength it is possible to imply higher compressive residual stress and therefore the effective stress range was reduced during cyclic loading.

Yildirim and Marquis [51] performed a comprehensive data analysis of 288 high frequency mechanical impact (HFMI) treated welds under constant amplitude cyclic loading at stress ratio R=0.1, including longitudinal fillet, cruciform and butt joints. The steel yield strength varied from 260 to 969MPa, and the plate thickness changed in the range of 5-30mm. A yield strength correction method was proposed that one fatigue class in strength (about 12.5%) is increased for every 200MPa increase in static yield strength. Fig.2.20 shows the proposed increase in the number of FAT classes as a function of yield strength, which will be introduced into new IIW guidance on fatigue strength improvement by HFMI [10].The solid line presents the proposed increase, and the broken line represents the increase for hammer-peened and needle-peened welds in the current IIW guideline [12].

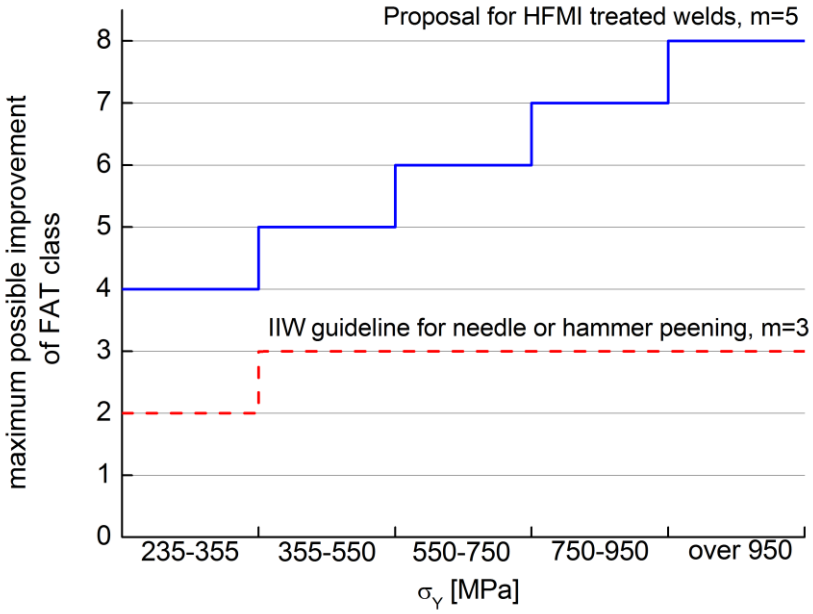

Figure 2.20 Proposed maximum increases in the number of FAT classes as a function of σ_Y (Yildirim & Marquis [51]).

2.2.3.4 Effect of corrosion

In the case of ship structures, the question was raised whether the fatigue strength improvement will be maintained in wet conditions where corrosion could remove the surface layer of compressive residual stress induced by UIT.

Tryfyakov et al. [52] reported the results of constant amplitude fully reversed (R=-1.0) fatigue testing performed on UIT-treated welds in air and synthetic seawater. For example, the fatigue strength of UIT joints at 10^7 cycles decreased from 170MPa to 100MPa in seawater.

Polezhayeva et al. [53] carried out the fatigue tests to confirm the benefits of ultrasonic peening for welded joints subjected to accelerated corrosion. The specimens with welded longitudinal attachments of ship steel DH36 were tested under axial cyclic loading, in the as-welded, UP treated and UP treated under corrosion conditions. Natural corrosion process during 1, 5 and 7.5 years was simulated by exposure of the specimens to a corrosive environment in a salt spray cabinet. The fatigue test results are shown in Fig.2.21. It should be noted that, for non-corroded, 1 and 5 year corroded UP specimens failures predominately occurred at the weld root, which suggest that the weld toe has lower stress concentration than the weld root. All 7.5 year corroded UP specimens failed from the weld toe which suggests the stress concentration moved from the weld root to the weld toe and fatigue strength was affected by the corrosion process. Compared to as-weld specimens, the fatigue improvement factor for 7.5 year corroded UP cases is about 1.6, so the beneficial effect is still present.

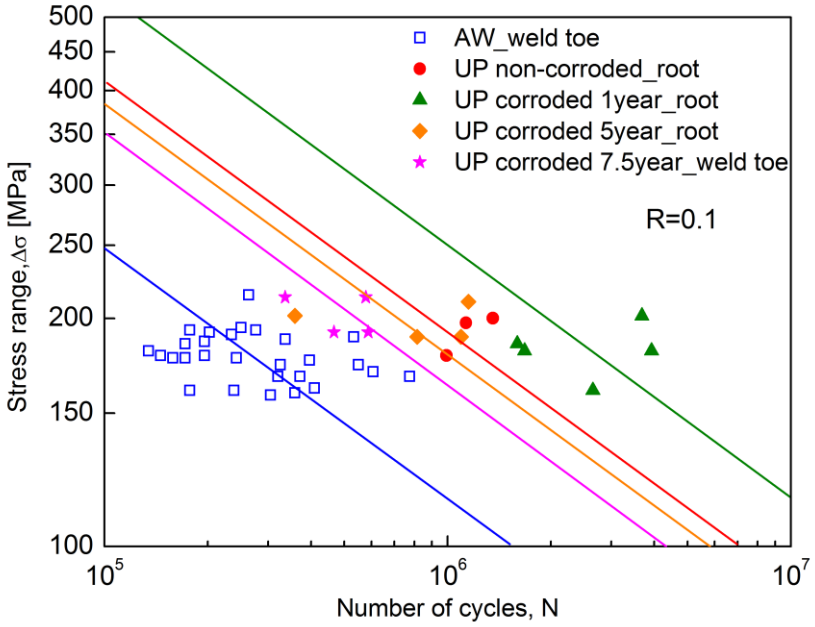

Figure 2.21 S-N curves of fatigue tests with different corrosion time (Polezhayeva et al. [53]).

2.2.3.5 Failure modes and crack growth behavior

Marquis [50] investigated the crack patterns of UIT-treated longitudinal fillet welds in high strength steels under constant amplitude (CA) and variable amplitude (VA) loading. Various failure modes occurred in the improved specimens tested using CA loading, including plate edge failures, failure from weld start/stop positions and root failures, as shown in Fig.2.22. On the other hand, it was observed that the as-weld and improved specimens under VA loading always failed at the weld toe. The compressive residual stress relaxation during VA loading was considered as primary reason for this failure location change.

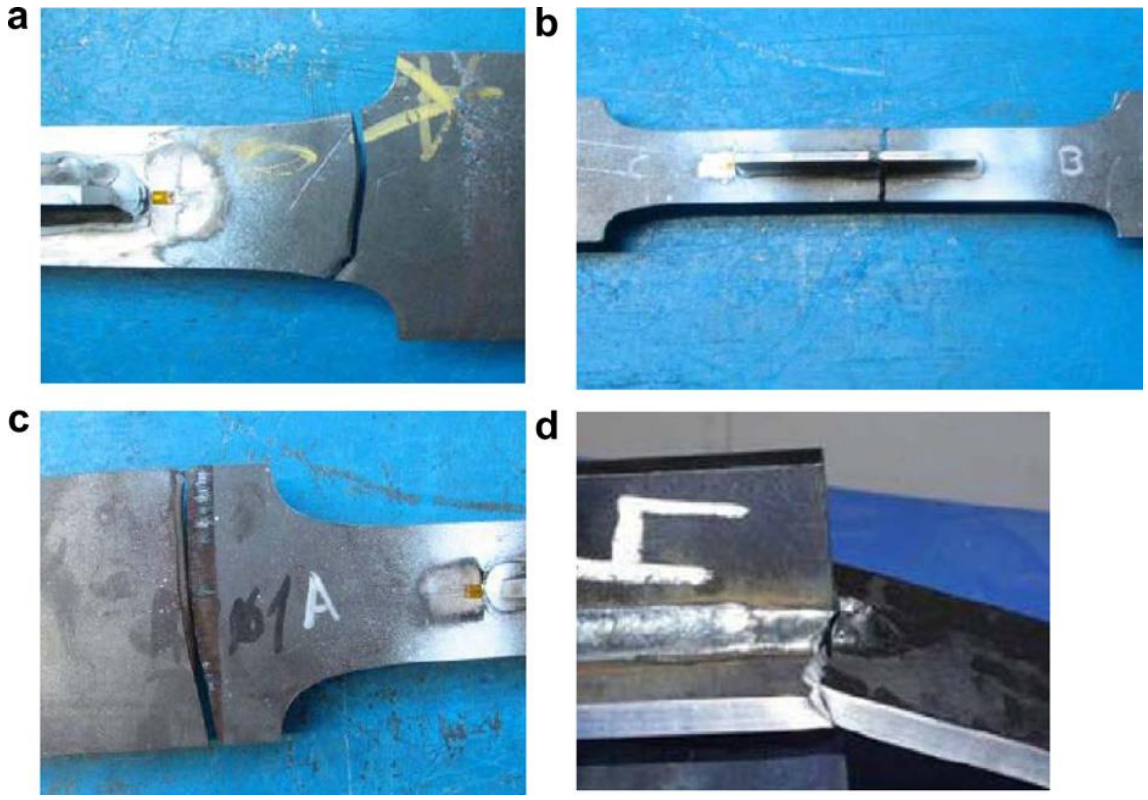

Figure 2.22 Failures observed in specimens under CA loading; (a) plate edge failure, (b) start/stop position failure, (c) fretting failure in the gripping end, (d) root side failure (Marquis [50]).

The similar study about failure positions in butt joints and longitudinal fillet joints improved by ultrasonic peening, low transformation temperature electrode and TIG dressing, under both constant and variable amplitude loadings were carried out by Huo et al.

[49], [54]. All of the as-weld specimens and improved specimens under VA loading always failed at the weld toe. Under CA loading, most of specimens subjected to high stress ranges failed at the weld toe, however, those tested at relative low stress ranges failed in the base metal.

Ghahremani and Walbridge [55] compared the crack front shape in the needle-peened specimens with dye penetrant and beach mark techniques. As shown in Fig.2.23, it was found that the cracks tended to grow linearly in the as-weld specimens, whereas the curved crack fronts occurred in the peened specimens. They concluded that the peening-induced compressive residual stress near the treated surface appeared to make it easier for the initiated surface crack to grow vertically in depth rather than horizontally in width.

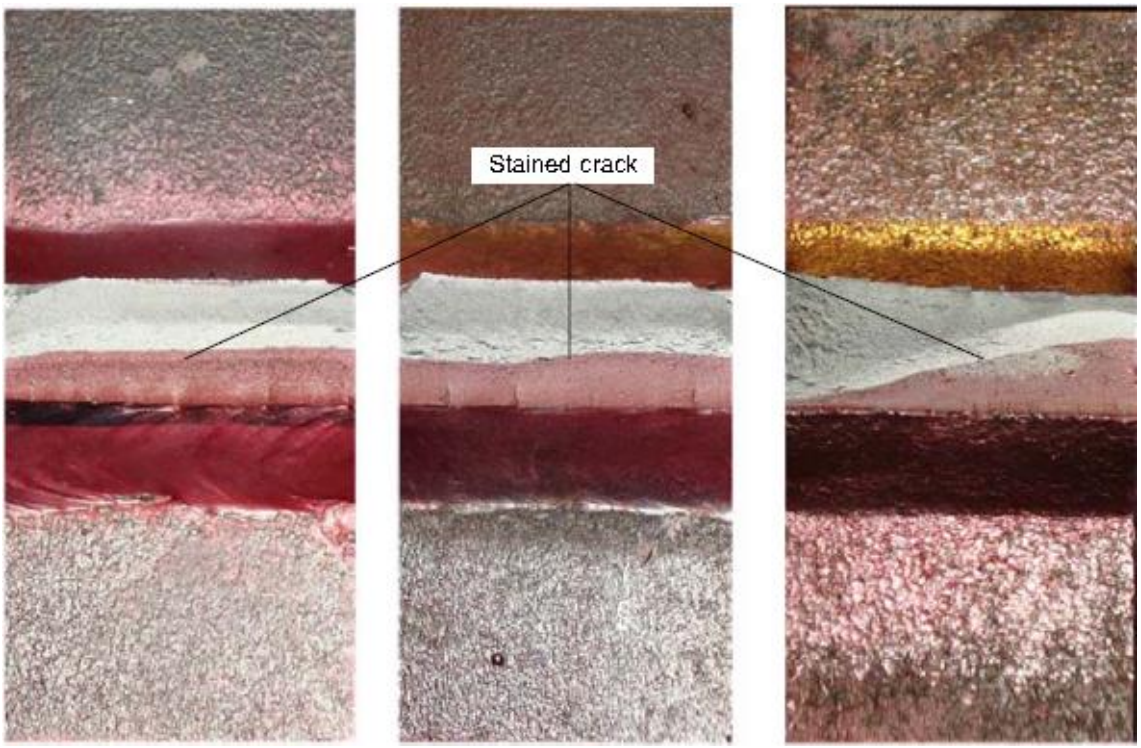

Figure 2.23 Fractured surfaces of stained specimens; left: as-weld under CA loading, middle: as-weld under VA loading, right: peened under CA loading (Ghahremani & Walbridge [55]).

2.2.3.6 Comparison of UIT with other post-weld methods

Because UIT provides many beneficial effects such as weld geometry improvement, compressive residual stress and plastic cold working, UIT is comparable to many other post-weld improvement methods.

With the interest in UIT, Statnikov [3] reported the results of experimental comparison between UIT and other conventional weld improvement treatments such as shot peening, hammer peening and TIG dressing, as shown in Fig.2.24. The results indicate that UIT is the most effective method to improve the fatigue performance.

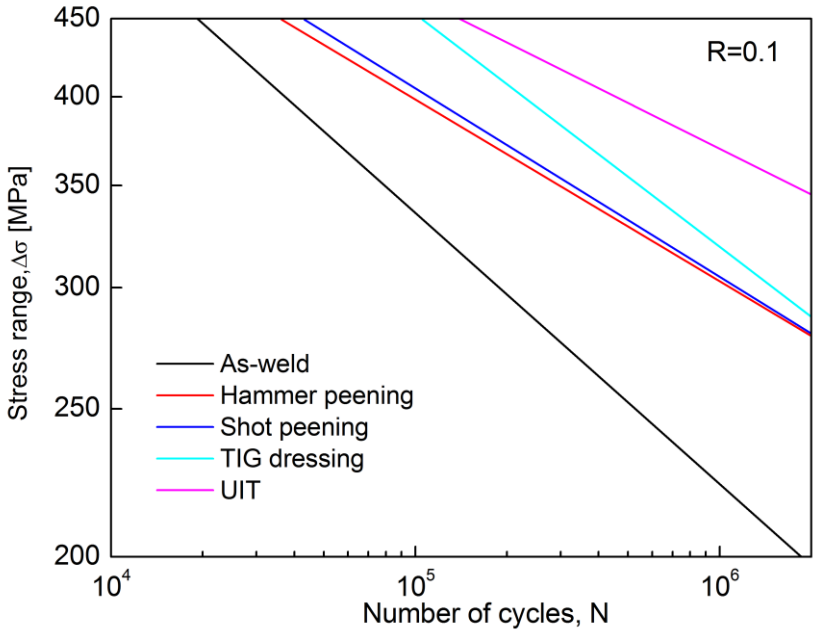

Figure 2.24 S-N curves for Weldox 420 fillet welds in the as-weld and improved conditions (Statnikov [3]).

Pedersen et al. [56] compared the fatigue enhancement of high-strength T-joints by three different post-weld treatments (burr grinding, TIG dressing and UIT). They focused on the medium cycle area (10,000-500,000 cycles) under high stress ranges up to the yield strength of the base metal. Several typical weld profiles from this work are shown in Fig.2.25. Based on the fatigue test results in Fig.2.26, it can be concluded that the TIG dressing is the most effective in the medium cycle regime; on the other hand UIT results in most improvement effect in the high cycle area.

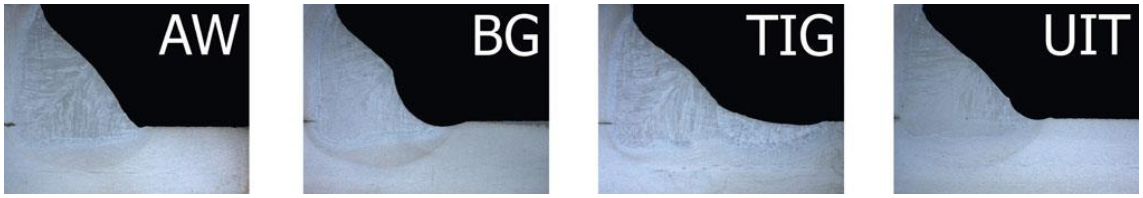

Figure 2.25 Examples of the weld profiles of as-weld, burr grinding, TIG dressing and UIT (Pedersen et al. [56]).

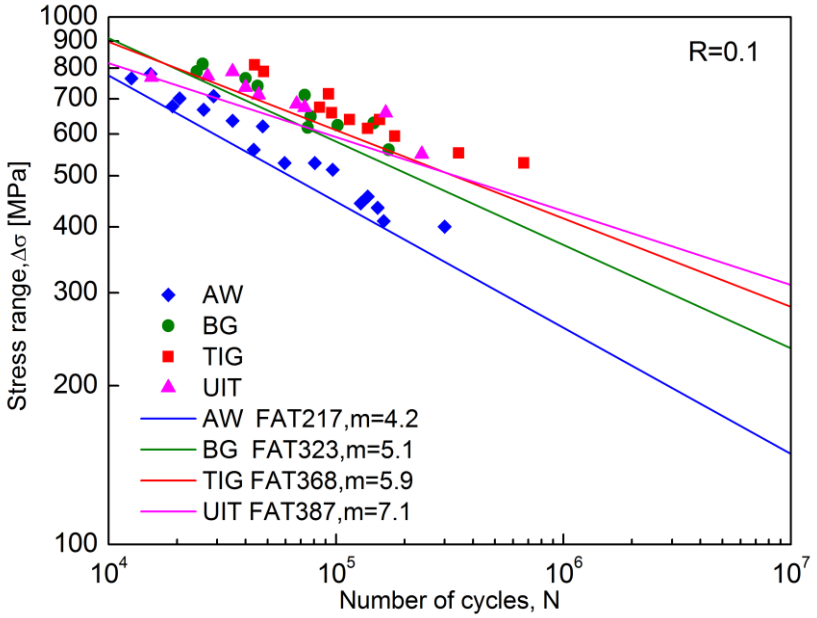

Figure 2.26 S-N curves for S700 T-joints in the as-weld and improved conditions (Pedersen et al. [56]).

2.2.4 Investigation of UIT-induced residual stress

Since the UIT-induced compressive residual stress is considered to be a main reason for the fatigue strength improvement, it is necessary to clarify the internal residual stress distribution after UIT, in order to better understand how to effectively improve fatigue life of steel structures by UIT. In the following sections, several investigation studies on UIT-induced residual stress distributions performed by experimental and numerical approaches will be reviewed.

2.2.4.1 Experimental measurement approach

An initial attempt to measure the magnitude and subsurface distribution of UIT-induced residual stress using both methods of neutron diffraction and X-ray diffraction together with layer removal technique is performed by Cheng et al. [6]. The measured in-depth residual stress distributions in two base metal specimens with different plate thickness are shown in Fig.2.27. It can be observed the compressive residual stress layer induced by UIT is about 1.5-1.7mm in depth and its depth appears independent of plate thickness. The peak compressive residual stress occurs at or near the surface beneath the treatment and exceeds the yield stress of the base metal.

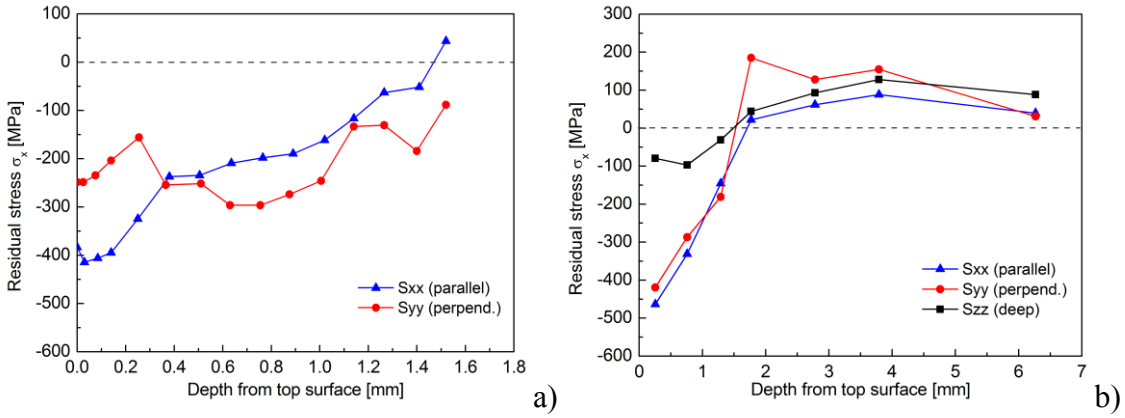

Figure 2.27 In-depth residual stress profiles in base metal specimens (A572 Gr.50 steel with yield strength 345MPa); (a) 25.4mm thick specimen by x-ray method, (b) in 12.7mm thick specimen by neutron diffraction method (Cheng et al. [6]).

Nitschke-Pagel et al. [57] carried out residual stress measurements on an UIT-treated butt-weld joint in high strength steel S690Q, by X-ray, neutron diffraction and hole drilling methods. As shown in Fig.2.28, the maximum of the compressive residual stress can be found in a depth about 0.3-0.4mm, and the compressive residual stress layer is extended to a depth about 2-3mm. The depth profiles determined with the hole drilling method and with neutron diffraction method well match with each other.

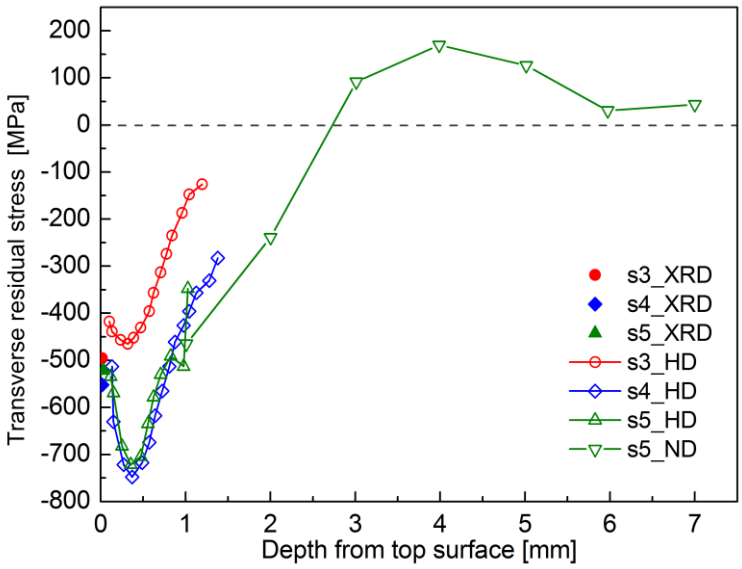

Figure 2.28 In-depth residual stress profiles in UIT-treated butt-weld joint, XRD: X-ray diffraction, HD: hole drilling, ND: neutron diffraction, s3-s5 represent the device treatment intensity, s1 is the lowest and s5 is the highest possible intensity (Nitschke-Pagel et al. [57]).

For the further investigation about the residual stress stability in hammer-peened weld joints under different loading conditions (quasi-static preload and fatigue loading), Tai and Miki [58] measured the evolution of 1mm-in-depth residual stress distribution under variable amplitude fatigue loading by incremental hold drilling method. As shown in Fig.2.29, the compressive residual stress near the surface is relaxed by the static tensile loading with 95% of maximum load before the fatigue test. After the occurrence of high preload, the residual stress distribution is slightly redistributed during fatigue loading. It should be noted that the tensile preload leads to the relaxation of compressive residual stress. It is explained that since at 1mm depth the initially existing tensile residual stress is relaxed due to tensile yield, the compressive residual stress should also reduce to balance.

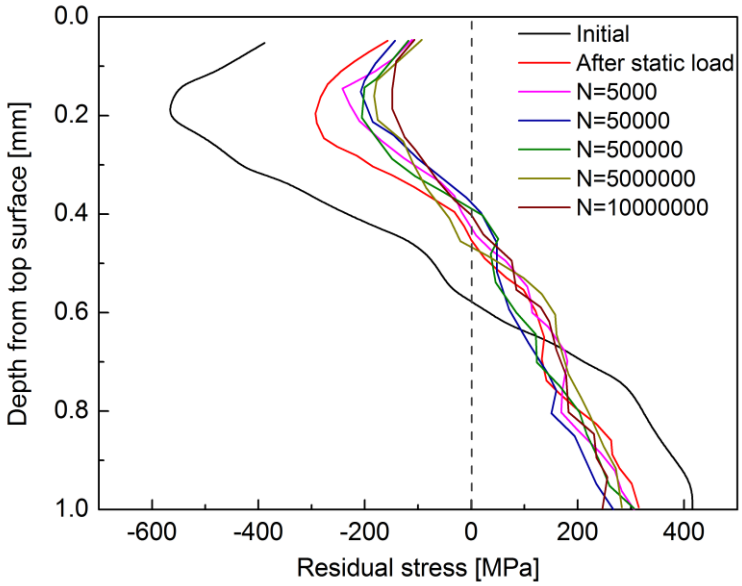

Figure 2.29 In-depth residual stress distributions during fatigue test (Tai & Miki [58]).

The effect of quasi-static preload and cyclic loading on the relaxation of the residual stress nearby the UIT-treated weld toe in longitudinal fillet joint is also investigated using X-ray diffraction method by Shimanuki and Tanaka [59]. As shown in Fig.2.30, compared to monotonic loading, the cyclic loadings with high stress ratio cause more relaxation of the UIT-induced compressive residual stress.

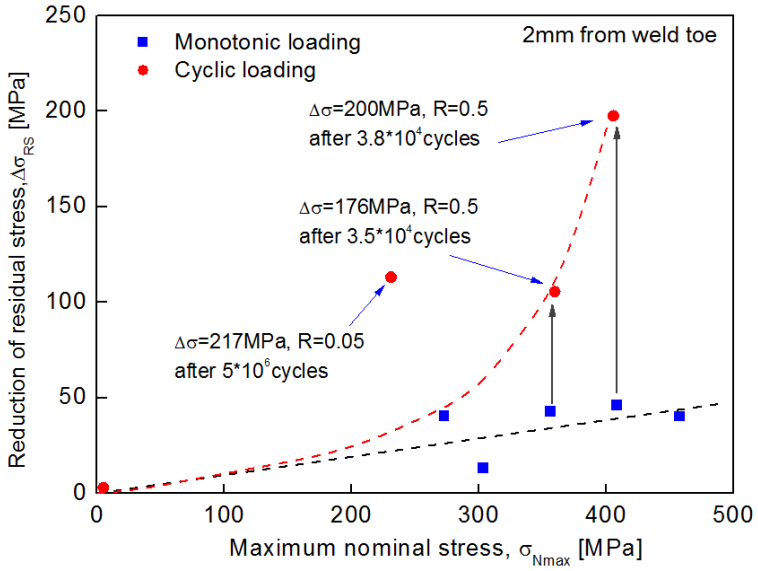

Figure 2.30 Effect of maximum nominal stress on residual stress change at the weld toe due to cyclic loading (Shimanuki & Tanaka [59]).

2.2.4.2 Numerical simulation approach

The residual stress induced by UIT has been recently evaluated by some studies using finite element (FE) analysis. There are mainly two groups of simulation methods for UIT process: quasi-static implicit and dynamic explicit methods. The former is modelled as pressing the pin at the weld to one prescribed depth by displacement control approach, rather than peening [60], [61], [62]. In the latter, the modelled pin impacts to a symmetry-cell model that is widely used in shot peening simulation, however, the welding residual stress has not taken into account [39], [63]. In addition, none of these simulation works has taken the above mentioned acoustic softening effect into account. The details about these FE models are summarized in Table 2.4.

Table 2.4 Summary of studies on numerical simulation of UIT

Ref	FE method	Target model	Pin model	Welding residual stress	Acoustic softening
Roy [60]	2D quasi-static	Isotropic hardening	Rigid	Yes	No
Weich [61]	3D quasi-static	Isotropic hardening	Elastic	No	No
Quilliec et al. [62]	3D quasi-static	Kinematic hardening	Elastic	No	No
Mordyuk et al. [39]	3D dynamic	Isotropic hardening	Rigid	No	No
Yang et al. [63]	3D dynamic	Isotropic hardening	Rigid	No	No

Roy [60] performed a 2D thermo-mechanical welding simulation and then a quasi-static contact analysis for the modified residual stress distribution due to UIT. The plane strain FE model consists of a rigid indenter pressing the weld toe of the cover-plate specimen following elastic-plastic material behaviour. As shown in Fig.2.31, the predicted residual stress obtained from an under-estimated indentation depth 0.001mm correlated with the measurement better.

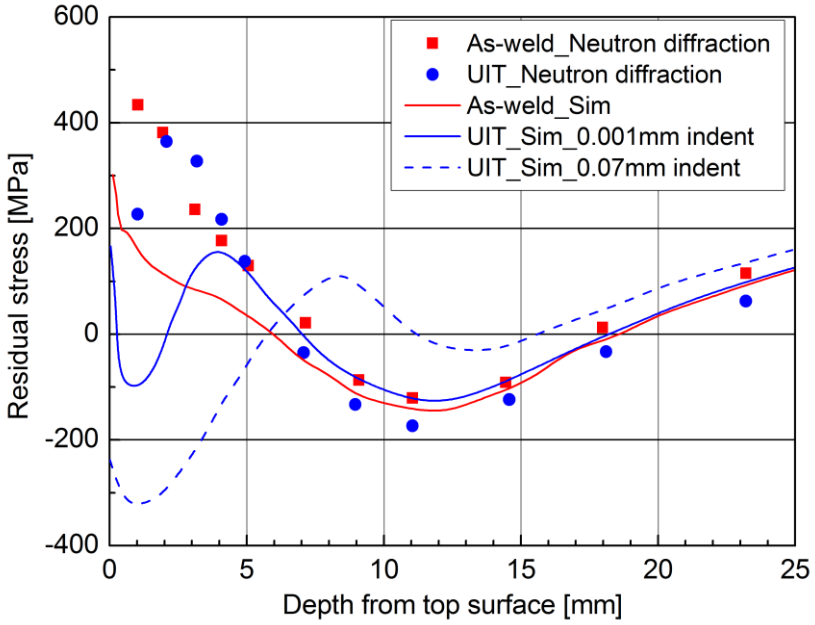

Figure 2.31 Predicted and measured in-depth residual stress profiles (Roy [60]).

Quilliec et al. [62] carried out a 3D displacement-controlled quasi-static analysis for UIT treatment to a cruciform joint, as shown in Fig.2.32. The material models of weld zone and base metal are assumed as linear kinematic hardening and elastic body, respectively. The influence of mesh sensitivity, indenter direction and diameter on predicted residual stress profiles, and residual stress relaxation during cyclic loading are investigated.

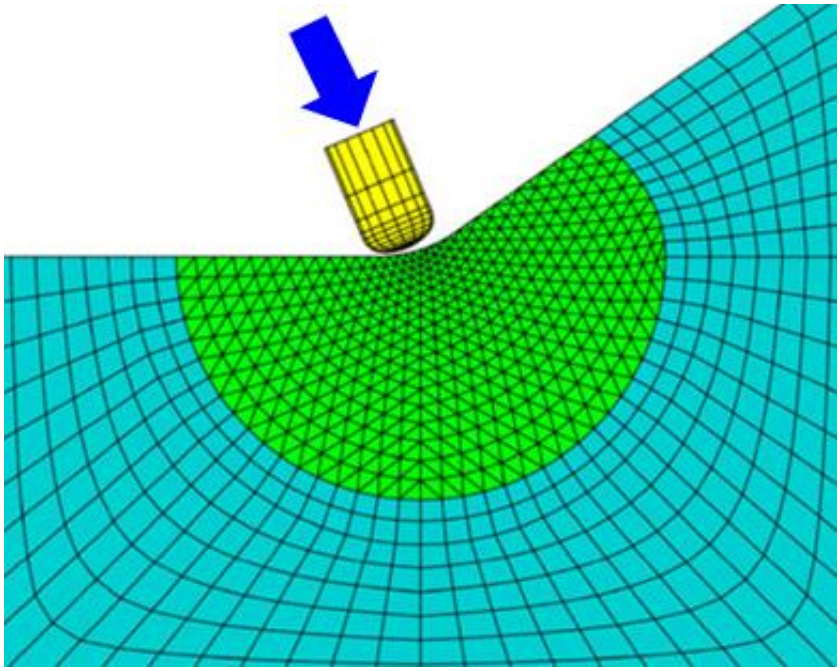

Figure 2.32 Quasi-static FE model for UIT process (Quilliec et al. [62]).

Yang et al. [63] developed a dynamic FE model of UIT with Johnson-Cook material model to consider the impact velocity and strain-rate dependent material properties, as shown in Fig.2.33. The impact velocity of the pin is assumed as the maximum velocity of the waveguide. The effect of impact velocity and coverage on predicted in-depth residual stress profiles and indentation shapes are investigated.

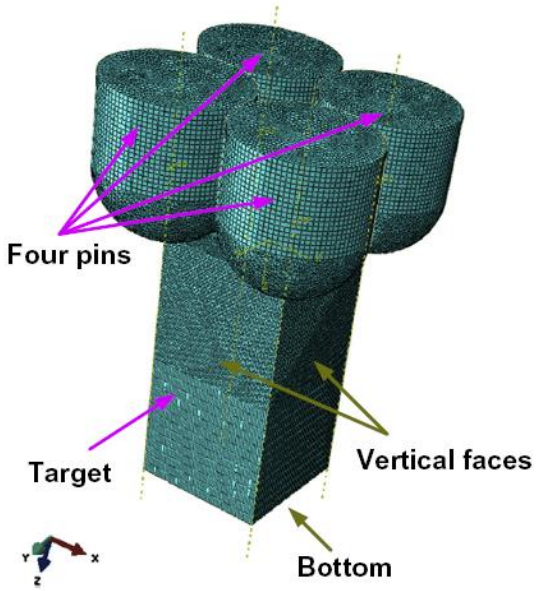

Figure 2.33 Dynamic FE model for UIT process (Yang et al. [63]).

CHAPTER 3

WELDING RESIDUAL STRESS ANALYSIS

3.1 Introduction

In this chapter, the numerical prediction method of welding residual stress distribution will be discussed in detail. The numerical analysis is carried out by means of uncoupled thermo-mechanical finite element method using commercial code SYSWELD [64]. In order to accurately capture the temperature field and welding residual stress distributions, it is necessary to employ a three-dimensional finite element model. The solution procedure for welding-induced residual stress analysis consists of two steps. First, the temperature distribution in the welding model is computed by thermal analysis. Then, the temperature history is employed as a thermal load in following mechanical analysis. In order to verify the accuracy of welding residual stress analysis, the predicted residual stress for a single weld bead laid down on the top surface of an austenitic stainless steel plate is investigated by comparing the measured results of the benchmark problem, which was established by European round-robin project called NeT.

3.2 Heat source and thermal analysis

Thermal analysis can be classified into three main parts: heat input, heat transportation and heat losses. The heat source of the welding process (i.e. the arc) generates a heat flux into the workpiece. This energy is distributed within the workpiece according to the Fourier's law of isotropic heat conduction. The heat losses out of the workpiece are governed by heat conduction, convection and radiation at the surfaces.

Based on a circular disc heat source model with a Gaussian distribution of the heat flux on the surface of the workpiece, Goldak et al. [65] developed a double ellipsoidal power density distribution of the heat source, which can be used to simulate different types of welding process with shallow or deep penetration. For gas metal arc welding (GMAW) or tungsten inert gas (TIG) welding, the Goldak's double ellipsoidal heat source is generally adopted. As shown in Fig.3.1, the heat flux distribution combines two different ellipsoidal regions. The heat fluxes, $q_f(x', y', z', t)$ and $q_r(x', y', z', t)$, describes the heat flux distributions in the front and rear quadrants respectively and can be expressed as,

$$q_f(x', y', z', t) = \frac{6\sqrt{3} f_f Q}{abc_f \pi \sqrt{\pi}} \exp(-3\frac{x'^2}{a^2}) * \exp(-3\frac{y'^2}{b^2}) * \exp(-3\frac{z'^2}{c_f^2})$$
$$q_r(x', y', z', t) = \frac{6\sqrt{3} f_r Q}{abc_r \pi \sqrt{\pi}} \exp(-3\frac{x'^2}{a^2}) * \exp(-3\frac{y'^2}{b^2}) * \exp(-3\frac{z'^2}{c_r^2}) \quad (3.1)$$

where *x'*, y' and z' are local coordinate fixed to the moving heat source; Q is the power input; f_f and f_r are the fractions of the heat deposited in the front and rear quadrants, and $f_f + f_r = 2.0$. The constants, a, b, c_f and c_r shown in Fig.3.1 are heat source parameters that define the size and shape of the ellipsoids.

In continuous acting welding the heat energy input rate Q, which is the principal parameters of welding heat source for the temperature field, is given by,

$$Q = \eta UI \quad (3.2)$$

where U is the voltage and I is the current; η is the heat efficiency considering the heat dissipation to the surrounding as a result of convection, radiation and the spray losses.

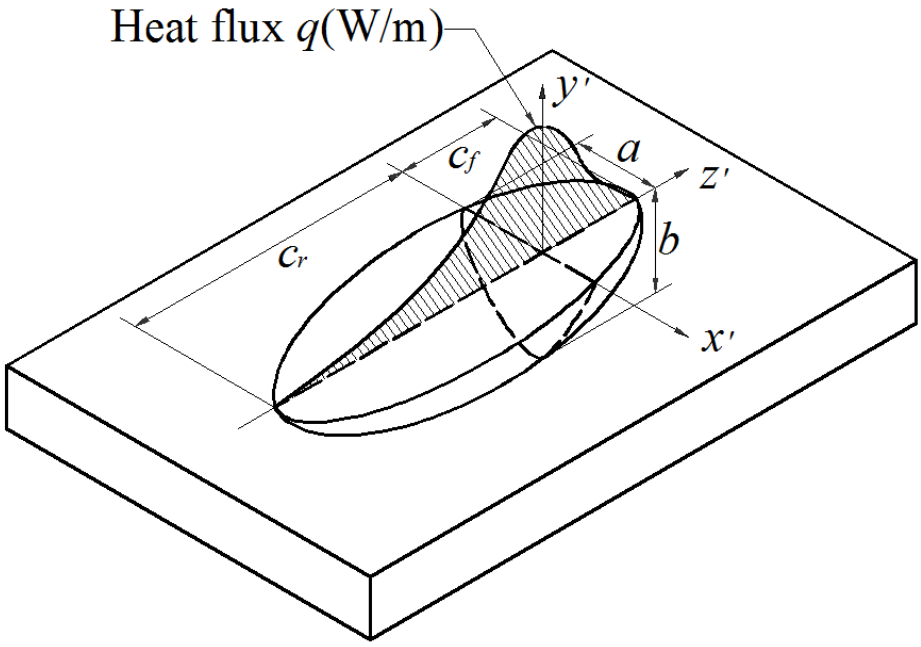

Figure 3.1 Goldak's double ellipsoidal heat source flux distribution (Goldak et al. [65]).

Based on the principle of conservation of energy, for homogeneous and isotropic continuum the instantaneous field equation of heat conduction is given by [66],

$$\rho c \frac{\partial T}{\partial t} = -\nabla^T \boldsymbol{q} + \dot{Q} \tag{3.3}$$

where T is the current temperature, $\dot{Q}$ is heat energy per unit volume, ρ is the density of the material, c is the specific heat , t is the time and $\boldsymbol{q}$ is the heat flux vector.

Fourier's law of isotropic heat conduction gives

$$\boldsymbol{q} = -k\nabla T \tag{3.4}$$

where k is the coefficient of thermal conductivity.

The combination of the above equations leads to the classical heat conduction equation:

$$\rho c \frac{\partial T}{\partial t} = \nabla^T (-k\nabla T) + \dot{Q} \tag{3.5}$$

Here, ρ is weakly temperature-dependent, k and c are strongly temperature-dependent. The solution of this equation is governed by the initial and boundary conditions, where initial condition is the initial temperature of the body, commonly defined as ambient temperature, and the boundary conditions are primarily responsible for heat dissipation due to convection and radiation on the surface.

The boundary condition for heat transfer by convection is given according to Newton's law,

$$q_c = h_c(T - T_0) \tag{3.6}$$

where q_c is the loss due to surface convection, h_c is convection heat transfer coefficient, T is the body temperature and T_0 is the ambient temperature.

The heat dissipation at the boundary by radiation is given according to Stefan-Boltzmann's law,

$$q_r = \sigma\varepsilon(T^4 - T_0^4) \tag{3.7}$$

where ε is the emissivity, σ is the Stefan-Boltzmann constant, and T and T_0 are the body and the ambient temperatures respectively.

3.3 Mechanical analysis

The thermal analysis is followed by a mechanical analysis where the nodal temperature histories calculated in thermal analysis are used as input data to calculate the resulting strains during welding.

The basis for classic finite elements in mechanics is the equilibrium equation written as,

$$\nabla^T \boldsymbol{\sigma} + \boldsymbol{b} = \mathbf{0} \tag{3.8}$$

where $\nabla^T \boldsymbol{\sigma}$ is the divergence of the stress field (transpose of the gradient matrix ∇) and $\boldsymbol{b}$ is the body force per unit volume.

In this work, the total strain can be written as follows,

$$\boldsymbol{\varepsilon} = \boldsymbol{\varepsilon}_{el} + \boldsymbol{\varepsilon}_{pl} + \boldsymbol{\varepsilon}_{th} \tag{3.9}$$

where the components on the right side of the equation represent elastic, plastic and thermal strain, respectively.

The generalised Hooke's law (constitutive equation) is expressed as,

$$\boldsymbol{\sigma} = \boldsymbol{C}\boldsymbol{\varepsilon}_{el} = \boldsymbol{C}(\boldsymbol{\varepsilon} - \boldsymbol{\varepsilon}_{pl} - \boldsymbol{\varepsilon}_{th}) \tag{3.10}$$

where $\boldsymbol{C}$ is the elasticity matrix.

And the kinematics equation for small deformation is,

$$\boldsymbol{\varepsilon} = \nabla \boldsymbol{u} \tag{3.11}$$

Therefore, if the elastic and thermal strains are known, the plastic strain needs to be defined in order to solve the following expression,

$$\nabla^T(\boldsymbol{C}(\nabla\boldsymbol{u}-\boldsymbol{\varepsilon}_{pl}-\alpha(\boldsymbol{T}-\boldsymbol{T}_0)))+\boldsymbol{b}=\boldsymbol{0} \tag{3.12}$$

where α is the isotropic temperature-dependent coefficient of thermal expansion and $\boldsymbol{T}$ is the temperature obtained from the thermal analysis.

To define the plastic strain, one requires yield criterion which allows evaluating if the solid behaves elastically or plastically. The yield criterion defines the elastic limit and is expressed as scalar yield function f. f=0 corresponds to the plastic surface in the stress space and f <0 corresponds to the domain of elasticity. In this work, the yield function based on von Mises criterion is employed as,

$$f(\sigma,\bar{\varepsilon}_{pl})=\frac{3}{2}\xi_{ij}\xi_{ij}-[\sigma_Y(\bar{\varepsilon}_{pl})]^2 \tag{3.13a}$$

$$\xi_{ij}=s_{ij}-\alpha'_{ij};\ \sigma_Y(\bar{\varepsilon}_{pl})=\sigma_0+r(\bar{\varepsilon}_{pl}) \tag{3.13b}$$

where s_{ij} is deviatoric stress; α'_{ij} is deviatoric back stress, σ_0 is initial yield stress, $r(\bar{\varepsilon}_{pl})$ is isotropic hardening modulus function, $\sigma_Y(\bar{\varepsilon}_{pl})$ is the flow stress function of effective plastic strain $\bar{\varepsilon}_{pl}$.

The material hardening model is considered to have an important effect on the predicted residual stress. Therefore in this work, two types of strain hardening models are compared in the analysis: isotropic hardening and kinematic hardening models, which are schematically depicted in Fig.3.2.

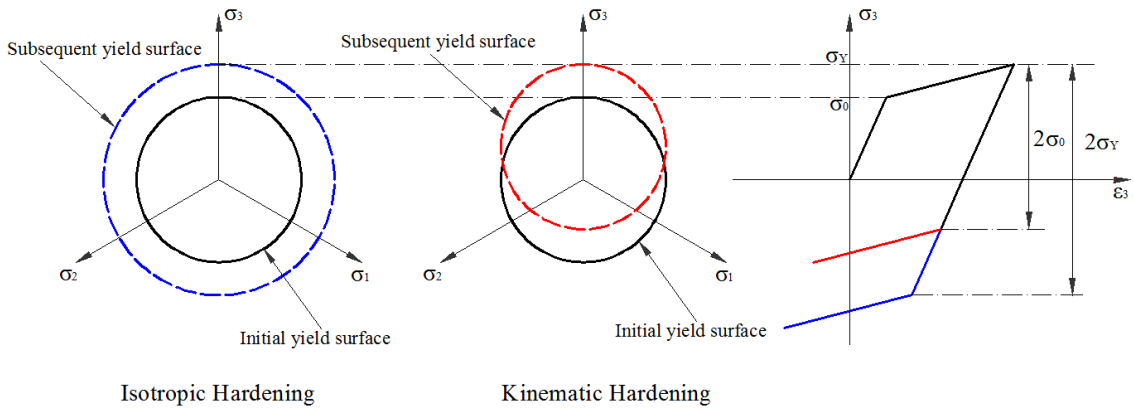

Figure 3.2 Comparison of isotropic and kinematic hardening models.

The isotropic hardening model is based on the assumption that the yield surface maintains its shape, center, and orientation, but uniformly expand about its center in the stress space as yielding occurs. The yield function is given as

$$f = \frac{3}{2} s_{ij} s_{ij} - [\sigma_Y(\bar{\varepsilon}_{pl})]^2 \tag{3.14}$$

It is clear that the isotropic hardening model neglects such path-dependent behaviour as the Bauschinger effect, since it assumes that a raised yield point in tension carries over equally in compression.

On the other hand, in the kinematic hardening model, the yield surface remains the same shape and size but merely translates in stress space. The total stress range is assumed to the twice the initial yield stress. The yield function is given as

$$f = \frac{3}{2}(s_{ij} - \alpha'_{ij})(s_{ij} - \alpha'_{ij}) - \sigma_0^2 \tag{3.15}$$

Such a plastic response is advantageous when attempting to describe the strain-path dependent behaviour, so the kinematic hardening model is commonly used in FE analysis relating to material response in cyclic loading.

In addition, the effect of "annealing temperature" on the predicted residual stress distribution is considered. Basically, annealing is a process in which a metal is heated to about 60%-70% of its melting temperature and then slowly cooled to soften the material and recover ductility. Recently, in the engineering weld modelling community, the term "annealing" has come to take a more particular meaning in that it is used to describe the erasure of previous strain hardening in a finite element analysis [67], [68]. In SYSWELD, when the temperature of material point exceeds annealing temperature the equivalent plastic strain is reset to zero, removing the prior isotropic hardening history of the material and returning the diameter of the yield surface to its value at zero plastic strain. A similar effect is achieved for kinematic hardening material by eliminating the back stress tensor and returning the yield surface center to the origin. If the temperature of the material point falls down below the annealing temperature, the material point can work harden again [69].

3.4 Validation of bead-on-plate welding simulation

3.4.1 Experimental work in NeT Task 1

The European Network on Neutron Techniques Standardization for Structural Integrity (NeT) was established in 2002, and over 35 academic and industrial organizations from Europe and beyond were involved. Task 1 was formed to examine the benchmark problem of a single weld bead laid down on the top surface of an austenitic steel plate [70]. This weld geometry produces a strongly three-dimensional residual stress distribution, which has been measured in the research scope using diverse methods, such as neutron diffraction (ND) method [69], [71], [72], [73] and deep hole drilling (DHD) method [74].

The nominally identical bead-on-plate of NeT Task1 is shown in Fig.3.3. The AISI 316L austenitic stainless was chosen as base metal. The nominal specimen dimensions were 120mm×180mm×17mm. A single tungsten inert gas (TIG) weld bead was deposited along the centreline using an automated procedure. The weld torch transverse distance between lines A and C is 60mm, but not the total bead length (which is somewhat longer). The welding process parameters are given in Table.3.1.

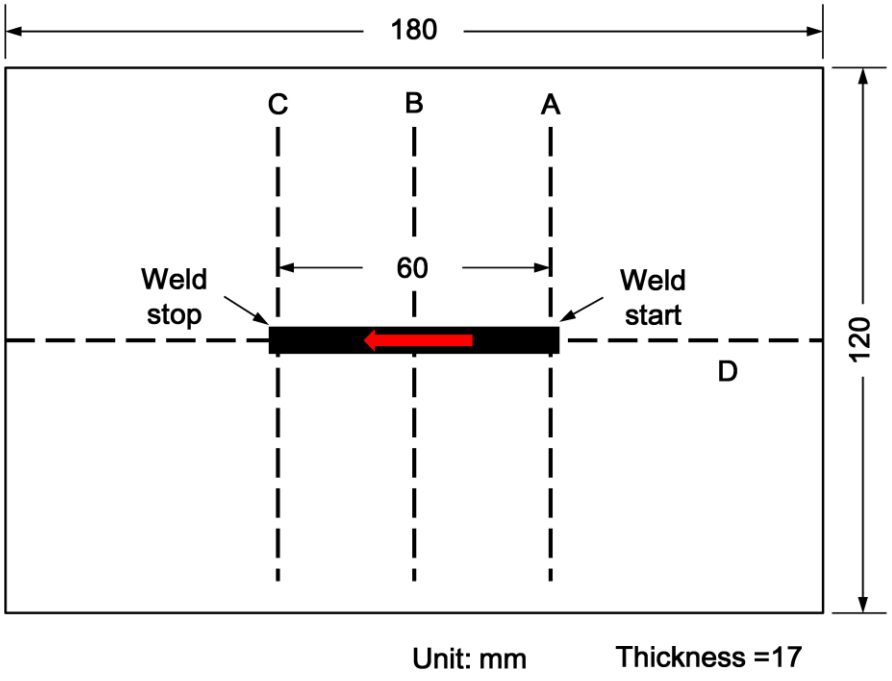

Figure 3.3 Schematic diagram of NeT single weld bead-on-plate specimen.

Table 3.1 Welding process parameters of Task 1

Heat input *HI* [J/mm]	Energy *W* [kJ]	Welding Speed *v* [mm/s]	Initial temperature T_o [^oC]
633	38	2.27	20

3.4.2 Finite element model

The three dimensional FE model generated by SYSWELD is shown in Fig.3.4. Due to the anticipated high temperature and stress gradients neat the weld bead, the mesh is finer in the vicinity of the weld region, and coarser far away from HAZ. The smallest element size is chosen as 0.5 mm(X-direction) ×0.5 mm(Y-direction) ×0.75mm (Z-direction). Three-point constraint is applied to prevent rigid body motion of the specimen during welding. The temperature-dependent thermal and mechanical properties of 316L stainless steel given by SYSWELD material database are adopted, which are shown in Fig.3.5.

The heat source fitting (HSF) tool is an available facility in SYSWELD, which enables the user to calibrate the parameters of a heat source and then use this heat source to perform the thermal analysis. The HSF supports a number of different pre-defined heat source models, all of which represent particular welding processes. As this analysis is concerned with a TIG weld, the Goldak's double ellipsoid model is selected. In order to calibrate the heat source model, a temperature contour plot showing the predicted weld fusion zone can be compared with the measured cross-section of the weld metal and/or heat affected zone (HAZ). If the weld pool boundary is correct, the temperature field outside this region will also be correct [69]. The initial temperature of the plate is set as 20^{o}C. The temperature of fusion zone is set to be at or above the melting temperature of 1400 ^{o}C. The parameters describing the heat source are adjusted iteratively until the predicted molten zone coincides with the measured macrographs of the specimen. Fig.3.6 shows the final predicted fusion zone. The predicted HAZ is shown as a series of contours between 800 ^{o}C and 1400 ^{o}C, however there are no identifiable microstructural features with which they may be compared. The final heat source parameters from calibration are summarized in Table 3.2.

The assumed welding period including both welding and cooling-down processes is 7200.0second (2 hours), in order to guarantee the temperature of specimen can cool down to ambient temperature.

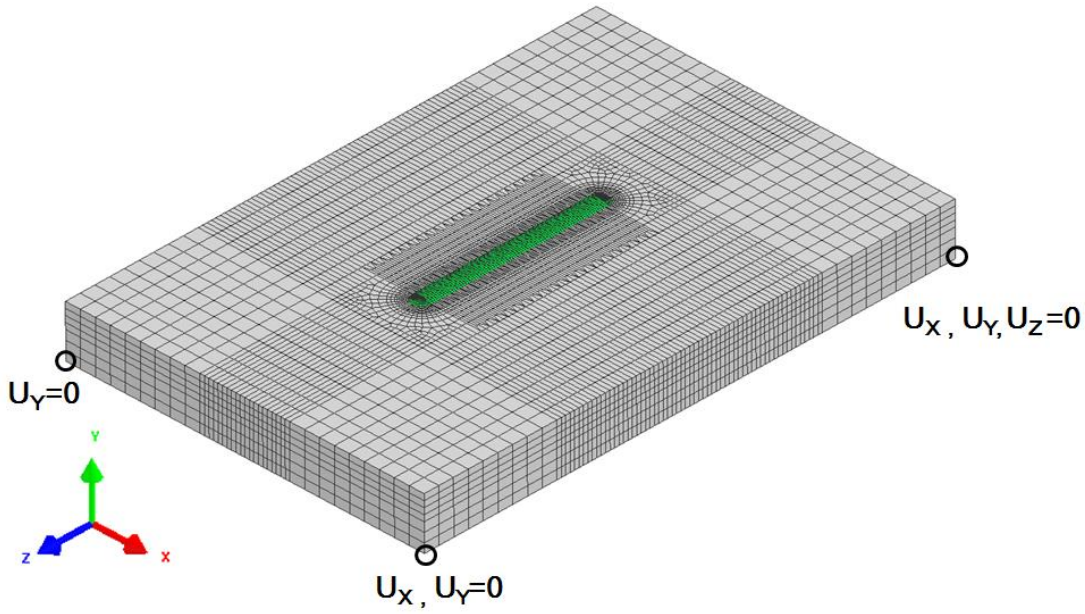

(a)

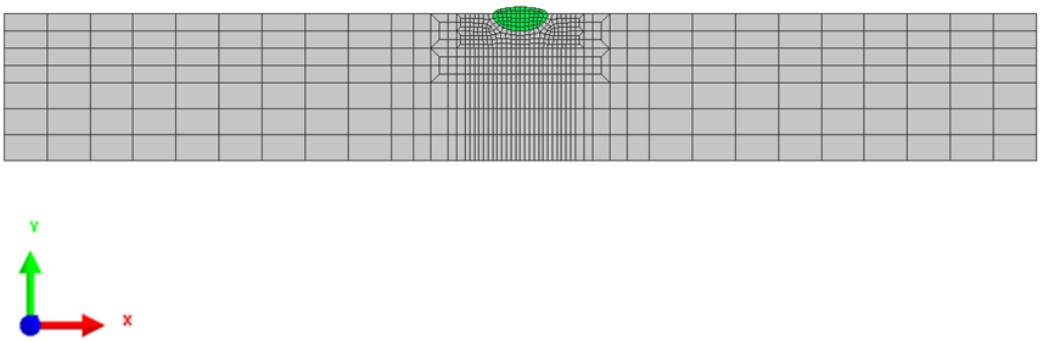

(b)

Figure 3.4 Finite element model; (a) 3D mesh, (b) mesh on middle section.

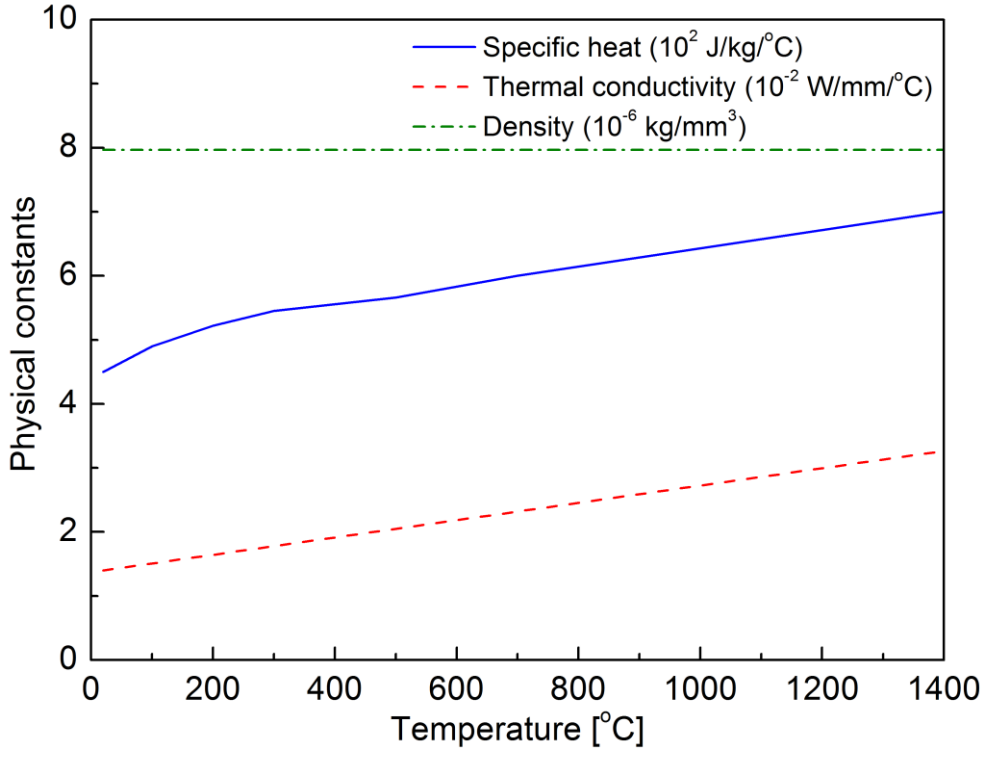

(a)

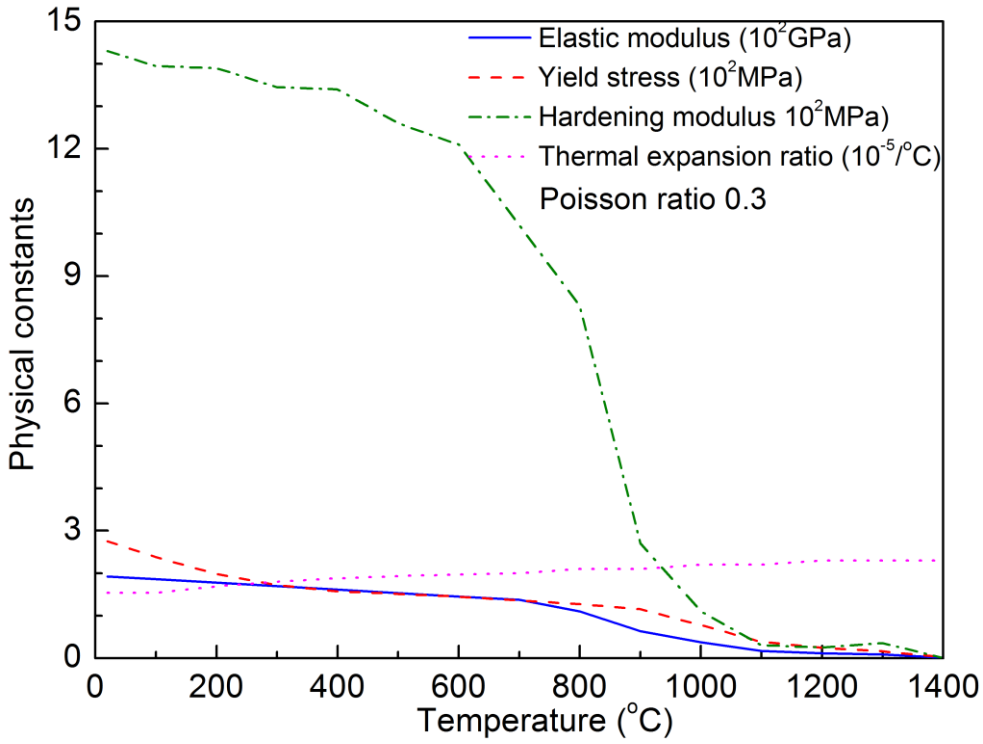

(b)

Figure 3.5 (a) Temperature-dependent thermal properties of stainless steel 316L, (b) Temperature-dependent mechanical properties of stainless steel 316L (SYSWELD [64]).

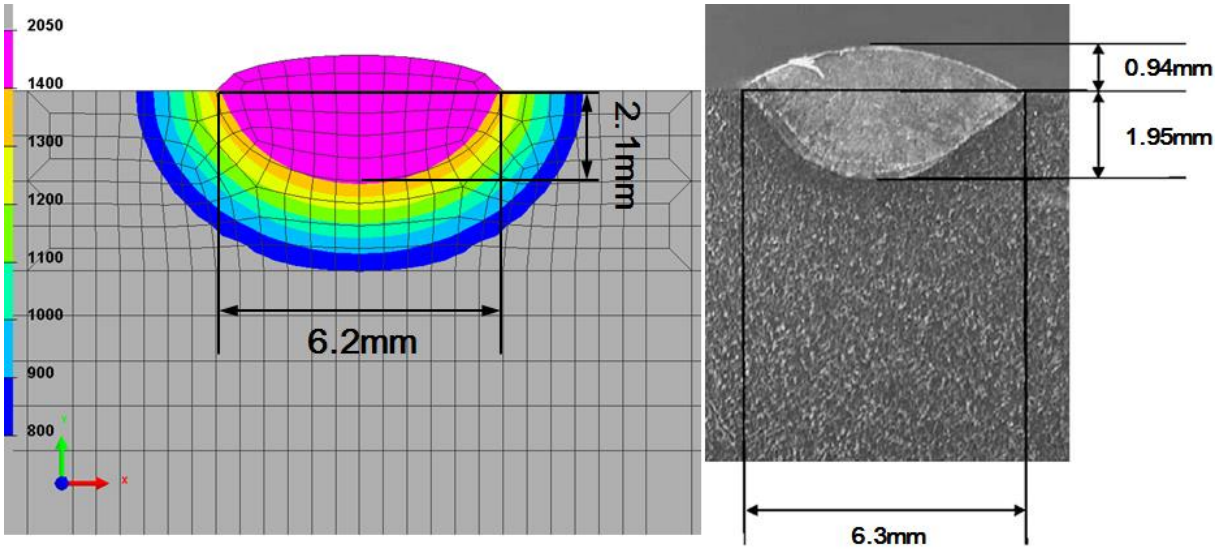

Figure 3.6 Comparison of macrostructure between prediction and measurement (Ohms et al.[72]).

Table 3.2 Heat source parameters

Heat input *HI* [J/mm]	Efficiency η [%]	Power ratio f_f / f_r	Velocity *v* [mm/s]
633	80	1.2	2.27
a [mm]	*b* [mm]	c_f [mm]	c_r [mm]
3.2	2	1.6	3.2

The mechanical analysis is conducted with two hardening models (bilinear isotropic hardening model and bilinear kinematic hardening model). The simulated results will be compared with the measured data to determine optimum material hardening model in the future simulation work. In addition, two annealing temperatures are set as 1400 ^{o}C [75] and 800 ^{o}C [76] to study its effect.

3.4.3 Welding residual stress results and observation

Fig.3.7 presents typical contour plots of transverse and longitudinal residual stresses, which act perpendicular to and parallel to the weld line respectively, viewed from the top of the plate, with a cross-section along the center of the weld bead. High tensile transverse residual stresses are predicted beneath the weld bead, and maximum transverse tensile stress is distributed at the weld stop end. The tensile stresses are balanced by transverse compressive stresses far away from the weld bead along the longitudinal direction. The longitudinal residual stresses are tensile at the weld centreline along the weld bead and compressive away from the weld bead along the transverse direction. They appear to be much less variation along the weld bead than predicted transverse stresses.

The residual stress measurements were carried out on the test specimens by various laboratories using different methods including neutron diffraction (ND) technique by Hofmann et al. [71], Ohms et al. [72], Pratihar et al. [73], Xu et al. [69] and deep hole drilling (DHD) technique by Ficquet et al. [74].

Fig.3.8 shows the comparisons between predicted residual stresses, with two hardening models and two annealing temperatures, and the measured data along line D2. Line D2 runs parallel to the weld bead on the symmetry plane at the center of the bead, 2mm under the top surface. From the figures, the predicted transverse residual stresses of all cases fall within the scatter band of the measurements. The peak transverse tensile stresses are predicted at the weld stop end, irrespective of material models. Longitudinal stresses are tensile along D2. The highest stresses are over-estimated by the model assuming isotropic hardening with annealing temperature 1400 ^{o}C and the lowest using kinematic hardening with annealing temperature 1400 ^{o}C. The annealing temperature lowered to 800 ^{o}C brings the predictions of the two hardening models together.

Transverse and longitudinal stresses on line B2, 2mm underneath the top surface at the middle length of the specimen, are plotted in Fig.3.9. There is generally good agreement between the predicted and measured transverse residual stress. The shapes of the predicted and measured longitudinal stress distributions agree well, but close to the weld bead, some divergence can be seen.

Line BD passes through the plate thickness at the weld mid-length. Transverse and longitudinal stresses along line BD are plotted in Fig.3.10. Transverse residual stresses are tensile from the top surface to the about 13mm depth and then become compressive, which agree well with measurement. The longitudinal residual stresses are tensile, but always over-predicted.

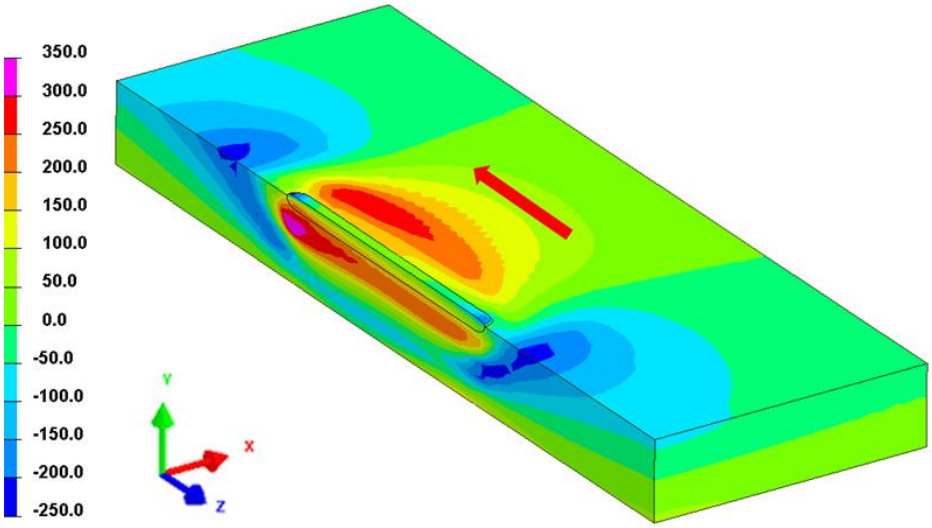

(a)

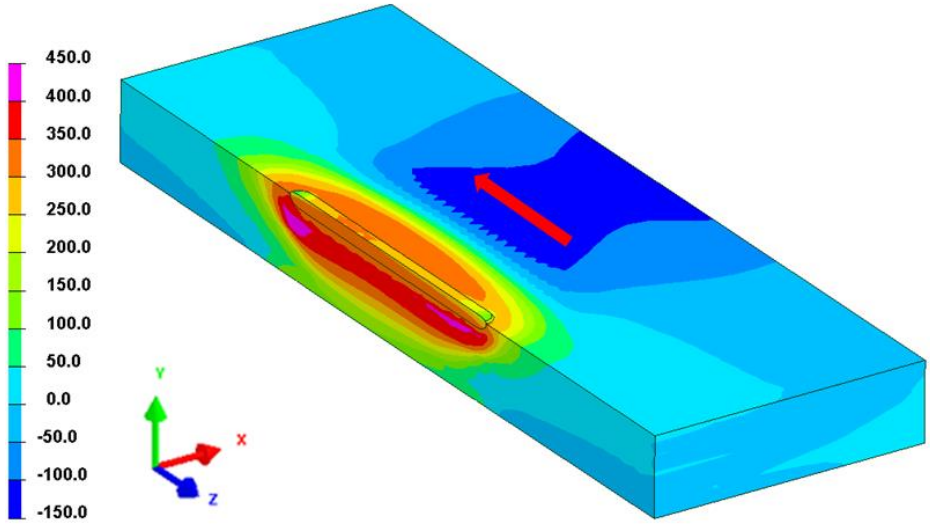

(b)

Figure 3.7 Typical contour plots of predicted residual stress distributions; (a) transverse residual stress, (b) longitudinal residual stress.

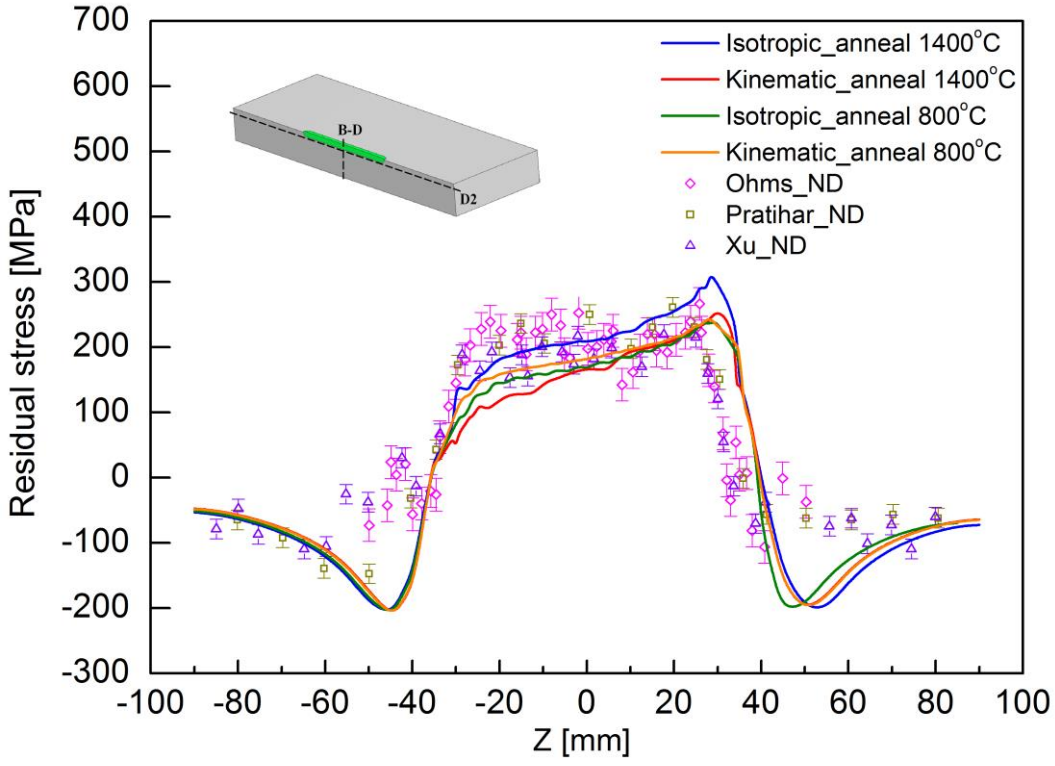

(a)

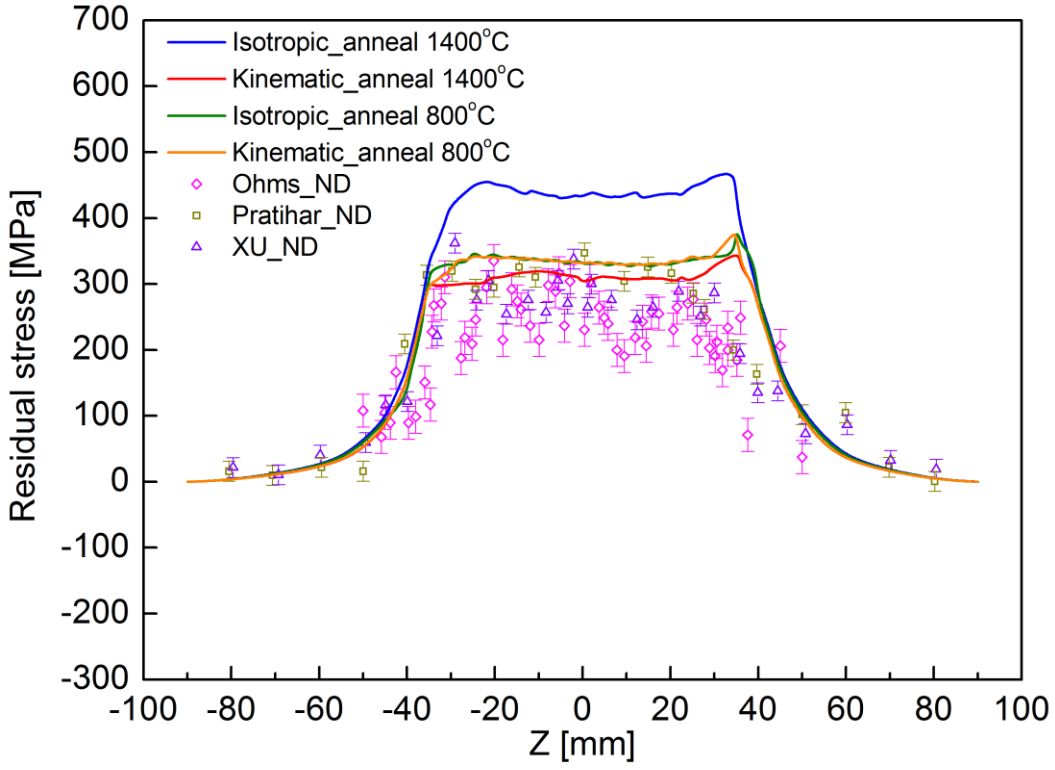

(b)

Figure 3.8 Comparison of the predicted stresses with measured data along D2; (a) transverse residual stress, (b) longitudinal residual stress.

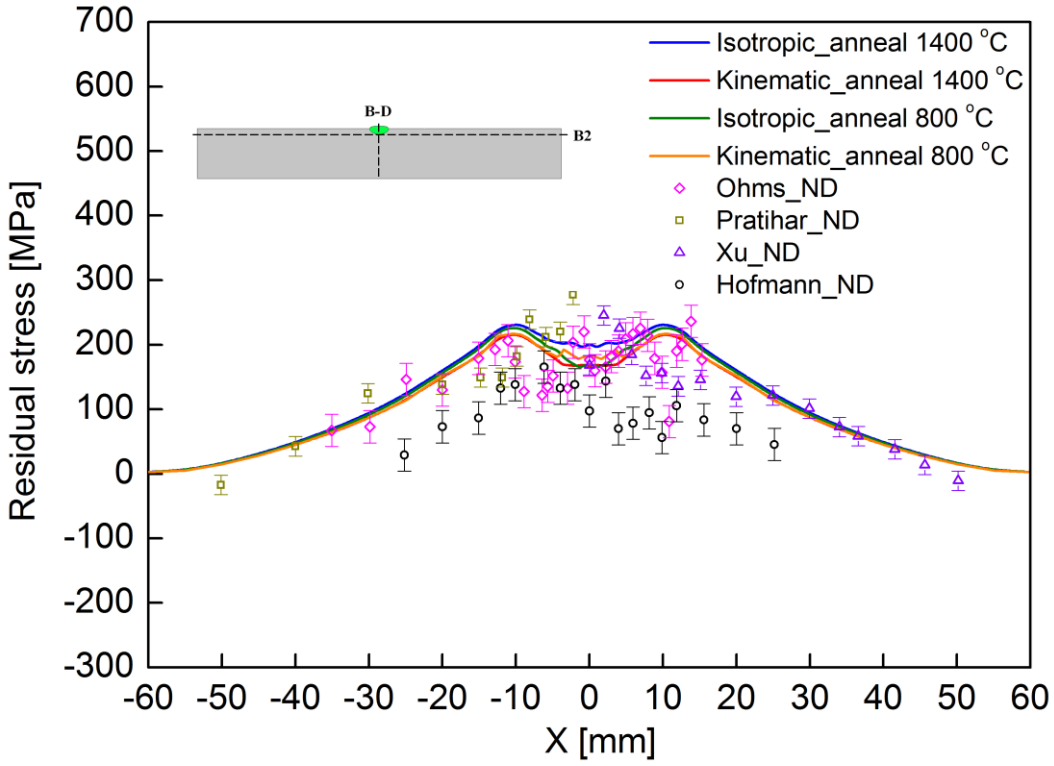

(a)

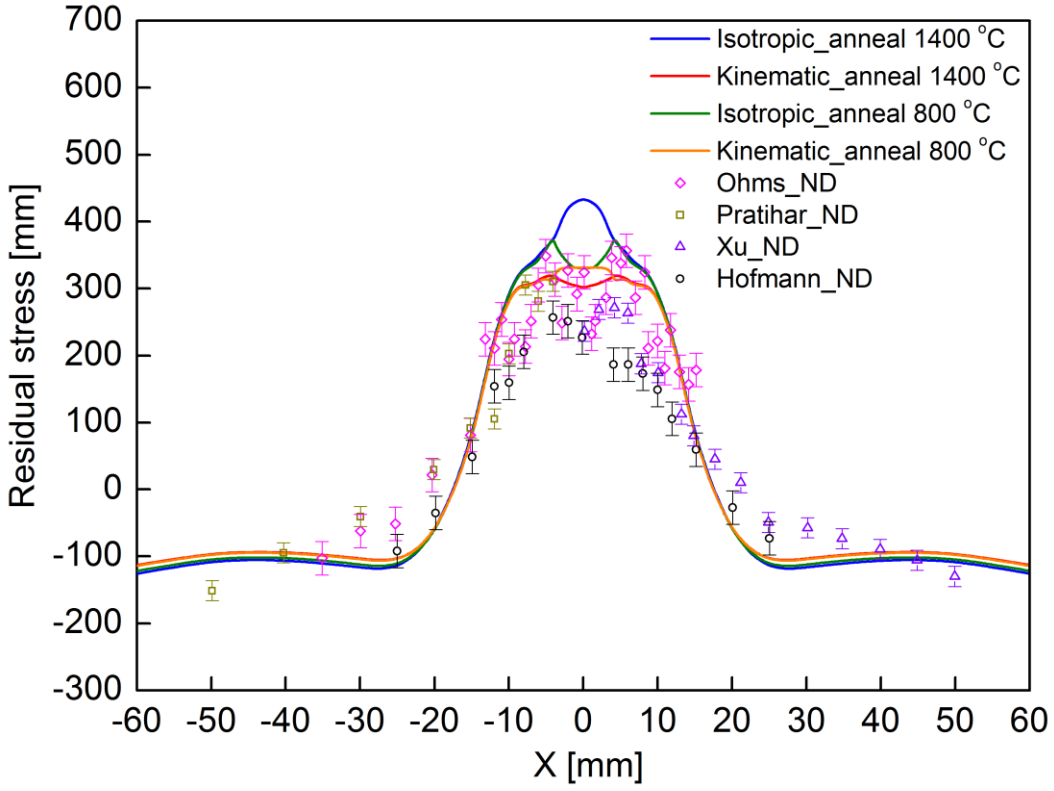

(b)

Figure 3.9 Comparison of the predicted stresses with measured data along B2; (a) transverse residual stress, (b) longitudinal residual stress.

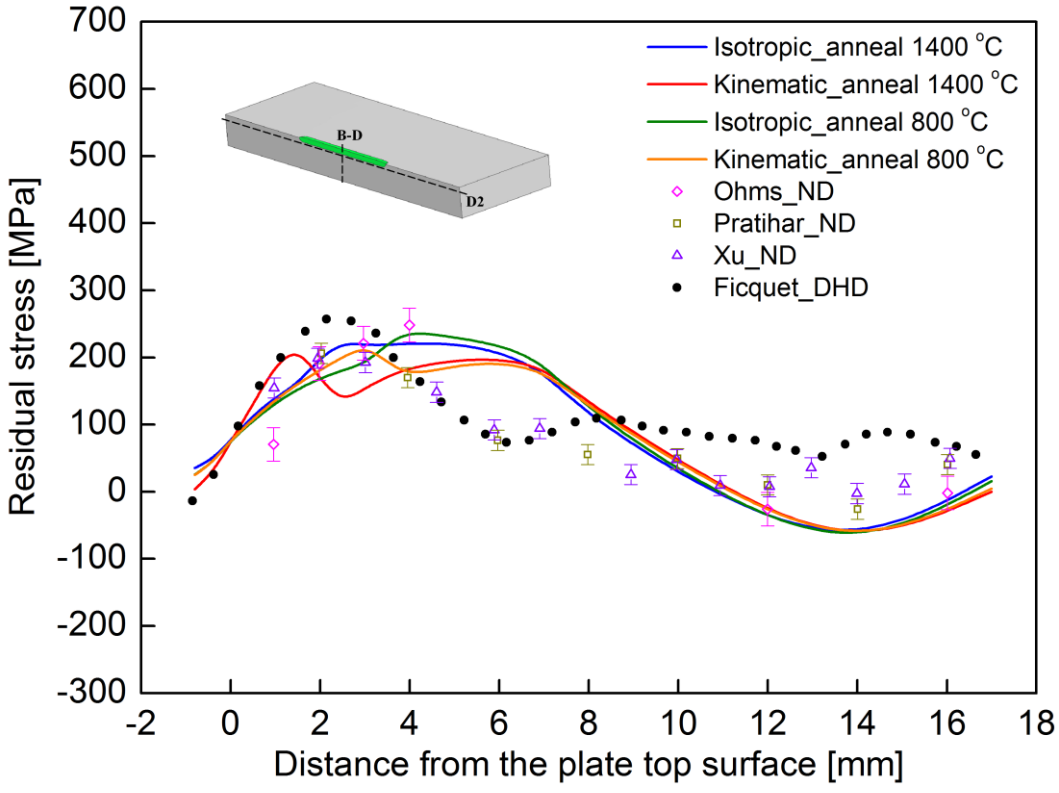

(a)

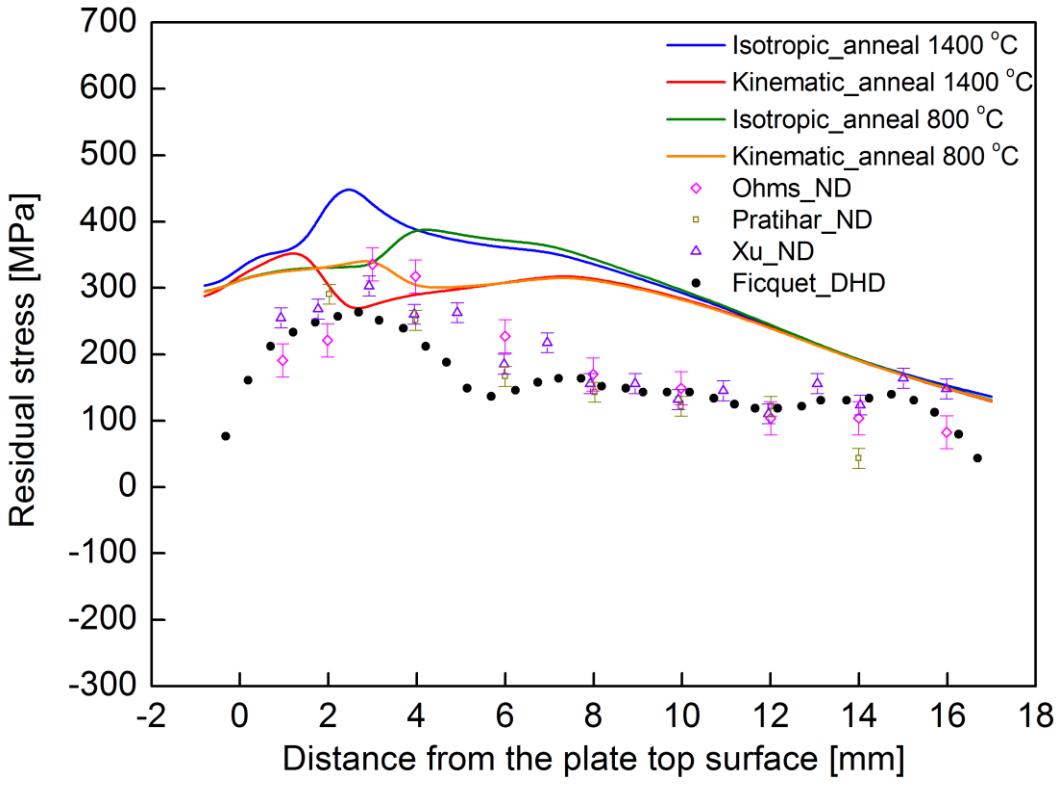

(b)

Figure 3.10 Comparison of the predicted stresses with measured data along BD; (a) transverse residual stress, (b) longitudinal residual stress.

From these results, it can be observed that the transverse residual stress around the weld metal are generally not sensitive to the material properties including hardening models and annealing temperature, while longitudinal stress are sensitive. Although accurate residual stress analysis can be conducted by combination of isotropic hardening and lower annealing temperature, the kinematic hardening is recommended, especially for the future prediction case of welds subjected to cyclic mechanical loading. In addition, the annealing temperature is to be set as 800 ^{o}C because it is much closer to the practical meanings.

CHAPTER 4

NUMERICAL SIMULATION OF ULTRASONIC IMPACT TREATMENT

4.1 Introduction

One of the primary reasons for the success of ultrasonic impact treatment in enhancing fatigue performance is to retard fatigue crack growth by introduction of beneficial compressive residual stresses at the treated weld toe through local plastic deformation. Some researches on experimental measurements of UIT-induced residual stress have been reviewed in Chapter 2. In spite of providing some characteristic, it has been realized that the usefulness of these measurements has been limited due to the considerable cost, time and skillful technique.

As an alternative, one novel 3D numerical simulation approach for the residual stress field prediction, including thermo-mechanical welding simulation by SYSWELD [64] and dynamic elastic-plastic FE analysis of UIT by explicit method in LS-DYNA Ver.971 [77], has been presented in this chapter. As discussed earlier, the high frequency impacts induced by uninterrupted oscillations during each ultrasonic impact and ultrasound induced material softening are the most important aspects of the UIT technology. To construct the UIT FE model, one simplified model to describe the ultrasonic impact phenomenon is first proposed based on existing experimental observations. The effect of mesh size, material damping and yield stress reduction due to acoustic softening on the predict-

ed impact-induced residual stress distribution are investigated in the following preliminary studies. Finally, the non-load-carrying cruciform joint, which has been used by Suzuki et al. [78] for measurement of residual stress by means of X-ray and neutron diffraction techniques, is modelled and analyzed. The model can then be calibrated with respect to the measured residual stress distributions before and after UIT at discrete locations and treated weld toe shape to provide a reasonably accurate prediction. The effect of preload on UIT-induced residual stress relaxation will also be simulated.

4.2 Modelling of ultrasonic impact

Based on the description of ultrasonic impact and the recording of the impacts generated by UIT [3], [79], one simplified model to describe this phenomenon is proposed as Fig.4.1. During one impact period T_{im}, it comprises both the ultrasonic impact period t_1 and pause between impacts t_2. The information about impact frequency f_{im}=100-120 Hz, ultrasonic oscillation frequency f_{ul}=27-44 kHz, relationship between the time of pin contacting the treated surface and one impact cycle t_1/T_{im}=0.1-0.3, has been given by Statnikov [3], [25]. In this work, the t_1 is assumed as 1 millisecond, in the case of impact frequency f_{im} of 100Hz and the relation t_1/T_{im}=0.1, which is in the range of ultrasonic impact time from hundreds of microseconds to units of milliseconds measured by Statnikov et al. [31]. The oscillations of pin at a frequency of 27 kHz, which mainly cause the plastic deformation, will recur about 30 times during reboundless contact phase up to 1 millisecond (equivalent to 30 times of high frequency impacts to the treated surface).

Another essential parameter is the impact velocity of the pin during reboundless period. For the impact velocity, it can be assumed here that all the ultrasonic impact on the treated surface will occur at the same velocity and an averaged velocity is considered. This averaged velocity is taken to be the maximum initial velocity of the waveguide [39], [63]. Considering that the sinusoidal harmonic signal delivered by the transducer is

$$x(t) = A\sin(2\pi f_{ul} t) \tag{4.1}$$

The velocity is

$$\frac{dx}{dt} = 2\pi f_{ul} A \cdot \cos(2\pi f_{ul} t) \tag{4.2}$$

and the maximum initial velocity is

$$V_{max} = 2\pi f_{ul} \tag{4.3}$$

where A represents the maximum displacement amplitude at the waveguide output end, f_{ul} represents the harmonic oscillation frequency of ultrasonic transducer.

For example, when the UIT equipment of Esonix 27 kHz type is used, the oscillating amplitude of the waveguide output end under loaded condition is measured as about 30 μm [30]. The impact velocity is calculated as 5m/s with these UIT equipment parameters. This value is considered as the averaged velocity of the impacts during the treatment process and will be reused as an input in the simulations.

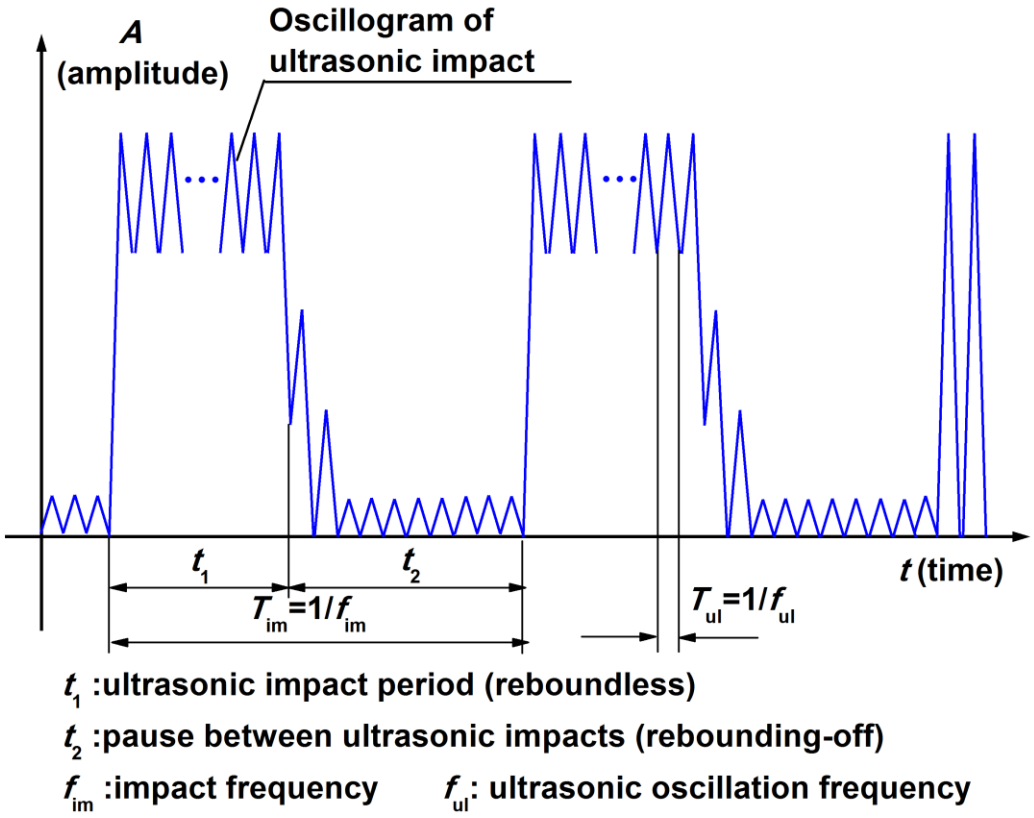

Figure 4.1 Modelling of ultrasonic impact.

4.3 Preliminary numerical investigations

For the sake of finding out the effects of smallest element size, material damping and degree of acoustic softening on the predicted impact-induced residual stress distributions, series of calculations with different parameters are performed by dynamic explicit FE analysis using LS-DYNA [77] in the following numerical investigations.

4.3.1 Finite element model

As shown in Fig.4.2, the three dimensional model used for preliminary numerical investigations, in which one single pin is controlled to vertically impinge onto the square plate at the same location, has been developed.

The dimension of the target plate is 24mm×24mm×6mm. For mesh sensitivity assessment and defining local mechanical properties due to acoustic softening effect, there is a refined region (4mm×4mm×3mm) coloured as red in the center of the plate top surface. The entire target plate is set up by 8-node linear solid elements with reduced-integration and hourglass control. The mesh is finer at the impact zone and coarser towards the outer region. The target plate is assumed to follow bilinear kinematic hardening behaviour with initial yield strength σ_o=390MPa and hardening modulus H=596MPa, which is based on material properties of structural steel SM490 in SYSWELD [64] material data base. The density ρ is set as 7,815kg/m^3.

The tip of 3-mm-diamter pin, which is commonly recommended for the treatment of steel welded assemblies, is modelled over a length of 5mm. The detailed shape is referred to the measured geometry by Le Quilliec et al. [62], as shown in Fig.4.3. Its mechanical behaviour is assumed to be elastic with an elastic modulus E=206GPa, Poisson's ratio ν=0.3 and measured mass of 1.5 gram. Both 8-node solid and 6-node wedge elements are used in the pin model.

As boundary conditions, all displacements of the nodes on the target plate bottom are restrained, and the pin is only allowed to freely move along Z-axis. The impact velocity of 5m/s is employed, and the pin is controlled to repeatedly impinge onto the target plate with same initial velocity using restart analysis option of LS-DYNA [77]. Moreover, the

contact surfaces definition is set between the pin tip and target plate with a Coulomb friction coefficient μ=0.5.

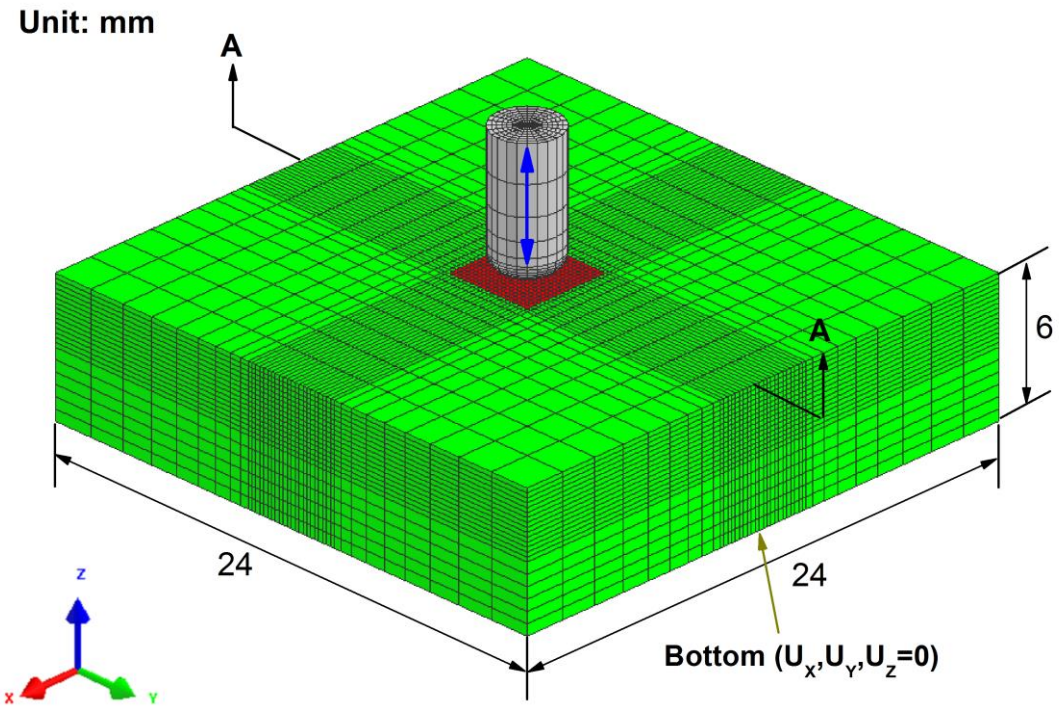

(a)

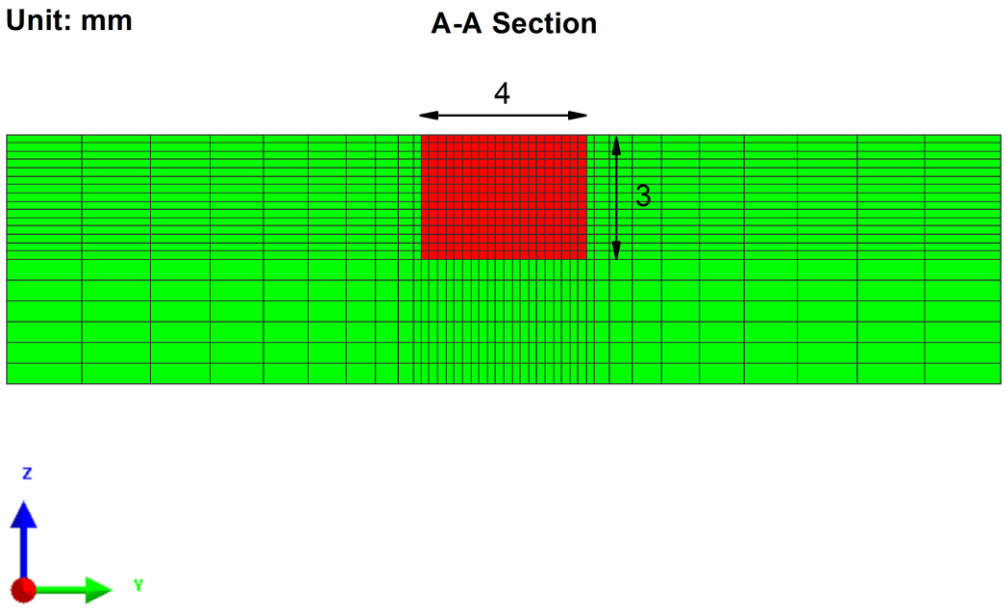

(b)

Figure 4.2 Finite element model used for preliminary investigation (a) 3D mesh, (b) mesh on section A-A.

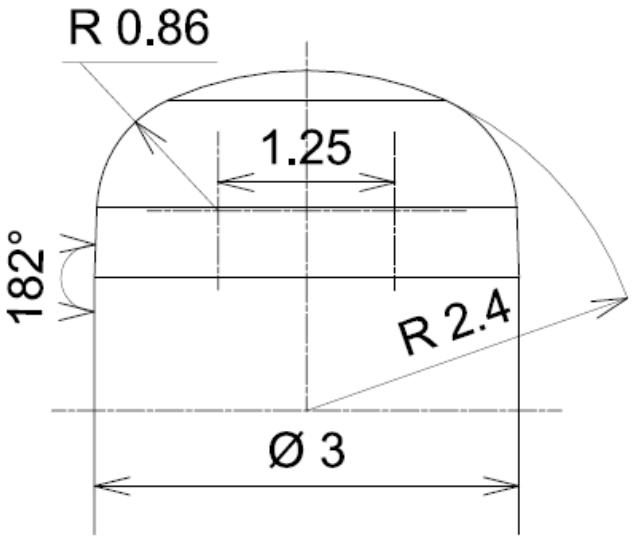

Figure 4.3 Measured geometry of the 3mm diameter pins (Le Quilliec et al. [62]).

4.3.2 Effect of mesh sensitivity

In explicit FE simulations, properly setting the minimum element size $L_{\min}$ would be of great importance since the size of the smallest elements determines the stable time increment and total solution time. The time increment (Δt) affects the convergence and accuracy of the results, so it is recommended to be not greater than the stability limit (Δt_s), according to the Courant-Fredrichs-Lewy condition [77].

$$\Delta t \le \Delta t_s = \frac{L_{\min}}{V_{sw}} = L_{\min}\sqrt{\frac{\rho}{E}} \tag{4.4}$$

where E and ρ are the elastic modulus and density of the material, $V_{sw} = \sqrt{E/\rho}$ is the stress wave speed in the material, for steel generally $V_s \approx 5000\text{m/s}$.

Three FE models, of which the cubic elements with edge of $L_{\min}$=0.05mm, 0.1mm and 0.2mm are subdivided in the above mentioned refined region, are created. Defining the different ratio of minimum element size $L_{\min}$ to the diameter of pin D, the convergence evaluation of induced residual stress has been performed by the simulation of single impact. The results are then extracted through different paths starting from the impact center, as shown in Fig.4.4.

The residual stresses (σ_x) along the in-depth and on-surface paths affected by mesh refinement are shown in Fig. 4.5 (a) and 4.5(b). It is observed that the results of the case of L_{min}=0.1mm is almost same as that with L_{min}=0.05mm, but quite different from that with L_{min}=0.2mm. In addition, the information about the element numbers and computational time of each case are summarized in Table.4.1. The specification of the computer used in this analysis is: Dell Precision 3610, CPU of Intel® Xeon 3.5GHz and RAM 32GB. Thus, to ensure computational efficiency, the minimum element size L_{min}=0.1mm will be selected for further simulation.

Table 4.1 Comparison of computational efficiency with different minimum element size

L_{min}	Element number	Calculation time
0.05 mm	660,000	1h55min
0.1 mm	129,600	14min
0.2 mm	33,600	3min

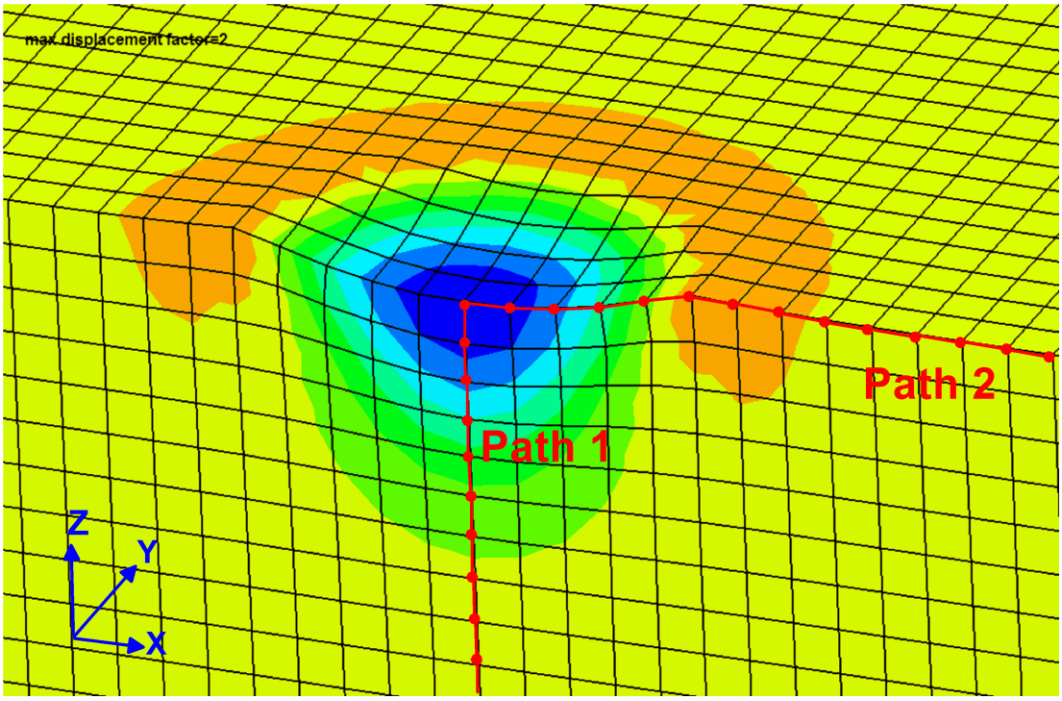

Figure 4.4 Illustration of in-depth (path 1) and on-surface (path 2) paths through which the numerical data have been extracted.

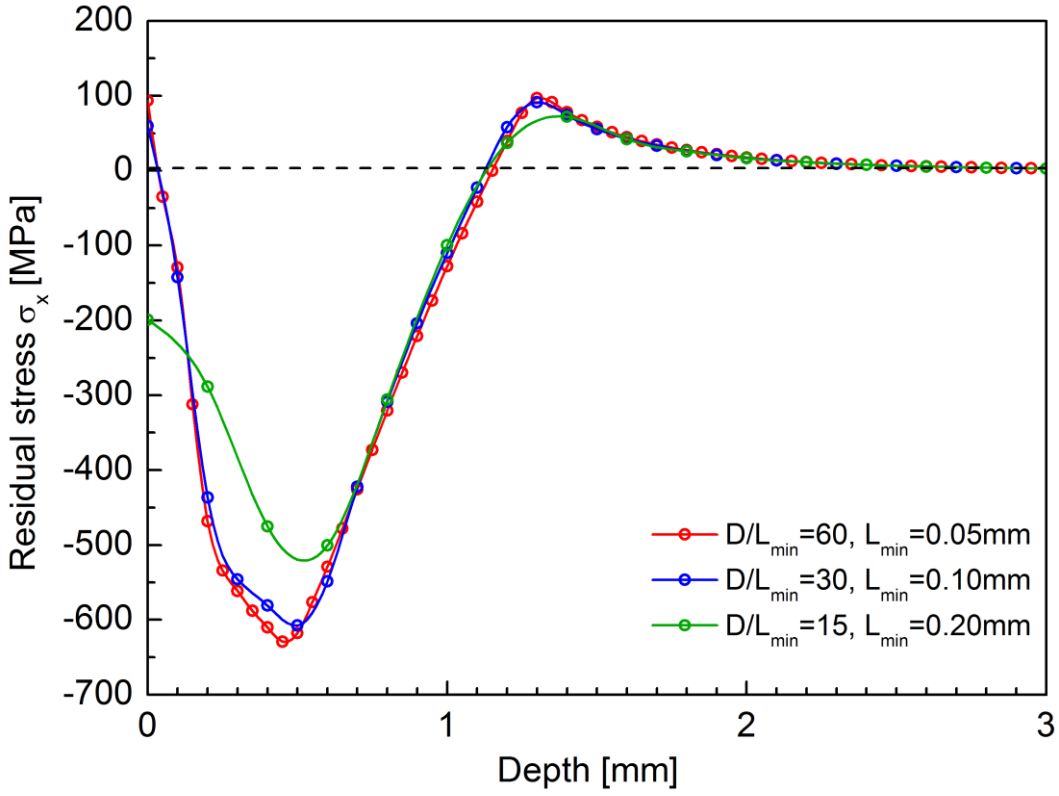

(a)

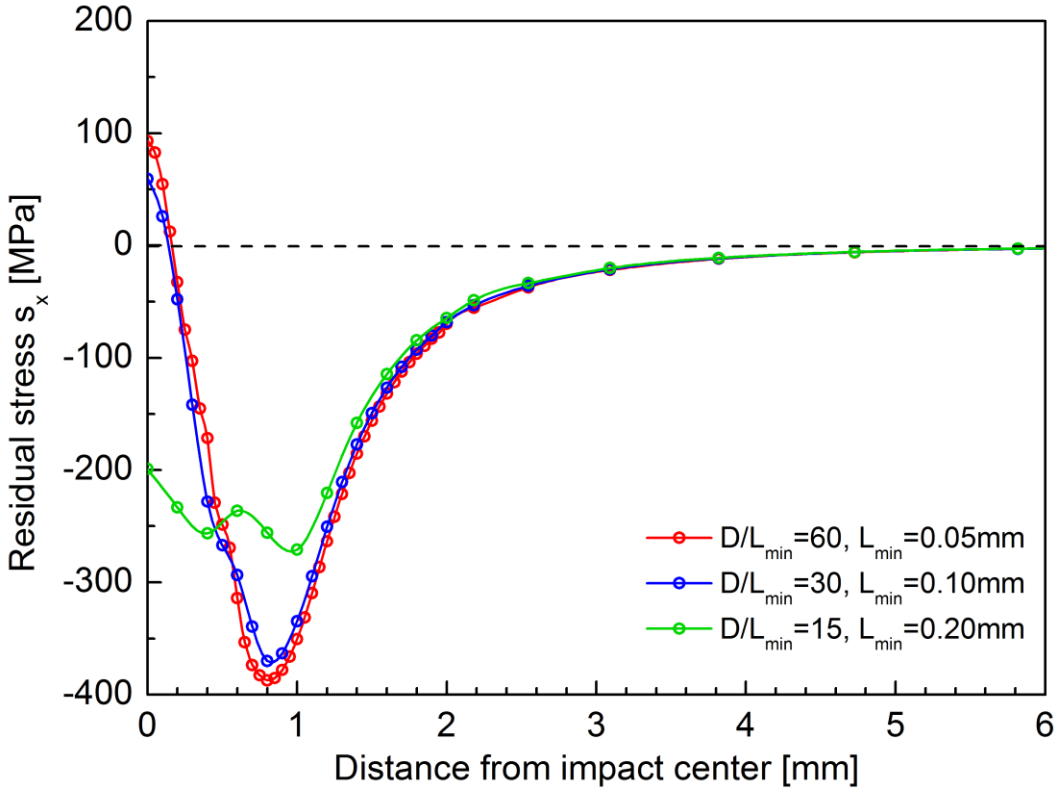

(b)

Figure 4.5 Effect of minimum element size on the simulated residual stress profile; (a) in-depth path (path1), (b) on-surface path (path2).

4.3.3 Effect of material damping

The numerical studies [80], [81] have shown that introducing damping is necessary to avoid unnecessary long post-impact residual oscillations which could accumulate leading to numerical instability.

In this FE model, the global material damping technique (mass proportional damping) is employed to allow impact energy to dissipate in a shorter computation time.

$$\boldsymbol{C} = \alpha \boldsymbol{M} = 2\omega_0 \xi \boldsymbol{M} \tag{4.5}$$

$$\omega_0 = \sqrt{\frac{k}{m}} = \frac{\pi}{2T}\sqrt{\frac{E}{\rho}} \approx 1.35 \times 10^6 / s \tag{4.6}$$

where $\boldsymbol{C}$ is the damping matrix, $\boldsymbol{M}$ is the mass matrix, α is the mass proportional damping factor, ξ is the corresponding damping ratio, E=206GPa is elastic modulus, ρ=7,815kg/m^3 and T=6mm are the density and thickness of the target plate.

Fig.4.6 shows the stabilization of surface residual stress at the impact center node during 5 times of impact with different values of ξ. Without damping, ξ=0.0, the surface residual stress is unstable, leading to accumulated residual oscillations. On the other hand, the results reveal that the additional damping ($0.1 \leq \xi \leq 0.5$) leads to a rapid decay of unwanted residual oscillations between impacts, while not influencing the results during impact. The stress oscillation amplitude decreases more rapidly with increasing value of ξ. It is therefore decided to select ξ=0.5 in the following study. Here, it should be noted that this global material damping is just a numerical tool and bears no physical meaning.

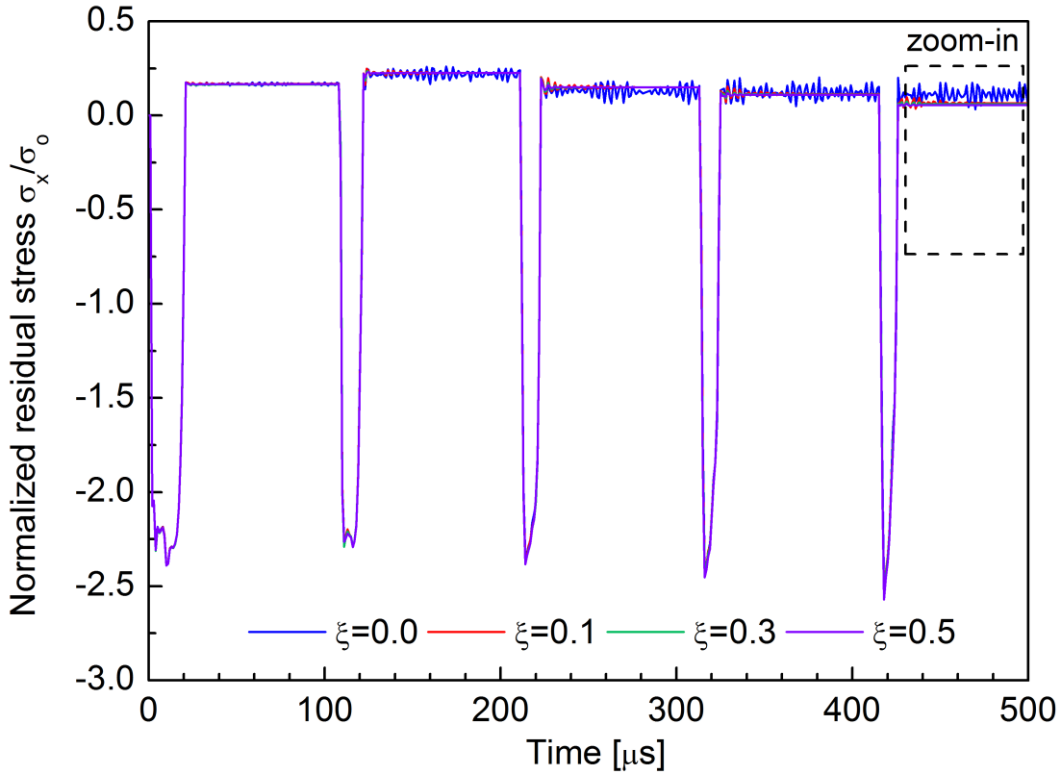

(a)

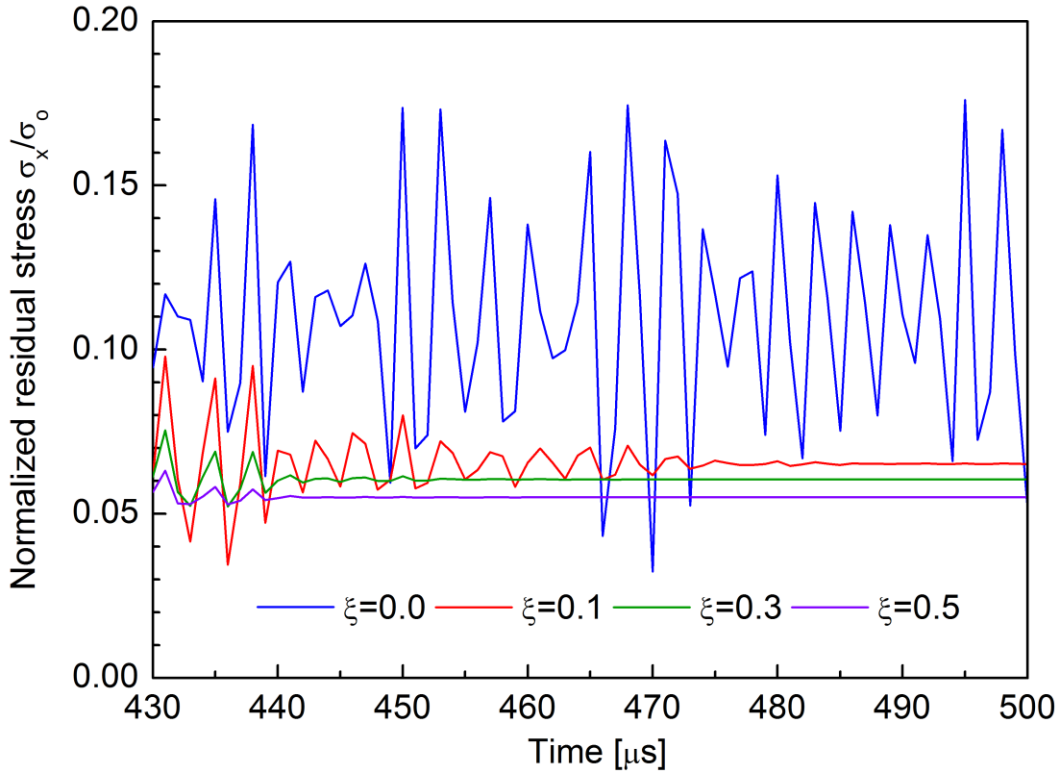

(b)

Figure 4.6 Effect of mass proportional damping on the stabilization of surface residual stress; (a) stress history of node at impact center during first 5 times of impacts, (b) stress history of node at impact center during 5th impact.

4.3.4 Effect of acoustic softening

Little previous researches have been focused on quantifying the effect of acoustic softening on yield stress reduction. Izumi et al. [34], [35] performed the compression test under ultrasonic excitation for different metals and found a linear relationship between the yield stress reduction and vibration amplitude. However, amplitudes only up to 14 μm were studied, for UIT process amplitude about 30 μm is often needed to create significant plastic deformation [30]. Acoustic softening during ultrasonic welding has been previously modelled by Siddiq et al. [38], but their work was only validated by the experimental data of aluminium measured by Langnecker [33]. To the best knowledge of the author, there is no model to directly quantify the acoustic softening due to UIT. Hence, in this work a yield stress reduction parameter η accounting for acoustic softening is employed to modify the already-known static stress-strain curve of the material as follows

$$\sigma_{\mathrm{as}} = \sigma_{\mathrm{o}}(1-\eta) \qquad \text{at certain plastic strain } \varepsilon_{pl} \tag{4.7}$$

where σ_{as} is the flow stress considering acoustic softening, σ_{o} is the flow stress without vibration and η ranges from 0 to 1 depending on the amount of acoustic softening. At a value of η=0, there is no acoustic softening in the material and it will deform normally. At a value of η=1, it represents the ultrasonic energy is sufficient to reduce the yield stress of the material to zero.

For a qualitative analysis about the effect of acoustic softening on impact-induced residual stress, the analysis with different yield stress reduction parameters η ranging from 0-60%, which is defined in the refined region in Fig.4.2, are performed. The corresponding hardening parameters in terms of true stress-true strain are taken as in Table 4.2 and Fig.4.7.

Table 4.2 Hardening parameters in terms of stress-strain considering acoustic softening

η=0% *		η=20%		η=40%		η=60%	
Plastic strain	Stress	Plastic strain	Stress	Plastic strain	Stress	Plastic strain	Stress
0	390	0	312	0	234	0	156
0.5	688	0.5	550.4	0.5	412.8	0.5	275.2

* For η=0%, the material properties of SM490 in SYSWELD [64] material database is used.

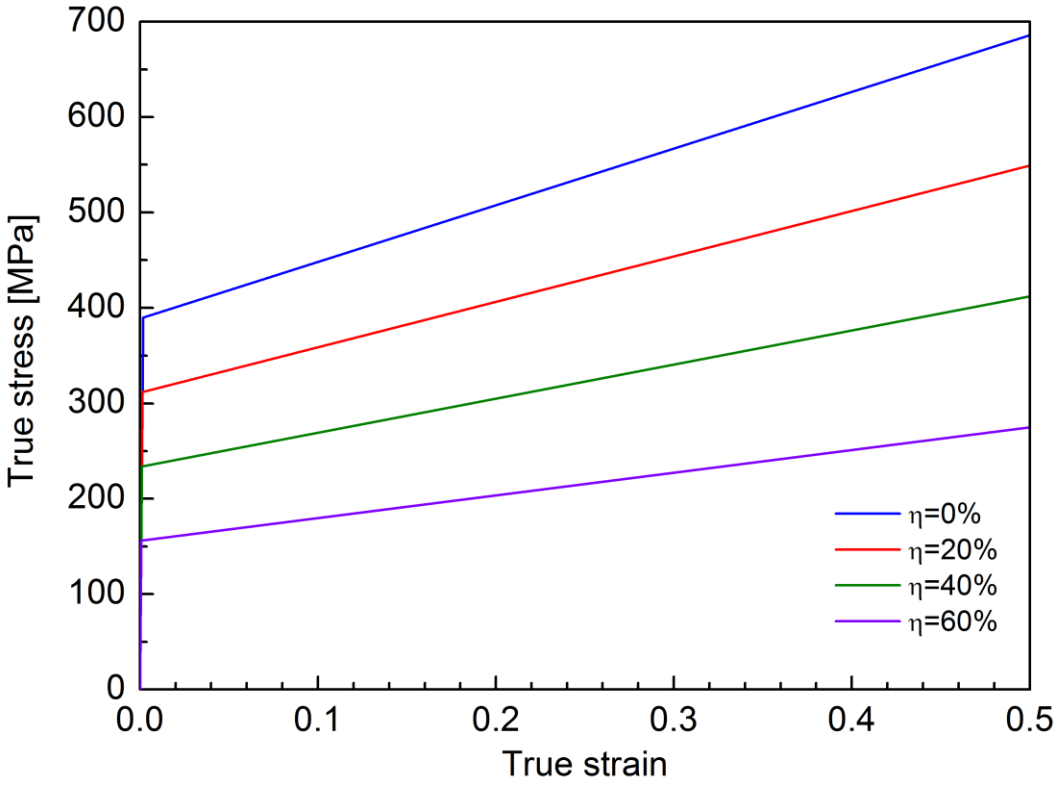

Figure 4.7 Mechanical properties considering acoustic softening.

Fig.4.8 shows the change of indentation depth during 30 times of impact (equivalent to one above mentioned ultrasonic impact). It can be seen that the indentation depth is increased with the peening, but this increases is almost saturated after 30 times of continuous peening. As the yield stress reduction parameters η is increased, the indentation becomes deeper, because the resistance necessary for plastic deformation is decreased due to acoustic softening. In the following study, the value of η should be determined with iterative adjustment by comparing the predicted indentation depth with experiment.

The evolutions of in-depth residual stress profiles considering different yield stress reduction parameters η are shown in Fig.4.9. It can be observed that in all the cases near the plate surface the compressive residual stress layer appears, and it almost becomes saturated with consecutive impacts up to 30 times. With more yield stress reduction due to acoustic softening, the depth of compressive residual stress layer extends more deeply on the contrary the peak value becomes less.

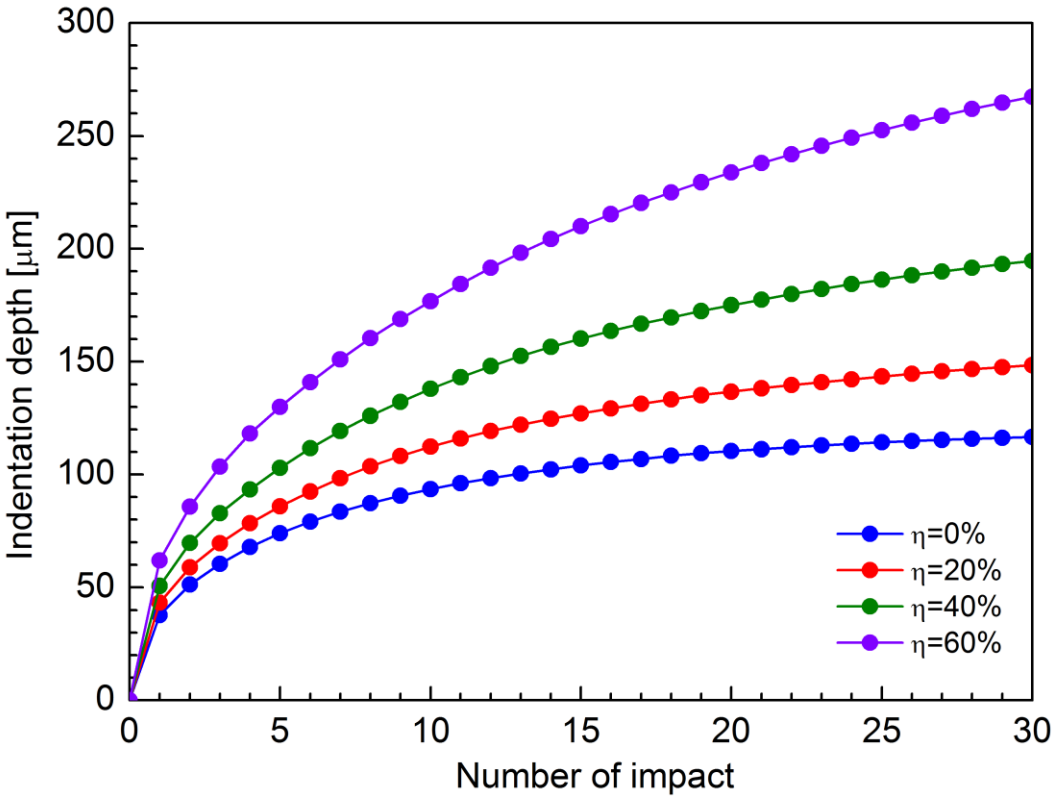

Figure 4.8 Evolution of indentation depth considering acoustic softening.

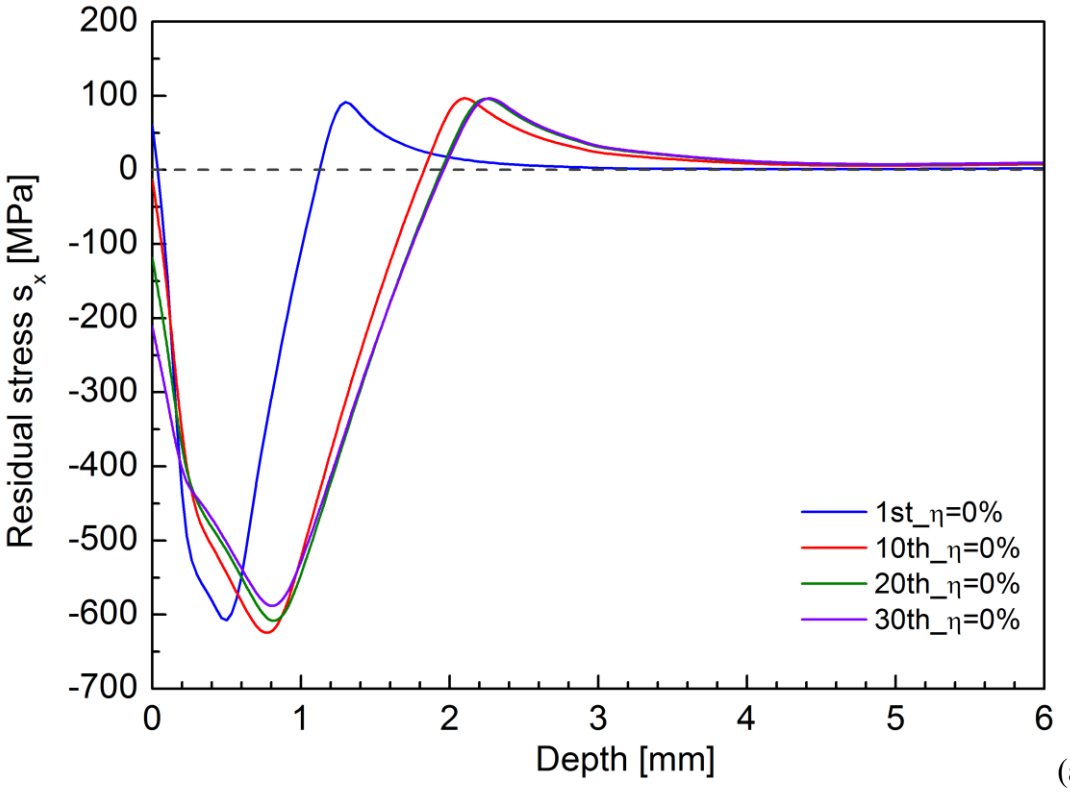
Residual stress s_x [MPa]
Depth [mm]
1st_η=0%
10th_η=0%
20th_η=0%
30th_η=0%

(a)

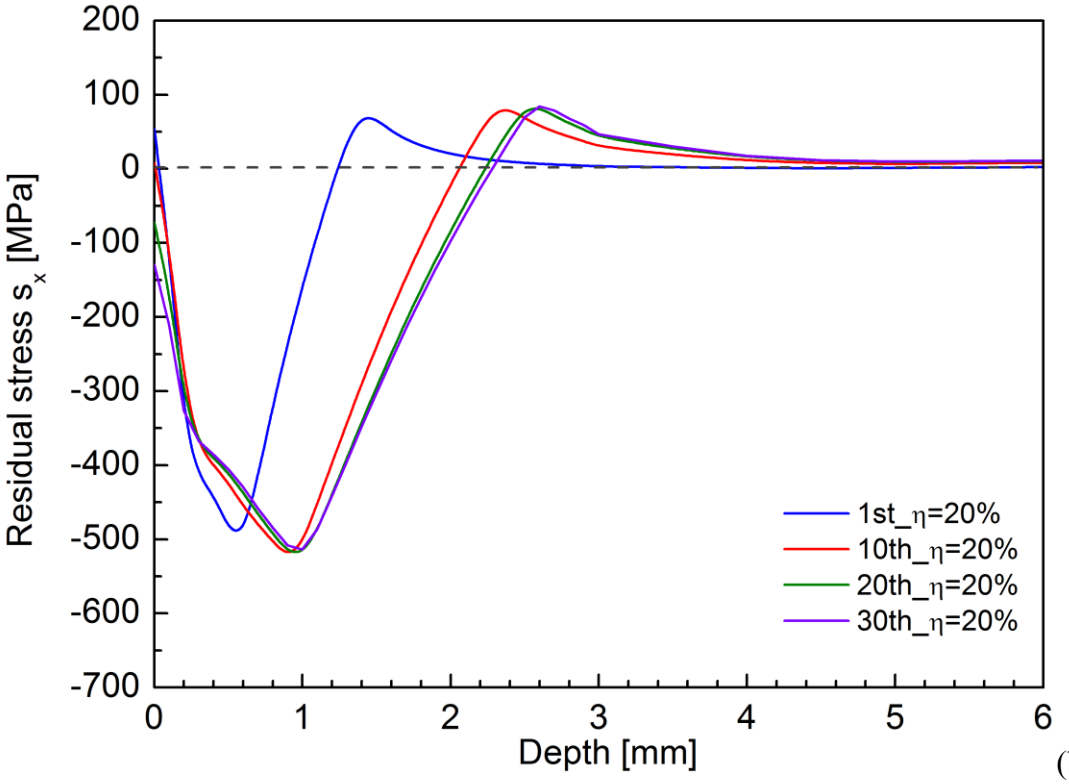
Residual stress s_x [MPa]
Depth [mm]
1st_η=20%
10th_η=20%
20th_η=20%
30th_η=20%

(b)

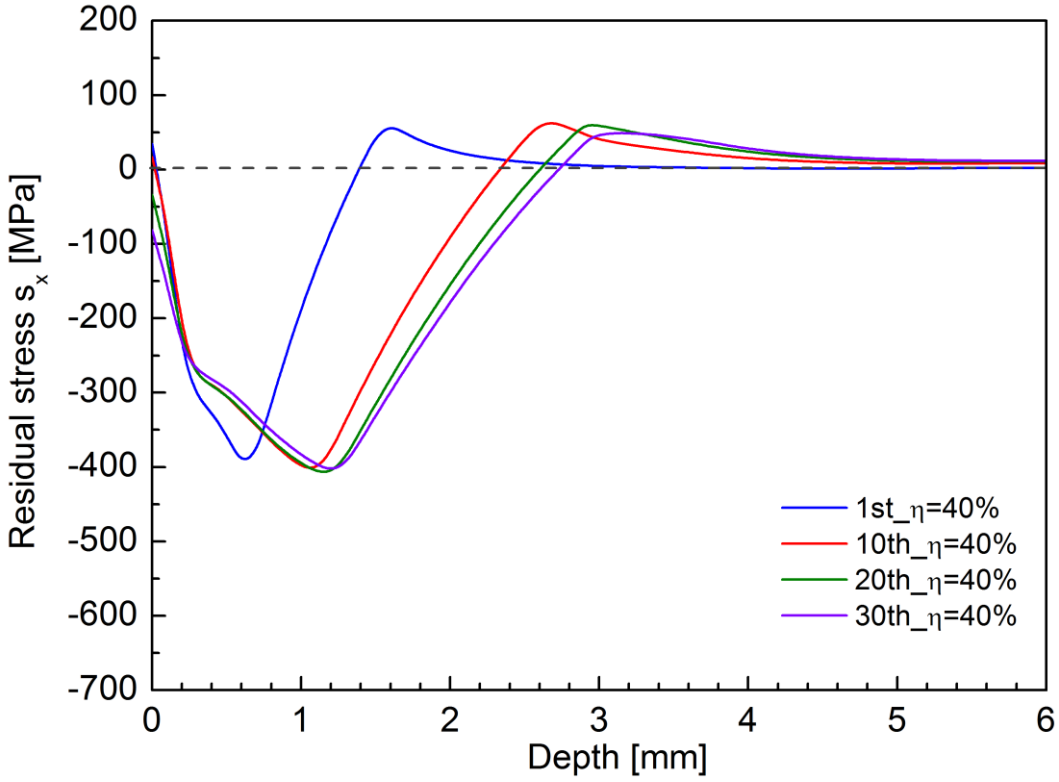

(c)

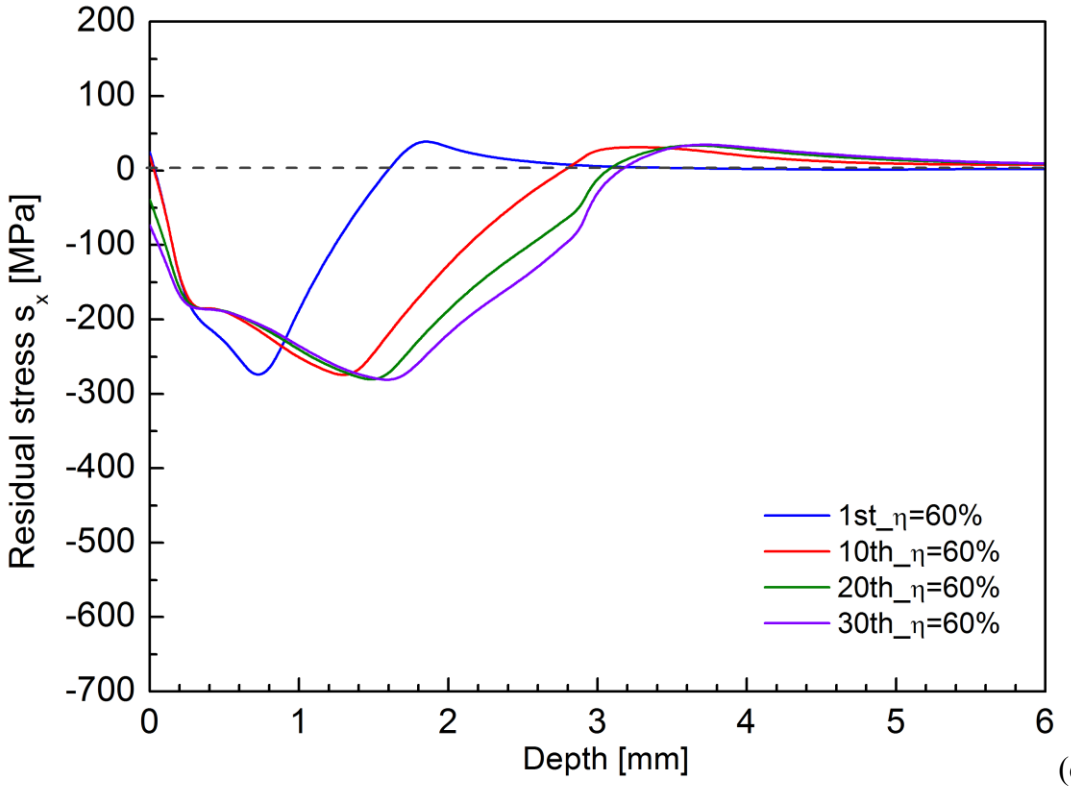

(d)

Figure 4.9 Evolution of in-depth residual stress profiles considering acoustic softening; (a) η=0%, (b) η=20%, (c) η=40%, (d) η=60%.

4.4 Numerical simulation of UIT-treated welded joints

Based on the above mentioned simulation work, one three dimensional simulation approach for UIT process of welded joints is set up by including the uncoupled thermo-mechanical welding simulation by SYSWELD [64], transfer of the results to the initial-stress state of a dynamic model of UIT by explicit method in LS-DYNA [77], as shown in Fig.4.10.

The predicted residual stress distributions and treated weld toe shape will be compared to the measured results for accuracy verification.

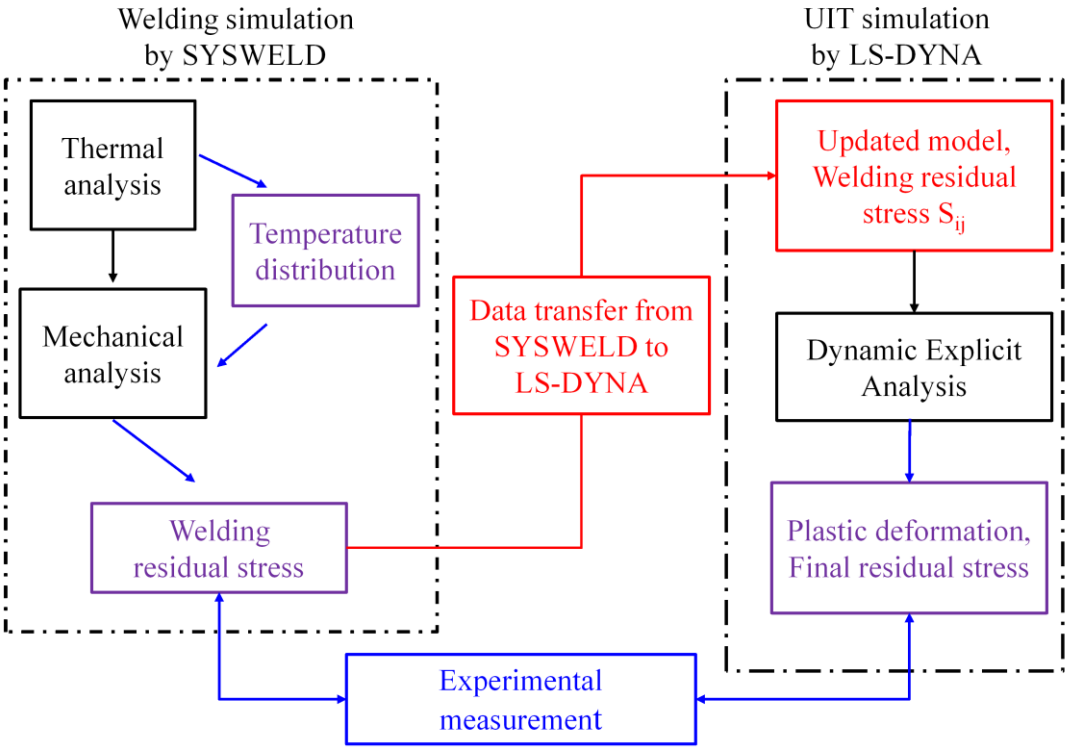

Figure 4.10 Flowchart of welding-UIT process simulation.

4.4.1 Analysis model and process parameters

A non-load-carrying cruciform joint used in the recent experimental work by Suzuki et al. [78] is selected as analysis object. Fig 4.11 shows the dimensions of the test specimen, which was welded using CO_2 fillet welding with JIS-SM490 base metal plate (nominal yield stress 390MPa). The welding parameters are given in Table.4.3, which will be considered in the welding simulation.

The welded joints were fabricated by one pass welding with leg length of 7 mm. The used UIT equipment was Esonix^{TM} 27 UIS. The operating frequency of ultrasonic generator was 27 kHz, shifting speed of 10mm/s, and 3-mm-diameter hardened metal pins.

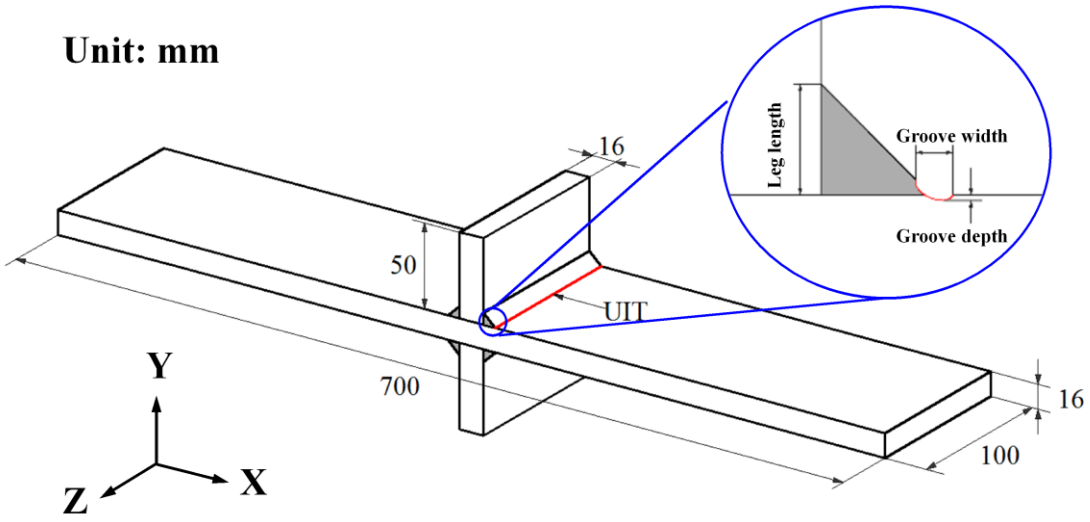

Figure 4.11 Geometry and dimensions of UIT specimen.

Table 4.3 Welding conditions

Welding wire	Wire diameter [mm]	Welding speed [mm/min]
SF-1	1.2	300
Current [A]	Voltage [V]	Arc efficiency
250	29	80%

4.4.2 Simulation of welding process

For welding simulation, a half symmetrical 3D model of cruciform joint is created according to the welded specimen geometry. This FE model has been constructed for a small width of 4mm, in order to effectively balance the accuracy and computational effort (see Fig.4.12). Therefore both sides of this segment are restrained in Z-direction, to simulate the specimen in plane strain state. The FE model mainly employs 8-node solid elements except for few wedge elements in the weld bead region. Near the weld toe, an extremely fine mesh (0.2mm×0.1mm×0.2mm) is required for the following UIT process simulation. The material of weld bead and base metal are assumed to be the same. The used temperature-dependent thermal and mechanical material properties of SM490 in SYSWELD [64] are illustrated in Fig.4.13.

In the first step of thermal analysis, heat input (1160 J/mm) given all at once to the weld bead and an initial temperature of 1400 ^{o}C for activation of the weld bead elements is assumed. Accompanying with heat convection and radiation, the cooling-down period between the subsequent weld is set as 1 hour. The total temperature-dependent heat transfer coefficient is employed as [64]:

$$h = \frac{\varepsilon\sigma(T^4 - T_0^4)}{T - T_0} + h_c \tag{4.8}$$

where h is the heat transfer coefficient (W/m^{2}K), T is the temperature of workpiece (^{o}C) and T_0 is the ambient temperature (^{o}C). The emissivity is defined to be ε=0.8 and σ=5.67×10^{-8}W/ (m^{2}K^4) is the Stefan-Boltzmann coefficient. The first term corresponds to the radiation. The second term h_c=25W/ (m^{2}K) is the convection coefficient.

The computed temperature distribution is used as input in the second step of mechanical analysis. The material model is assumed to follow von Mises yield criterion with bilinear kinematic hardening. In addition, the annealing temperature is set as 800 ^{o}C above which the prior strain hardening history of the material is removed and equivalent plastic strain is reset to zero.

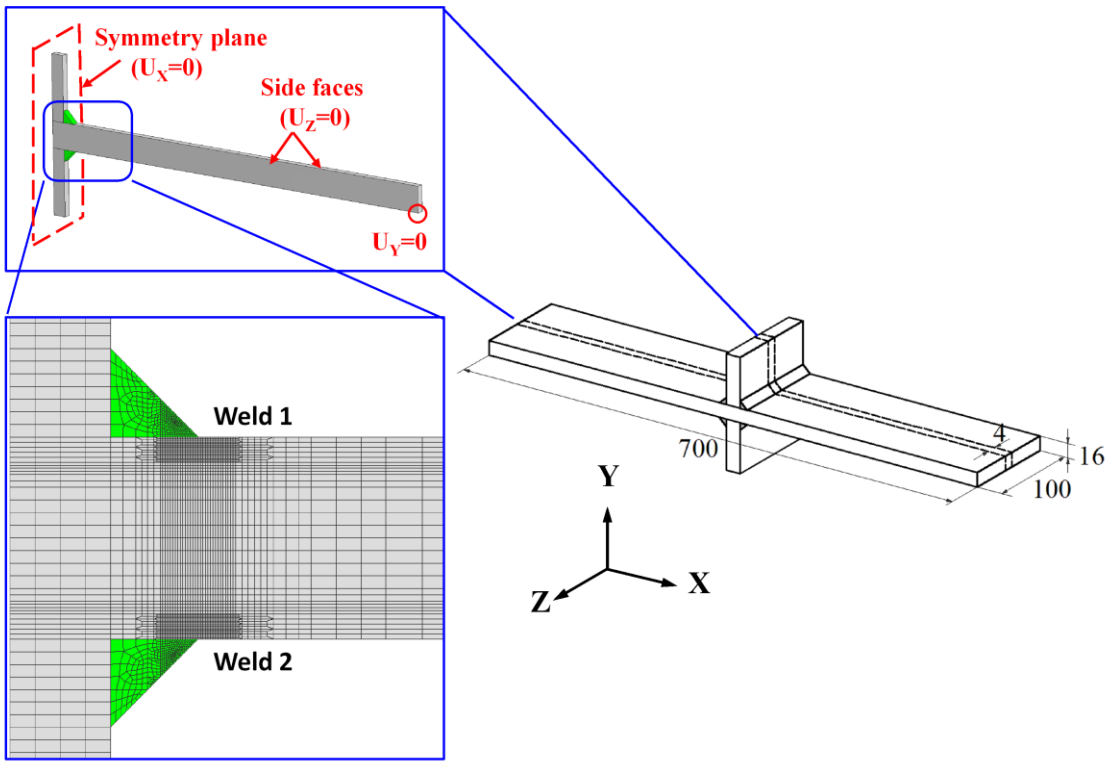

Figure 4.12 Finite element model for welding simulation.

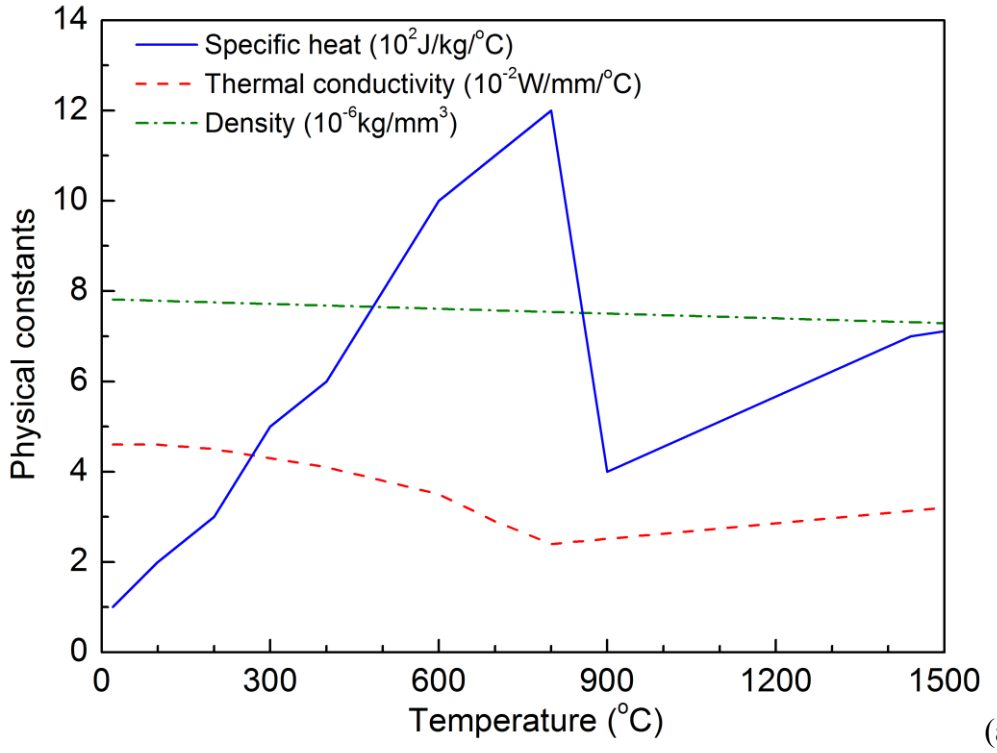

(a)

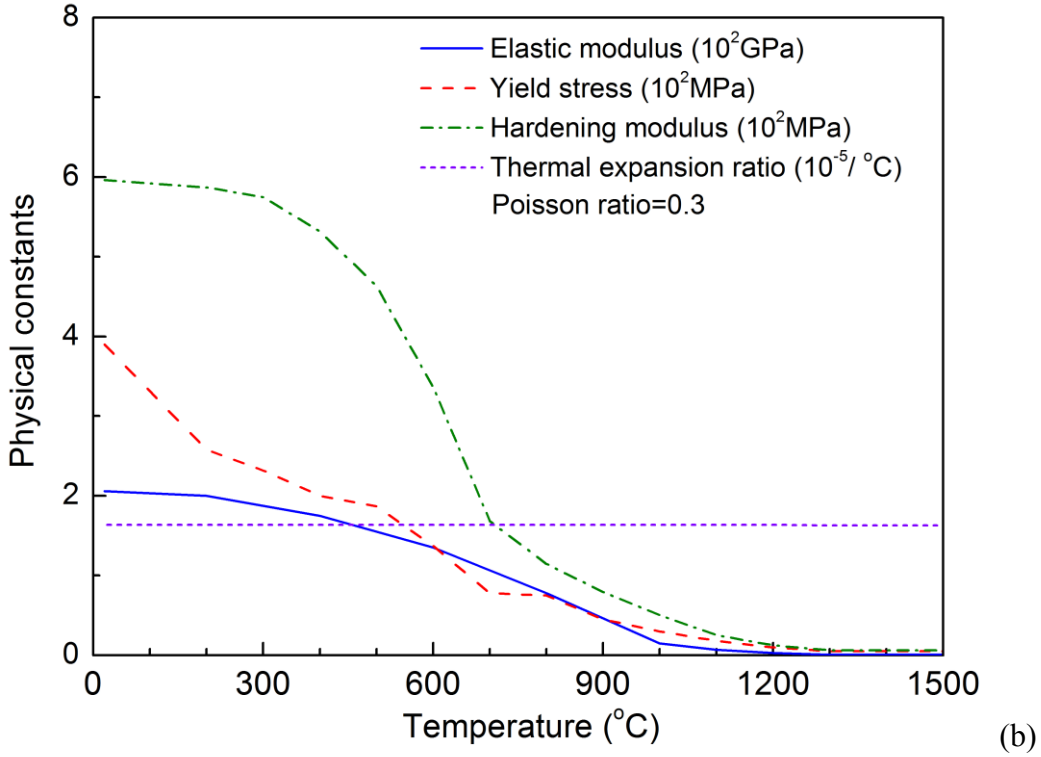

(b)

Figure 4.13 (a) Temperature-dependent thermal properties of structural steel SM490, (b) Temperature-dependent mechanical properties of structural steel SM490 (SYSWELD [64]).

4.4.3 Simulation of UIT process

After welding simulation in SYSWELD [64], the results of cruciform joint including element information, the distributions of as-weld residual stress and plastic strain are imported into LS-DYNA [77] as the initial-stress state of a dynamic model of UIT.

Considering the constraint conditions during actual UIT process (see Fig.4.14), the simulated boundary conditions of the FE model are shown in Fig.4.15. The bottom of the attachment, which is on the opposite side with respect to the being treated weld toe, is restrained against Y-direction and symmetric boundary conditions (U_X=0) are applied in the middle of the specimen. The both sides of this segment are restrained in Z-direction to simulate the plane strain state. The pins are angled at 67.5^o to the top and bottom of the specimen and allowed to freely move along its own central axis. According to Eq. (4.3), the impact velocity is estimated as 5m/s with corresponding equipment parameters, i.e. oscillation frequency of 27 kHz and amplitude of 30 μm under loaded condition [30]. The pin is controlled to continuously impinge the weld toe at the same location for 30 times (equivalent to one ultrasonic impact as mentioned before) by using restart analysis option of LS-DYNA [77]. After each ultrasonic impact, the pin is moved 0.4mm along the weld line to achieve a smooth peened groove with reasonable calculation efforts. The material proportional damping with damping ratio ξ=0.5 and Coulomb friction coefficient μ=0.5 are applied. The weld toe on the top surface is first peened, and that on the bottom surface is subsequently treated.


a)
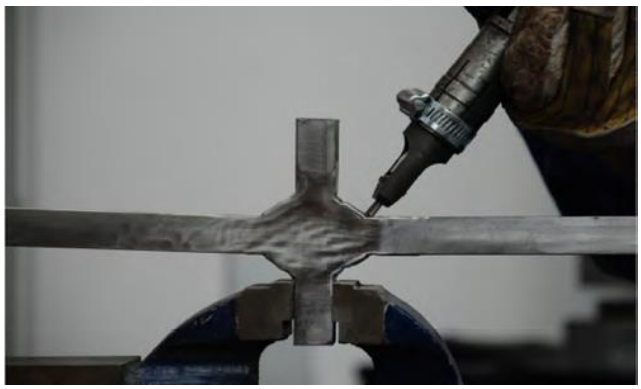
b)

Figure 4.14 Constraint conditions of UIT process (Dürr [82], Ermolaeva & Hermans [83])

The tips of 3-mm-diameter pins are modelled as elastic body with elastic modulus of 206 GPa, Poisson's ratio of 0.3 and measured mass of 1.5 gram. The material of welded joint is assumed to follow bilinear kinematic hardening behaviour. To consider the acoustic softening effect in Eq. (4.7), the parameter η is selected as 40% by trial and error, so that predicted groove depth fits to the experimental results, which will be discussed in the following section 4.4.5.2. The softening zone (SZ) around the weld toe in Fig.4.15 are assumed to be affected by acoustic softening during peening, of which each depth is determined as 8mm according to measured residual stress reduction in 16-mm thickness specimen [9], and the remain zones (NSZ) are not affected by softening. The mechanical properties considering acoustic softening are shown in Fig.4.16.

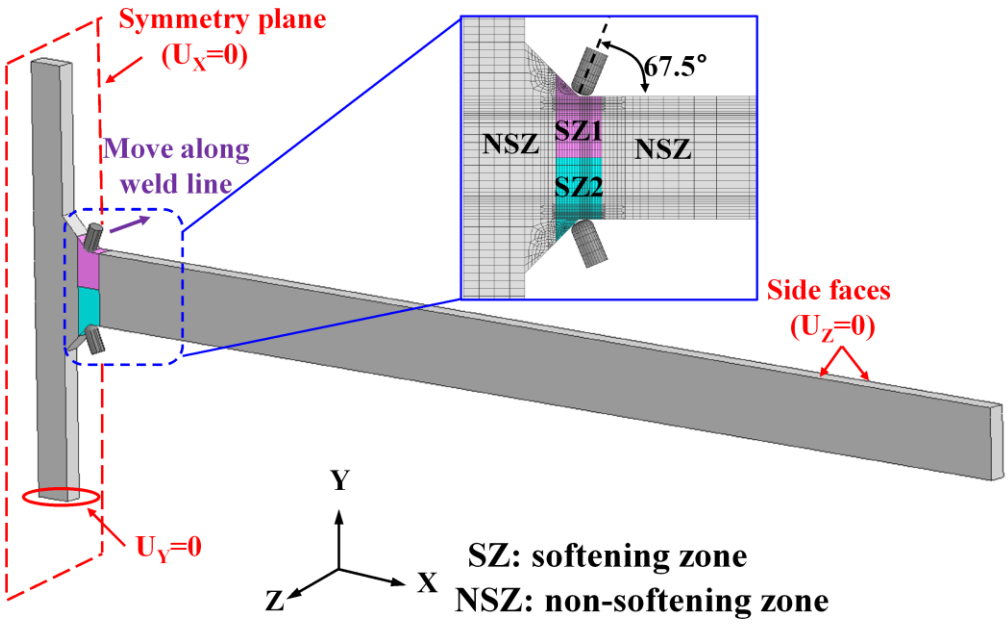

Figure 4.15 Finite element model for UIT simulation.

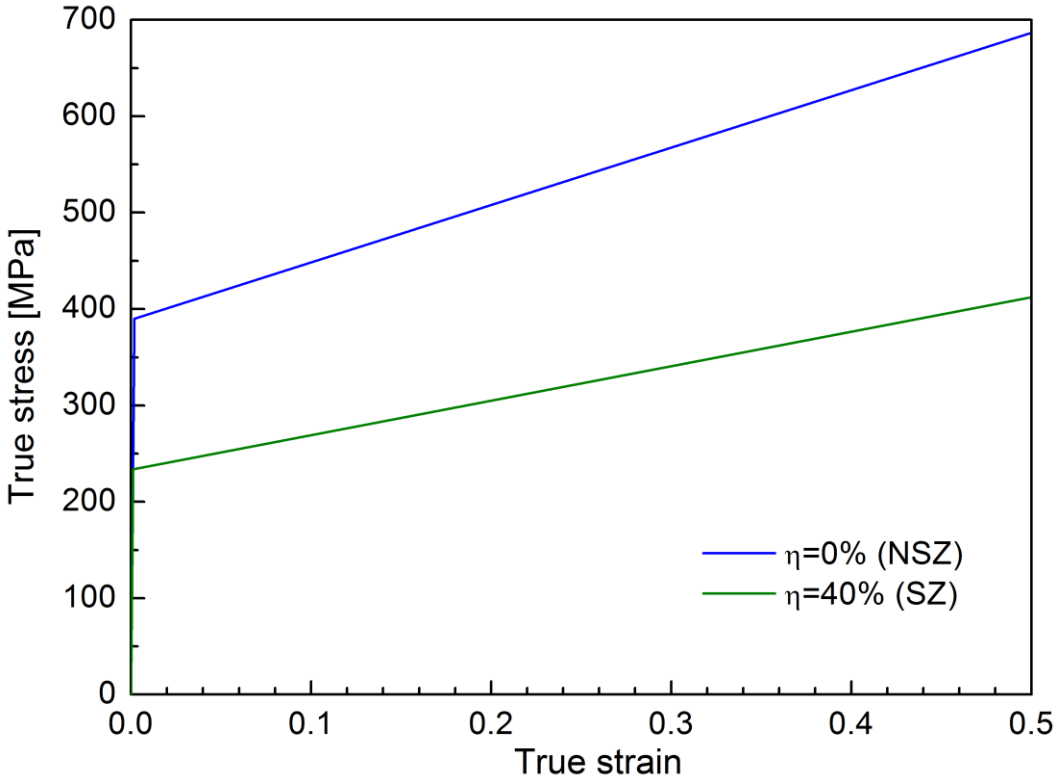

Figure 4.16 Mechanical properties considering acoustic softening.

4.4.4 Simulation of preload after UIT

The static loading on a ship structure induced by water pressure before service, such as a tank test and launching, can cause relatively high static stresses at welded joints, compared with cyclic loading induced by waves during service. Due to these static preloads, the UIT-induced compressive residual stress may be relaxed to a great extent by the elastic-plastic deformation behaviour of the material. Therefore, it is necessary to identify the effect of preload on the UIT improvement stability.

As illustrated in Fig.4.17, the simulation case that the UIT-treated cruciform is gradually loaded to preload P_{max} and then unloaded to zero is performed by implicit quasi-static analysis in LS-DYNA [77]. As above mentioned, acoustic softening is an instantaneous phenomenon; meaning that the yield stress reduction diminishes once the ultrasonic vibration is switched off. Therefore, the mechanical properties of η=0% in Fig.4.16 will be used for the welded joint model.

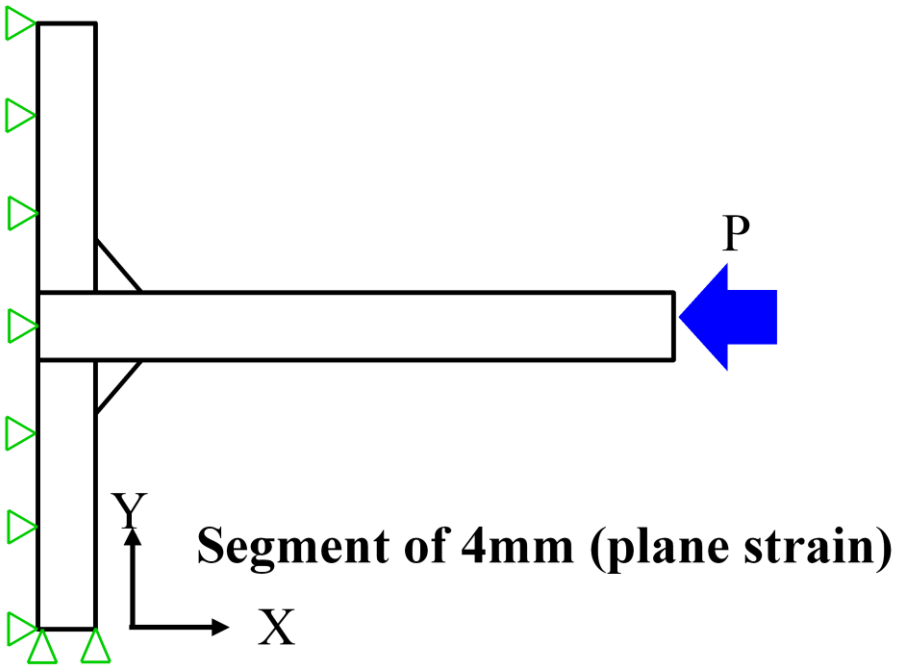

(a)

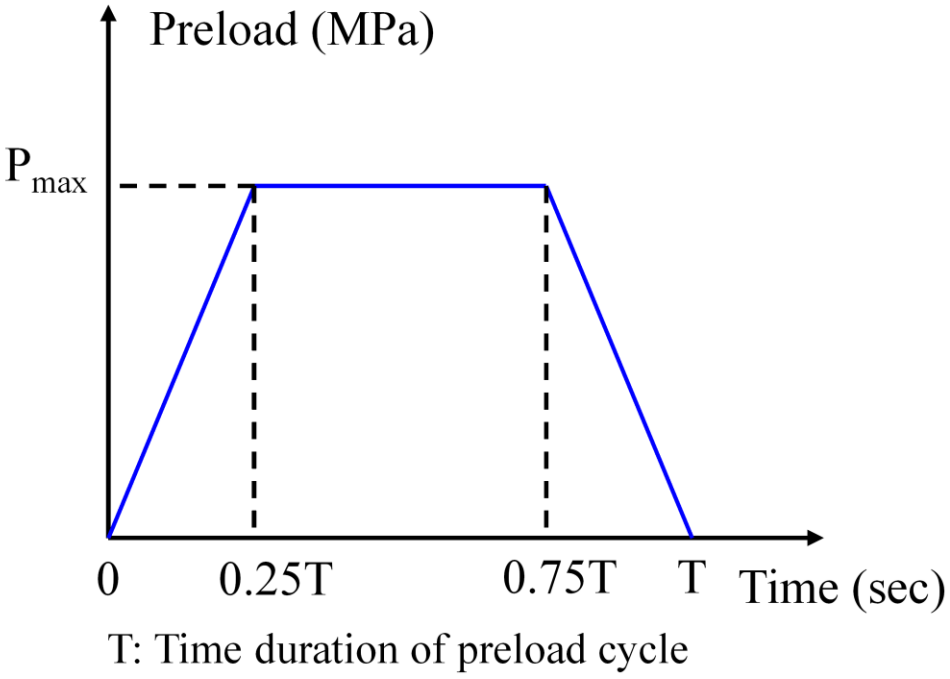

(b)

Figure 4.17 (a) Schematic illustration of UIT-treated cruciform joint subjected to preload, (b) Load history of preload.

4.4.5 Validation of welding-UIT simulation

4.4.5.1 Results of welding simulation

Fig.4.18 shows the predicted highest temperature distribution in cruciform joint. It can be confirmed that all the elements in weld bead region have been molten over 1400^{o}C during welding. In principle, the predicted boundaries of molten zone should coincide with the measured macrographs to achieve better accuracy.

The contour plots of transverse residual stress σ_x predicted by SYSWELD and that re-mapped in LS-DYNA are shown in Fig.4.19 (a) and (b), respectively. It shows good agreement with each other, ensuring that the original welding residual stress field is retained after the stress initialization in LS-DYNA. The distributions of residual stress σ_x extracted though in-depth and on-surface defined paths are shown in Fig.4.20. High tensile transverse residual stress are predicted near the both surfaces and balanced by compressive residual stress in the middle of the main-plate. The maximum transverse tensile stress up to 326 MPa is predicted at the weld toe on the top surface.

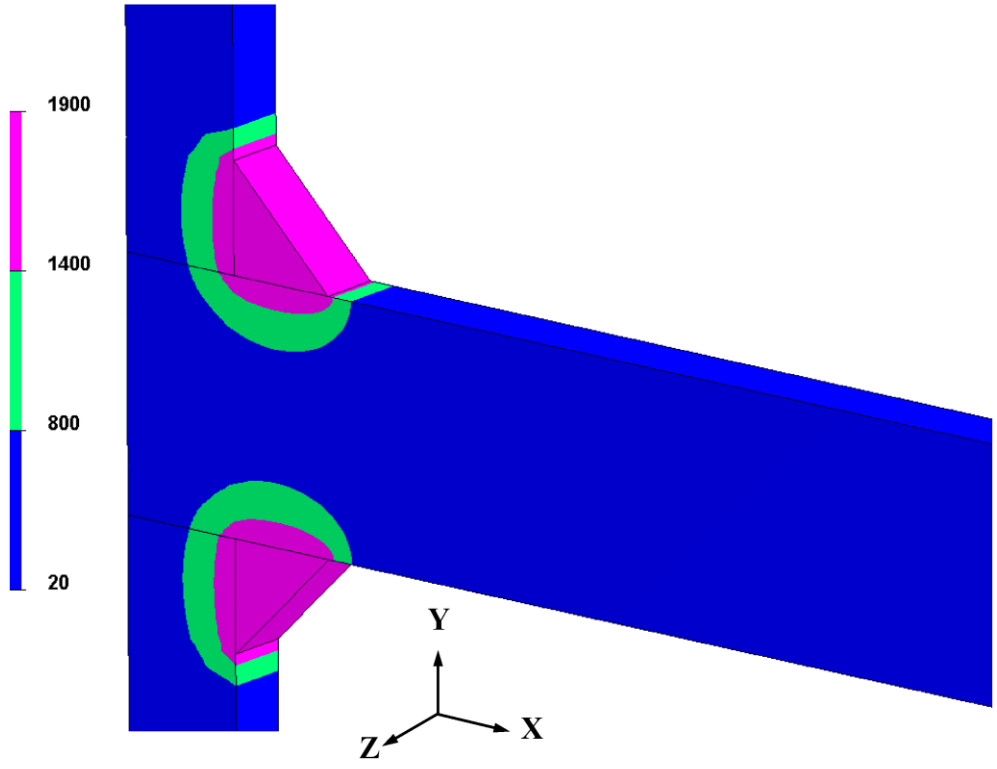

Figure 4.18 Predicted highest temperature distribution.

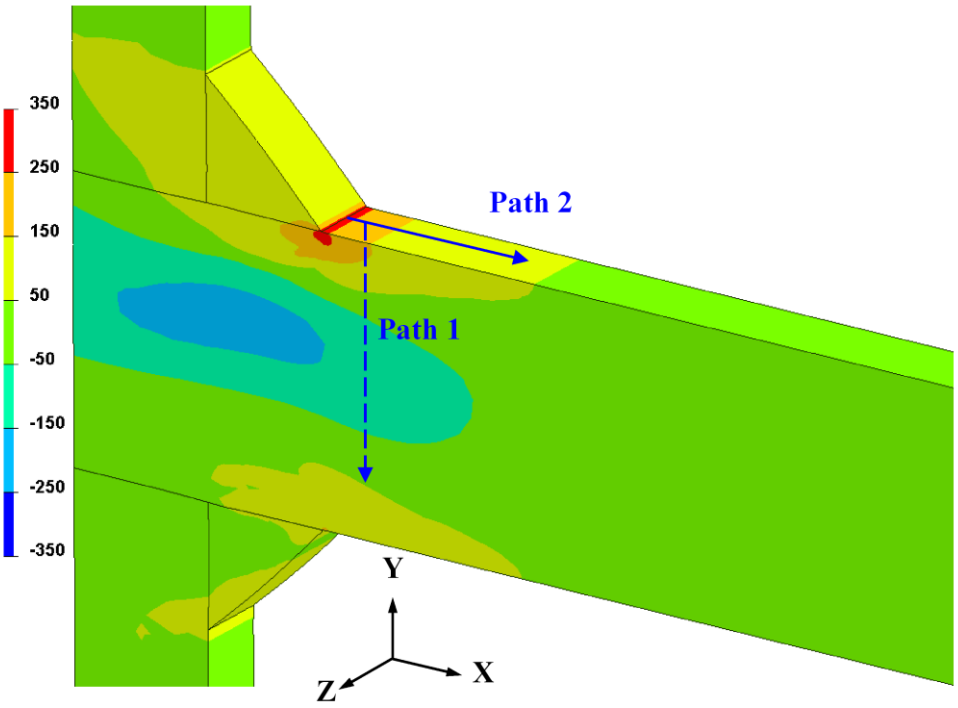

(a)

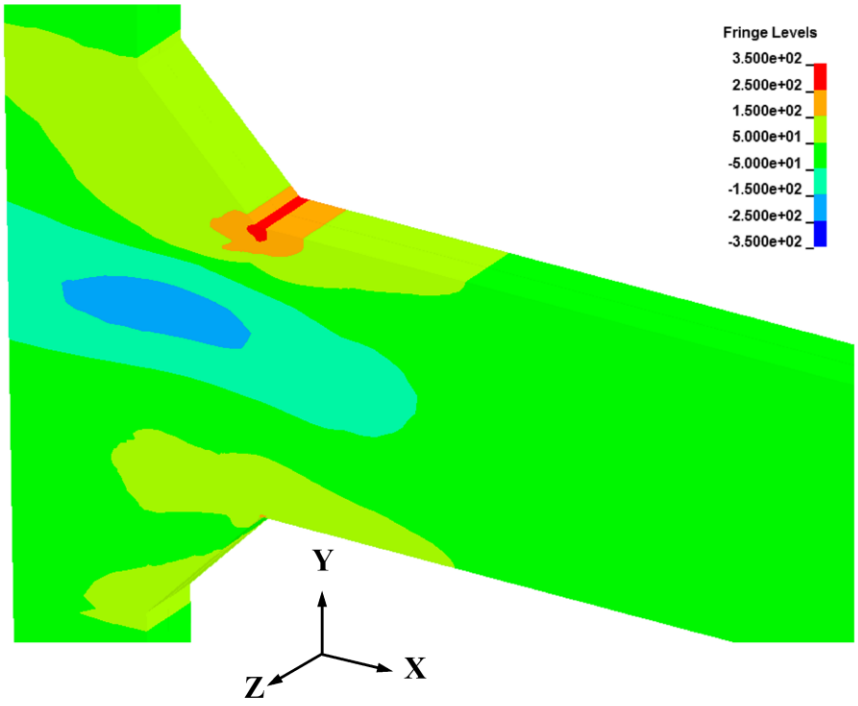

(b)

Figure 4.19 Contour plots of transverse residual stress; (a) predicted by SYSWELD, (b) remapped in LS-DYNA.

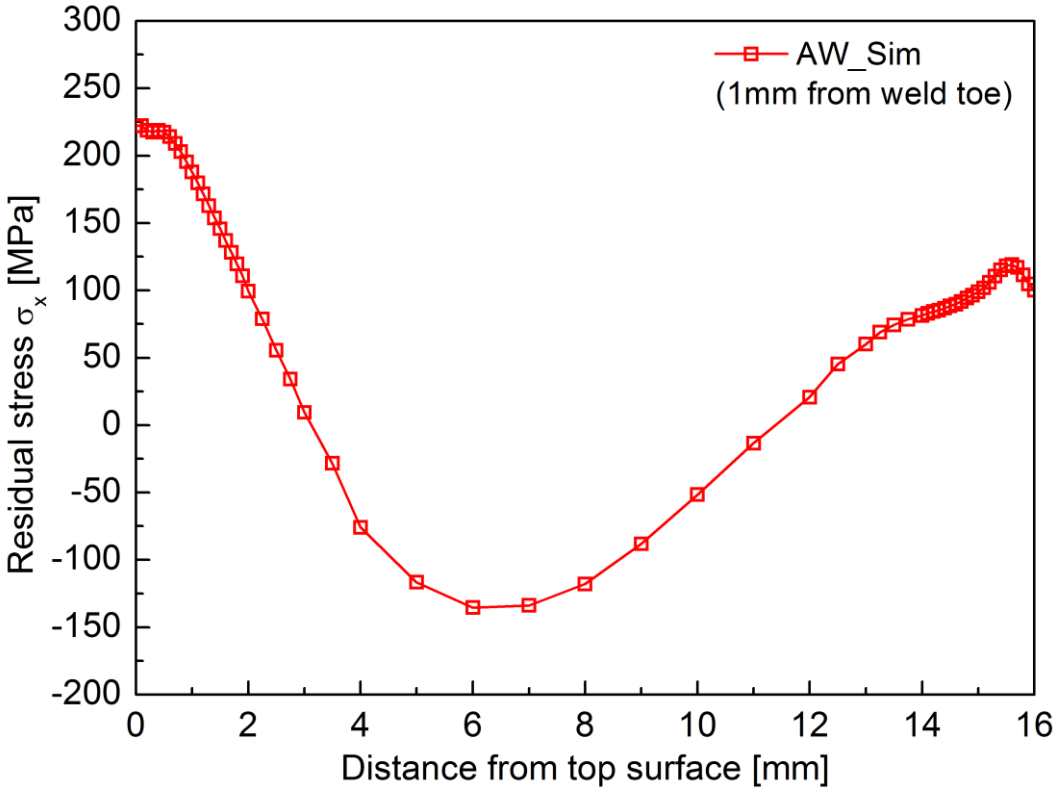

(a)

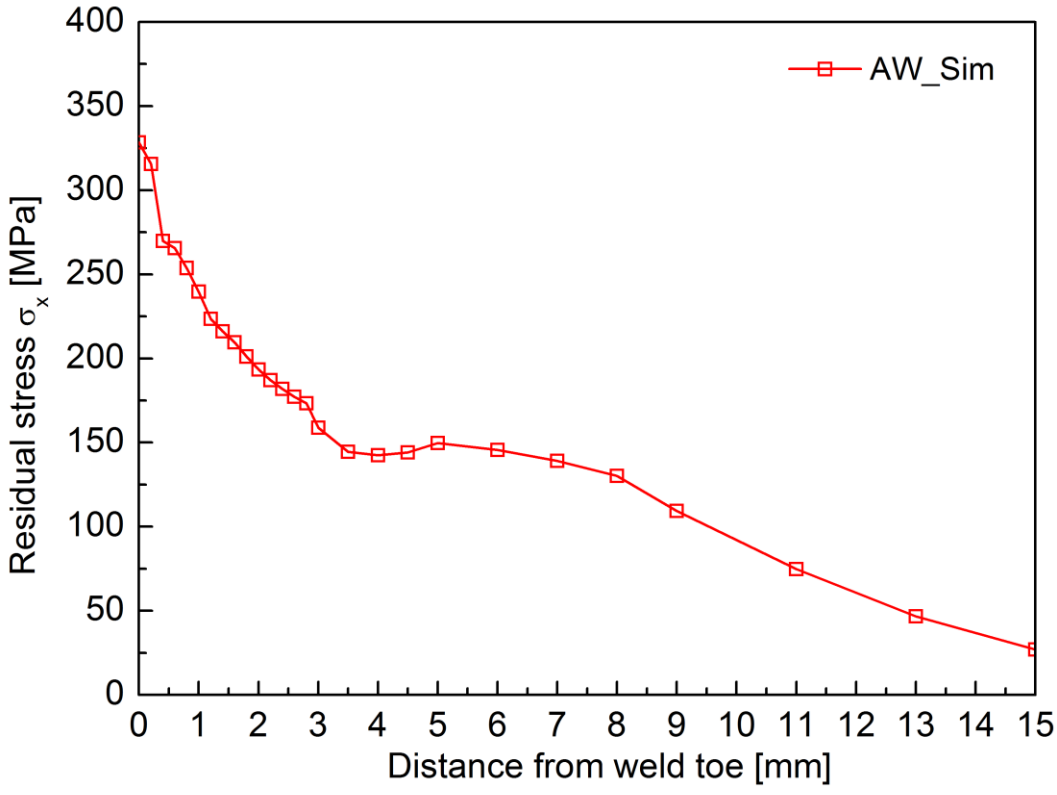

(b)

Figure 4.20 Predicted profiles of as-weld transverse residual stress; (a) in-depth (path1 in Fig.4.19a), (b) on top surface (path 2 in Fig.4.19a).

4.4.5.2 Determination of acoustic softening parameter

The acoustic softening parameter η is selected by trial and error so as to match the experimental measured indentation depth d and weld toe radius r on a cross-section [78] with the predicted ones after one ultrasonic impact, as shown in Fig.4.21. It can be seen that it is easier to form a smooth change of the shape at the weld toe when the resistance necessary for plastic deformation is decreased due to acoustic softening, and the parameter η=40% lead to good agreement between the predicted and measured weld toe shape. This result is comparable to the measured yield strength reduction of 45% under direct ultrasonic energy 600 Watt [37], while the consumed power of 27 kHz-type UIT equipment is 600-1200 Watt [30].

The internal residual stress profiles during 30 times of pin's impinging (one ultrasonic impact without translation along weld line) are shown in Fig.4.22. Having introduced the yield strength reduction due to acoustic softening, the compressive residual stress layer is deepened approximately by 2mm after 30 times of continuous peening, while the maximum value decreases in comparison with that without acoustic softening (see Fig. 4.22b).

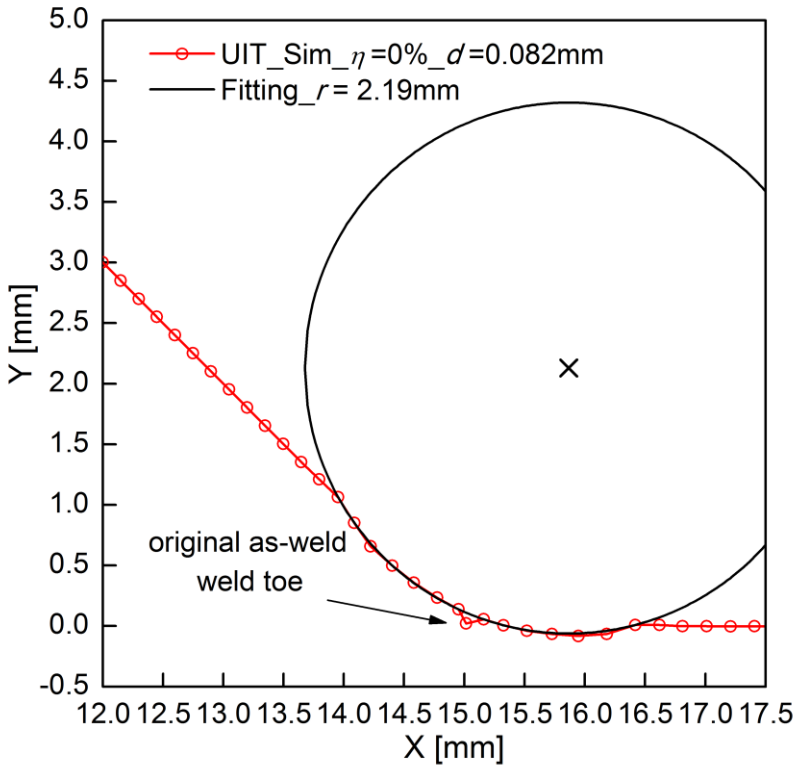

(a)

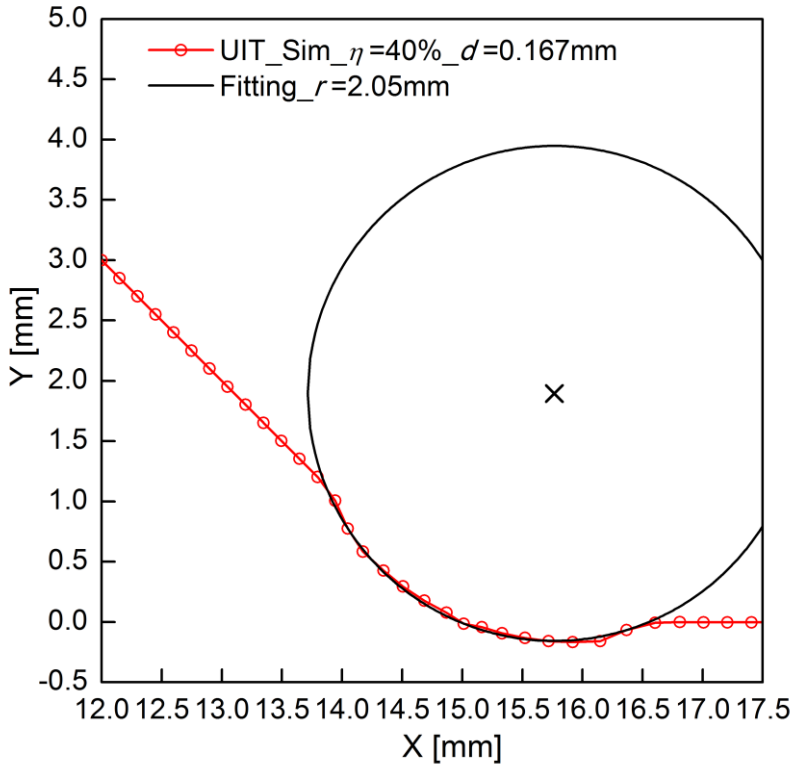

(b)

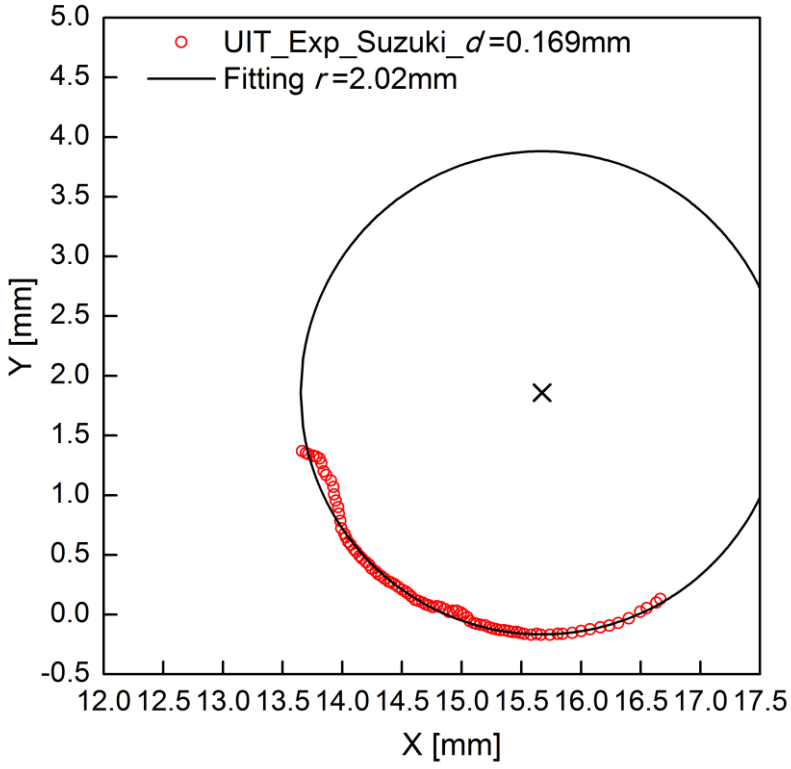

(c)

Figure 4.21 Determination of acoustic softening by comparing the treated weld toe shape; (a) simulated with η=0%, (b) simulated with η=40%, (c) measured by Suzuki et al [78].

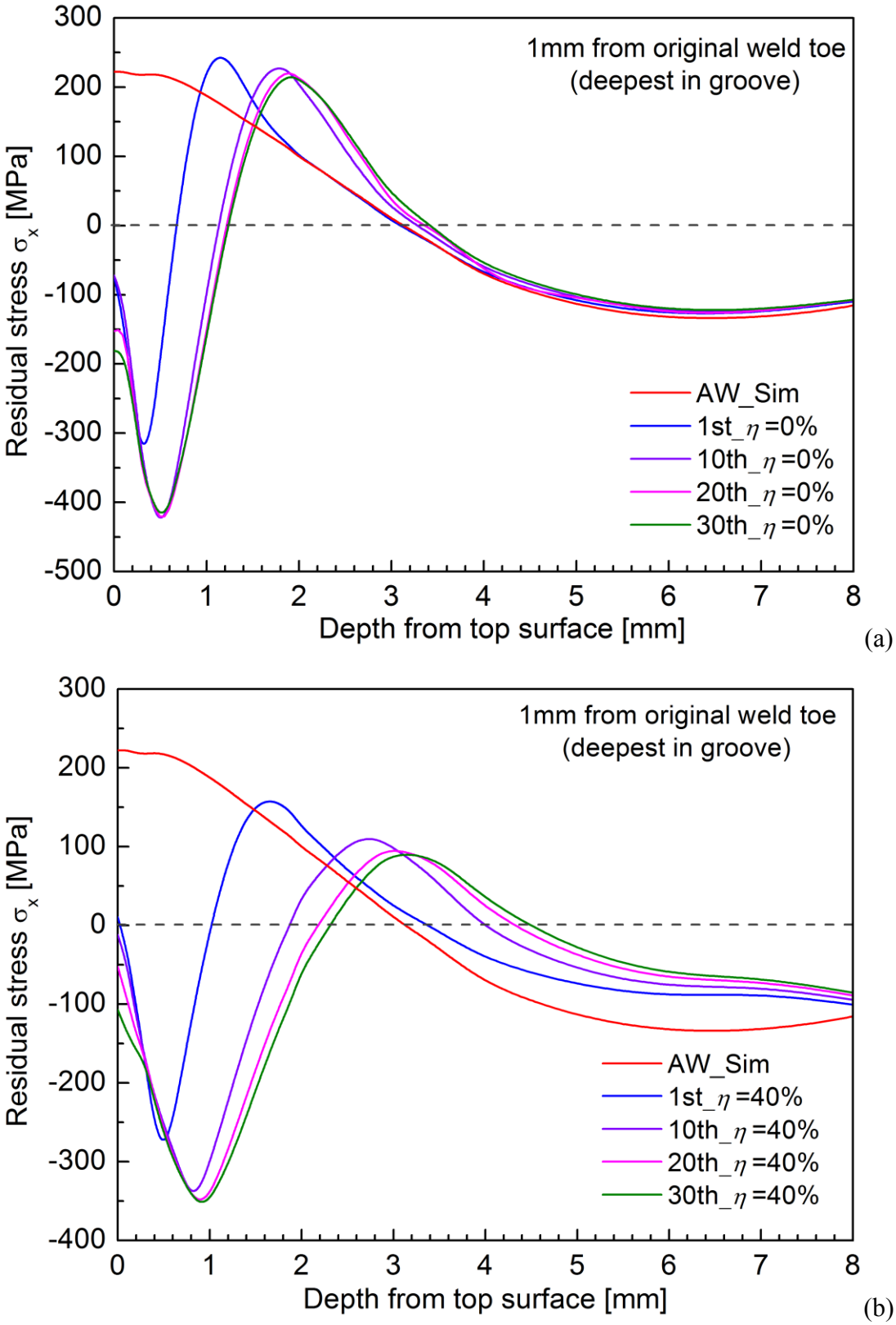

Figure 4.22 Evolution of in-depth transverse residual stress distributions during one ultrasonic impact; (a) simulated without acoustic softening, (b) simulated with acoustic softening η=40%.

4.4.5.3 Internal residual stress distributions before and after UIT

In practice, the peening tool is travelling along the weld line, until the original shape of the weld toe disappears and the smooth groove is formed. Therefore, considering the movement of the pin, the distributions of transverse residual stress σ_x and weld toe shape before and after UIT are illustrated in Fig.4.23. It can be confirmed that the tensile welding residual stress at the weld toe has been changed to significant compressive residual stress. The step-by-step movement of 0.4 mm provides sufficient overlapping of the impacts, leading to a smooth change of the predicted weld toe shape.

In order to verify the accuracy of the simulation, the predicted residual stress distributions along the depth direction are compared with those measured by Suzuki et al. [78] using X-ray and neutron diffraction methods, as shown in Fig.4.24. There are fairly good agreements between the numerical and experimental results, which provides some verification of the finite element model. From the predicted results, it can be observed that after UIT the significant compressive residual stress layer has been introduced to surface layers and balanced by tensile stress for equilibrium in the middle of the plate. The penetration depth of compressive residual stress has extended to about 3mm from surfaces. The maximum value of compressive residual stress about 250-300MPa are predicted and measured at about 1mm depth from the surfaces. Slight over-estimation of UIT compressive residual stress on the surface is seen, however, great variation has been observed in the X-ray measured surface stress [84]. So it is necessary to compare the simulation with more experimental results in the future.

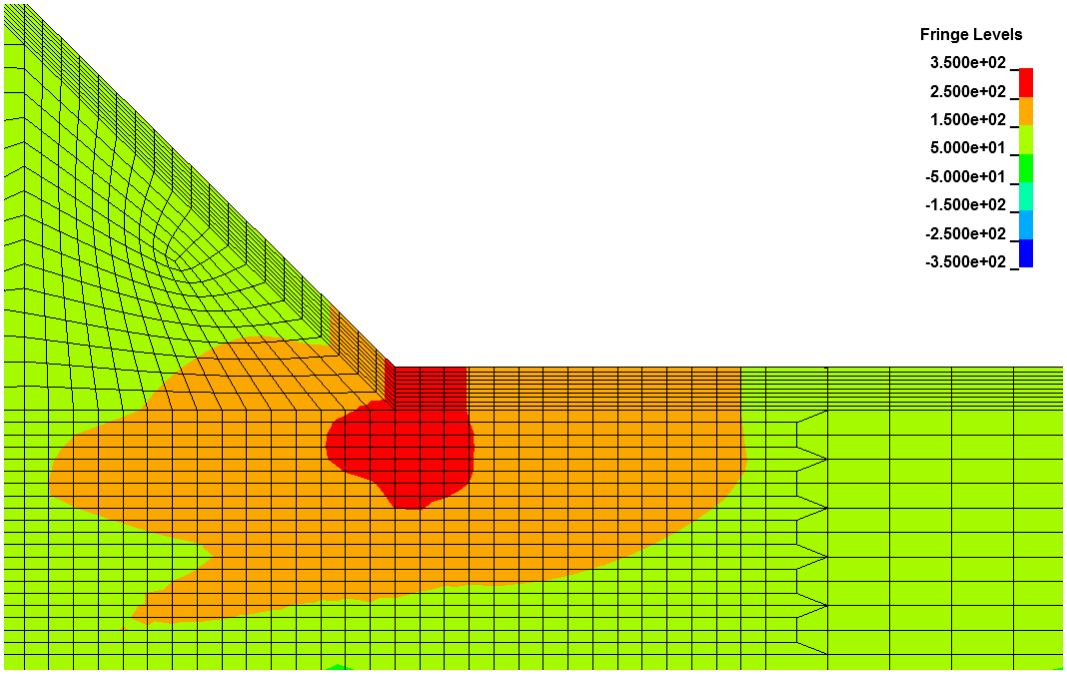

(a)

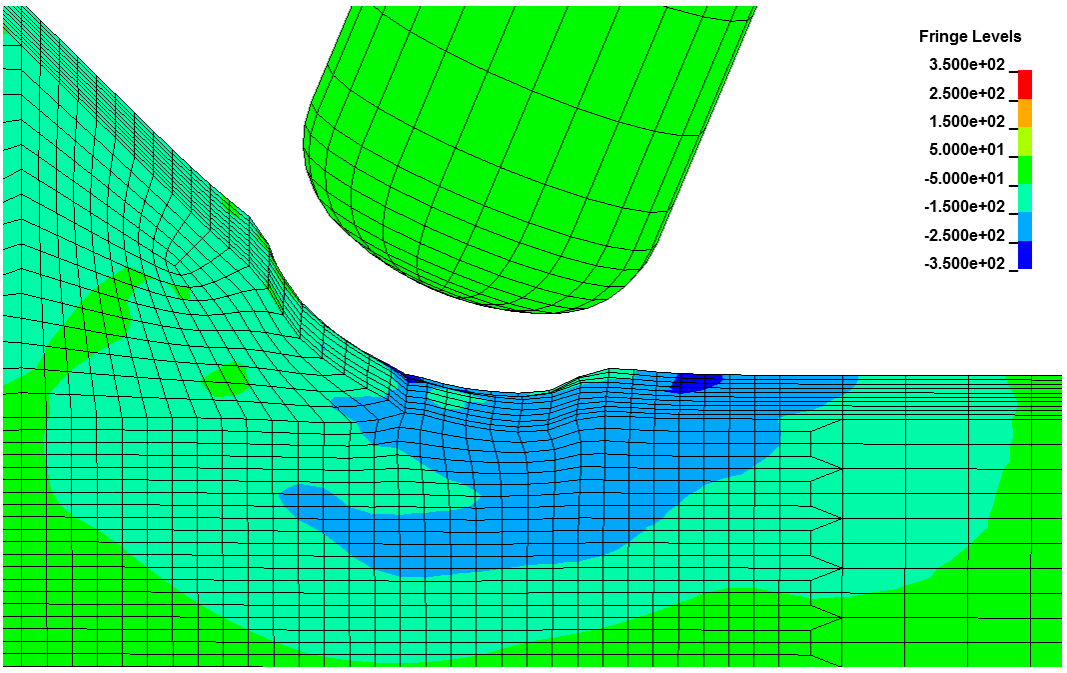

(b)

Figure 4.23 Transverse residual stress distributions and plastic deformation at the weld toe; (a) as-weld, (b) UIT with η=40%.

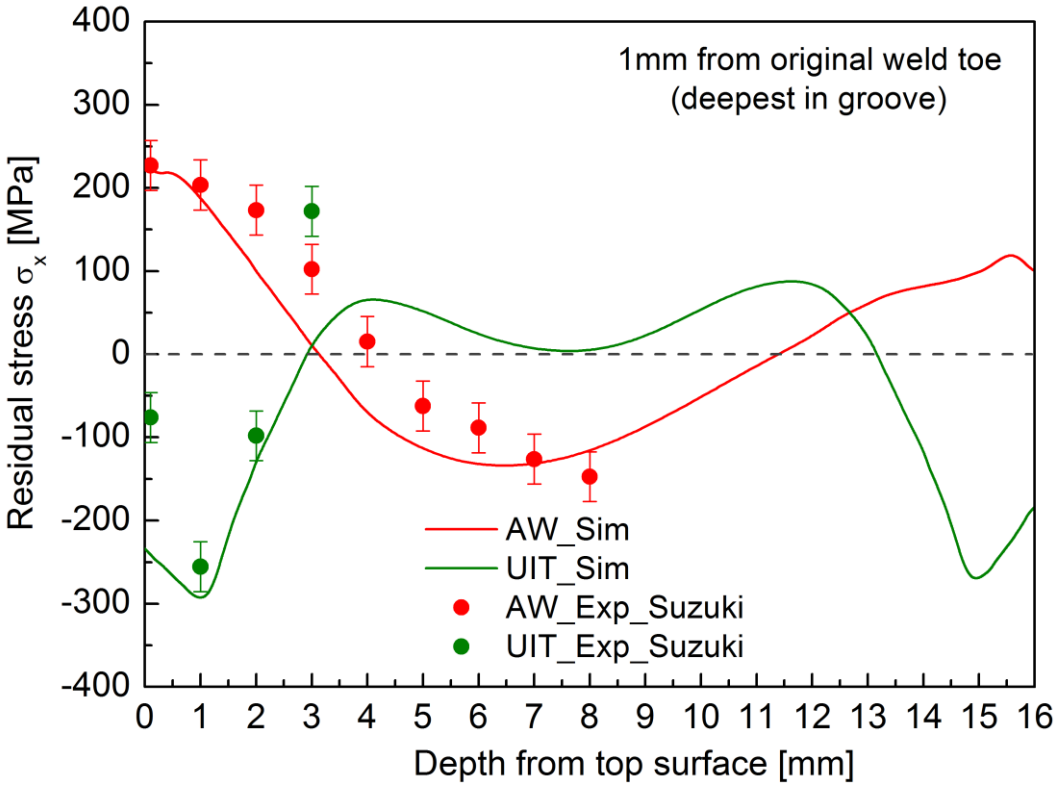

(a)

Figure 4.24 Distribution of transverse residual stress of as-weld and UIT specimens in the depth direction, and comparison with experimental results (Suzuki et al. [78]).

4.4.5.4 Residual stress distributions after preloads

In order to investigate the influence of the preloads on the stability of UIT improvement, Okawa et al.[48] performed the fatigue test after preloading the cruciform joint in steel AH36 (equivalent to SM490). The preload is: (a) tensile stress of 90% of the base metal yield strength named as T351 or (b) compressive stress of 60% of the base metal yield strength named as C234.

The simulations of UIT-induced compressive residual stress relaxation by the same pre-load conditions as those in Okawa et al. [48] have been performed. Fig.4.25 shows the surface residual stress distributions nearby the weld toe before and after preloads. From the figure, both the predicted and measured results show the similar trend that the compressive residual stresses are decreased after preloads of either tension or compression. Relative high compressive residual stresses are still remained even after the application of the preloads.

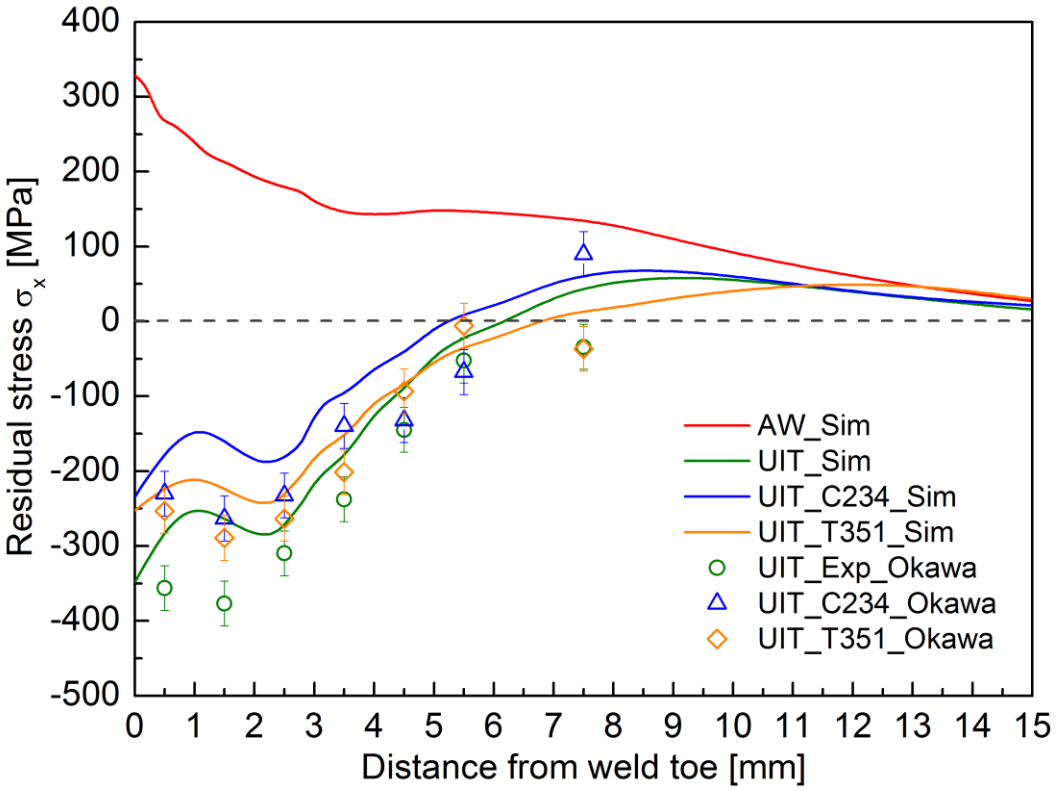

Figure 4.25 Comparison of predicted surface residual stress change nearby the weld toe by preload with experiment (Okawa et al. [48]).

For comparable analysis, the simulations of another four preloads after UIT have been added. The added cases are: (a) tensile preloads of 50% and 80% of yield strength named as T195 and T312, (b) compressive preloads of 50% and 80% of yield strength named as C195 and C312, respectively.

Figure 4.26 (a) and (b) show the predicted relaxation of residual stress along on-surface and in-depth directions after tensile preloads. Under tension, by increasing the magnitude from 50% to 80% of the yield stress, no significant changes of the residual stress field could be seen. Only extremely high tensile preload T351 leads to 40-100MPa reduction of compressive residual stress near the weld toe. This can be explained by the histories of in-depth stress distributions at peak values of each tensile preload case, as shown in Fig.4.26(c). At the peak values of T195 and T312 preloads, the through-thickness stress state are still in elastic region. On the other hand, the yielding in tension seems to occur around 4 and 12 mm depth where the tensile residual stresses originally exist, when it reaches maximum value of preload T351. Since the tensile residual stress would decrease due to this yielding, the compressive residual stress should reduce to balance.

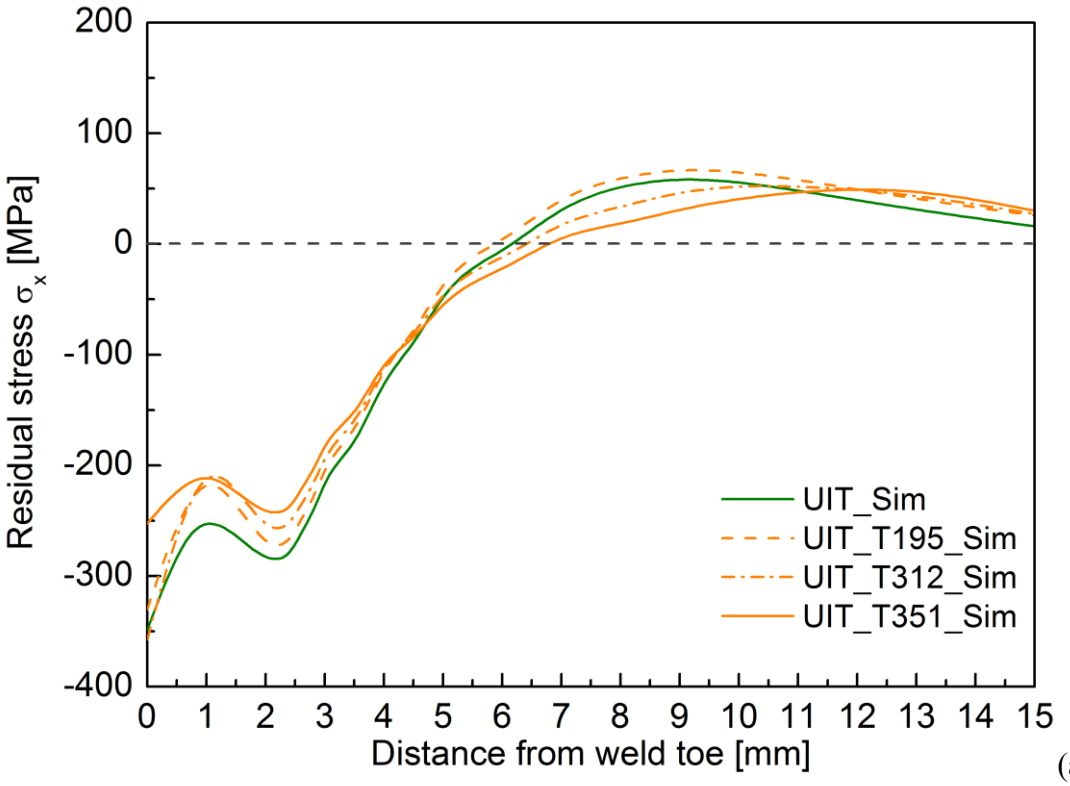

(a)

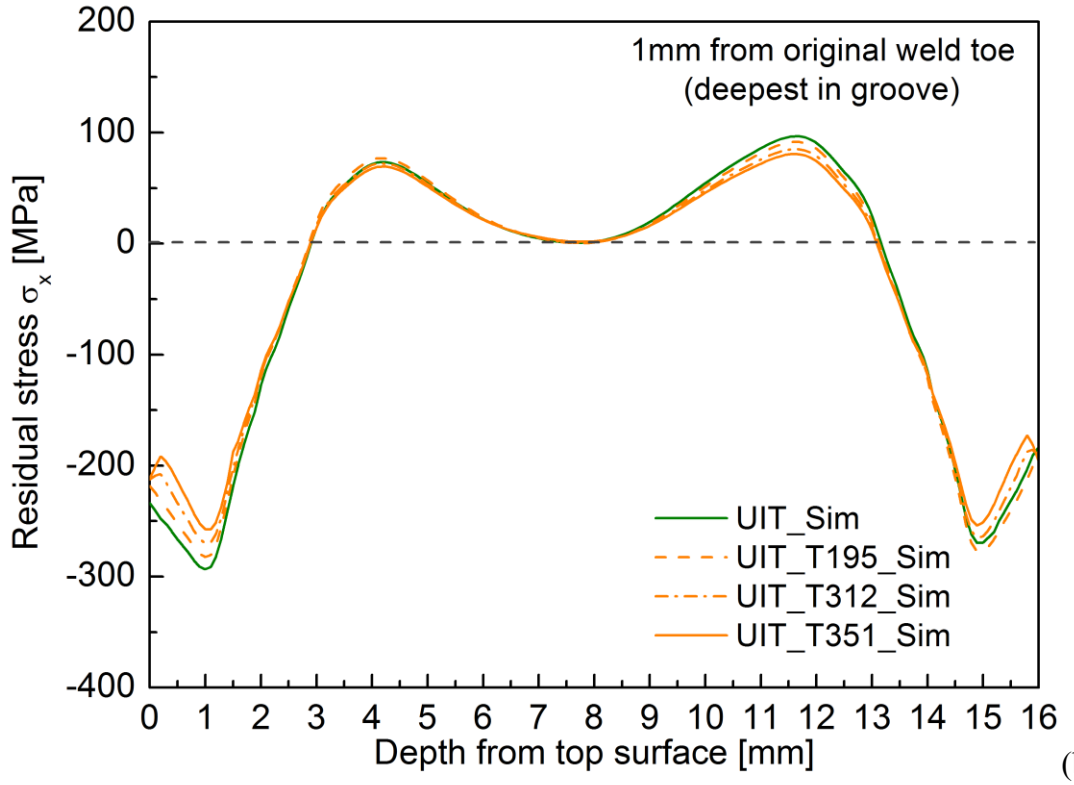

(b)

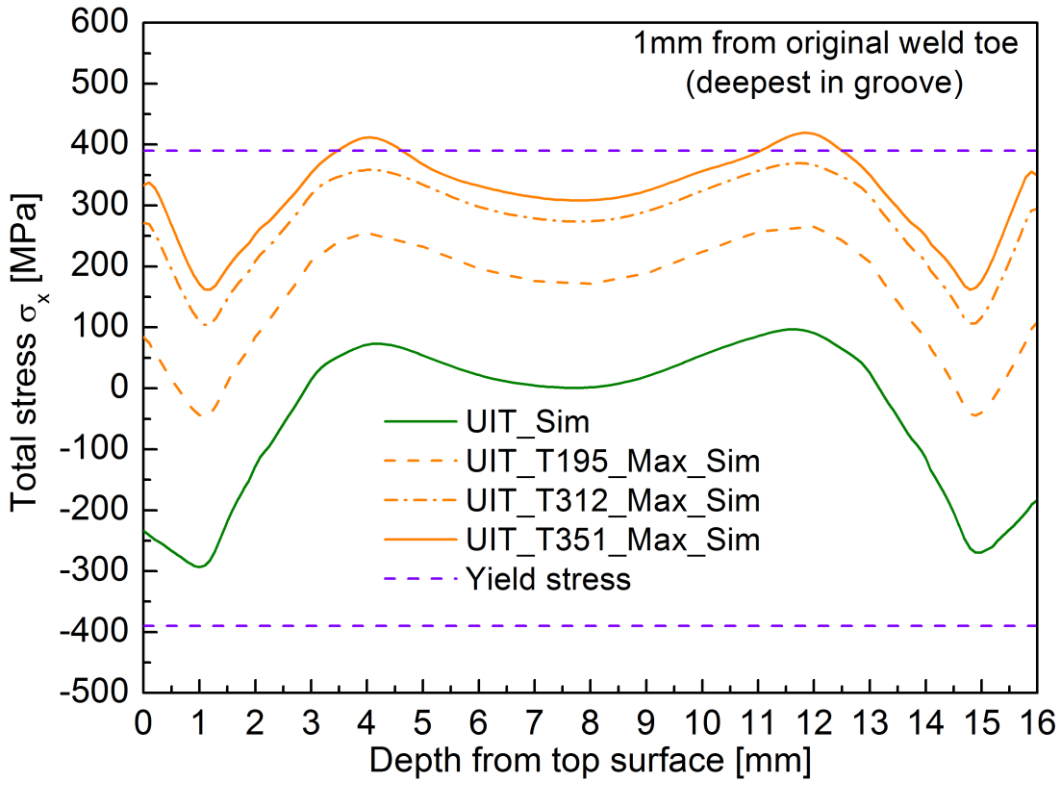

(c)

Figure 4.26 Predicted residual stress change near the weld toe by tensile preloads; (a) on surface after preloads, (b) in depth after preloads, (c) in depth at the maximum values of preloads.

Figure 4.27 (a) and (b) show the relaxation of residual stress on surface and in depth directions after compression preloads. It can be seen that the compressive preloads cause more relaxation of compressive residual stress than tensile preloads. In Fig.4.27(c), the in-depth stress distributions at peak values of each compressive preload case are shown. Near the both surface layers, the yielding in compression due to compressive preloads can be observed. The plasticization of surface regions are considered to extend more deeply with increasing value of compressive preloads, which leads to more relaxation of compressive residual stresses.

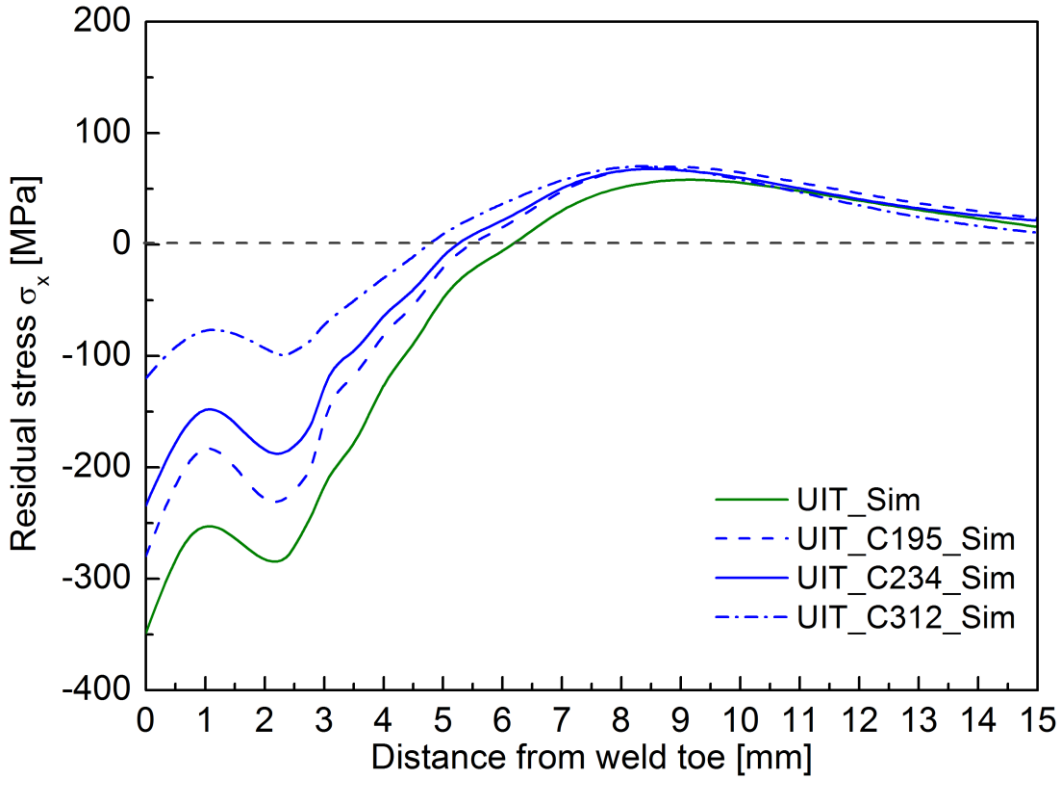

(a)

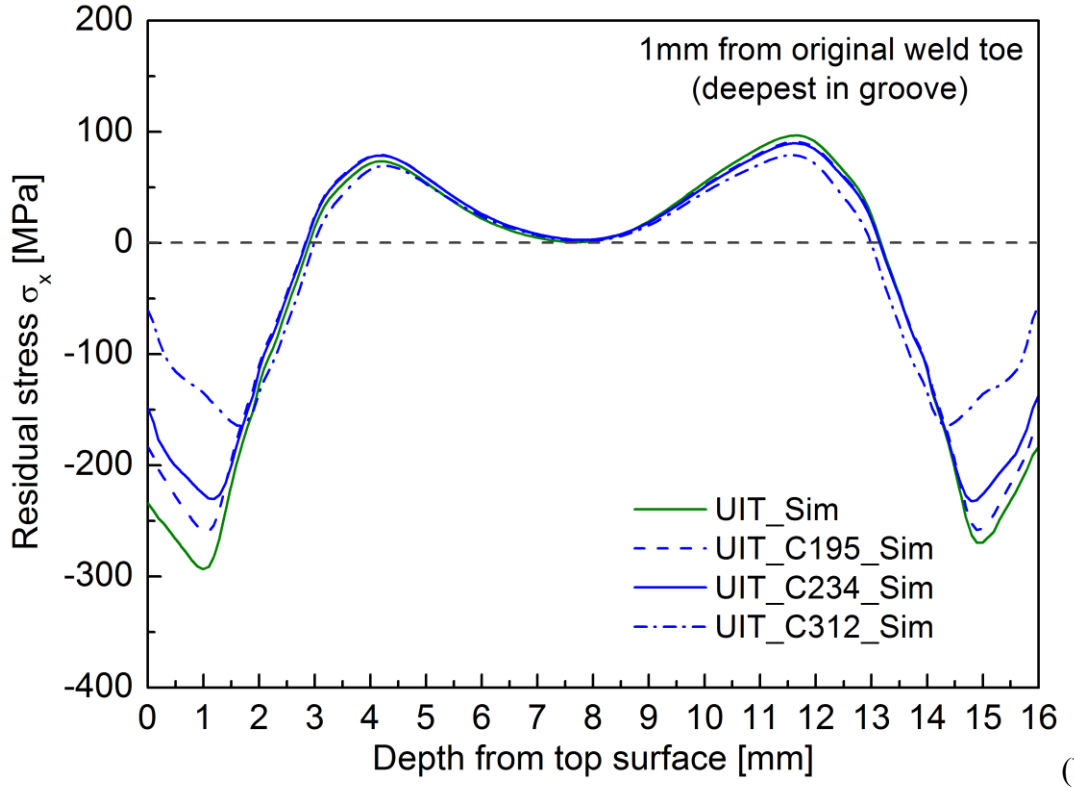

(b)

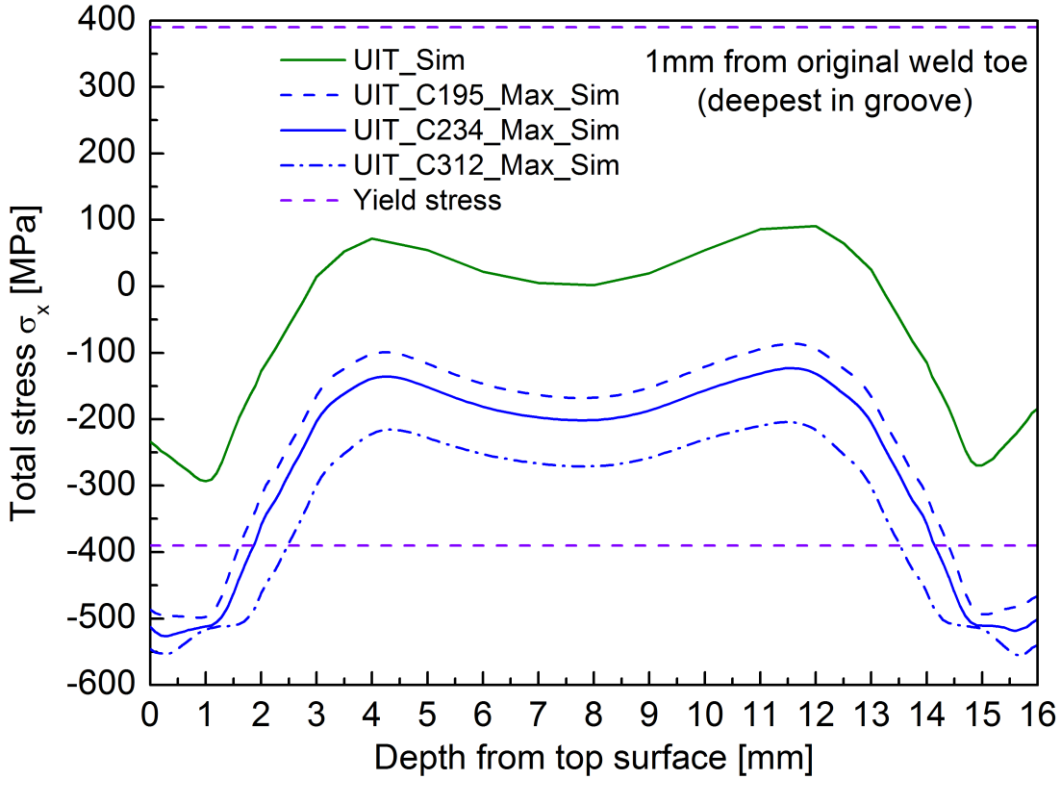

(c)

Figure 4.27 Predicted residual stress change near the weld toe by compressive preloads; (a) on surface after preloads, (b) in depth after preloads, (c) in depth at the maximum values of preloads.

CHAPTER 5

FATIGUE STRENGTH ASSESSMENT OF UIT WELDED JOINTS

5.1 Introduction

In this chapter, the analytical work based on the fracture mechanics is performed to evaluate the improved fatigue strength of welded joints by UIT. The fatigue behaviour in welded joint can be approximated as a finite thickness plate with a semi-elliptical surface flaw, which is subjected to the same stress field as that in the actual welded joint [93]. Firstly, the stress intensity factor of semi-elliptical surface crack in finite-thickness plate under through-thickness arbitrary stress distribution is evaluated by the weight-function method. With the application of the weight function standardized by code API 579-1[85], the accuracy of the calculated stress intensity factors will be verified by the comparison with the solutions of finite element analysis [86],[87], [88]. The modified Paris-Elber law is then employed to predict the fatigue crack growth life of welded joints. The fatigue strengths of as-weld and UIT welded joints under constant amplitude cyclic loading (R=0.1) are evaluated and verified with corresponding fatigue test results [48], [78]. Moreover, the influence of high stress ratio and preload on UIT improvement will also be numerically investigated.

5.2 Stress intensity factor (SIF) of semi-elliptical surface crack in finite-thickness plate

5.2.1 The weight function method

For a semi-elliptical surface crack in a plate of finite thickness (see Fig.5.1), the empirical equation of stress intensity factor K_I proposed by Raju and Newman [89], [90] has been widely used, however, only available for remote tension stress and bending stress.

$$K_I = (\sigma_t + H\sigma_b)\sqrt{\frac{\pi a}{Q}}F(\frac{a}{T},\frac{a}{c},\frac{c}{B},\varphi) \tag{5.1}$$

where a is surface crack depth, c is half crack length, φ is parametric angle of the ellipse, B is plate width, T is plate thickness, F and H are the boundary correction factors and Q is the complete elliptical integral of the second kind. The useful approximation for Q is given by

$$\begin{aligned} Q &= 1.0 + 1.464(\frac{a}{c})^{1.65} && \text{for } \frac{a}{c} \le 1.0 \\ Q &= [1.0 + 1.464(\frac{c}{a})^{1.65}](\frac{a}{c})^2 && \text{for } \frac{a}{c} > 1.0 \end{aligned} \tag{5.2}$$

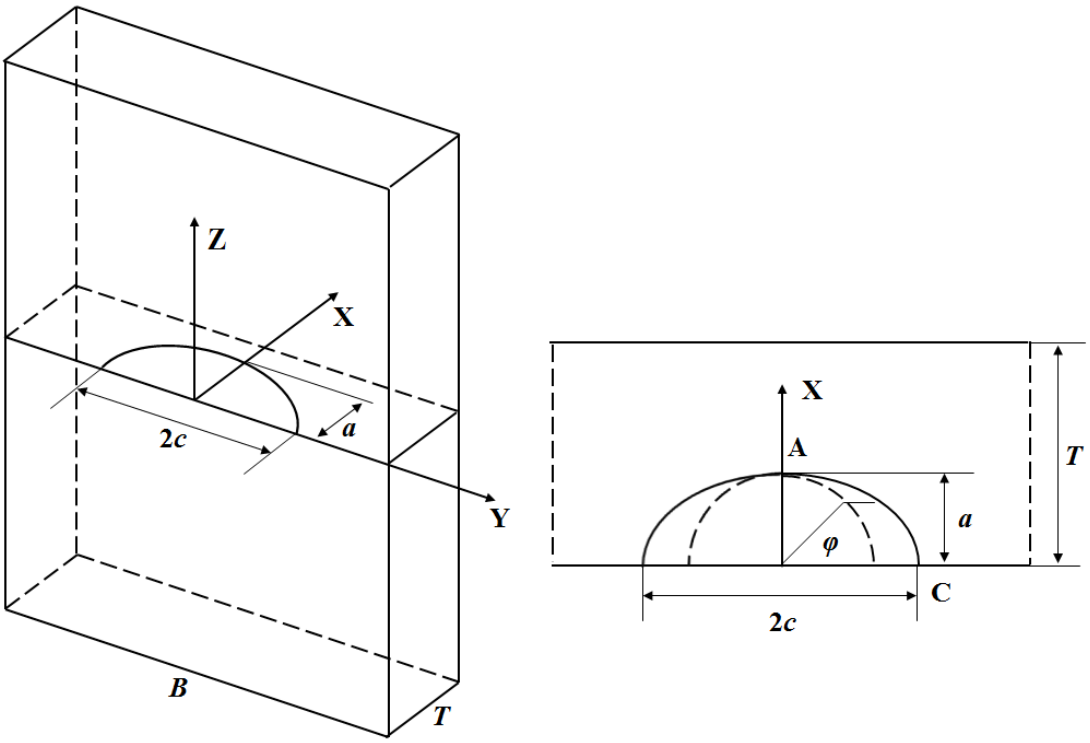

Figure 5.1 Semi-elliptical surface crack in a finite thickness plate.

For more complicated stress distributions due to stress concentration and residual stresses, there are commonly two approaches for the stress intensity factor evaluations. One is to fit the stress distribution, which is normal to the crack surface, into a third-order polynomial equation over the crack depth, and then to calculate the corresponding stress intensity factor with standardized influence coefficients in codes API 579-1[85] or ASME [91].

As the arbitrary stress distribution cannot be well approximated by a polynomial fit, an alternate method is the weight function method. The weight function technique for calculating stress intensity factors is based on the principle of superposition, as illustrated in Fig.5.2. Taking a one-dimensional crack as example for simplicity, it can be found that the stress intensity factor for a cracked body (Fig.5.2a) subjected to the external loading system S is the same as the stress intensity factor in a geometrically identical body (Fig.5.2c) with the local stress field $\sigma(x)$ applied onto the crack surfaces. The local stress field $\sigma(x)$ induced in the prospective crack plane by load S is determined from an uncracked body (Fig.5.2b). The stress intensity factor for a cracked body with loading applied onto crack surfaces can be calculated by integrating the product of the weight function $m(x,a)$ and the stress distribution $\sigma(x)$ as

$$K_I = \int_0^a \sigma(x) m(x,a) dx \tag{5.3}$$

where a is the crack length in Fig.5.2.

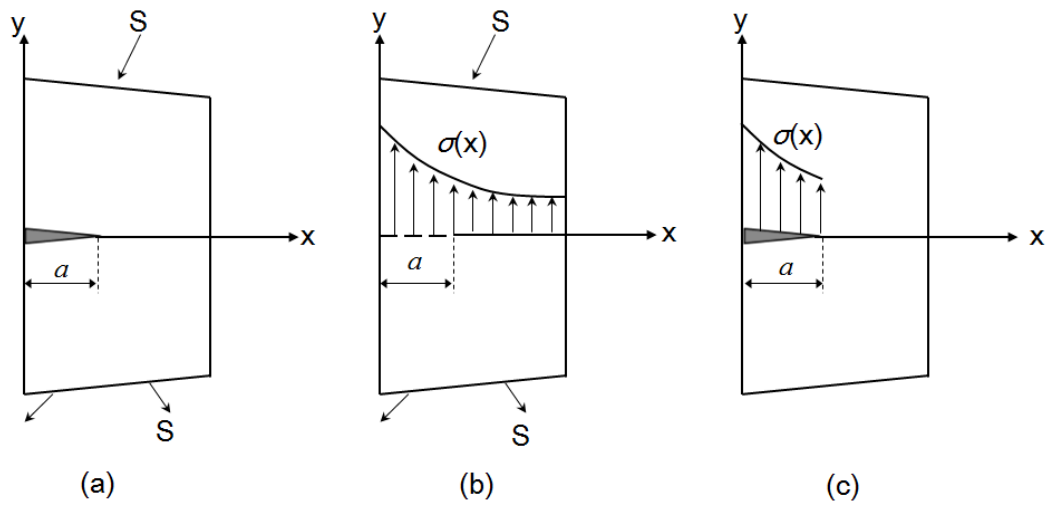

Figure 5.2 Schematic illustration of principle of superposition.

For the surface crack in the finite-thickness plate (as shown in Fig.5.1) subjected to one-dimensional variation of arbitrary stress distribution along thickness direction, the stress intensity factors based on weight function method for deepest point A and surface point C have been standardized by code API 579-1 [85]

$$K_{\mathrm{I}}^{\mathrm{A}} = [\int_0^a \sigma(x) m^{\mathrm{A}}(x;a,c)dx] \cdot [\sec(\frac{\pi c}{B}\sqrt{\frac{a}{T}})]^{0.5} \tag{5.4a}$$

$$K_{\mathrm{I}}^{\mathrm{C}} = [\int_0^a \sigma(x) m^{\mathrm{C}}(x;a,c)dx] \cdot [\sec(\frac{\pi c}{B}\sqrt{\frac{a}{T}})]^{0.5} \tag{5.4b}$$

where $\sigma(x)$ is the stress distribution varying along thickness direction, $m^{\mathrm{A}}(x;a,c)$ and $m^{\mathrm{C}}(x;a,c)$ are the weight functions for the deepest point A and surface point C.

For the deepest point A, the universal weight function is given by

$$m^{\mathrm{A}}(x;a,c) = \frac{2}{\sqrt{2\pi(a-x)}}[1 + M_1(1-\frac{x}{a})^{1/2} + M_2(1-\frac{x}{a}) + M_3(1-\frac{x}{a})^{3/2}] \tag{5.5}$$

where the crack tip along thickness direction locates at x=a. The constants M_1, M_2, M_3 are given by

$$M_1 = \frac{\pi}{\sqrt{2Q}}(4Y_0 - 6Y_1) - \frac{24}{5} \tag{5.6a}$$

$$M_2 = 3 \tag{5.6b}$$

$$M_3 = 2(\frac{\pi}{\sqrt{2Q}}Y_0 - M_1 - 4) \tag{5.6c}$$

where Q is the complete elliptical integral of the second kind in Eq.(5.2), Y_0 and Y_1 are the influence factor formulas of crack depth a, half crack length c and plate thickness T.

For applicable ranges of aspect ratio $0.0<a/c\leq 1.0$, the Y_0 and Y_1 are respectively expressed as [85]

$$Y_0 = B_0 + B_1(\frac{a}{T})^2 + B_2(\frac{a}{T})^4 + B_3(\frac{a}{T})^6 \tag{5.7a}$$

$$B_0 = 1.0929 + 0.2581(\frac{a}{c}) - 0.7703(\frac{a}{c})^2 + 0.4394(\frac{a}{c})^3 \tag{5.7b}$$

$$B_1 = 0.456 - 3.045(\frac{a}{c}) + 2.007(\frac{a}{c})^2 + \frac{1.0}{0.147 + (\frac{a}{c})^{0.688}} \quad (5.7c)$$

$$B_2 = 0.995 - \frac{1.0}{0.027 + (\frac{a}{c})} + 22.0(1.0 - \frac{a}{c})^{9.953} \quad (5.7d)$$

$$B_3 = -1.459 + \frac{1.0}{0.014 + \frac{a}{c}} - 24.211(1.0 - \frac{a}{c})^{8.071} \quad (5.7e)$$

and

$$Y_1 = A_0 + A_1(\frac{a}{T})^2 + A_2(\frac{a}{T})^4 + A_3(\frac{a}{T})^6 \quad (5.8a)$$

$$A_0 = 0.4537 + 0.1231(\frac{a}{c}) - 0.7412(\frac{a}{c})^2 + 0.46(\frac{a}{c})^3 \quad (5.8b)$$

$$A_1 = -1.652 + 1.665(\frac{a}{c}) - 0.534(\frac{a}{c})^2 + \frac{1.0}{0.198 + (\frac{a}{c})^{0.846}} \quad (5.8c)$$

$$A_2 = 3.418 - 3.126(\frac{a}{c}) - \frac{1.0}{0.041 + (\frac{a}{c})} + 17.259(1.0 - \frac{a}{c})^{9.286} \quad (5.8d)$$

$$A_3 = -4.228 + 3.643(\frac{a}{c}) + \frac{1.0}{0.02 + \frac{a}{c}} - 21.924(1.0 - \frac{a}{c})^{9.203} \quad (5.8e)$$

In the recent experimental studies [92], from the compressive residual stress region induced by hammer peening, the initial cracks with aspect ratio over 1.0 have been observed. Therefore, as a supplement, the influence factors Y_0 and Y_1 for $1.0<a/c\leq 2.0$ derived by Wang and Lambert [88] are employed as

$$Y_0 = B_0 + B_1(\frac{a}{T})^2 + B_2(\frac{a}{T})^4 \quad (5.9a)$$

$$B_0 = 1.112 - 0.00923(\frac{a}{c}) + 0.02954(\frac{a}{c})^2 \quad (5.9b)$$

$$B_1 = 1.138 - 1.134(\frac{a}{c}) + 0.3073(\frac{a}{c})^2 \quad (5.9c)$$

$$B_2 = -0.9502 + 0.8832(\frac{a}{c}) - 0.2259(\frac{a}{c})^2 \quad (5.9d)$$

and

$$Y_1 = A_0 + A_1(\frac{a}{T})^2 + A_2(\frac{a}{T})^4 \tag{5.10a}$$

$$A_0 = 0.4735 - 0.2053(\frac{a}{c}) + 0.03662(\frac{a}{c})^2 \tag{5.10b}$$

$$A_1 = 0.7723 - 0.7265(\frac{a}{c}) + 0.1837(\frac{a}{c})^2 \tag{5.10c}$$

$$A_2 = -0.2006 - 0.9829(\frac{a}{c}) + 1.237(\frac{a}{c})^2 - 0.3554(\frac{a}{c})^3 \tag{5.10d}$$

For the surface point C, the universal weight function is given by

$$m^{\mathrm{C}}(x;a,c) = \frac{2}{\sqrt{\pi x}}[1 + N_1(\frac{x}{a})^{1/2} + N_2(\frac{x}{a}) + N_3(\frac{x}{a})^{3/2}] \tag{5.11}$$

where the crack tip along thickness direction locates at x=a. The constants N_1, N_2, N_3 are given by

$$N_1 = \frac{\pi}{\sqrt{4Q}}(30F_1 - 18F_0) - 8 \tag{5.12a}$$

$$N_2 = \frac{\pi}{\sqrt{4Q}}(60F_0 - 90F_1) + 15 \tag{5.12b}$$

$$N_3 = -(1 + N_1 + N_2) \tag{5.12c}$$

where Q is the complete elliptical integral of the second kind in Eq.(5.2), F_0 and F_1 are the influence factor formulas of crack depth a, half crack length c and plate thickness T.

Within the range of aspect ratio $0.0<a/c\leq 1.0$, the F_0 and F_1 are respectively expressed as [85]

$$F_0 = [C_0 + C_1(\frac{a}{T})^2 + C_2(\frac{a}{T})^4]\sqrt{\frac{a}{c}} \tag{5.13a}$$

$$C_0 = 1.2972 - 0.1548(\frac{a}{c}) - 0.0185(\frac{a}{c})^2 \tag{5.13b}$$

$$C_1 = 1.5083 - 1.3219(\frac{a}{c}) + 0.5128(\frac{a}{c})^2 \tag{5.13c}$$

$$C_2 = -1.101 + \frac{0.879}{0.157 + \frac{a}{c}} \tag{5.13d}$$

and

$$F_1 = [D_0 + D_1(\frac{a}{T})^2 + D_2(\frac{a}{T})^4]\sqrt{\frac{a}{c}} \tag{5.14a}$$

$$D_0 = 1.2687 - 1.0642(\frac{a}{c}) + 1.4646(\frac{a}{c})^2 - 0.725(\frac{a}{c})^3 \tag{5.14b}$$

$$D_1 = 1.1207 - 1.2289(\frac{a}{c}) + 0.5876(\frac{a}{c})^2 \tag{5.14c}$$

$$D_2 = 0.19 - 0.608(\frac{a}{c}) + \frac{0.199}{0.035 + \frac{a}{c}} \tag{5.14d}$$

Within the range of aspect ratio $1.0<a/c\leq 2.0$, the F_0 and F_1 are respectively given by [88]

$$F_0 = [C_0 + C_1(\frac{a}{T})^2 + C_2(\frac{a}{T})^4]\sqrt{\frac{a}{c}} \tag{5.15a}$$

$$C_0 = 1.34 - 0.2872(\frac{a}{c}) + 0.06611(\frac{a}{c})^2 \tag{5.15b}$$

$$C_1 = 1.882 - 1.7569(\frac{a}{c}) + 0.4423(\frac{a}{c})^2 \tag{5.15c}$$

$$C_2 = -0.1493 + 0.01208(\frac{a}{c}) + 0.02215(\frac{a}{c})^2 \tag{5.15d}$$

and

$$F_1 = [D_0 + D_1(\frac{a}{T})^2 + D_2(\frac{a}{T})^4]\sqrt{\frac{a}{c}} \tag{5.16a}$$

$$D_0 = 1.12 - 0.2442(\frac{a}{c}) + 0.06708(\frac{a}{c})^2 \tag{5.16b}$$

$$D_1 = 1.251 - 1.173(\frac{a}{c}) + 0.2973(\frac{a}{c})^2 \tag{5.16c}$$

$$D_2 = 0.04706 - 0.1214(\frac{a}{c}) + 0.04406(\frac{a}{c})^2 \tag{5.16d}$$

5.2.2 Integration approach

When stress distribution $\sigma(x)$ is obtained from experimental measurements or numerical stress analysis, the stress data are usually extracted at discrete locations. A typical example is a set of stress values at discrete nodal points from FE analysis of a structural component in the absence of a crack. The discrete data points of through-thickness stress distribution can be written in a piece-wise linear format, as illustrated in Fig.5.3.

$$\sigma_i(x) = k_i x + b_i \qquad (x_i < x < x_{i+1}) \text{ for } i = 1,..., N_{\text{inp}} - 1 \tag{5.17a}$$

$$k_i = \frac{\sigma(x_{i+1}) - \sigma(x_i)}{x_{i+1} - x_i} \tag{5.17b}$$

$$b_i = \sigma(x_i) - x_i k_i \tag{5.17c}$$

where k_i and b_i are the slope and constant of piece-wise representation of actual stress over the interval between x_i and x_{i+1}, respectively. N_{inp} is the number of discrete input data of the actual stress distribution. $\sigma(x_i)$ is the discrete data point of stress at position x_i, and $\sigma_i(x)$ is the piece-wise linear representation of actual stress distribution over the interval between x_i and x_{i+1}.

As the crack tip is at $x=a$, it is supposed to arrange a set of stress data on the crack surface for the integration in Eq. (5.4). $\sigma(x_j)$ represents the interpolated stress value at position x_j

$$x_j = \frac{a}{N_{\text{intp}} - 1}(j-1) \quad \text{for } j = 1,..., N_{\text{intp}} \tag{5.18a}$$

$$\sigma(x_j) = k_i x_j + b_i \quad (x_i \le x_j \le x_{i+1}) \tag{5.18b}$$

where N_{intp} is the number of interpolated discrete data of stress distribution on crack surface. In this work, the value of N_{intp} is set much greater than that of N_{inp} for guaranteeing calculation accuracy.

By the same manner, the piece-wise representation $\sigma_j(x)$ of interpolated stress over the interval between x_j and x_{j+1} is given by

$$\sigma_j(x) = k_j x + b_j \qquad (x_j < x < x_{j+1}) \text{ for } j = 1,..., N_{\text{intp}} - 1 \tag{5.19a}$$

$$k_j = \frac{\sigma(x_{j+1}) - \sigma(x_j)}{x_{j+1} - x_j} \tag{5.19b}$$

$$b_j = \sigma(x_j) - x_j k_j \tag{5.19c}$$

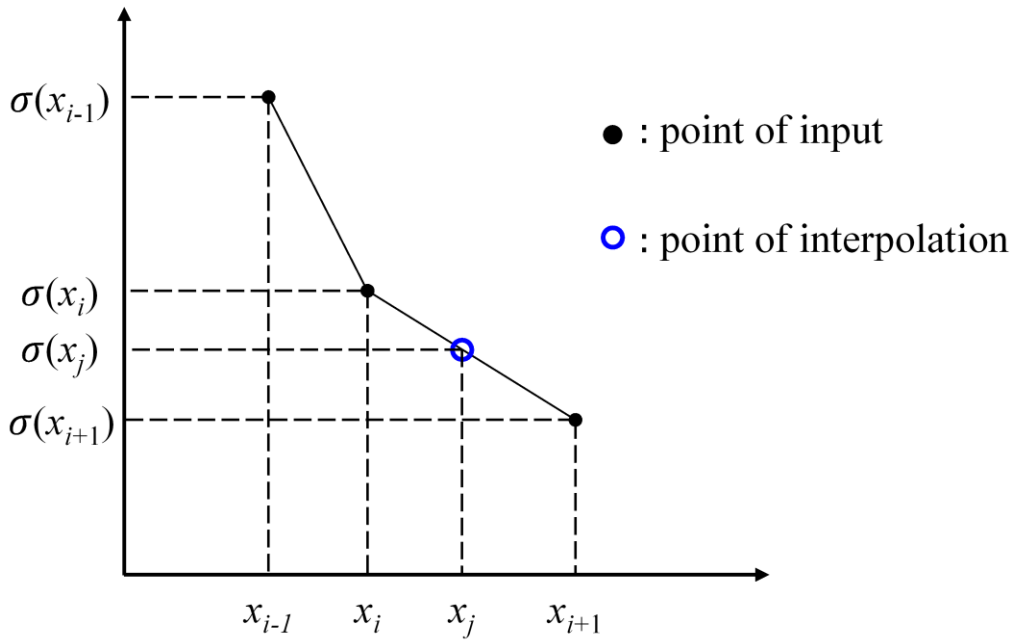

Figure 5.3 Piece-wise representation of specified stress data at discrete locations.

For the deepest point A in Fig.5.1, the stress intensity factor is given by substituting Eq. (5.5) into Eq. (5.4a)

$$K_{IA} = \{\int_0^a \frac{2\sigma(x)}{\sqrt{2\pi(a-x)}}[1 + M_1(1-\frac{x}{a})^{1/2} + M_2(1-\frac{x}{a}) + M_3(1-\frac{x}{a})^{3/2}]dx\} \cdot f_B \qquad (5.20)$$

where $f_B = [\sec(\frac{\pi c}{B}\sqrt{\frac{a}{T}})]^{0.5}$ is the finite width correction factor.

And Eq. (5.20) can be rewritten as

$$K_{IA} = \{\sqrt{\frac{2}{\pi}}\int_0^a \sigma(x)[\frac{1}{\sqrt{a-x}} + \frac{1}{\sqrt{a}}M_1 + \frac{\sqrt{a-x}}{a}M_2 + \frac{a-x}{a\sqrt{a}}M_3]\,dx\} \cdot f_B \qquad (5.21)$$

Substituting the piece-wise linear representation of the through-thickness stress distribution on the crack surface given by Eq. (5.19) into Eq. (5.21), it can be written as

$$K_{IA}(k_j, b_j) = (K_{IM0} + K_{IM1} * M_1 + K_{IM2} * M_2 + K_{IM3} * M_3) \cdot f_B \qquad (5.22a)$$

with the following relationships as

$$K_{IM0} = \frac{2\sqrt{2}}{3\sqrt{\pi}} \sum_{j=1}^{N_{intp}-1} [(k_j x_j + 2k_j a + 3b_j)\sqrt{a-x_j} - (k_j x_{j+1} + 2k_j a + 3b_j)\sqrt{a-x_{j+1}}] \qquad (5.22b)$$

$$K_{\mathrm{IM1}} = \sqrt{\frac{2}{a\pi}} \sum_{j=1}^{N_{\mathrm{intp}}-1} \left[\frac{k_j}{2}(x_{j+1}^2 - x_j^2) + b_j(x_{j+1} - x_j)\right] \tag{5.22c}$$

$$\begin{aligned} K_{\mathrm{IM2}} = \frac{2}{15a}\sqrt{\frac{2}{\pi}} \sum_{j=1}^{N_{\mathrm{intp}}-1} & \left[(3k_j x_j + 2k_j a + 5b_j)(a - x_j)^{3/2}\right. \\ & \left. -(3k_j x_{j+1} + 2k_j a + 5b_j)(a - x_{j+1})^{3/2}\right] \end{aligned} \tag{5.22d}$$

$$\begin{aligned} K_{\mathrm{IM3}} = \frac{1}{a\sqrt{a}}\sqrt{\frac{2}{\pi}} \sum_{j=1}^{N_{\mathrm{intp}}-1} & \left[\frac{k_j}{3}(x_j^3 - x_{j+1}^3) + \frac{1}{2}(k_j a - b_j)x_{j+1}^2\right. \\ & \left. -\frac{1}{2}(k_j a - b_j)x_j^2 + b_j a(x_{j+1} - x_j)\right] \end{aligned} \tag{5.22e}$$

For the surface point C in Fig.5.1, the stress intensity factor is given by substituting Eq. (5.11) into Eq. (5.4b)

$$K_{IC} = \left\{\int_0^a \frac{2\sigma(x)}{\sqrt{\pi x}}\left[1 + N_1\left(\frac{x}{a}\right)^{1/2} + N_2\left(\frac{x}{a}\right) + N_3\left(\frac{x}{a}\right)^{3/2}\right]dx\right\} \cdot f_B \tag{5.23}$$

where $f_B = \left[\sec\left(\frac{\pi c}{B}\sqrt{\frac{a}{T}}\right)\right]^{0.5}$ is the finite width correction factor.

And Eq. (5.23) can be rewritten as

$$K_{IC} = \left\{\frac{2}{\sqrt{\pi}}\int_0^a \sigma(x)\left[\frac{1}{\sqrt{x}} + \frac{1}{\sqrt{a}}N_1 + \frac{\sqrt{x}}{a}N_2 + \frac{x}{a\sqrt{a}}N_3\right]dx\right\} \cdot f_B \tag{5.24}$$

Substituting the piece-wise linear representation of the through-thickness stress distribution on the crack surface given by Eq. (5.19) into Eq. (5.24), it can be written as

$$K_{IC}(k_j, b_j) = (K_{\mathrm{IN0}} + K_{\mathrm{IN1}} * N_1 + K_{\mathrm{IN2}} * N_2 + K_{\mathrm{IN3}} * N_3) \cdot f_B \tag{5.25a}$$

with the following relationships as

$$K_{\mathrm{IN0}} = \frac{4}{3\sqrt{\pi}} \sum_{j=1}^{N_{\mathrm{intp}}-1} \left[\sqrt{x_{j+1}}(k_j x_{j+1} + 3b_j) - \sqrt{x_j}(k_j x_j + 3b_j)\right] \tag{5.25b}$$

$$K_{\mathrm{IN1}} = \frac{1}{\sqrt{\pi a}} \sum_{j=1}^{N_{\mathrm{intp}}-1} \left[x_{j+1}(k_j x_{j+1} + 2b_j) - x_j(k_j x_j + 2b_j)\right] \tag{5.25c}$$

$$K_{\mathrm{IN2}} = \frac{4}{15a\sqrt{\pi}} \sum_{j=1}^{N_{\mathrm{intp}}-1} \left[x_{j+1}^{3/2}(3k_j x_{j+1} + 5b_j) - x_j^{3/2}(3k_j x_j + 5b_j)\right] \tag{5.25d}$$

$$K_{\mathrm{IN3}} = \frac{1}{3a\sqrt{a\pi}} \sum_{j=1}^{N_{\mathrm{intp}}-1} \left[x_{j+1}^2(2k_j x_{j+1} + 3b_j) - x_j^2(2k_j x_j + 3b_j)\right] \tag{5.25e}$$

5.2.3 Validation of SIF calculation

In order to verify the accuracy of the calculated stress intensity factors based on weight function method, four types of loading are assumed to be applied onto the crack surfaces in each crack geometry case, with the following stress distributions

$$\sigma(x) = \sigma_0(1-\frac{x}{a})^n \text{ for } n = 0,1,2,3 \tag{5.26}$$

where σ_0 is the nominal stress, and a is the crack depth. The constant, linear, quadratic and cubic applied stress distributions are shown in Fig.5.4.

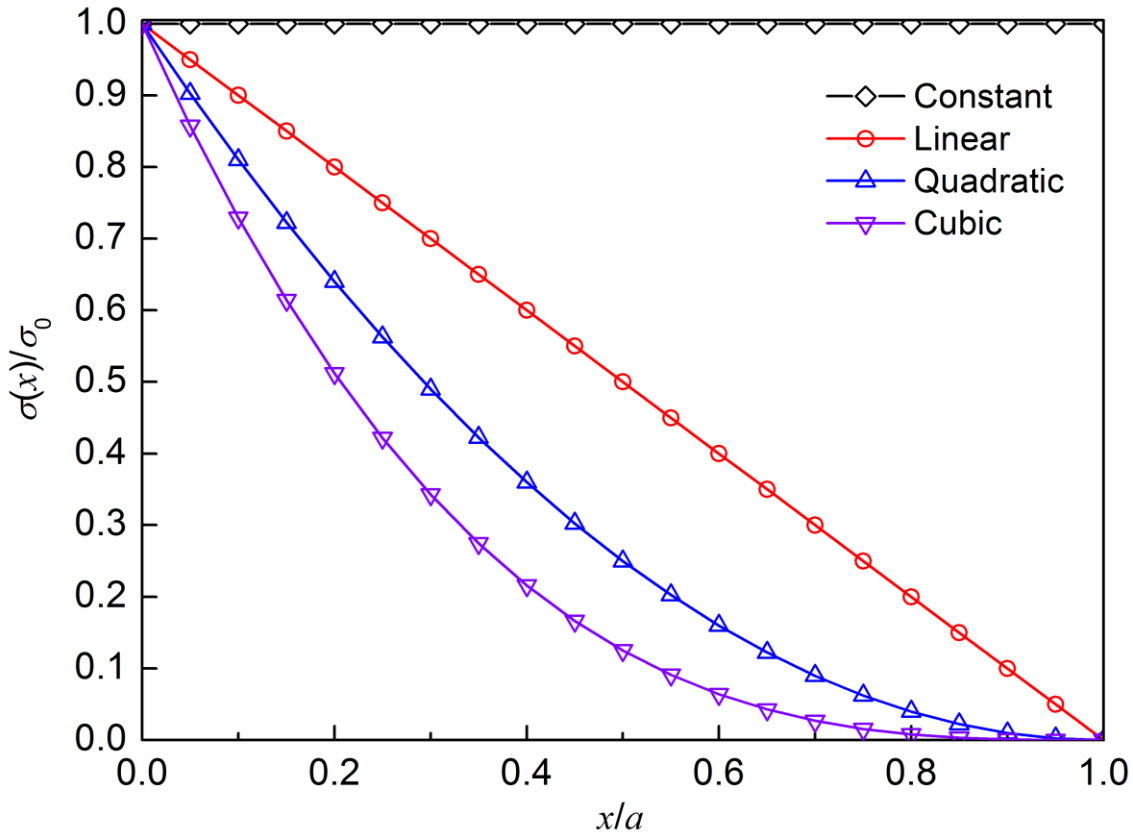

Figure 5.4 Applied stress distributions on the crack surface.

The corresponding finite element results of the stress intensity factor for the deepest and surface points calculated by Shiratori et al. [86] and Wang & Lambert [87],[88] are chosen as reference solutions, with aspect ratios a/c of 0.05,0.1,0.2,0.4,0.6, 1.0, 1.5 and 2.0, and a/T values of 0.2, 0.4, 0.6 and 0.8. It should be noted that in these finite element models, the width of the flat plate was large enough ($B/c \geq 10$) so that the finite width free

boundary had a negligible effect on the stress intensity factor, i.e. finite width correction factor f_B approaches to 1.

The stress intensity factor results are normalised as follows

$$F = \frac{K_I}{\sigma_0 \sqrt{\pi a / Q}} \tag{5.27}$$

where F is the boundary correction factor and Q is the complete elliptical integral of the second kind given by Eq. (5.2). The results of boundary correction factor calculated by weight function method and the reference solutions by FEM are compared in Fig.5.5-5.8 for constant, linear, quadratic and cubic stress fields, respectively.

For the whole regions of $0.05 \le a/c \le 2.0$ and $0.2 \le a/T \le 0.8$, the difference between the stress intensity factors calculated from the weight function method and all the finite element results are generally below 10%, which is good in industrial applications. Overall, good agreements can be confirmed for the following fatigue crack growth prediction.

From the results, it can be observed that at the same value of a/T, the stress intensity factors for the deepest point become greater with decreasing value of a/c, however, those for the surface point show an opposite tendency.

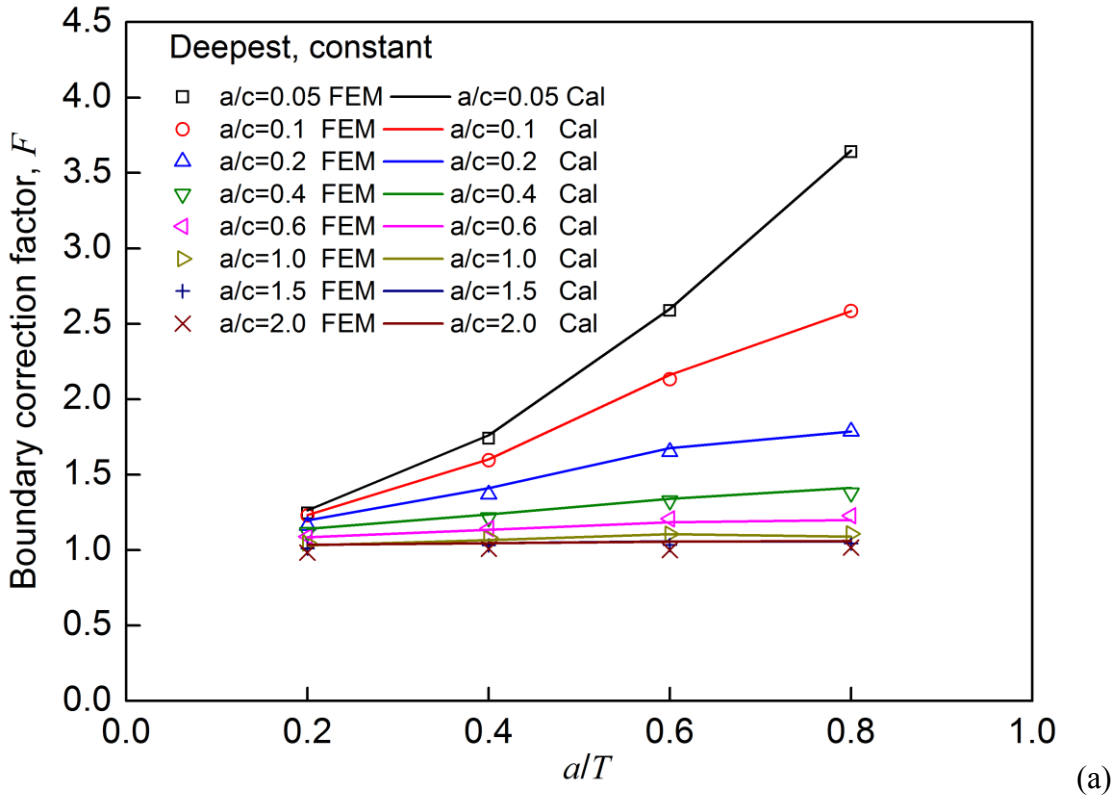

(a)

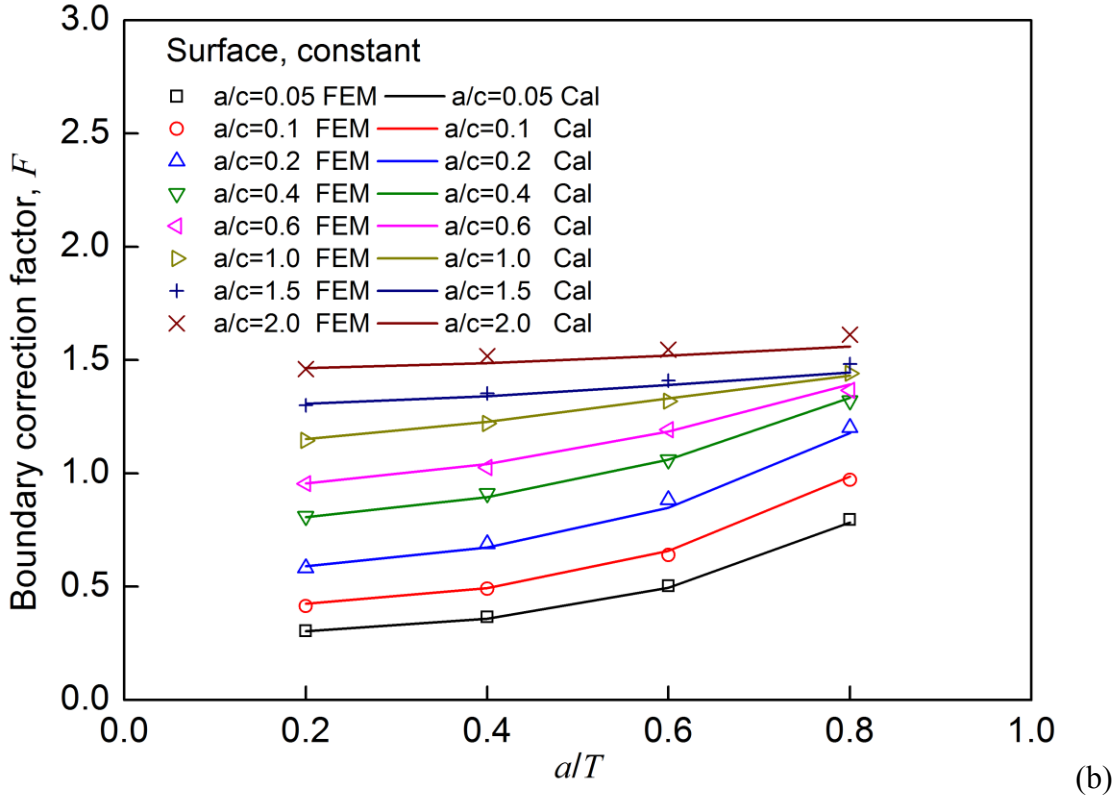

(b)

Figure 5.5 Comparison of boundary correction factors obtained from weight function method and FEM data for constant stress distribution; (a) deepest point, (b) surface point.

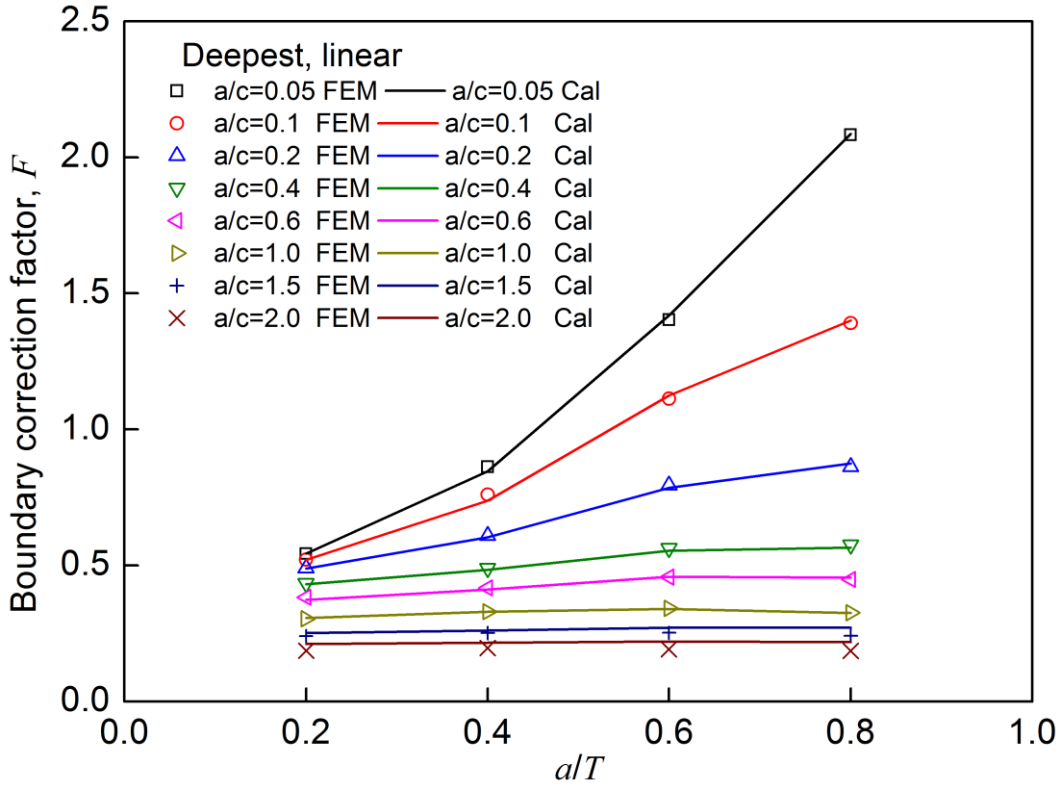

(a)

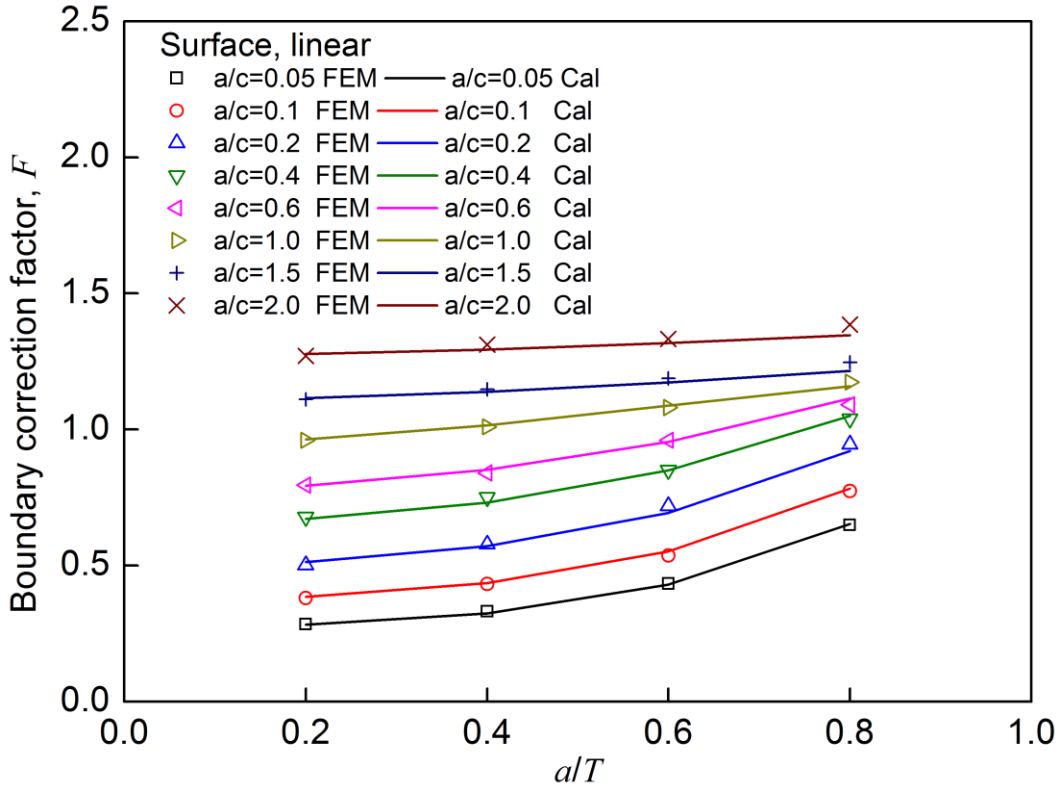

(b)

Figure 5.6 Comparison of boundary correction factors obtained from weight function method and FEM data for linear stress distribution; (a) deepest point, (b) surface point.

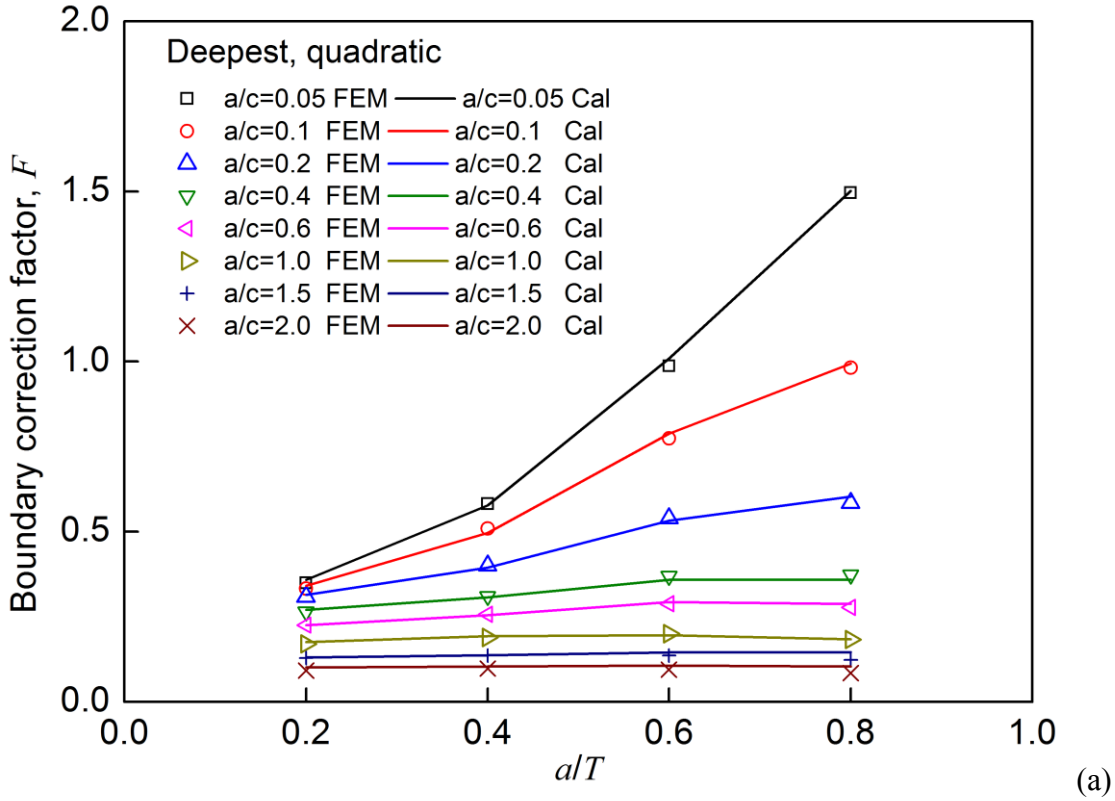

(a)

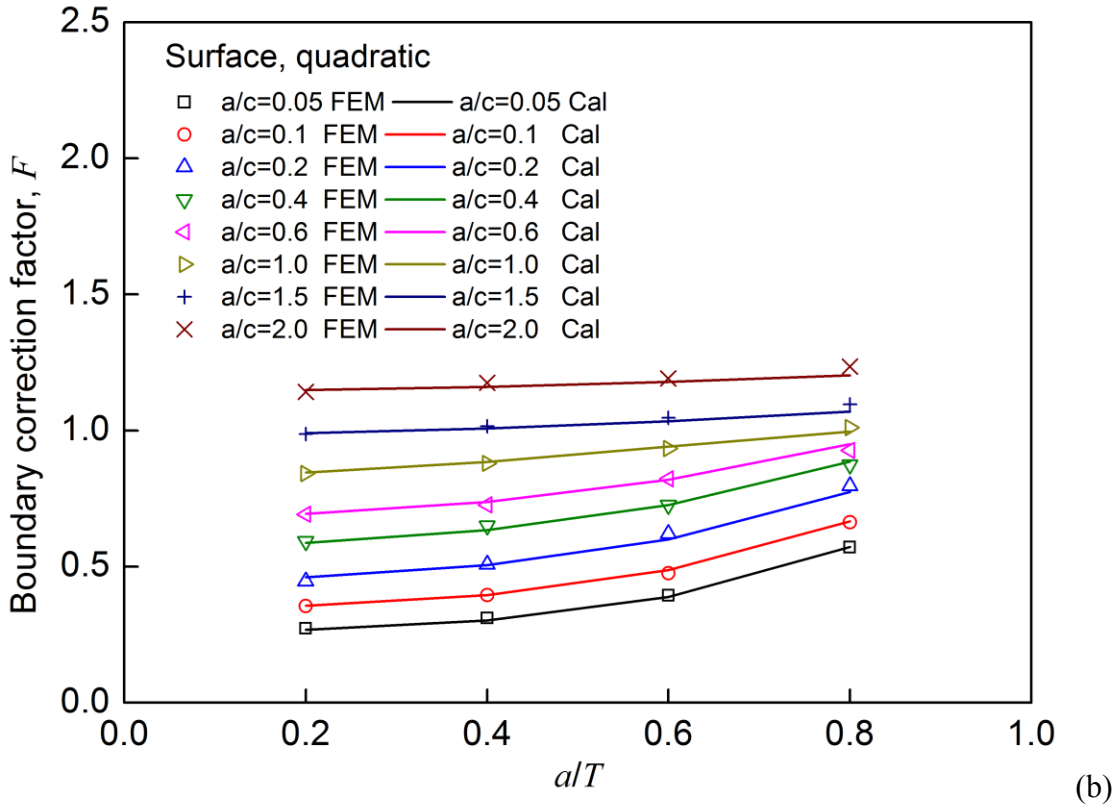

(b)

Figure 5.7 Comparison of boundary correction factors obtained from weight function method and FEM data for quadratic stress distribution;(a) deepest point, (b) surface point.

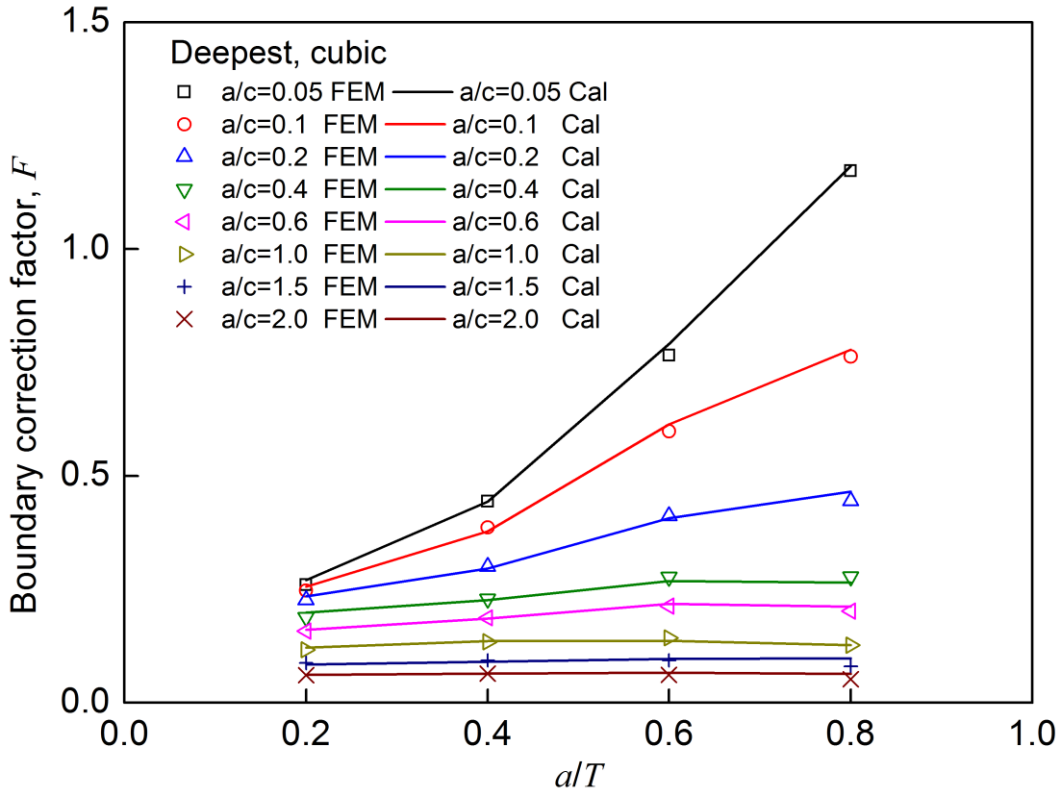

(a)

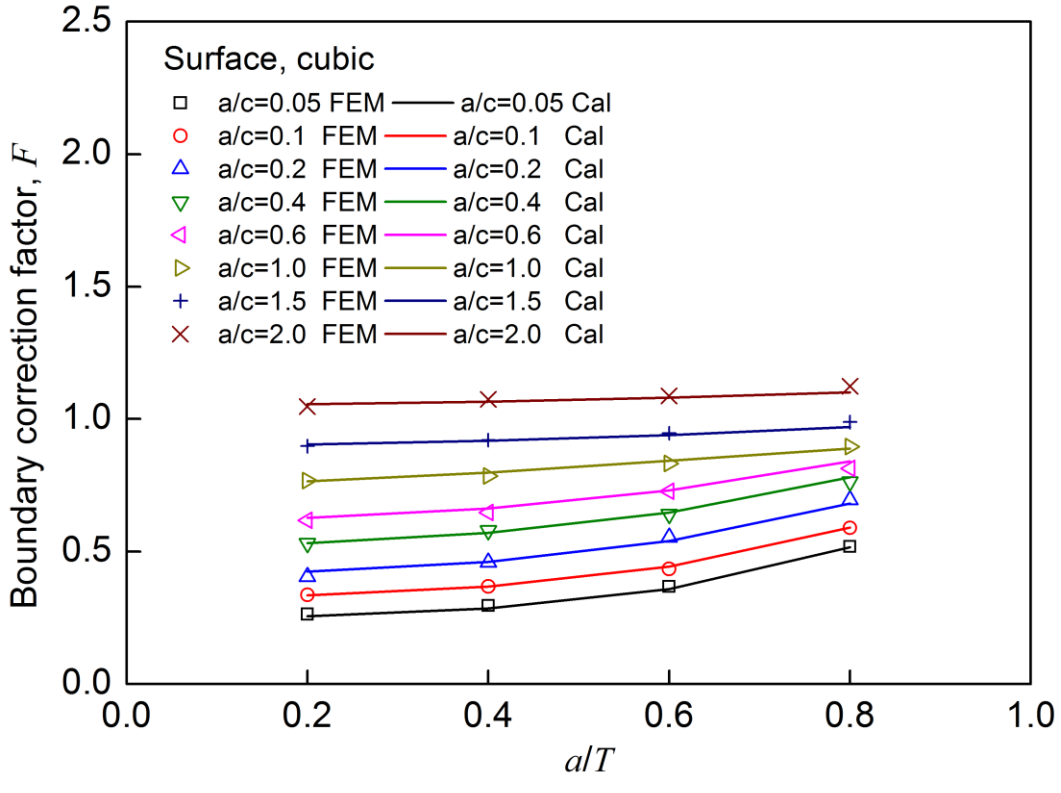

(b)

Figure 5.8 Comparison of boundary correction factors obtained from weight function method and FEM data for cubic stress distribution ;(a) deepest point, (b) surface point.

5.3 Fracture mechanics based method for fatigue strength evaluation

5.3.1 Fatigue crack growth prediction method

The fatigue behaviour of welded joints is numerically analysed based on a fracture mechanics method here. In order to simplify the problem, the above discussed finite thickness plate with a semi-elliptical surface flaw is employed instead of the weld joint being considered. Because it has been demonstrated for relative small cracks, the stress intensity factor values related to different structural component geometries are very similar to one another provided that the stress field acting on the defect faces is the same, i.e. the boundary effects can be negligible for small cracks embedded in a given stress field [93], [94].

The simplified simulation procedures of surface crack growth in welded joints under constant amplitude cyclic loading are summarized as follows:

1. Perform stress analysis of the uncracked weld joint, to determine the in-depth stress distributions along the assumed crack path, including applied stress σ_{app}, considering joint type and weld toe shape, and the residual stress σ_{res}.
2. Determine the initial crack size with depth a_0 and half crack length c_0.
3. Calculate stress intensity factors K_{max} , K_{min}, K_{res} for maximum, minimum applied stress and residual stress, respectively, and effective stress ratio R_{eff} for the deepest point A and surface point C with the current crack depth a_i and half crack length c_i

$$\Delta K = (K_{max} + K_{res}) - (K_{min} + K_{res}) = (K_{max} - K_{min})_{\text{at A or C}} \tag{5.28}$$

$$R_{eff} = \frac{K_{min} + K_{res}}{K_{max} + K_{res}} \tag{5.29}$$

   where ΔK represents the total stress intensity factor range.
4. Calculate the effective stress intensity factor ranges ΔK_{eff} for deepest point A and surface point C according to the effective stress ratio R_{eff}, respectively

$$(\Delta K_{eff})_{\text{at A or C}} = \begin{cases} 0 & K_{max} + K_{res} \le 0 \\ \Delta K / (1.5 - R_{eff}) \text{ for } & R_{eff} < 0.5 \\ \Delta K & R_{eff} \ge 0.5 \end{cases} \tag{5.30}$$

5. Calculate the crack growth rate at deepest point A and surface point C based on modified Paris-Elber law, which uses the effective stress intensity factor range, ΔK_{eff}, and the threshold value, $(\Delta K_{\text{eff}})_{\text{th}}$, to simply take the crack closure effect into account .

$$da/dN = C[(\Delta K_{\text{eff}}^{\text{A}})^m - (\Delta K_{\text{eff}})_{\text{th}}^m] \tag{5.31a}$$

$$dc/dN = C[(\Delta K_{\text{eff}}^{\text{C}})^m - (\Delta K_{\text{eff}})_{\text{th}}^m] \tag{5.31b}$$

where C and m are material constants.

6. For a given increment of cycle number ΔN, the growth increments of crack depth Δa_i and half crack length Δc_i are estimated as

$$\Delta a_i = (da/dN)_i * \Delta N \tag{5.32a}$$

$$\Delta c_i = (dc/dN)_i * \Delta N \tag{5.32b}$$

then the new crack depth a_{i+1} and half crack length c_{i+1} become

$$a_{i+1} = a_i + \Delta a_i \tag{5.33a}$$

$$c_{i+1} = c_i + \Delta c_i \tag{5.33b}$$

7. Step (3)-(6) will be repeated until the crack depth reaches the prescribed final depth a_{f}, and the corresponding cycle number N_{f} is the final crack propagation life.

In this work, the material constants and threshold value of effective stress intensity factor range are set as C=1.45×10^{-11}, m=2.75, and $(\Delta K_{\text{eff}})_{\text{th}}$=2.45 MPa$\sqrt{\text{m}}$, which are referred to code WES2805-97 [95]. The cycle number increment ΔN is set as 200, which is considered to give enough accuracy for constant amplitude cyclic loading cases.

5.3.2 Prediction of surface crack growth in flat plate

Here, two simple calculation cases, that initial surface cracks (a_0=1mm, c_0=1mm) and (a_0=1mm, c_0=5mm) are assumed to propagate in the flat plate of thickness T=16mm under the stress conditions of applied stress range $\Delta\sigma_{app}$= 200MPa and stress ratio R=0.0, are performed. The calculation is continued until the crack depth reaches 80% of plate thickness (a_f=12.8mm).

The predicted crack propagation lives of the two cases are compared in Fig.5.9. It can be observed that even though the applied stress condition is same, the predicted crack growth life is greatly affected by the initial crack aspect ratio a_0/ c_0. In other words, with the same initial crack depth, the crack growth life of low aspect ratio semi-elliptical surface crack is shorter than that of semi-circular surface crack.

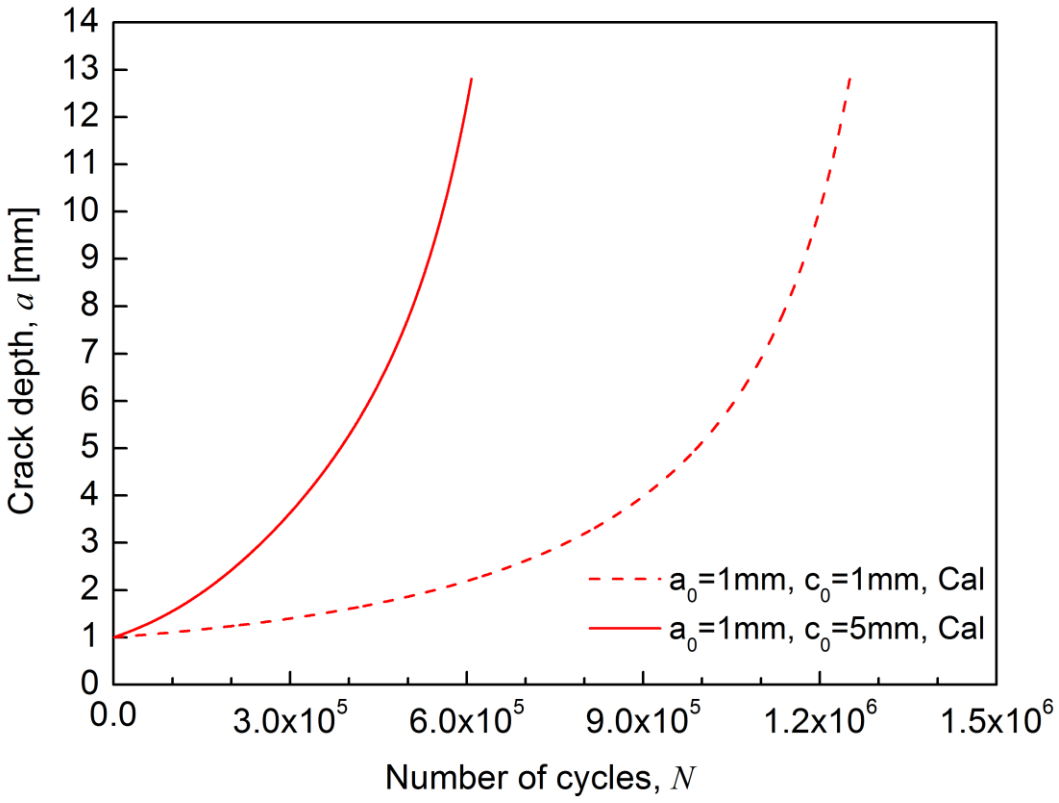

Figure 5.9 Predicted surface crack growth lives in flat plate under $\Delta\sigma_{app}$= 200MPa and R=0.0.

Moreover, the predicted crack shape evolution, which is compared with the results calculated by program SCANP.2014, is shown in Fig.5.10. From the figure, it can be observed that the initial semi-circular and semi-elliptical cracks under tension load are predicted to gradually grow to a semi-elliptical shape of about 0.7-0.8 aspect ratio, by both the current calculation and SCANP. The similar trend, that irrespective of the initial crack shape, the crack tends to an optimum aspect ratio independent of applied stress range but affected by loading mode (e.g., tension, bending, etc.), has been experimentally verified [90].

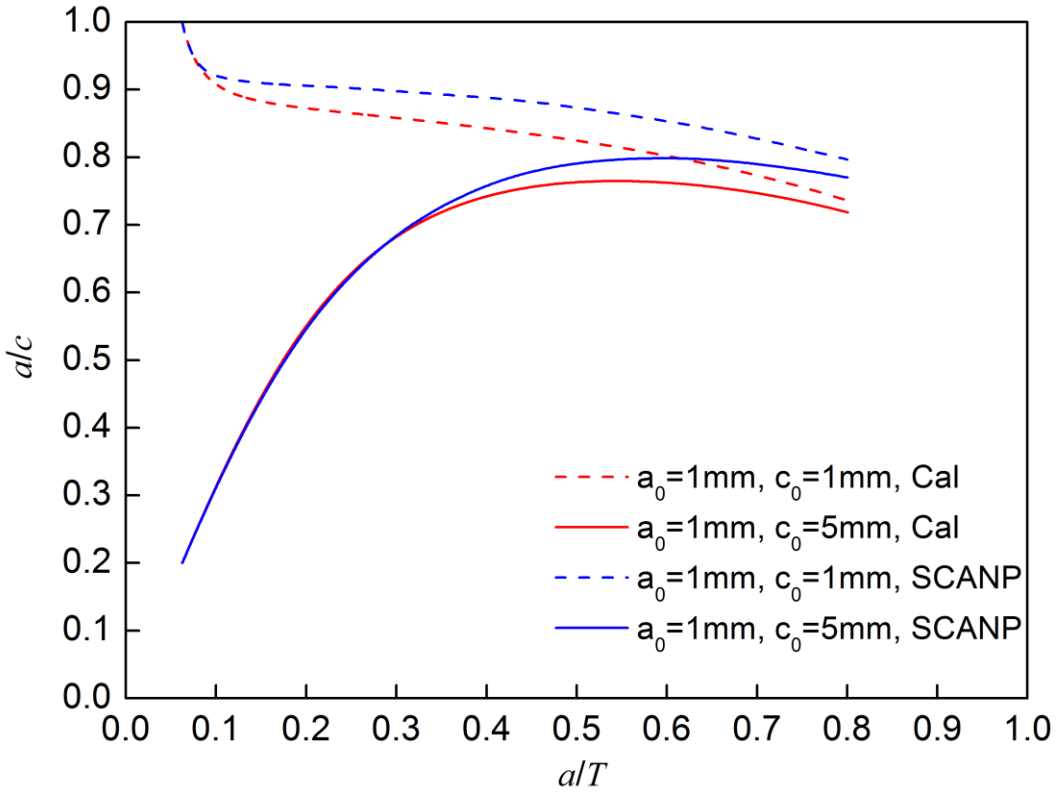

Figure 5.10 Predicted surface crack shape evolution under tension.

5.3.3 Prediction of fatigue strengths of cruciform joints

The fatigue life of the as-weld and UIT non-load-carrying cruciform joints, which are used by Suzuki et al. [78] as previously shown in Fig.4.11, will be estimated here. In this calculation, a single semi-circular crack of depth 0.2mm is assumed to initiate and propagate at the weld toe in the center of specimen width, and the calculation is continued until the crack depth reaches 80% of plate thickness T, as shown in Fig.5.11.

The effective stress intensity factors ΔK_{eff} for the deepest point A and surface point C will be calculated taking into account the stress distributions along the crack path, including the predicted residual stresses due to welding and UIT peening reported in Chapter 4.

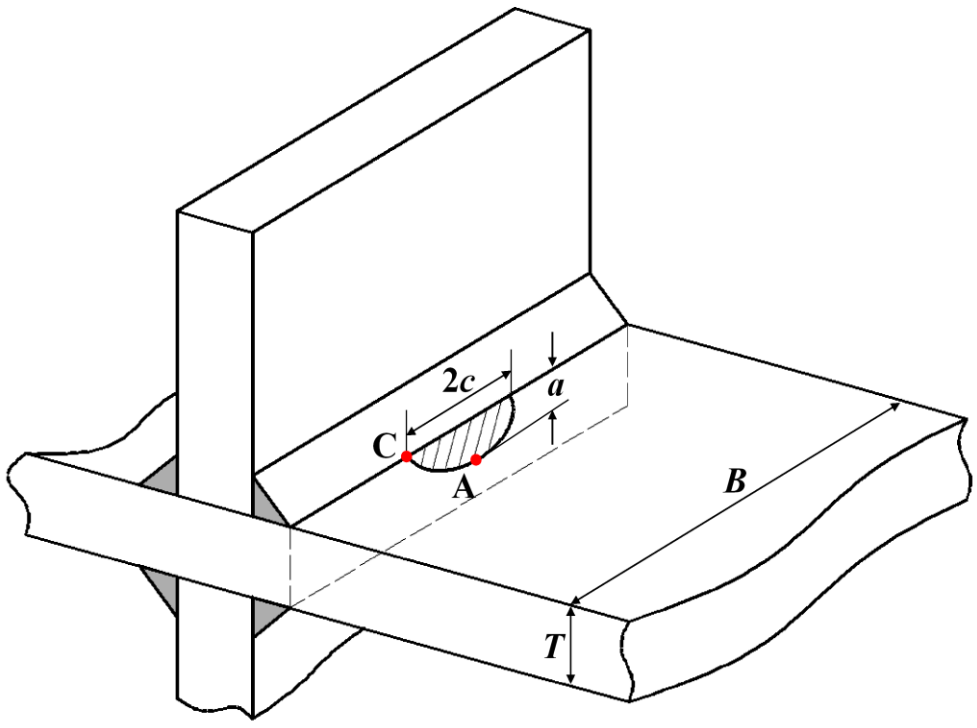

Figure 5.11 Surface crack at the weld toe of cruciform joint.

5.3.3.1 Estimation of stress concentration

With respect to fatigue strength improvement, UIT has the benefit of producing a smooth transition from weld metal to base metal, leading to a reduction of local stress concentration. Generally, the local stress concentration nearby the weld toe is evaluated by FE model in which the very fine mesh is generated to consider the actual weld toe radius shape [8],[45] . In this work, the estimation formula of stress concentration factor, K_t, at weld toe of non-load-carrying fillet joints under tension load proposed Tsuji [96] is employed, instead of the time-consuming FE method. The parameters defined in Tsuji's equation including the thickness of the main and attachment plates T and T_p, leg length l, flank angle θ and toe radius r are shown in Fig.5.12.

$$K_t = 1 + [1.348 + 0.397 \ln(\frac{S}{T})] \cdot Q^{0.467} \cdot f_\theta \tag{5.35a}$$

with

$$Q = (\frac{l}{r}) * \frac{1}{2.8(W/T) - 2} \tag{5.35b}$$

$$f_\theta = [1 - \exp(-0.9\sqrt{\frac{W}{2l}} \cdot \theta)] / [1 - \exp(-0.9\sqrt{\frac{W}{2l}} \cdot \frac{\pi}{2})] \tag{5.35c}$$

where the flank angle θ is kept constant at $\pi/4$, parameters $W=T+2l$ and S= T_p+2l, $T=T_p=16$mm, $l=7$mm.

According to the measured weld toe shape by Suzuki et al. (2014), the toe radius r of the as-weld and UIT specimen are assumed as 0.25mm and 2.0mm, respectively. Hence, the stress concentration factors K_t of as-weld and UIT specimen are calculated as 4.22 and 2.22, respectively.

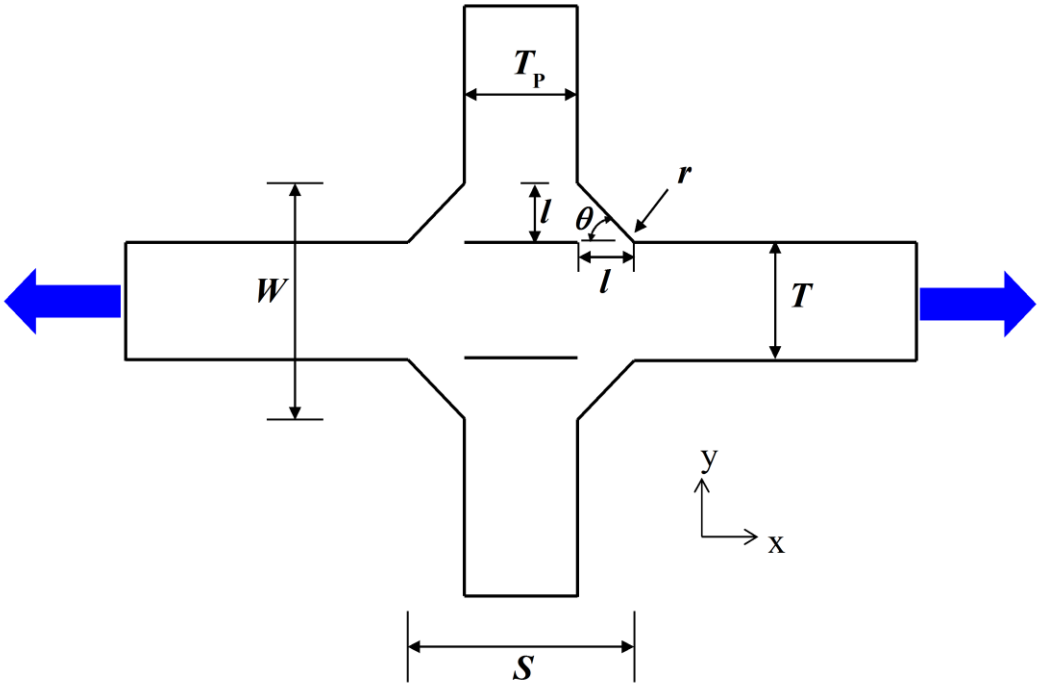

Figure 5.12 Weld geometry parameters for non-load-carrying cruciform joint under tension load.

5.3.3.2 Applied stress distribution along the crack path

In order to obtain the elastic stress distribution along the crack path, it is assumed that the crack initiate from the weld toe and propagate through the base metal along a path running perpendicular to the loading direction.

Under tension load, the stress distribution near the weld toe is determined from the estimation equation (Eq.5.36 and Fig.5.13) proposed by Glinka [97], taking K_t so obtained by Eq. (5.35) into account

$$\sigma_x(y) = \frac{K_t \sigma_n}{2\sqrt{2}}\left[\left(\frac{r}{y + r/2}\right)^{1/2} + \frac{1}{2}\left(\frac{r}{y + r/2}\right)^{3/2}\right] \tag{5.36}$$

where σ_n is the nominal stress, and r represents notch-tip radius (weld toe radius).

The stress apart from the weld toe is calculated by elastic finite element analysis (FEA). The stress distribution from the surface to the mid-thickness is synthesized from the results of these calculations. The combined stress distributions are shown in Fig.5.14.

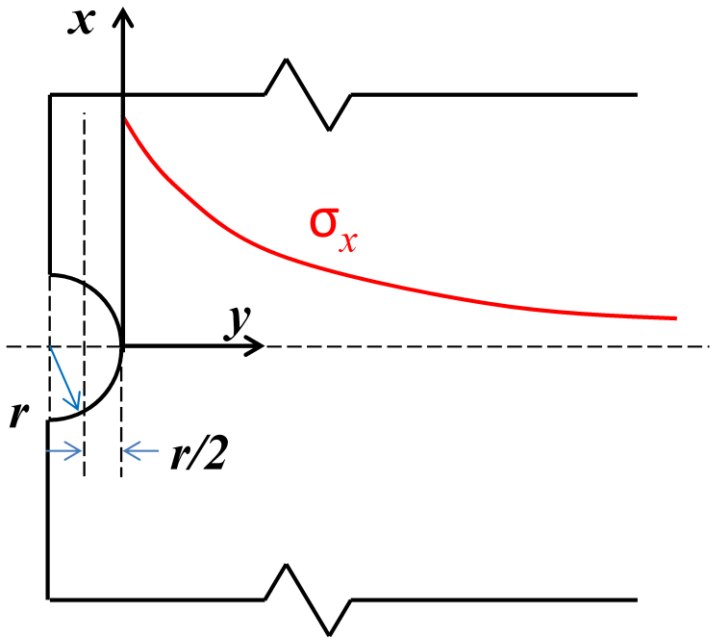

Figure 5.13 Symbol and coordinate used in Glinka's equation.

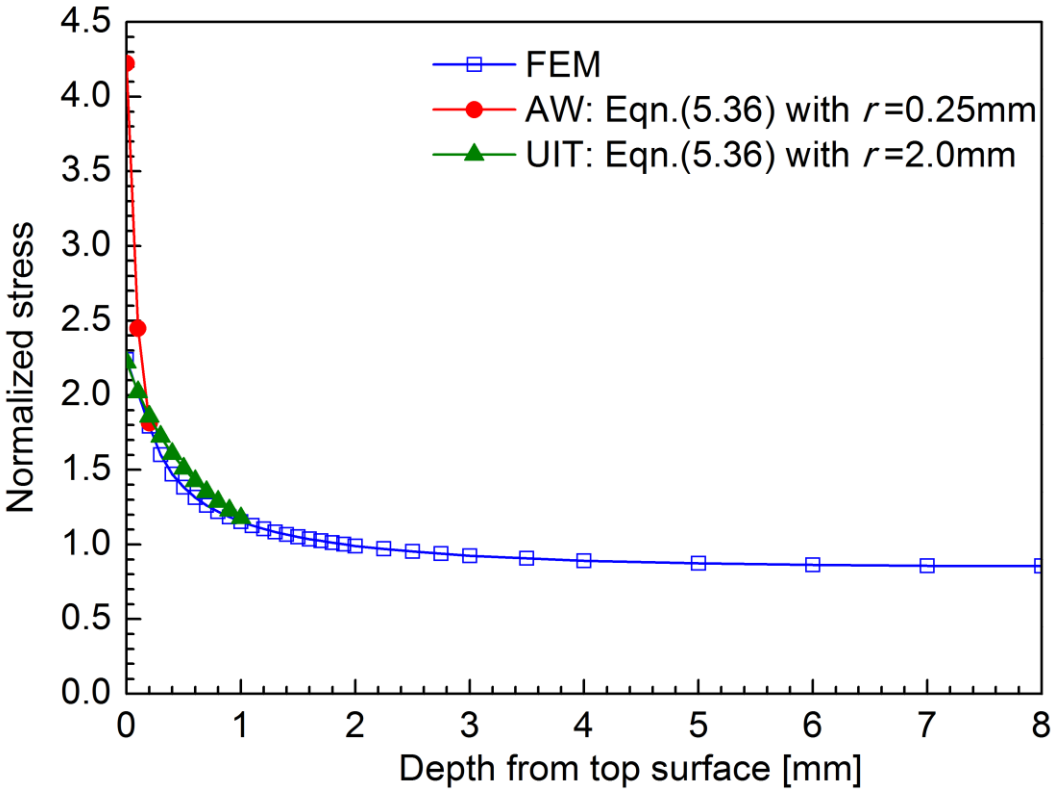

Figure 5.14 Assumed stress distribution near the weld toe.

5.3.3.3 Results of estimations and experiments (R=0.1)

Under the constant amplitude cyclic loading of R=0.1, the results of estimations, experiments given by Suzuki et al. [78], Okawa et al. [48] and FAT-values recommended by Marquis et al. [10] are compared in Fig.5.15. It should be noted here that FAT represents IIW fatigue class, i.e. the nominal stress range in megapascals corresponding to 95% survival probability at 2×10^6 cycles to failure. Considering the case of a transverse welds in high-strength steel (yield strength 355-550 MPa) which in as-weld condition is classified as FAT80 (slope m=3), the UIT treatment results in a FAT value of 140 (m=5).

From the Fig.5.15, it can be seen that the predicted fatigue strengths of as-weld and UIT cases show a good agreement with fatigue test results. These results demonstrate that the proposed fatigue life prediction method clearly distinguishes the difference of fatigue strengths of as-weld and UIT weld joints, by taking the properly evaluated stress concentration and residual stress distribution near the weld toe into account. Moreover, the experimental and predicted results of UIT case both show a greater improvement than the recommended FAT class but a similar slope m about 5. It should be noted that since multi initial crack followed by crack coalescence are not considered in this work, the present simulation results in a slight over-estimation of the as-weld case at high applied stress range. Referring to the simple calculation in Fig.5.9, it may be easier to understand that the occurrence of single shallow surface crack formed by coalescence of multi initial crack would accelerate the crack growth.

The predicted evolution of surface crack shapes of as-weld and UIT cases are compared in Fig.5.16. In as-weld joint, the crack growth along surface direction is more prominent than that along thickness direction because of the high tensile welding residual stress and stress concentration near the weld toe surface. On the other hand, the UIT-induced compressive residual stress and lower stress concentration state lead to a relatively higher aspect ratio of the UIT case, compared to that of as-weld case. It may explain the experimentally observed linear crack front in the as-weld specimen and curved crack front in the peened specimen, as previous reviewed in section 2.2.3.5.

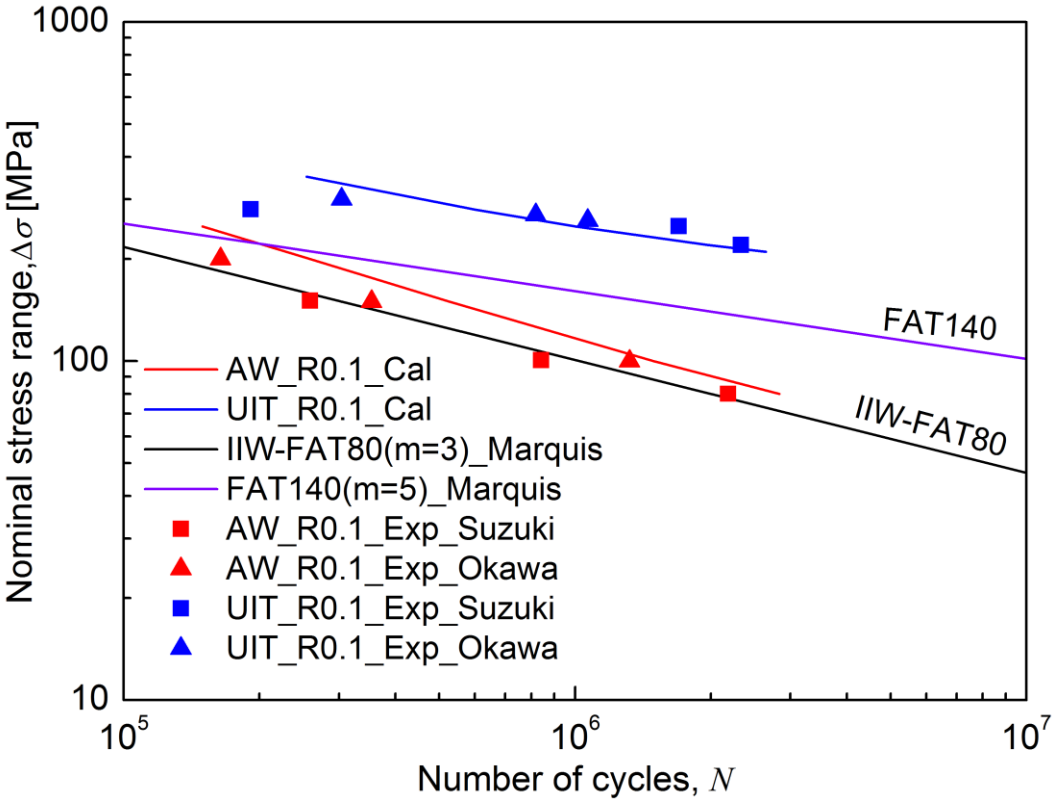

Figure 5.15 Validation of predicted S-N curves of as-weld and UIT joint (R=0.1).

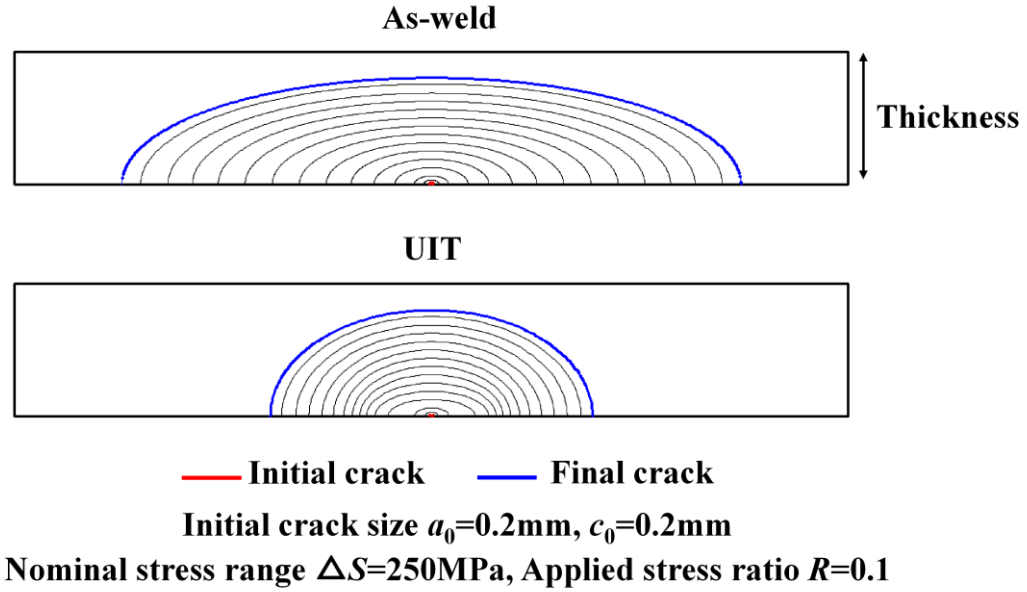

Figure 5.16 Predicted evolution of surface crack shapes.

5.3.3.4 Effect of high stress ratio and preload on UIT improvement

The fatigue strength of a welded joint is not sensitive to the stress ratio because the local stress ratio at the as-weld toe is generally high due to the tensile welding residual stress. However, the UIT changes tensile residual stress into compression at the weld toe, and the local stress ratio near the weld toe is decreased so as to enhance fatigue strength of UIT joint; hence, the effect of UIT-improved fatigue strength may be reduced at the condition of high stress ratio.

In order to investigate the effect of high stress ratio on fatigue strength of welded joints improved by UIT, the predicted and test results of UIT joint at the stress ratio of 0.5 are shown in Fig.5.17. Compared to the case of UIT joint at the stress ratio of 0.1, the fatigue strength improved by UIT at stress ratio of 0.5 has been obviously decreased, but it is still fairly higher than that of as-weld joint.

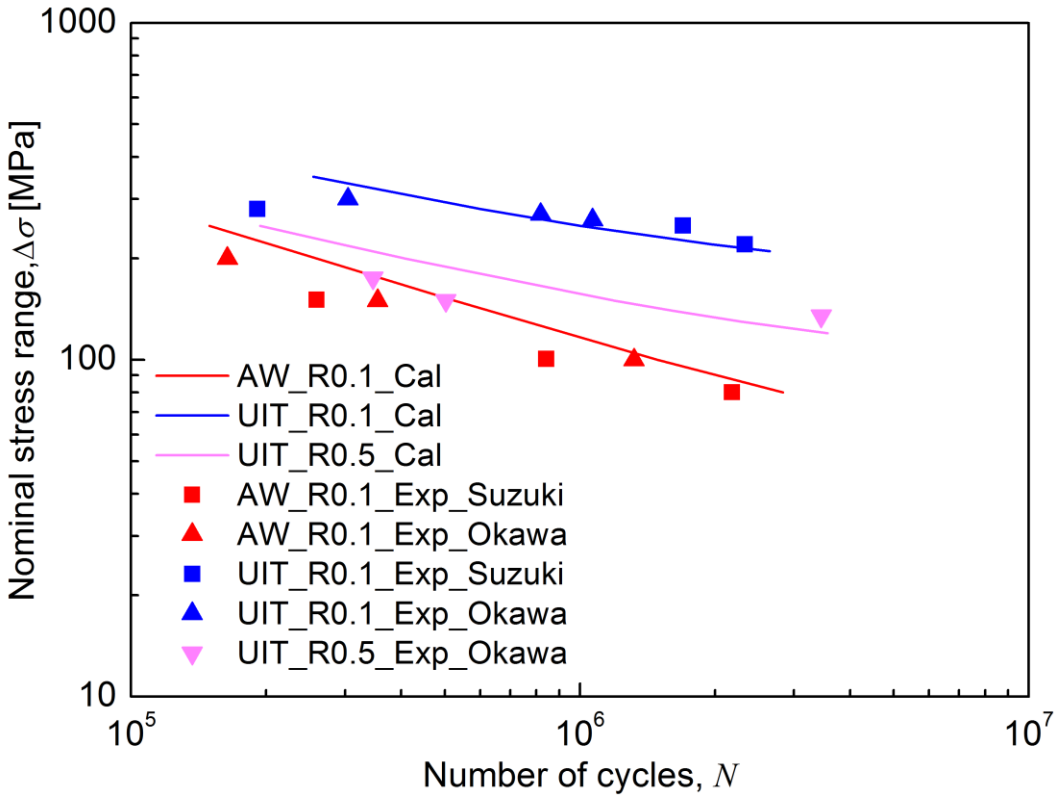

Figure 5.17 Effect of high stress ratio on fatigue strength improvement by UIT.

Based on the predicted in-depth residual stress distribution in UIT joint after tensile preload of 351MPa or compressive preload of 234MPa in section 4.4.5.4, the fatigue strengths of UIT-joint after preloads are evaluated, which are compared to the experimental results of Okawa et al. [48], as shown in Fig.5.18. After application of these preloads, the fatigue strengths of UIT-treated weld joint are slightly decreased, because there are still relatively high compressive residual stress remained near the weld toe. In addition, the fatigue strengths at 2×10^6cyles of each welded joint are summarized in Table.5.1. The good agreement between calculations and experiments can be confirmed, including considering the effects of stress ratio and preload on UIT improvement.

Table 5.1 Fatigue strength at 2×10^6cyles (MPa)

Cases	Experiment	Calculation
AW_R0.1	83	92
UIT_R0.1	236	229
UIT_R0.5	140	139
UIT+preload_R0.1*	205	210

* Averaged results of UIT_C234_R0.1 and UIT_T351_R0.1

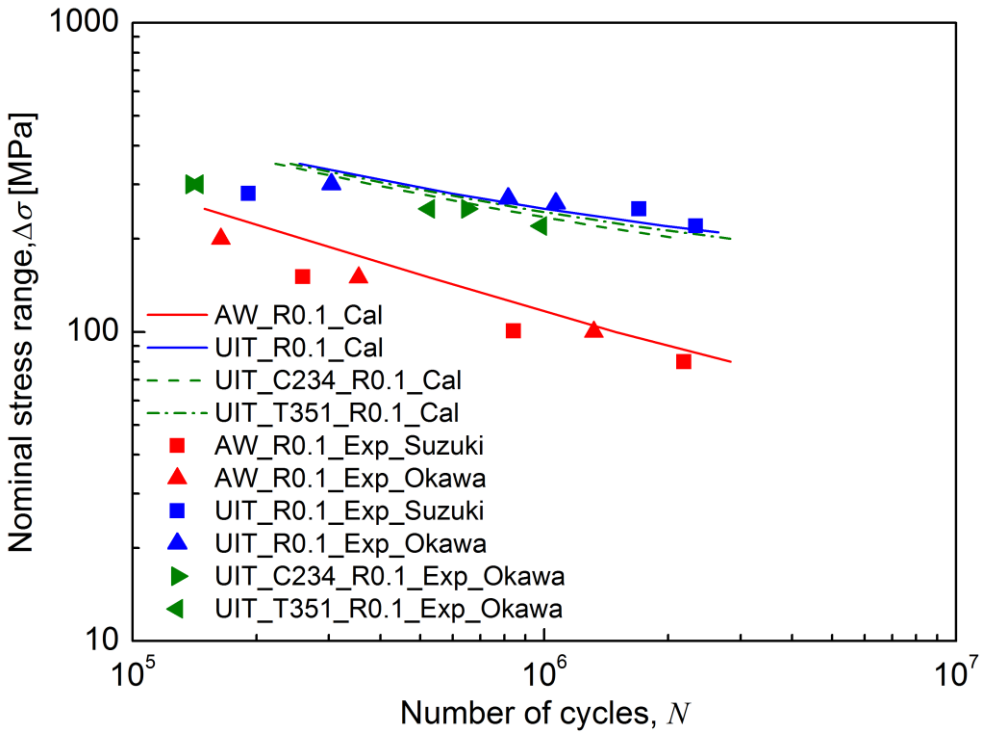

Figure 5.18 Effect of preload on fatigue strength improvement by UIT.

CHAPTER 6

CONLUSIONS AND RECOMMENDATIONS

6.1 Conclusions

The primary aim is to numerically investigate the mechanisms involved in the ultrasonic impact treatment (UIT) process and how these affect the fatigue strengths of the welded joints.

One new three-dimensional simulation approach has been developed, including thermo-mechanical welding simulation, dynamic elastic-plastic FE analysis of UIT-process and a fracture mechanics based evaluation of fatigue strengths of welded joints improved by UIT. The actual welding and UIT process parameters and local mechanical characteristics due to acoustic softening are considered, so that the proposed FE model may provide an effective tool to optimize the UIT-process in engineering structures. Finally, based on the predicted results of this work, the following conclusions may be drawn:

- For accurate welding residual stress analysis, the combination of kinematic hardening model and hypothetical annealing temperature 800 ^{o}C is recommended.

- Based on the existing experimental observations, simplified models to describe phenomena “ultrasonic impact” and “acoustic softening” have been proposed.

- The predicted deformation and compressive residual stress layer are found to be more pronounced when acoustic softening occurs, which is necessary to be considered in UIT simulation.

- The predicted internal residual stress distributions and weld toe shapes before and after UIT have been compared with experimental results, showing a fairly good agreement with each other. Therefore, the effectiveness of the proposed FE model can be confirmed.

- Taking the properly predicted residual stress and stress concentration state into account, the fracture mechanics based method could well quantitatively evaluate the fatigue strength improvement by UIT.

- From the predicted results, it can be found that the UIT-induced compressive residual stress would be more relaxed with higher compressive preloads. On the other hand, except extremely high tensile ones, the compressive residual stresses are expected to be maintained after tensile preloads. Overall, relatively high compressive residual stresses and fatigue strength improvement by UIT are still remained even after the occurrence of preloads.

- Although the fatigue strength of UIT-treated welded joints decreases with increasing stress ratio, it is still high than that of as-weld joints within the lower stress ranges.

6.2 Recommendations for future work

The following is a list of recommended areas for future research:

- In this work, the yield stress reduction due to acoustic softening effect has been indirectly calibrated with measured UIT-treated weld toe shape by trial and error. To have a more reliable physical FE model representing the UIT process, it is suggested to integrate an ultrasonic transducer to a tensile test machine to measure the material properties at different ultrasonic intensities, i.e. Young's modulus and yield stress. Moreover, an appropriate definition of ultrasonic energy distribution under the treated surface is required.

- The numerical analysis for other types of UIT-treated welded joints such as boxing fillet weld and butt welds are supposed to be performed with the proposed simulation approach, and validated with experimental measurements.

- For further investigation about the possibility of UIT-induced residual stress relaxation due to overload, the effects of larger compressive load and various welded joint types should be experimentally and numerically investigated.

- Only the calculation of single surface crack growth has been made in the current work, so it is realized the fatigue crack growth prediction of multiple initial cracks at the weld toe would be useful to improve the prediction accuracy.

- The area-integration weight functions for stress intensity factors of surface crack under arbitrary two-dimensional stress distributions in complex welded structures should be investigated.

REFERENCES

[1] Manteghi, S., & Maddox, S. J. Methods for fatigue life improvement of welded joints in medium and high strength steels. *IIW Document*, XIII-2006-04, 2004.

[2] ISSC Committee III.2: Fatigue and Fracture, *Proceedings of 18th International Ship and Offshore Structures Congress*, Vol.1, pp.365-434, 2012.

[3] Statnikov, E. Physics and mechanism of ultrasonic impact treatment. *IIW Document*, XIII-2004-04, 2004.

[4] Nose, T., & Okawa, T. Approaches for fundamental principles 2: total solution for fatigue of steel. *Nippon Steel Technical Report*, No. 101, pp. 158-163, 2012.

[5] Nose, T, Shimanuki, H., & Nakashima, K. Effects of ultrasonic peening on fatigue life in welded joints: application of anti-fatigue technologies to welded structures. *Conference Proceedings the Japan Society of Naval Architects and Ocean Engineers*, Vol. 5E, pp.75-76, 2007.

[6] Cheng, X., Fisher, J. W., Prask, H. J., Gnäupel-Herold, T., Yen, B. T., & Roy, S. Residual stress modification by post-weld treatment and its beneficial effect on fatigue strength of welded structures. *International Journal of Fatigue*, Vol. 25(9), pp. 1259-1269, 2003.

[7] Weich, I. Edge layer condition and fatigue strength of welds improved by mechanical post-weld improvement. *Welding in the World*, Vol. 55(1-2), pp.3-12, 2011.

[8] Yekta, R. T., Ghahremani, K., & Walbridge, S. Effect of quality control parameter variations on the fatigue performance of ultrasonic impact treated welds. *International Journal of Fatigue*, Vol. 55, pp. 245-256, 2013.

[9] Gao, H., Dutta, R. K., Huizenga, R. M., Amirthalingam, M., Hermans, M. J. M., Buslaps, T., & Richardson, I. M. Stress relaxation due to ultrasonic impact treat-

ment on multi-pass welds. *Science and Technology of Welding and Joining*, Vol. 19(6), pp. 505-513, 2014.

[10] Marquis, G. B., Mikkola, E., Yildirim, H. C., & Barsoum, Z. Fatigue strength improvement of steel structures by high-frequency mechanical impact: proposed fatigue assessment guidelines. *Welding in the World*, Vol.57 (6), pp. 803-822, 2013.

[11] Kirkhope, K. J., Bell, R., Caron, L., Basu, R. I., & Ma, K. T. Weld detail fatigue life improvement techniques. Part 1: review. *Marine structures*, Vol.12 (6), pp. 447-474, 1999.

[12] Haagensen, P. J., & Maddox, S. J. IIW Recommendations on Post Weld Improvement of Steel and Aluminum. *IIW Document*, XIII-1815-00, 2006.

[13] Marquis, G., & Barsoum, Z. Fatigue strength improvement of steel structures by high-frequency mechanical impact: proposed procedures and quality assurance guidelines. *Welding in the World*, Vol. 58(1), pp. 19-28, 2014.

[14] International Association of Classification Societies. Common structural rules for bulk carriers and oil tankers. Release January 2014.

[15] American Bureau of Shipping: Commentary on the guide for the fatigue assessment of offshore structures. Updated July 2014.

[16] Det Norske Veritas- Germanischer Lloyd. RP-C203 Fatigue design of offshore steel structures. Updated June 2014.

[17] Lloyd's Register. Shipright FDA, Level 1 procedure-structural detail design guide. 2009.

[18] Ryu, H. R., Kim, W. S., Ha, W. I., Kang, S. W., & Kim, M. H. Effect of toe grinding on fatigue strength of ship structure. *Journal of Ship Production*, Vol. 24(3), pp.152-160, 2008.

[19] Zhang, Y. H., & Maddox, S. J. Fatigue life prediction for toe ground welded joints. *International Journal of Fatigue*, Vol. 31(7), pp. 1124-1136, 2009.

[20] Perović, Z. D. Investigation of the fatigue strength of the welded joints treated by TIG dressing. *Archives of Materials Science*, Vol. 28(1-4), pp.113-117, 2007.

[21] Simoneau, M. R., Thibault, M. D., & Fihey, M. J. L. A Comparison of Residual Stress in Hammer-Peened, Multi-Pass Steel Welds–A514 (S690Q) and S41500. *Welding in the World*, Vol.53 (5-6), pp.124-134, 2009.

[22] Athreya, B. P., Singh, N. P., Pan, L., Huang, W., Jarrett, M., & Forck, J. A computational approach for fatigue life prediction in shot peened welded specimens. *Welding in the World*, Vol.57 (5), pp.675-684, 2013.

[23] Ohta, A., Watanabe, O., Matsuoka, K., Siga, C., Nishijima, S., Maeda, Y., & Kubo, T. Fatigue Strength Improvement of Box Welded Joints by Using Low Transformation Temperature Welding Material. *Quarterly Journal of the Japan Welding Society,* Vol. 18(1), pp.141-145, 2000. (In Japanese)

[24] Barsoum, Z., & Gustafsson, M. Fatigue of high strength steel joints welded with low temperature transformation consumables. *Engineering Failure Analysis*, Vol.16 (7), pp.2186-2194, 2009.

[25] Statnikov, E. Guide for application of ultrasonic impact treatment improving fatigue life of welded structures. *IIW Document*, XIII-1957-99, 1999.

[26] Applied Ultrasonics. http://www.appliedultrasonics.com/

[27] Roy, S., & Fisher, J. W. Enhancing fatigue strength by ultrasonic impact treatment. *International Journal of Steel Structures*, Vol. 5(3), pp.241-252, 2005.

[28] Lihavainen, V. M., Marquis, G., & Statnikov, E. Fatigue strength of a longitudinal attachment improved by ultrasonic impact treatment. *Welding in the World*, Vol. 48(5-6), pp. 67-73, 2004.

[29] Roy, S., Fisher, J. W., & Yen, B. T. Fatigue resistance of welded details enhanced by ultrasonic impact treatment (UIT). *International Journal of Fatigue*, Vol. 25(9), pp.1239-1247, 2003.

[30] Galtier, A., & Statnikov, E. The influence of ultrasonic impact treatment on fatigue behavior of welded joints in high-strength steel. *Welding in the World*, Vol. 48 (5-6), pp.61-66, 2004.

[31] Statnikov, E. S., Korolkov, O. V., & Vityazev, V. N. Physics and mechanism of ultrasonic impact. *Ultrasonics*, Vol.44, pp. 533-538, 2006.

[32] Blaha, F., & Langenecker, B. Tensile deformation of zinc crystal under ultrasonic vibration. Naturwissenschaften, Vol. 44, pp. 556-556, 1955.

[33] Langenecker, B. Effects of ultrasound on deformation characteristics of metals. *IEEE transactions on sonics and ultrasonics,* Vol. 13(1), pp. 1-8. 1966.

[34] Izumi, O., Oyama, K., & Suzuki, Y. On the superimposing of ultrasonic vibration during compressive deformation of metals. *Transactions of the Japan institute of metals*, Vol. 7(3), pp. 158-161, 1966.

[35] Izumi, O., Oyama, K., & Suzuki, Y. Effects of superimposed ultrasonic vibration on compressive deformation of metals. *Transactions of the Japan institute of metals*, Vol. 7(3), pp. 162-167, 1966.

[36] Daud, Y., Lucas, M., & Huang, Z. Modelling the effects of superimposed ultrasonic vibrations on tension and compression tests of aluminum. *Journal of Materials Processing Technology*, Vol. 186(1), pp. 179-190, 2007.

[37] Shalvandi, M., Hojjat, Y., Abdullah, A., & Asadi, H. Influence of ultrasonic stress relief on stainless steel 316 specimens: A comparison with thermal stress relief. *Materials & Design*, Vol. 46, pp. 713-723, 2013.

[38] Siddiq, A., & Ghassemieh, E. Thermomechanical analyses of ultrasonic welding process using thermal and acoustic softening effects. *Mechanics of Materials*, Vol. 40(12), pp. 982-1000, 2008.

[39] Mordyuk, B.N., & Prokopenko, G.I. Ultrasonic impact peening for surface properties' management. *Journal of Sound and Vibration*, Vol. 308(3), pp. 855-866, 2007.

[40] Nevill, G. E., & Brotzen, F. R. The effect of vibrations on the static yield strength of a low-carbon steel. *Proceeding-American Society for Testing Material*, Vol.57, pp.751-758, 1957.

[41] Kirchner, H. O. K., Kromp, W. K., Prinz, F. B., & Trimmel, P. Plastic deformation under simultaneous cyclic and unidirectional loading at low and ultrasonic frequencies. *Materials science and engineering*, Vol. 68(2), pp. 197-206, 1985.

[42] Eaves, A. E., Smith, A. W., Waterhouse, W. J., & Sansome, D. H. Review of the application of ultrasonic vibrations to deforming metals. *Ultrasonics*, Vol. 13(4), pp. 162-170, 1975.

[43] Yao, Z., Kim, G. Y., Faidley, L., Zou, Q., Mei, D., & Chen, Z. Effects of superimposed high-frequency vibration on deformation of aluminum in micro/meso-scale upsetting. *Journal of Materials Processing Technology*, Vol. 212(3), pp. 640-646, 2012.

[44] Wang, T., Wang, D., Huo, L., & Zhang, Y. Discussion on fatigue design of welded joints enhanced by ultrasonic peening treatment (UPT). *International Journal of Fatigue*, Vol. 31(4), pp.644-650, 2009.

[45] Mori, T., Shimanuki, H., & Tanaka, M. M. Effect of UIT on fatigue strength of web-gusset welded joints considering service condition of steel structures. *Welding in the World*, Vol. 56(4), pp. 141-149, 2012.

[46] REFRESH- Extension of the fatigue life of existing and new welded steel structures. 2010.

[47] Deguchi, T., Mouri, M., Hara, J., Kano, D., Shimoda, T., Inamura, F., & Koshio, K. Fatigue strength improvement for ship structures by Ultrasonic Peening. *Journal of marine science and technology*, Vol.17 (3), pp.360-369, 2012.

[48] Okawa, T., Shimanuki, H., Funatsu, Y., Nose, T., & Sumi, Y. Effect of preload and stress ratio on fatigue strength of welded joints improved by ultrasonic impact treatment. *Welding in the world*, Vol. 57(2), pp. 235-241, 2013.

[49] Huo, L., Wang, D., & Zhang, Y. Investigation of the fatigue behavior of the welded joints treated by TIG dressing and ultrasonic peening under variable-amplitude load. *International Journal of Fatigue*, Vol. *27*(1), pp. 95-101, 2005.

[50] Marquis, G. Failure modes and fatigue strength of improved HSS welds. *Engineering Fracture Mechanics*, Vol. 77(11), pp. 2051-2062. 2010.

[51] Yildirim, H. C., & Marquis, G. B. Fatigue strength improvement factors for high strength steel welded joints treated by high frequency mechanical impact. *International Journal of Fatigue*, Vol. 44, pp. 168-176, 2012.

[52] Tryfyakov, V. I., Mikheev, P. P., Kudryavtsev, V. F., & Reznik, D. N. Ultrasonic Impact Peening Treatment of Welds and Its Effect on Fatigue Resistance in Air and Seawater. *Offshore Technology Conference*, pp.183-193, 1993.

[53] Polezhayeva, H., Howarth, D., Kumar, M., Kang, J. K., Ermolaeva, N., & Lee, J. Y. Effect of Ultrasonic Peening on Fatigue Strength of Welded Marine Structures-Lloyd's Register Research Programme. *The Twenty-fourth International Ocean and Polar Engineering Conference*, pp. 359-365. 2014.

[54] Lixing, H., Dongpo, W., Wenxian, W., & Yufeng, Z. Ultrasonic peening and low transformation temperature electrodes used for improving the fatigue strength of welded joints. *Welding in the World*, Vol. 48(2), pp. 34-39, 2004.

[55] Ghahremani, K., & Walbridge, S. Fatigue testing and analysis of peened highway bridge welds under in-service variable amplitude loading conditions. *International Journal of Fatigue*, Vol. 33(3), pp. 300-312, 2011.

[56] Pedersen, M. M. M., Mouritsen, M. O. Ø., Hansen, M. M. R., Andersen, M. J. G., & Wenderby, M. J. Comparison of Post-Weld Treatment of High-Strength Steel Welded Joints in Medium Cycle Fatigue. *Welding in the World*, Vol. *54*(4), pp. 208-217, 2010.

[57] Nitschke-Pagel, T., & Dilger, K. Residual stresses and near-surface material condition of welded high strength steels after different mechanical post-weld treatments. *The Twentieth International Offshore and Polar Engineering Conference*, pp.269-275, 2010.

[58] Tai, M. & Miki, C. Improvement Effects of Fatigue Strength by Burr Grinding and Hammer Peening Under Variable Amplitude Loading. *Welding in the World*, Vol. 56(7-8), pp.109-117, 2012.

[59] Shimanuki, H., & Tanaka, M. Application of fatigue crack initiation suppression technology of welded structures by UIT, *NIPPON STEEL & SUMITOMO METAL CORPORATION Technical Report,* No.400, pp. 100-107, 2014.

[60] Roy, S. Experimental and analytical evaluation of enhancement in fatigue resistance of welded details subjected to post-weld ultrasonic impact treatment. Doctoral dissertation. Lehigh University, 2006.

[61] Weich, I. Fatigue behavior of mechanical post weld treated welds depending on mechanical post weld treated welds depending on the edge layer condition. Doctoral dissertation, Technischen Universität Brauschweig, 2008 (in German).

[62] Le Quilliec, G., et al: Mechanics and modelling of high frequency mechanical impact and its effect on fatigue. *Welding in the World*, Vol.57 (1), pp. 97-111, 2013.

[63] Yang, X.J., et al.: Optimization of the fatigue resistance of AISI304 stainless steel by ultrasonic impact treatment. *International Journal of Fatigue*, Vol.61, pp.28-38, 2014.

[64] SYSWELD Ver.2014, ESI GROUP.

[65] Goldak, J., Chakravarti, A., & Bibby, M. A new finite element model for welding heat sources. *Metallurgical transactions B*, Vol.15 (2), pp.299-305, 1984.

[66] Masubuchi, Ki. Analysis of welded structures: Residual stresses, distortion, and their consequences. *Pergamon Press*, 1980.

[67] Keavey, M., Mark, A., Dai, H., & Withers, P. J. Annealing Models in Welding Simulation: Conservative and Non-Conservative Residual Stress Distributions. *ASME 2010 Pressure Vessels and Piping Division/K-PVP Conference,* pp.1377-1384.2010.

[68] Liang, W., Murakawa, H., & Deng, D. Investigation of welding residual stress distribution in a thick-plate joint with an emphasis on the features near weld end-start. *Materials & Design*, Vol. 67, pp. 303-312, 2015.

[69] Xu, J. J., Gilles, P., Duan, Y. G., & Yu, C. Temperature and residual stress simulations of the NeT single-bead-on-plate specimen using SYSWELD. *International Journal of Pressure Vessels and Piping*, Vol. 99, pp. 51-60, 2012.

[70] Smith, M. C., & Smith, A. C. NeT bead-on-plate round robin: Comparison of residual stress predictions and measurements. *International Journal of Pressure Vessels and Piping*, Vol. 86(1), pp. 79-95, 2009.

[71] Hofmann, M., & Wimpory, R. C. NET TG1: Residual stress analysis on a single bead weld on a steel plate using neutron diffraction at the new engineering instrument 'STRESS-SPEC'. *International Journal of Pressure Vessels and Piping*, Vol. 86(1), pp.122-125, 2009.

[72] Ohms, C., Wimpory, R. C., Katsareas, D. E., & Youtsos, A. G. NET TG1: Residual stress assessment by neutron diffraction and finite element modeling on a single bead weld on a steel plate. *International Journal of Pressure Vessels and Piping*, Vol. 86(1), pp. 63-72, 2009.

[73] Pratihar, S., Turski, M., Edwards, L., & Bouchard, P. J. Neutron diffraction residual stress measurements in a 316L stainless steel bead-on-plate weld specimen. *International Journal of Pressure Vessels and Piping*, Vol. 86(1), pp. 13-19, 2009.

[74] Ficquet, X., Smith, D. J., Truman, C. E., Kingston, E. J., & Dennis, R. J. Measurement and prediction of residual stress in a bead-on-plate weld benchmark specimen. *International Journal of Pressure Vessels and Piping*, Vol. 86(1), pp. 20-30, 2009.

[75] Bate, S. K., Charles, R., & Warren, A. Finite element analysis of a single bead-on-plate specimen using SYSWELD. *International Journal of Pressure Vessels and Piping*, Vol. 86(1), pp. 73-78, 2009.

[76] Xu, J. J., Gilles, P., & Duan, Y. G. Simulation and Validation of Welding Residual Stresses Based on Non‐Linear Mixed Hardening Model. *Strain*, Vol. 48(5), pp.406-414, 2012.

[77] LS-DYNA Keyword User's Manual, Ver.971, 2007.

[78] Suzuki, T., Okawa, T., Shimanuki, H., Nose, T., Ohta, N., Suzuki, H., & Moriai, A. Effect of ultrasonic impact treatment (UIT) on fatigue strength of welded joints. *Advanced Materials Research*, Vol. 996, pp.736-742, 2014.

[79] Statnikov, E. Method for modifying or producing materials and joints with specific properties by generating and applying adaptive impulses a normalizing energy thereof and pauses there between. U.S.Patent No.7, 301,123, 2007.

[80] Meguid, S. A., Shagal, G., & Stranart, J. C. 3D FE analysis of peening of strain-rate sensitive materials using multiple impingement model. *International Journal of Impact Engineering*, Vol. *27*(2), pp. 119-134, 2002.

[81] Kim, T., Lee, H., Hyun, H. C., & Jung, S. Effects of Rayleigh damping, friction and rate-dependency on 3D residual stress simulation of angled shot peening. *Materials & Design*, Vol.46, pp.26-37, 2013.

[82] Dürr, A. Fatigue resistance of welded high strength steel structures using UIT post weld treatment, PhD thesis, Universität Stuttgart, 2007

[83] Ermolaeva, N. S., & Hermans, M. J. Research on Post-weld Impact Treatments of High-strength Steel. *The 24th International Ocean and Polar Engineering Conference*, pp. 410-417, 2014.

[84] Yildirim, H. C., & Marquis, G. B. A round robin study of high-frequency mechanical impact (HFMI)-treated welded joints subjected to variable amplitude loading. *Welding in the World*, Vol. 57(3), pp. 437-447, 2013.

[85] American Petroleum Institute. API 579-1 Recommended Practice for Fitness-For-Service, 2007.

[86] Shiratori, M., Miyoshi. T., & Tanigawa, K. Analysis of stress intensity factors for surface cracks subjected to arbitrarily distributed surface stresses. Transactions of the Japan Society of Mechanical Engineers A Vol.52 (474), pp.390–398, 1986 (in

Japanese).

[87] Wang, X., & Lambert, S. B. Stress intensity factors for low aspect ratio semi-elliptical surface cracks in finite-thickness plates subjected to non-uniform stresses. *Engineering Fracture Mechanics*, Vol. 51(4), pp. 517-532, 1995.

[88] Wang, X., & Lambert, S. B. Stress intensity factors and weight functions for high aspect ratio semi-elliptical surface cracks in finite-thickness plates. *Engineering fracture mechanics*, Vol. 57(1), pp.13-24, 1997.

[89] Raju, I. S., & Newman, J. C. Stress-intensity factors for a wide range of semi-elliptical surface cracks in finite-thickness plates. *Engineering Fracture Mechanics*, Vol. 11(4), pp. 817-829, 1979.

[90] Newman, J. C., & Raju, I. S. An empirical stress-intensity factor equation for the surface crack. *Engineering Fracture Mechanics*, Vol. 15(1), pp.185-192, 1981.

[91] ASME Code, Boiler& P. V. Rules for in-service inspection of nuclear power plant components. *An International Code, ASME, New York,* 2007.

[92] Tai, M., & Miki, C. Fatigue strength improvement by hammer peening treatment—verification from plastic deformation, residual stress, and fatigue crack propagation rate. *Welding in the World*, Vol. 58(3), pp. 307-318, 2014.

[93] Carpinteri, A., Brighenti, R., Huth, H. J., & Vantadori, S. Fatigue growth of a surface crack in a welded T-joint. *International Journal of Fatigue*, Vol. 27(1), pp.59-69, 2005.

[94] Carpinteri, A., Ronchei, C., Scorza, D., & Vantadori, S. Fracture mechanics based approach to fatigue analysis of welded joints. *Engineering Failure Analysis,* Vol. 49, pp.67-78, 2015.

[95] The Japan Welding Engineering Society. WES 2805 Method of assessment for flaws in fusion welded joints with respect to brittle fracture and fatigue crack growth, 1997.

[96] Tsuji, I. Estimation of stress concentration factor at weld toe of non-load carrying fillet welded joint. *The Japanese Society of Naval Architects and Ocean Engineers*, Vol.80, pp. 241-251, 1990 (in Japanese).

[97] Glinka, G. Calculation of inelastic notch-tip strain-stress histories under cyclic loading. *Engineering Fracture Mechanics*, Vol. 22(5), pp. 839-854, 1985.

APPENDIX A: LIST OF PUBLICATIONS FROM THIS RESEARCH

Published

1. Yuan, K.L. and Sumi, Y. Effect of Ultrasonic Impact Treatment (UIT) on Fatigue Life of Non-load-carrying Cruciform Joint. *Conference Proceedings JASNAOE*, Vol. 20, pp. 483-486, 2015.
2. Yuan, K.L. and Sumi, Y. Numerical Simulation of Ultrasonic Impact Treatment (UIT) Process of Welded Joints. *Conference Proceedings JSCES*, Vol. 20, B-6-1(6 pages), 2015.

Submitted and Accepted

1. Yuan, K.L. and Sumi, Y. Modelling of Ultrasonic Impact Treatment (UIT) of Welded Joints and Its Effect on Fatigue Strength. *Proceedings of 5th International Conference on Crack Path* (accepted).
2. Yuan, K.L. and Sumi, Y. Analysis on Fatigue Strength Improvement for Non-load-carrying Cruciform Joints by Ultrasonic Impact Treatment (UIT). *Journal of the Japan Society of Naval Architects and Ocean Engineers* (accepted).

Poster Presentation

Yuan, K.L., Sumi, Y and Shimanuki, H. Modelling and Simulation of Ultrasonic Impact Treatment (UIT) Process of Welded Joints, *JASNAOE*, Nagasaki, Japan, November 20, 2014

APPENDIX B: KEYWORD FILE OF LS-DYNA

B.1 Explicit Dynamic Finite Element Analysis of UIT

```
$ LS-DYNA Keyword file written by Jvision x64 3.1.5
$ Date: 2015/Jan/19(Mon) 09:39:15
$
*KEYWORD
$
$--------------------------------------------------------------------------------$
$     CONTROL BLOCK
$--------------------------------------------------------------------------------$
$
*CONTROL_ENERGY
$     hgen      rwen    slnten     rylen
         2         1         2         1
$
*CONTROL_HOURGLASS
$      ihq        qh
         6 0.0500000
$
*CONTROL_TERMINATION
$   endtim    endcyc     dtmin    endeng    endmas
 0.0002000
$
$--------------------------------------------------------------------------------$
$     DEFINE BLOCK
$--------------------------------------------------------------------------------$
$
$
*DEFINE_COORDINATE_NODES_TITLE
$                                                                         title
PIN AXIS
$      cid        n1        n2        n3      flag       dir
         1      8592    178964    170932                 Y
$
*DEFINE_CURVE_TITLE
$                                                                         title
material damping
$     lcid      sidr       sfa       sfo      offa      offo    dattyp
         1
$                  a1                  o1
 0.00000000000000000   500000.0000000000
 0.00020000000000000   500000.0000000000
$
$--------------------------------------------------------------------------------$
$     MAT BLOCK
$--------------------------------------------------------------------------------$
$
*MAT_PLASTIC_KINEMATIC_TITLE
$                                                                         title
```

```
S355J2
$      mid        ro         e        pr      sigy      etan      beta
         1 7.815e-09 206000.00 0.3000000 390.00000 596.00000 0.0000000
$      src       srp        fs        vp

$
*MAT_PLASTIC_KINEMATIC_TITLE
$                                                                             title
40% reduction
$      mid        ro         e        pr      sigy      etan      beta
         2 7.815e-09 206000.00 0.3000000 234.00000 357.60000 0.0000000
$      src       srp        fs        vp

$
*MAT_ELASTIC_TITLE
$                                                                             title
PIN
$      mid        ro         e        pr        da        db         k
         3 1.954e-08 206000.00 0.3000000
$
$-------------------------------------------------------------------------------$
$     SECTION BLOCK
$-------------------------------------------------------------------------------$
$
*SECTION_SOLID_TITLE
$                                                                             title
S355J2_PART1
$    secid    elform       aet
         1         1
$
*SECTION_SOLID_TITLE
$                                                                             title
S355J2 PART2
$    secid    elform       aet
         2         1
$
*SECTION_SOLID_TITLE
$                                                                             title
SOFTENING_PART1
$    secid    elform       aet
         3         1
$
*SECTION_SOLID_TITLE
$                                                                             title
SOFTENING_PART2
$    secid    elform       aet
         4         1
$
*SECTION_SOLID_TITLE
$                                                                             title
SOFTENING_PART3
$    secid    elform       aet
         5         1
$
*SECTION_SOLID_TITLE
$                                                                             title
SOFTENING_PART4
$    secid    elform       aet
         6         1
$
*SECTION_SOLID_TITLE
$                                                                             title
PIN
$    secid    elform       aet
         7         1
```

```
$
$-------------------------------------------------------------------------------$
$     PART BLOCK
$-------------------------------------------------------------------------------$
$
$
*PART
$                                                                 heading
S355J2_PART1
$      pid     secid       mid     eosid      hgid      grav    adpopt      tmid
         1         1         1
$
*PART
$                                                                 heading
S355J2_PART2
$      pid     secid       mid     eosid      hgid      grav    adpopt      tmid
         2         2         1
$
*PART
$                                                                 heading
SOFTENING_PART1
$      pid     secid       mid     eosid      hgid      grav    adpopt      tmid
         3         3         2
$
*PART
$                                                                 heading
SOFTENING_PART2
$      pid     secid       mid     eosid      hgid      grav    adpopt      tmid
         4         4         2
$
*PART
$                                                                 heading
SOFTENING_PART3
$      pid     secid       mid     eosid      hgid      grav    adpopt      tmid
         5         5         1
$
*PART
$                                                                 heading
SOFTENING_PART4
$      pid     secid       mid     eosid      hgid      grav    adpopt      tmid
         6         6         1
$
*PART
$                                                                 heading
PIN
$      pid     secid       mid     eosid      hgid      grav    adpopt      tmid
         7         7         3
$
$-------------------------------------------------------------------------------$
$     DATABASE BLOCK
$-------------------------------------------------------------------------------$
$
*DATABASE_ELOUT
$       dt    binary      lcur     ioopt      dthf     binhf
 0.0000010         1
$
*DATABASE_GLSTAT
$       dt    binary      lcur     ioopt      dthf     binhf
 0.0000010         1
$
*DATABASE_MATSUM
$       dt    binary      lcur     ioopt      dthf     binhf
 0.0000010         1
$
*DATABASE_NODOUT
```

```
$       dt    binary      lcur     ioopt      dthf     binhf
 0.0000010         1
$
*DATABASE_RCFORC
$       dt    binary      lcur     ioopt      dthf     binhf
 0.0000010         1
$
*DATABASE_BINARY_D3PLOT
$       dt      lcdt      beam     npltc    psetid
 0.0000050
$
*DATABASE_EXTENT_BINARY
$    neiph     neips    maxint    strflg    sigflg    epsflg    rltflg    engflg
                                      1
$   cmpflg    ieverp    beamip     dcomp      shge     stssz    n3thdt   ialemat
                                                                    2
$  nintsld   pkp_sen      sclp     hydro     msscl     therm    intout     nodout
                                                                  ALL       ALL
$     dtdt

$
*DATABASE_HISTORY_SOLID
$      id1       id2       id3       id4       id5       id6       id7       id8
     65606     65906     66206     66506     66806     67106     67406     67706
      .
      .
      .
    125886    126186    130046    130346    142566    142866    143166    143466
$
$--------------------------------------------------------------------------------$
$     SET BLOCK
$--------------------------------------------------------------------------------$
$
*SET_NODE_TITLE
$                                                                             title
SYM_X
$      sid       da1       da2       da3       da4
         1
$     nid1      nid2      nid3      nid4      nid5      nid6      nid7      nid8
      8454      8457      8465      8470      8475      8480      8508      8509
      .
      .
      .
    178803    178808    178813    178818    178842    178847    178852    178857
$
*SET_PART_TITLE
$                                                                             title
Slave_part
$      sid       da1       da2       da3       da4
         1
$     pid1      pid2      pid3      pid4      pid5      pid6      pid7      pid8
         1         2         3         4         5         6
$
*SET_NODE_TITLE
$                                                                             title
LOWER ATTACHMENT_FIX_Y
$      sid       da1       da2       da3       da4
         2
$     nid1      nid2      nid3      nid4      nid5      nid6      nid7      nid8
     16522     16523     16524     16525     16526     24639     24640     24641
      .
      .
      .
    170746    170747    170748    170749    178862    178863    178864    178865
$
```

```
*SET_NODE_TITLE
$                                                                         title
Upper Attachment_FIX_Y
$      sid       da1       da2       da3       da4
         3
$     nid1      nid2      nid3      nid4      nid5      nid6      nid7      nid8
     16477     16478     16479     16480     16481     24594     24595     24596
      .
      .
      .
    170701    170702    170703    170704    178817    178818    178819    178820
$
*SET_NODE_TITLE
$                                                                         title
FIX_Z
$      sid       da1       da2       da3       da4
         4
$     nid1      nid2      nid3      nid4      nid5      nid6      nid7      nid8
      8430      8431      8432      8436      8437      8438      8442      8443
      .
      .
      .
    178857    178858    178859    178860    178861    178862    178863    178864
$
*SET_NODE_TITLE
$                                                                         title
pin
$      sid       da1       da2       da3       da4
         5
$     nid1      nid2      nid3      nid4      nid5      nid6      nid7      nid8
    178964    178965    178966    178967    178968    178969    178970    178971
     .
     .
     .
    181281    181282    181283    181284    181285    181286    181287    181288
$
$-------------------------------------------------------------------------------$
$     BOUNDARY BLOCK
$-------------------------------------------------------------------------------$
$
*BOUNDARY_SPC_SET_ID
$       id                                                                heading
$ nid/nsid       cid      dofx      dofy      dofz     dofrx     dofry     dofrz
         1SYM_X
         1                  1
         2lower attachment_FIX_Y
         2                            1
         3FIX_Z PLANE STRAIN
         4                                      1
         4PIN
         5         1         1                  1         1         1         1
$
$-------------------------------------------------------------------------------$
$     DAMPING BLOCK
$-------------------------------------------------------------------------------$
$
*DAMPING_PART_MASS_SET
$ pid/psid      lcid        sf      flag
         1         1
$
$-------------------------------------------------------------------------------$
$     INITIAL BLOCK
$-------------------------------------------------------------------------------$
$
$
```

```
*INITIAL_STRESS_SOLID
$      eid      nint     nhisv     large     ivflg
$    sigxx     sigyy     sigzz     sigxy     sigyz     sigzx       eps
     38886         1
 52.884850-92.845380 379.68454-29.406170 0.0000010 0.0000010 0.0025080
      .
      .
      .
      8065         1
 10.703320 80.346710 452.71207 51.599120 0.0000060 0.0000000 0.0139430
$
*INITIAL_VELOCITY_GENERATION
$       id      styp     omega        vx        vy        vz     ivatn
$       xc        yc        zc        nx        ny        nz     phase
         7         2          -1913.8000-4619.2000

$
$-------------------------------------------------------------------------------$
$     CONTACT BLOCK
$-------------------------------------------------------------------------------$
$
*CONTACT_AUTOMATIC_SURFACE_TO_SURFACE
$      ssid      msid     sstyp     mstyp    sboxid    mboxid       spr       mpr
         1         7         2         3
$       fs        fd        dc        vc       vdc    penchk        bt        dt
 0.5000000
$      sfs       sfm       sst       mst      sfst      sfmt       fsf       vsf
 10.000000 10.000000
$
$-------------------------------------------------------------------------------$
$     NODE BLOCK
$-------------------------------------------------------------------------------$
$
*NODE
$    nid               x               y               z      tc      rc
    8430 11.318905000000 1.7023126000000 0.0000000000000
    .
    .
    .
  181291 18.733500000000 5.2617786000000 0.3846980900000
$
$-------------------------------------------------------------------------------$
$     ELEMENT_SOLID BLOCK
$-------------------------------------------------------------------------------$
$
*ELEMENT_SOLID
$    eid     pid
$     n1      n2      n3      n4      n5      n6      n7      n8      n9     n10
    7926       2
    8430    8431   16548   16547    8432    8432   16549   16549
    .
    .
    .
  167660       7
  181285  181286  181291  181290  179054  179055  179060  179059
$
*END
```

B.2 Implicit Static Finite Element Analysis of Preload after UIT

```
$ LS-DYNA Keyword file written by Jvision x64 3.1.5
$ Date: 2015/Feb/10(Tue) 10:04:45
$
*KEYWORD
$
$--------------------------------------------------------------------------------$
$     CONTROL BLOCK
$--------------------------------------------------------------------------------$
$
*CONTROL_ENERGY
$     hgen      rwen    slnten     rylen
         2         1         2         1
$
*CONTROL_HOURGLASS
$      ihq        qh
         6 0.0500000
$
*CONTROL_TERMINATION
$   endtim    endcyc     dtmin    endeng    endmas
 2.1320000
$
*CONTROL_IMPLICIT_GENERAL
$   imflag       dt0    imform      nsbs       igs     cnstn      form    zero_v
         4 0.0050000                              1
$
*CONTROL_IMPLICIT_AUTO
$    iauto    iteopt    itewin     dtmin     dtmax     dtexp     kfail    kcycle
         1        11         5 0.0000010 0.0500000 0.0000100
$
*CONTROL_IMPLICIT_SOLVER
$   lsolvr    lprint     negev     order      drcm    drcprm   autospc   autotol
         4         1         2         0
$
*CONTROL_IMPLICIT_SOLUTION
$   nsolvr    ilimit    maxref     dctol     ectol     rctol     lstol    abstol
         2         1       100 0.0010000 0.0100000
$    dnorm    diverg     istif   nlprint    nlnorm   d3itctl     cpchk
                                       1
$
$--------------------------------------------------------------------------------$
$     DEFINE BLOCK
$--------------------------------------------------------------------------------$
$
*DEFINE_CURVE_TITLE
$                                                                             title
Preload
$     lcid      sidr       sfa       sfo      offa      offo    dattyp
         2
$                 a1                  o1
  0.1320000000000000 0.00000000000000000
  0.6320000000000000   234.0000000000000
   1.632000000000000   234.0000000000000
   2.132000000000000 0.00000000000000000
$
$--------------------------------------------------------------------------------$
$     MAT BLOCK
$--------------------------------------------------------------------------------$
$
*MAT_PLASTIC_KINEMATIC_TITLE
$                                                                             title
```

```
S355J2
$      mid        ro          e        pr      sigy      etan      beta
         1 7.815e-09 206000.00 0.3000000 390.00000 596.00000 0.0000000
$      src       srp        fs        vp

$
$-------------------------------------------------------------------------------$
$     SECTION BLOCK
$-------------------------------------------------------------------------------$
$
*SECTION_SOLID_TITLE
$                                                                         title
S355J2_PART1
$    secid    elform       aet
         1         1
$
*SECTION_SOLID_TITLE
$                                                                         title
S355J2 PART2
$    secid    elform       aet
         2         1
$
*SECTION_SOLID_TITLE
$                                                                         title
SOFTENING_PART1
$    secid    elform       aet
         3         1
$
*SECTION_SOLID_TITLE
$                                                                         title
SOFTENING_PART2
$    secid    elform       aet
         4         1
$
*SECTION_SOLID_TITLE
$                                                                         title
SOFTENING_PART3
$    secid    elform       aet
         5         1
$
*SECTION_SOLID_TITLE
$                                                                         title
SOFTENING_PART4
$    secid    elform       aet
         6         1
$

$-------------------------------------------------------------------------------$
$     PART BLOCK
$-------------------------------------------------------------------------------$
$
*PART
$                                                             heading
S355J2_PART1
$      pid     secid       mid     eosid      hgid      grav    adpopt      tmid
         1         1         1
$
*PART
$                                                             heading
S355J2_PART2
$      pid     secid       mid     eosid      hgid      grav    adpopt      tmid
         2         2         1
$
*PART
$                                                             heading
```

```
SOFTENING_PART1
$      pid     secid       mid     eosid      hgid      grav    adpopt      tmid
         3         3         1
$
*PART
$                                                                 heading
SOFTENING_PART2
$      pid     secid       mid     eosid      hgid      grav    adpopt      tmid
         4         4         1
$
*PART
$                                                                 heading
SOFTENING_PART3
$      pid     secid       mid     eosid      hgid      grav    adpopt      tmid
         5         5         1
$
*PART
$                                                                 heading
SOFTENING_PART4
$      pid     secid       mid     eosid      hgid      grav    adpopt      tmid
         6         6         1
$
$--------------------------------------------------------------------------------$
$     DATABASE BLOCK
$--------------------------------------------------------------------------------$
$
*DATABASE_ELOUT
$       dt    binary      lcur     ioopt      dthf     binhf
 0.0010000         1
$
*DATABASE_GLSTAT
$       dt    binary      lcur     ioopt      dthf     binhf
 0.0010000         1
$
*DATABASE_MATSUM
$       dt    binary      lcur     ioopt      dthf     binhf
 0.0010000         1
$
*DATABASE_NODOUT
$       dt    binary      lcur     ioopt      dthf     binhf
 0.0010000         1
$
*DATABASE_RCFORC
$       dt    binary      lcur     ioopt      dthf     binhf
 0.0010000         1
$
*DATABASE_BINARY_D3PLOT
$       dt      lcdt      beam     npltc    psetid
 0.0010000
$
*DATABASE_EXTENT_BINARY
$    neiph     neips    maxint    strflg    sigflg    epsflg    rltflg    engflg
                                      1
$   cmpflg    ieverp    beamip     dcomp      shge     stssz    n3thdt   ialemat
                                                                    2
$  nintsld   pkp_sen      sclp     hydro     msscl     therm    intout    nodout
                                                                  ALL       ALL
$     dtdt

$
*DATABASE_HISTORY_SOLID
$      id1       id2       id3       id4       id5       id6       id7       id8
     65606     65906     66206     66506     66806     67106     67406     67706
     .
     .
```

```
    125886    126186    130046    130346    142566    142866    143166    143466
$
$-------------------------------------------------------------------------------$
$     SET BLOCK
$-------------------------------------------------------------------------------$
$
*SET_NODE_TITLE
$                                                                         title
SYM_X
$      sid       da1       da2       da3       da4
         1
$     nid1      nid2      nid3      nid4      nid5      nid6      nid7      nid8
      8454      8457      8465      8470      8475      8480      8508      8509
      .
      .
    178803    178808    178813    178818    178842    178847    178852    178857
$
*SET_SEGMENT_TITLE
$                                                                         title
load
$      sid       da1       da2       da3       da4
         1
$       n1        n2        n3        n4        a1        a2        a3        a4
     13206     13207     21324     21323
      .
      .
    169902    170409    178526    178019
$
*SET_NODE_TITLE
$                                                                         title
LOWER ATTACHMENT_FIX_Y
$      sid       da1       da2       da3       da4
         2
$     nid1      nid2      nid3      nid4      nid5      nid6      nid7      nid8
     16522     16523     16524     16525     16526     24639     24640     24641
      .
      .
    170746    170747    170748    170749    178862    178863    178864    178865
$
*SET_NODE_TITLE
$                                                                         title
Upper Attachment_FIX_Y
$      sid       da1       da2       da3       da4
         3
$     nid1      nid2      nid3      nid4      nid5      nid6      nid7      nid8
     16477     16478     16479     16480     16481     24594     24595     24596
      .
      .
    170701    170702    170703    170704    178817    178818    178819    178820
$
*SET_NODE_TITLE
$                                                                         title
FIX_Z
$      sid       da1       da2       da3       da4
         4
$     nid1      nid2      nid3      nid4      nid5      nid6      nid7      nid8
      8430      8431      8432      8436      8437      8438      8442      8443
      .
      .
    178857    178858    178859    178860    178861    178862    178863    178864
$
$-------------------------------------------------------------------------------$
$     BOUNDARY BLOCK
$-------------------------------------------------------------------------------$
$
```

```
*BOUNDARY_SPC_SET_ID
$       id                                                                  heading
$ nid/nsid       cid      dofx      dofy      dofz     dofrx     dofry     dofrz
         1SYM_X
         1                   1
         2upper attachment_FIX_Y
         3                              1
         3FIX_Z PLANE STRAIN
         4                                        1
$
$-------------------------------------------------------------------------------$
$     LOAD BLOCK
$-------------------------------------------------------------------------------$
$
$
*LOAD_SEGMENT_SET
$     ssid      lcid        sf        at
         1         2
$
$-------------------------------------------------------------------------------$
$     RESTART BLOCK
$-------------------------------------------------------------------------------$
$
$
*STRESS_INITIALIZATION
$     pido      pidn
         1         1
         2         2
         3         3
         4         4
         5         5
         6         6
$
$-------------------------------------------------------------------------------$
$     NODE BLOCK
$-------------------------------------------------------------------------------$
$
$
*NODE
$    nid               x               y               z      tc      rc
    8430 11.318905000000 1.7023126000000 0.0000000000000
    .
    .
  178866 8.0000000000000-56.000000000000-4.0000000000000
$
$-------------------------------------------------------------------------------$
$     ELEMENT_SOLID BLOCK
$-------------------------------------------------------------------------------$
$
$
*ELEMENT_SOLID
$    eid     pid
$     n1       n2      n3      n4      n5      n6      n7      n8      n9     n10
    7926       2
    8430    8431   16548   16547    8432    8432   16549   16549
    .
    .
  165685       1
  178860  178865  178866  178861  170743  170748  170749  170744
$
*END
```

B.3 Restart Analysis Control (C-language)

```
#include<stdio.h>
#include<direct.h>
#include<stdlib.h>
#include <windows.h>

int main()
{
	char rootdirectory[1024];
	char directory[1024];


	_getcwd(directory, sizeof(directory));
	printf("in %s¥n", directory);
	// to modify the current directory as that of calculation
	_chdir("K:/UIT_FINAL_BOTHSIDE/UIT_Cruciform/40% reduction_5ms");
	_getcwd(rootdirectory, sizeof(rootdirectory));
	printf("in %s¥n", rootdirectory);



	char newcommand[1024];
	char newdir[1024];
	char olddir[1024];
	char oldfilename[1024];

	sprintf_s(olddir, "2th");
	//
	_chdir(olddir);
	//
	system("ls-dyna_smp_s_R700_winx64_ifort101.exe i=2th.key r=d3dump01");
	_chdir(rootdirectory);


	// change the number of i, for setting the start of calculation
	for (int i = 3; i <= 660; i++) {
		sprintf_s(newdir, "%dth", i);
		if (i <= 10) {
			sprintf_s(oldfilename, "d3dump0%d", i - 1);
		}
		if (i > 10) {
			sprintf_s(oldfilename, "d3dump%d", i - 1);
		}

		//
		sprintf_s(newcommand, "copy ¥"%s¥¥%s¥"  ¥"%s¥"", olddir, oldfilename,
newdir);
		system(newcommand);
		_chdir(newdir);
		// unit of sleep function is milisecond
		Sleep(5000);
```

```
                //
                sprintf_s(newcommand, "ls-dyna_smp_s_R700_winx64_ifort101.exe i=%dth.key
r=%s", i, oldfilename);
                system(newcommand);

                _chdir(rootdirectory);
                sprintf_s(olddir, "%s", newdir);
        }

        return(0);
}
```